Imperial College London
Department of Chemistry

# Understanding the Environmental Degradation of Methylammonium Lead Iodide Perovskite

Nicholas Paul Aristidou

Submitted in part fulfillment of the requirements
for the degree of Doctor of Philosophy at
Imperial College London, September 2018


I hereby declare that this thesis and the work reported herein was composed by and originated entirely from me. Information derived from the published and unpublished work of others has been acknowledged in the text and references are given in the list of sources.

Nicholas Paul Aristidou (2018)

## Abstract

Hybrid lead halide perovskite semiconductors have accelerated to the forefront of photovoltaics. These materials possess highly desirable features including, fast charge transport, high extinction coefficients, large spectral overlap and solution process-ability. As a result of these, low-cost devices have emerged boasting impressive power conversion efficiencies in excess of 20%. The rapid development of this technology is in part due to the materials versatility allowing numerous device configurations and fabrication techniques to be employed. Unfortunately, the excitement surrounding perovskites is hampered by their inability to withstand environmental stress. These systems have been found to exhibit significant performance losses and undergo irreversible material degradation when exposed to oxygen and light. Highlighted from these initial findings is that under these conditions, the reactive oxygen species superoxide can form and breakdown the perovskite crystal.

A greater understanding of the mechanistic action leading to the generation of superoxide has been achieved through a powerful combination of experimental and computational results. The work has examined the role of material selection in the fabrication of devices. In addition the role of morphology of the perovskite has also been examined, where electron extraction from the perovskite layer is critical in achieving long term stability. The driving force for separation and the velocity at which electrons can be extracted are critical components in the effectiveness of an electron extraction layer in aiding stability enhancements. Rapid oxygen diffusion and iodide vacancies have been identified as key contributors to the mechanistic formation of superoxide. In order to achieve this a unique combination of isothermal gravimetric analysis and Time-of-Flight secondary ion mass spectrometry were employed. Critically these showed the rapid uptake of oxygen and the ubiquitous presence of these species after exposure to air. Inspired by these results, new methods have been developed to generate perovskite solar cells with increased performance life-time. The work herein, has also identified the impact of the selection of the organic cation and exchanging the halide upon the stability towards oxygen and light. Furthermore, the consequence of introducing moisture into the equation has been considered and revealed greater detail about the mechanistic formation of superoxide from these species.

The generation of superoxide in perovskite materials for photovoltaic applications is highly undesirable and persists as a key issue regarding their commercial employment. However,

inspired by the fact photo-absorbers can generate superoxide a new application where the generation of the species could be used in a productive way is explored. To this end, the generation of superoxide from the organic polymer P3HT is explored. The production of superoxide from films is then harnessed to react with another species in a solution media. This simulation, leads to potential application where a contaminated solution, for example with a biological species, could be cleaned by addition of a P3HT film, oxygen and light. Here, the superoxide species would form from the film and then react and denature the contaminant.

## Acknowledgements

I would like to thank the following people for their generous support and guidance throughout this research.

Saif Haque, who has kindly allowed me to pursue my research interests and provided me valuable discussions and help throughout the whole project. His open door has been vital to my work and has helped spark the numerous experiments required to create successful pieces of work or to discuss food options and his great recommendation of Pic's peanut butter.

Chris Eames, for his invaluable skill in computational chemistry that has helped elevate the quality of the discussion of the experimental work. The complimentary studies conducted have provided insights that have enormously improved my understanding of the field. I'd also like to thank the following collaborators for their contributions, be it their experimental skill or their informative discussions. Mohammed Mohktar, Jan Kosco, Alex Aziz, Seb Pont, Dan, Bryant and Eurig Jones.

To the Haque group who have made the PhD experience what it has been. Their presence and support in and out of the lab have contributed to my experience and it is one that I will not forget.

Finally, I'd like to thank my wife and my family for their enduring support and love.

To my Wife, Tia and my Family.

*We are what we repeatedly do. Excellence, then, is not an act, but a habit.*

- Aristotle

**Fast oxygen diffusion and iodide defects mediate oxygen-induced degradation of perovskite solar cells.** Nicholas Aristidou, Christopher Eames, Irene Sanchez-Molina, Xiangnan Bu, Jan Kosco, M. Saiful Islam and Saif A. Haque. Nature Communications, **8**, 2017.

**Insights into the increased degradation rate of CH3NH3PbI3 solar cells in combined water and O2 environments.** Nick Aristidou, Christopher Eames, M. Saiful Islam and Saif A. Haque. Journal of Materials Chemistry A, **5**, 25469-25475, 2017.

**Tuning CH3NH3Pb(I1xBrx)3 perovskite oxygen stability in thin films and solar cells.** Sebastian Pont, Daniel Bryant, Chieh-Ting Lin, Nicholas Aristidou, Scot Wheeler, Xuerui Ma, Robert Godin, Saif A. Haque and James R. Durrant. Journal of Materials Chemistry A, **20**, 2017.

**Light and oxygen induced degradation limits the operational stability of methylammonium lead triiodide perovskite solar cells.** Daniel Bryant, Nicholas Aristidou, Sebastian Pont, Irene Sanchez-Molina, Thana Chotchunangatchaval, Scot Wheeler, James R. Durrant and Saif A. Haque. Energy Environmental Sciences, **9**, 1655-1660, 2016.

**CH3NH3PbI3 films prepared by combining 1- and 2-step deposition: how crystal growth conditions affect properties.** Muhamad Z. Mokhtar, Mu Chen, Eric Whittaker, Bruce Hamilton, Nicholas Aristidou, Simko Ramadan, Ali Gholinia, Saif A. Haque, Paul O'Brien and Brian R. Saunders. Physical Chemistry Chemical Physics, **10**, 2017.

**Toward Improved Environmental Stability of Polymer:Fullerene and Polymer: Non-fullerene Organic Solar Cells: A Common Energetic Origin of Light and Oxygen Induced Degradation.**,Emily M. Speller, Nicholas Aristidou, Mark F. Wyatt, Laia Francs, George Fish, Hyojung Cha, Harrison Ka Hin Lee, Joel Luke, Andrew Wadsworth, Iain McCulloch be, Ji-Seon Kim, Saif Haque, James R. Durrant, Stoichko D. Dimitrov, Wing C. Tsoi, Zhe., submitted to Energy Environ. Sci., 2018.

**Surface Passivation of Perovskite Films via Iodide Salt Coatings for Enhanced Stability of Organic Lead Halide Perovskite Solar Cells.**,Xiangnan Bu Robert J. E. Westbrook Luis Lanzetta, Dong Ding, Thana Chotchuangchutchaval, Nicholas Aristidou, Saif A. Haque, Sol. RPL, 2018.

**Evidence for surface defect passivation as the origin of the remarkable photostability of unencapsulated perovskite solar cells employing aminovaleric acid as a processing additive**,Chieh-Ting Lin, Francesca De Rossi, Jinhyun Kim, Jenny Baker, Jonathan Ngiam, Bob Xu, Sebastian Pont, Nicholas Aristidou, Saif A.Haque, Trystan Watson, Martyn A McLachlan, James R Durrant, Accepted to Journal of Materials Chemistry A, 2019.

# Contents

# List of Tables

# List of Figures

# Nomenclature

**List of Abbreviations**

ABO Anti-Bonding Orbital

AM 1.5 Air Mass 1.5

AO Atomic Orbital

BO Bonding Orbital

c-Si crystalline Silicon

CB Conduction Band

CR Charge Recombination

CS Charge Separation

DCSC Dye sensitized solar cell

EDX Energy Dispersive X-Ray Spectroscopy

EQE External Quantum Efficiency

ETL Electron transport layer

FF Fill Factor

HOMO Highest occupied molecular orbital

HTL Hole transport layer

HTM Hole Transporting material

IGA Isothermal Gravimetric Analysis

$J_{sc}$ Short Circuit Current

LUMO Lowest unoccupied molecular orbital

MA Methylammonium

MAI Methylammonium Iodide

MAPI/$CH_3NH_3PbI_3$ Methylammonium Lead Triiodide

MO Molecular Orbital

mp- Mesoporous

PCE Power Conversion Efficiency

PL Photoluminescence

PV Photovoltaic

SC Solar cell

SCL Space charge layer

SEM Scanning Electron Microscopy

TAS Transient Absorption Spectroscopy

TCO Transparent conducting oxide

ToF-SIMS Time of Flight Secondary Ion Mass Spectrometry

TRPL Time-resolved photoluminescence

$V_{oc}$ Open Circuit voltage

XRD X-Ray Diffraction Spectroscopy

# Chapter 1

# Introduction

## 1.1 Overview - A Global Issue

A seismic shift in the way the planet produces energy is required. Currently, over 85% of the worlds primary energy sources are from non-renewable fossil fuels, such as coal, oil and gas.[1] With a growing population and increasing living standards we have seen global energy demands rise. Consequently, fossil fuels are being consumed at an ever increasing rate to meet demand. Of concern, is the prediction that the demand for oil will exceed supply in the next two decades. It is also anticipated that a 12 TW increase in the energy supply is required to meet the predicted 30 TW/yr consumption of energy in 2050.[2]

Due to this reliance on fossil fuels, the human population has created an inherently unstable system that will only last as long as we have readily accessible access to these fuel sources. Although this clear and unavoidable fact exists, the world is reluctant to change with the USA seeking to exploit shale gas and the UK resorting to fracking to obtain fuel sources too, with this expected to start in 2018.[3, 4] Even in Germany, which has sought a shift away from nuclear energy after the Fukishima disaster currently provides over 40% of its energy from coal.[5] Similar trends in continued consumption of fossil fuels are observed across the globe. Further issues regarding the worlds energy system arise from a socio-economic standpoint and an environmental aspect. Over 1 billion people still have no access to electricity and over 2 billion

can only cook using biomass fuel sources. Our increased consumption of fossil fuels, is increasing the rate at which the human race is polluting the atmosphere with carbon dioxide emissions ($CO_2$) and other greenhouse gases that are contributing to global warming. This demonstrates the moral obligation we have to create a more resilient, accessible and environmentally friendly energy system that can meet world demands.

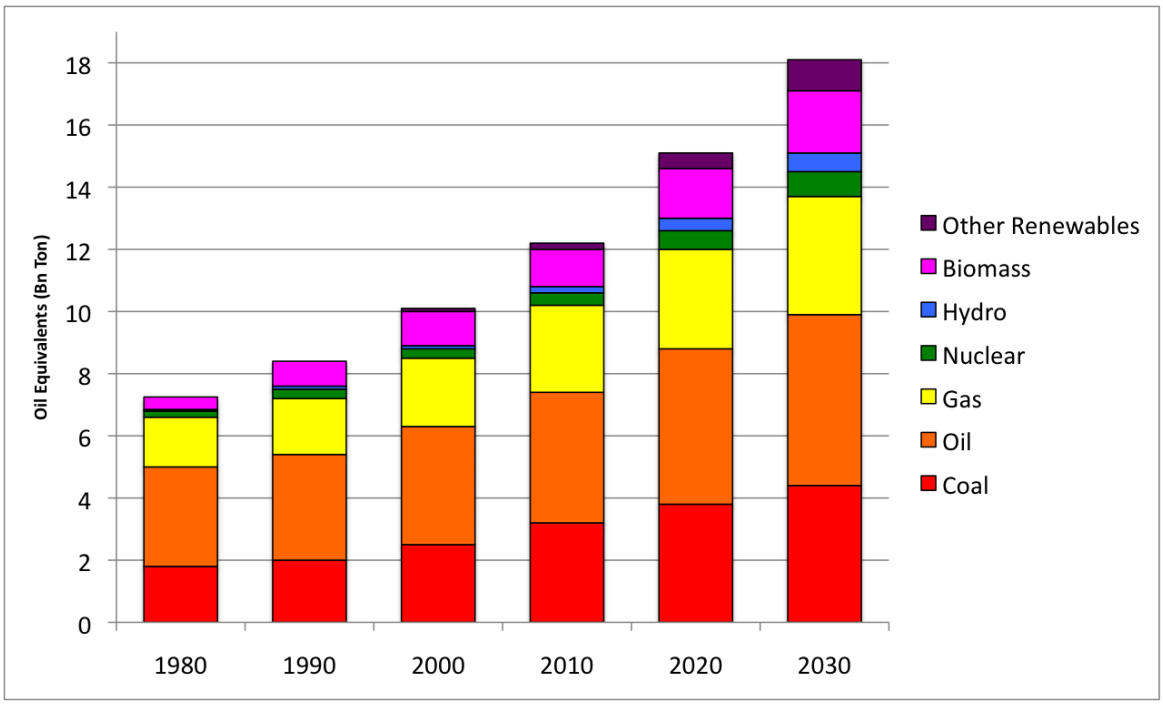


Figure 1.1: World energy consumption from 1980 to the predicted consumption in 2030. As of 2015, over 85% of the global energy supply was from fossil fuels. figure data adapted from the world energy council.[1]

If energy consumption is set to continue at the alarming rate, that is predicted as shown in Figure 1.1, the combined effect of the greenhouse gases emitted could cause a 3.6°C increase in global temperatures. This exceeds the agreed United Nations target of a 2°C increase. The augmented ghg emissions could see a 0.2°C increase every decade.[3, 6] The impacts of these increasing temperatures are far reaching and we have begun to see the impacts already. Glaciers are retreating, water levels are rising and extreme weather is impacting agriculture and leading to catastrophic natural disasters. Increasing earths median temperature will also have economic impacts and provides the largest danger to global health. The need for change is clear and a monumental shift away from non-renewable energy sources to cleaner alternatives is required. Figure 1.2 depicts the predicted increase of earths median temperature where an increase of 8°F

is anticipated to be observed from 1900 to 2100.

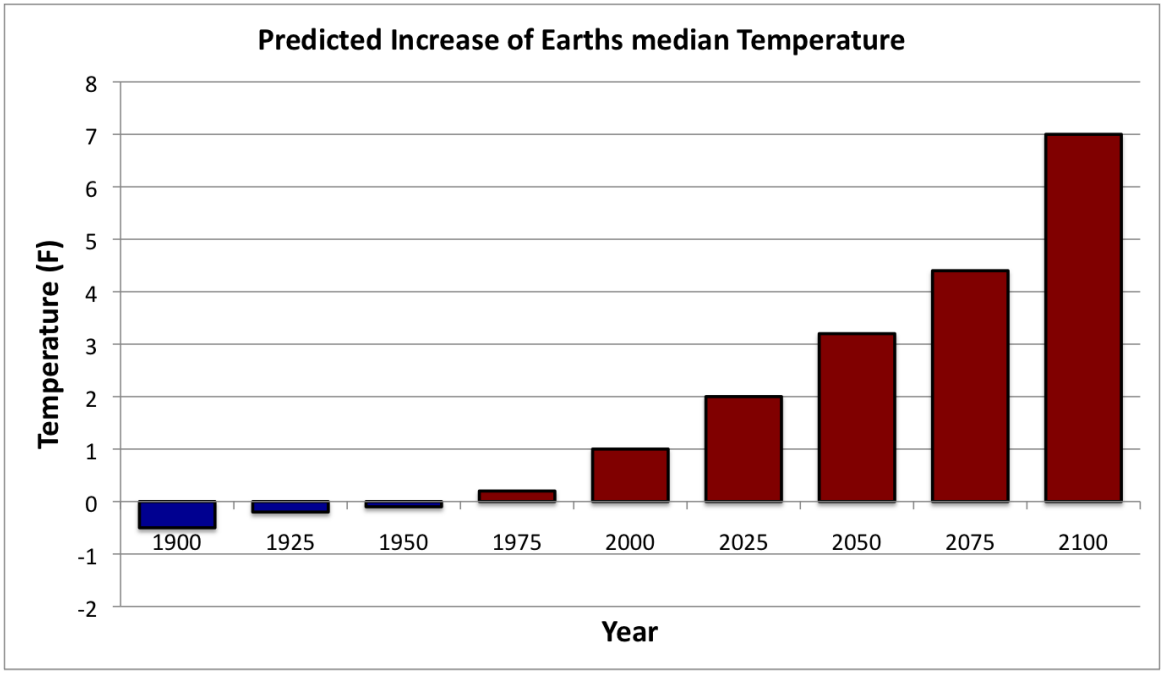


Figure 1.2: Temperature Increase as a result from increasing ghg emissions from burning fossil fuels. Figure created from data obtained from the Carbon dioxide information analysis center.[6]

## 1.2 A Way Forward - Solar Energy

Diversifying our energy supply to include more green and renewable sources, such as solar, wind and hydropower are required to overcome the issues from our reliance on fossil fuels. To date the progress in this movement has seen forecasts in energy production from renewable technologies rise from 5% to 14% by 2035.[4] However, EU subsidy cuts may hamper this progress as investments in clean technologies has fallen in recent years. Additionally, issues surrounding mass scale production, low efficiency and high costs have yielded high barriers to market for these technologies and reduced their impact on our energy supply.

Of the renewable energy sources, solar power has the greatest potential for transforming our energy market. Solar irradiation is the most abundant energy commodity, with each year over 2000 times our current annual energy consumption hitting the earths surface. This also represents a 100 fold more energy than is stored in the worlds fossil fuel reserves.[7, 8] The abundance of energy sources is pictorially represented in Figure 1.3. The potential of solar

dwarfs even that of any other renewable resource. Support for this energy source has been increasing and can be noted by the support in subsidies Germany has offered to the solar industry. The German government has committed 100 billion Euros worth of investment over the next 20 years to alleviate their reliance on coal and nuclear power.[5] Furthermore, the sector is valued at $140bn per year and is set to see annual growth in excess of 30%.[9, 10] It is clear that if we seek a cleaner technology that can truly meet the global energy demands and provide greater access to electricity, harnessing the power of the sun lies at the heart of any real attempt to solve our issues.

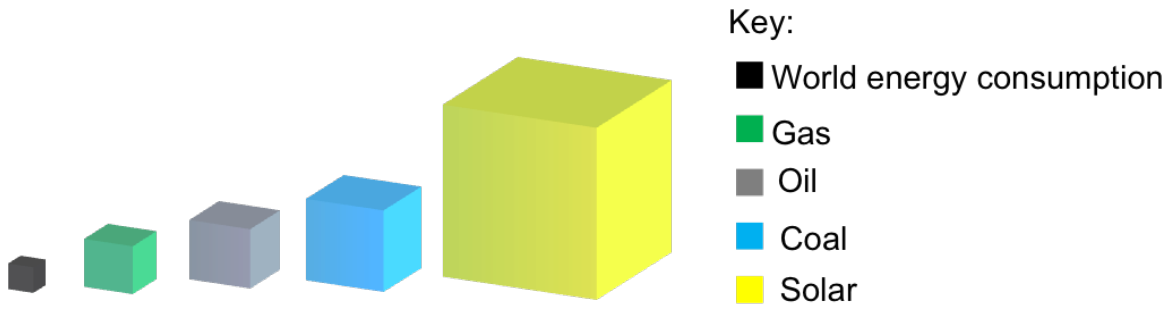


Figure 1.3: Comparison of the energy stored in solar compared to other energy sources. Fossil fuels are expressed as a function of their total reserves, whilst solar represents its total yearly potential. The amount of Energy stored in sunlight is 2200 times larger than annual global energy consumption.[8]

### 1.2.1 Photovoltaics

Having established the abundance and universal accessibility of solar energy, it is essential to generate cost effective ways of turning it into electrical energy. Two technologies exist in this field, which are photovoltaics (PV) and solar thermal (ST). The latter relies on heat from solar illumination to generate electricity by utilizing a heat engine and thus requires high temperatures. As a result, installations using ST technology are large scale and cover vast areas to obtain effective power conversion efficiencies (PCEs). In contrast, PV technology exploits solar cells (SCs) to capture the photons and promote charges against a potential gradient, allowing them to do electrical work. Inherently this system can be more scalable and economically efficient. Where SC units can be deployed in single households, in remote areas or even in a large array to form a power station. The natural abundance of solar energy means that using 10% efficient

solar cells alone and covering just 0.5% of the surface of the earth we could satisfy the global energy demand.[7, 9] This unique combination of scalability, decentralization and ability to tap into the largest renewable energy commodity makes PVs the most suitable technology to meet the future needs of our energy supply. Currently, the PV technology in the commercial market is dominated by crystalline silicon solar cells. This material yields highly efficient conversion of sunlight to electrical energy at 20% affording levelized cost of electricity now comparable to fossil fuel based energy production.[11] However, as a mature technology silicon has little room for greater enhancements in efficiency that would help make the technology more favorable. Research has now turned to alternative materials that may offer these same characteristics, but potentially with less energy intensive production (cheaper to manufacture) and with other unique features. A new generation of solution processed materials for solar harvesting have emerged with promising solar to electricity conversion to compete with silicon based solar cells. Being solution processed these materials also offer the potential for cheaper manufacturing and could be the solution to low cost solar energy conversion. They also offer the unique feature of being able to be manufactured on flexible substrates or even woven into fabrics. Despite this, these next generation materials suffer from poor operational stability. This thesis looks to address this fundamental instability and offer methods to produce more resistant and long living materials for efficient, low cost solar energy conversion.

# References

[1] *World Energy Council, World Energy Outlook*, 2014.

[2] *US Energy Information Administration, international Energy Outlook*, 2015.

[3] *International Energy Agency, World Energy Outlook*, 2013.

[4] *BP Energy outlook 2035, Statistical Review of World Energy, 2013*, 2013.

[5] *German energy policy is expensive harmful and short-sighted*, Financial Times, 16 march 2014.

[6] *Carbon Dioxide Information Analysis Center*, 2012.

[7] N. S. Lewis, *Science*, 2007, **315**, 798–801.

[8] T. C. Sum, N. Mathews, *Energy Environ. Sci.*, 2014, **7**, 25182534.

[9] *World Energy Council*, 2015.

[10] U. S. department of Energy, *Basic Research Needs for Solar Energy Utilization*, 2005.

[11] M. A. Green, K. Emery, Y. Hishikawa, W. Warta, E. D. Dunlop, *Prog. Photo. Res. App.*, 2012, **20**, 606–614.

# Chapter 2

# Background and Theory

## 2.1 Semiconductors - Light Harvesting

Solar cells are based on semiconductor materials that allow for the absorption of light and thus the conversion of photon energy into electrical energy. Semiconductors are critical for this conversion and allow for the three fundamental processes for solar cell operation:

i. Light harvesting, photon absorption to generate an exciton (an electron-hole pair)

ii. Charge seperation (CS), the splitting of the exciton into free charge carriers and prevent recombination back to the ground state.

iii. Charge transport (CT), the resulting free charges, polarons, must be transported to their respective electrodes and extracted to do electrical work.

Semiconductors are a special class of materials that have characteristics between those of conductors and insulators. The fact they can allow for the above processes to occur is fundamental to the success of solar cell function. These features need to be optimised, whilst charge recombination is minimised for optimal conversion of photon energy to electrical energy.

### 2.1.1 Electronic Band Structure

Electrons exist in discrete quantum energy levels, atomic orbitals (AOs). When atoms combine to form molecules their atomic orbitals overlap and the energy levels split resulting in a pair of

molecular orbitals (MOs). One at a lower energy (Bonding orbital) and the other at a higher energy (anti-bonding orbital), as demonstrated in the figure below. As the number of atoms combining increases to form larger more complex molecules, the discrete molecular orbitals begin to merge. The decreasing spacing between molecular orbitals eventually results in the formation of continuous energy levels, bands. This behavior is noted in complex systems, such as crystal structures that can be thought of as an infinite number of AO's linearly combining to form an infinite number of molecular orbitals with little to no spacing between the energy levels. the process of band formation is also demonstrated in the following Figure 2.1.

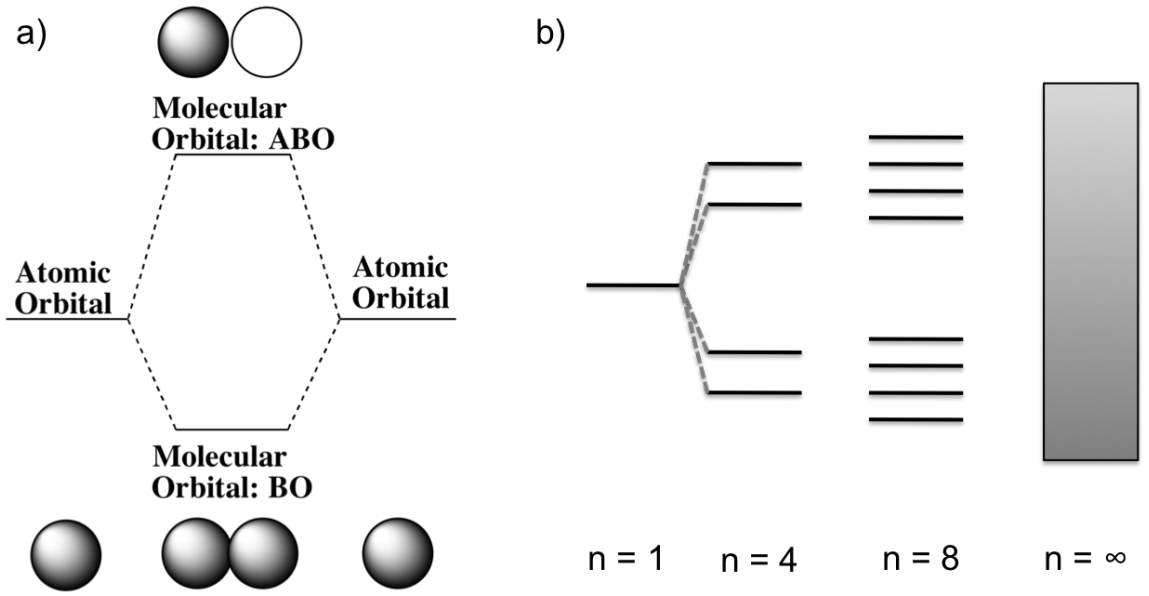


Figure 2.1: Illustrations to show the linear combination of atomic orbitals forming a) bonding and anti-bonding molecular orbitals. b) The formation of continuous bands as the number of atomic orbitals combining increases and the energy spacing between molecular orbitals decreases. Where n is the number of constituent orbitals.

Bands can form with space between them, forbidden energy levels that electrons can not occupy. The band formed from the bonding orbitals is the valence band (VB) and is populated with electrons. Whilst the band formed from the anti-bonding orbitals is the conduction band (CB) and is empty at 0K. When electrons populate the CB they are mobile and can move freely in the material. This is also true for the holes that are formed in the VB, when an electron is promoted from the VB to the CB. This electron/hole mobility allows for the material to conduct electricity and produce an electrical current.[1] The difference in energy between the edges of the

CB and the VB, causes the distinction and contrast in behaviour between metals, semiconductors and insulators. The energy difference is known as the band gap ($\Delta E_g$) and represents the range of energies in which no MOs exist. It is noted that following definitions of a metal, insulator and semiconductor are obeyed whilst at room temperature. In metals, conductors, there is no band gap and the edges of the VB and CB overlap. Consequently, excitation of an electron from the VB to the CB occurs with ease. In the situations where there is a band gap, the magnitude of the gap determines the observed behaviour of the material. When $\Delta E_g > 4eV$ the material is an insulator, as the band gap prevents the promotion of an electron and therefore no electrical conduction is possible. On the other hand, if $\Delta E_g$ lies within 0.5 - 4eV electron promotion is possible if sufficient energy is provided.[1] The class of materials that fall in this category are semiconductors. This allows them to exhibit properties between these two other extremes depending on the magnitude of the energy applied to the system. Sufficient energy can be provided in the form of heat, light or electrical energy to cause the semiconductor to display electrical conductivity. The magnitude of the band gap will determine how much energy is required for excitation and thus impact the intrinsic electrical conductivity. A larger band gap will require more energy for electron promotion and thus the semiconductor will have a lower intrinsic conductivity. Band structures leading to the classification of conductors, insulators and semiconductors are shown in Figure 2.2 below.

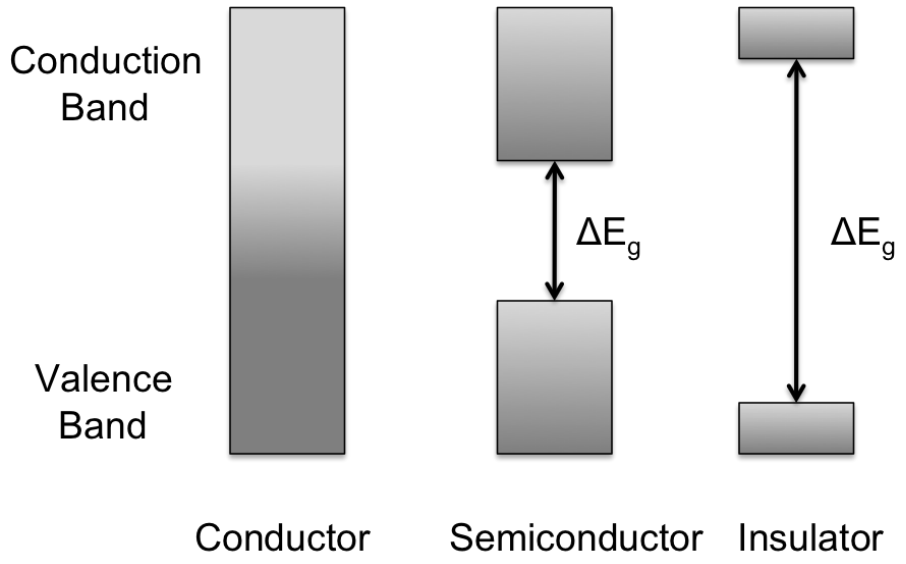


Figure 2.2: Illustration of band gap magnitude creating the classification of materials: Conductor, semiconductor and insulator.

Electrons will occupy the lowest energy possible at absolute zero, due to a lack of kinetic energy. These electrons and their electrochemical potential are defined by the Fermi level, $E_f$. Increasing temperature causes electron promotion and results in a distribution of electrons into higher energy states. Once thermal equilibrium has been achieved the probability of finding an electron at a given energy, E, can be given by the Fermi-Dirac distribution[2]

$$f(E, E_F, T) = \frac{1}{exp((E - E_F)/k_B T) + 1} \tag{2.1}$$

The range of forbidden energies in semiconductors means the Fermi level sits within the band gap. At ambient temperatures, the electron density in the CB will be relatively low and lead to a low intrinsic conductivity. The conductivity of the material can be altered by an electron or hole dopant. This causes new energy states to arise within the band gap allowing the electrons or holes to more readily leave the bonding orbitals and thus make the material more conductive. Consequently, this also changes the electrochemical potential and shifts the Fermi level. The directionality of the shift is dictated by the nature of the dopant. For example, if an electron deficient dopant is introduced electrons are withdrawn from the CB and the Fermi level moves towards the VB edge (p-type doping). In contrast, if an electron rich dopant is employed the Fermi Level shifts to the CB edge (n-type doping).[3] The shifting of the Fermi-level due to p- and n- type dopants is depicted in Figure 2.3 with respect to an undoped (intrinsic) semiconductor.

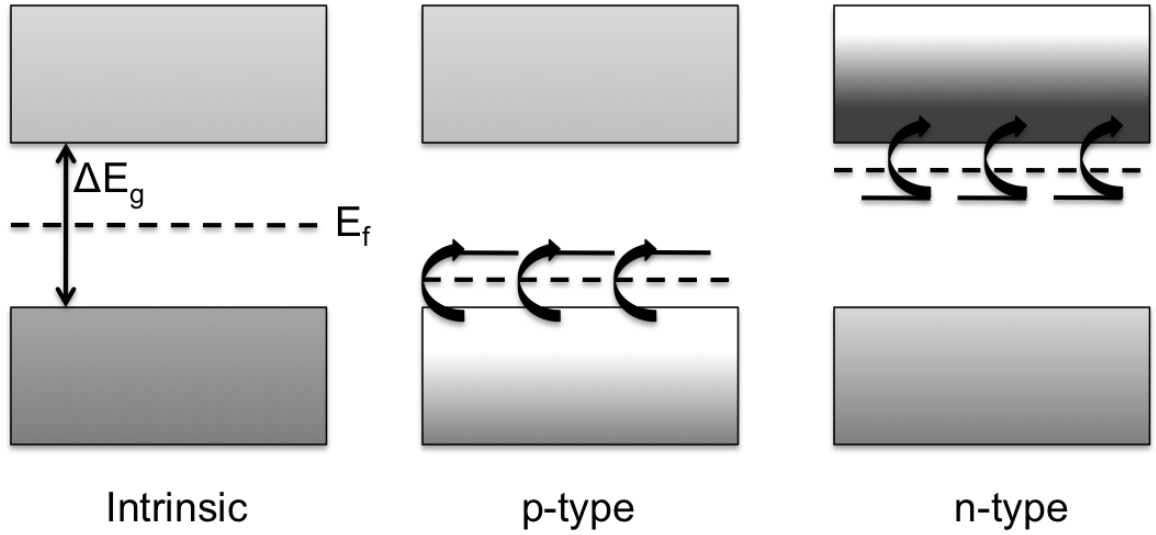


Figure 2.3: Graphical representation of the introduction of inter-band gap states, resulting from p- and n-type doping.

Shifts in the Fermi level, weather introduced intentionally into an intrinsic semiconductor (via dopants forming extrinsic semiconductors) or unintentionally (defects or grain boundaries) can manifest in an increased conductivity. However, they can also cause sites for charge recombination and interfere with the electric field between the interface of materials.[4] The influence of traps especially on the surface becomes increasingly important when the dimensionality of crystals are changed. Solution processing generally leads to increased defect presence by increasing the surface area and the number of grain boundaries and so surface to volume ratio plays an important role on the conductivity of the semiconductor by altering the number of trap sites.[5, 3]

## 2.2 Electron Transfer

Electron transfer is the process of an electron relocating from a donor (D) species to an acceptor (A). This type of reaction is observed in numerous processes, from biological systems to the photo-oxidation of water.[6, 7] In photovoltaics, this transfer is critical to the spatial separation of an exciton at donor-acceptor semiconductor interface. Additionally, the process of electron transfer can occur from a semiconductor to a parasitic species, removing the photo-generated electron the material. This may impact the performance of the semiconductor and could consequently cause stability issues, the resulting species that accepted the electron may react

with the semiconductor. The theory of electron transfer was first described by Marcus,[8] and the rate of electron transfer ($K_{eltr}$) is described by Fermi's golden rule, and depends on the electronic coupling ($V^2$) and the isoenergetic requirement described by the Frank-Condon Factor (FC):

$$k_{eltr} = \frac{2\pi}{\hbar}.V_{DA}^2.FC \tag{2.2}$$

The electronic coupling between the donor and acceptor, relies on the spatial overlap of their respective wavefunctions. This invokes that the rate of electron transfer is a function of distance and can be viewed as the process of electron tunneling. Where the electron wavefunction of the donor species has finite amplitude on the acceptor species. Hence, providing other energy requirements are satisfied, if an acceptor species comes within sufficient range the orbitals will overlap and the electron transfer will occur. The shorter the separation generates a larger overlap of the wavefunctions and leads to a faster rate of transfer.[9] This relation can be described by the following equation:

$$V_{DA}^2 \propto < \Psi_D | \Psi_A > \propto exp(-\beta.r) \tag{2.3}$$

$\beta$ represents the tunneling coefficient and depends on the height of the potential barrier and the medium (solvent and it dielectic constant) between the donor acceptor pair. The distance, r, between the species dictates the rate by controlling the magnitude of the electronic coupling. This process of wavefunction overlap is illustrated in Figure 2.4 below.

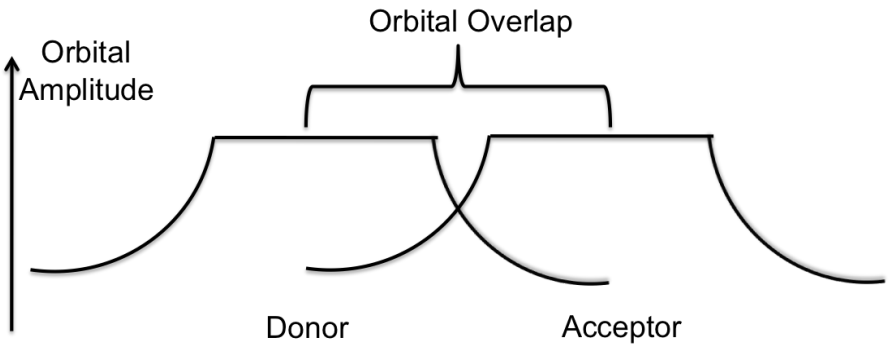


Figure 2.4: Illustration of the distance dependence of the electronic orbital overlap between a donor-acceptor pair.

The other factor involved in determining the rate of electron transfer is the Frank-Condon

factor. This factor yields the origins of the energy dependence and arises as the starting D-A pair will undergo a geometric distortion to match the equilibrium geometry of the products. The energy required for this distortion, is the reorganization energy, $\lambda$. This distortion energy is used in Marcus theory, where a simple harmonic oscillator potential with a reaction co-ordinate is used to describe the electron transfer process. Here, the reaction co-ordinate represents the amount of charge transfered. In this model, the activation barrier ($\Delta$G*) and the free energy change ($\Delta$G) impact the rate of transfer. Where, $\Delta$G is the difference in energy separating the starting and final equilibrium potentials. Increasing the free energy decreases the activation energy until, $\Delta G = \lambda$. Once this condition is met the process becomes activationless. Beyond this condition, increasing the free energy increases the activation barrier. This is known as the Marcus inverted region. Hence, large energy differences slow down the rate of electron transfer via inducing a larger activation barrier to generate the required geometrical equilibrium positions for the transfer to occur.[8, 9, 10] The impact of changing the free energy through the reorganization energy and beyond is graphically depicted in the following Figure 2.5.

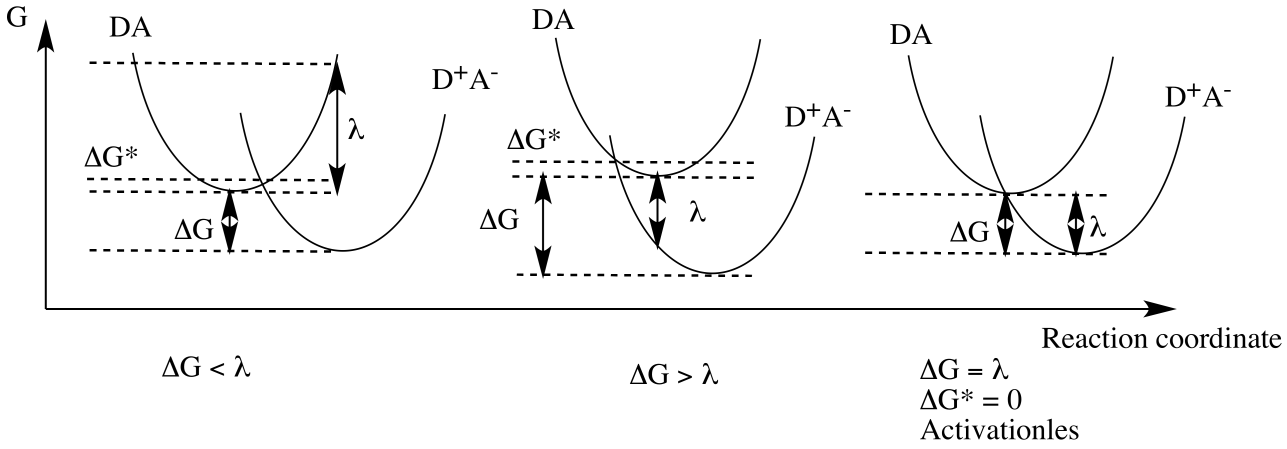


Figure 2.5: Illustration of the free energy profiles used in the Marcus description of electron transfer. Where, $\Delta$G is the free energy change and $\Delta$G* is the activation barrier

### 2.2.1 Transient Absorption Spectroscopy

In semiconductor photo-physics, electron transfers play a vital role in leading to the separation of coulombically bound electron-hole pairs. Photo-excited electrons undergo transfers at semiconductor-semiconductor interfaces and at semiconductor-electrode interfaces. Transient

absorption spectroscopy (TAS) is a technique that allows the observation of short lived electronic species by employing a pump-probe system. TAS, then allows for the study of charge carrier life-time and charge carrier yields. This allows for powerful information about the ability of an interface to separate excitons and hence how efficient the electron transfer is. Additionally, the effects of charge recombination can be monitored. TAS works by employing a pulsed laser to excite a photoactive layer and is then monitored with a probe light. The difference in absorption ($\Delta$OD) of the probe wavelength before and after excitation is compared. The difference arises as the absorption properties of a material in its ground state and excited state are different. Absorption intensity is governed by Beer-Lambert's law and is a function of the extinction coefficient ($\epsilon$), the concentration (c) and the path length (l):

$$OD = \epsilon.c.l \tag{2.4}$$

After excitation from the pump source one material will form excitons, these can then move to interfaces and undergo charge separation. Either the electron or the hole will be transfered depending on the acceptor material. The probe beam (with a specific wavelength) measures the resulting transient species by contrasting the change in absorption of the wavelength of the film before and after the electron (or hole) has transfered. It then follows that $\Delta$OD is proportional to the number of charge carriers generated. More carriers generated leads to a greater change in absorption, the yield of free charges increase. Measuring this absorption change as a function of time allows for a kinetic trace to be produced and the life-time of charge carriers can be determined. This provides information about the charge recombination effects in the materials. Shorter lived transient species undergo more parasitic charge recombination events that are detrimental to solar cell performance. The technique can also be used to generate a $\Delta$OD spectrum for the transient species, by fixing the time and altering the wavelength of the probe. For example, the spectrum generated could correspond to that of an oxidized material that has accepted a hole from the photo-excited layer. The wavelength that generates that largest magnitude is used as the probe wavelength in kinetic studies. These processes are illustrated in Figure 2.6.

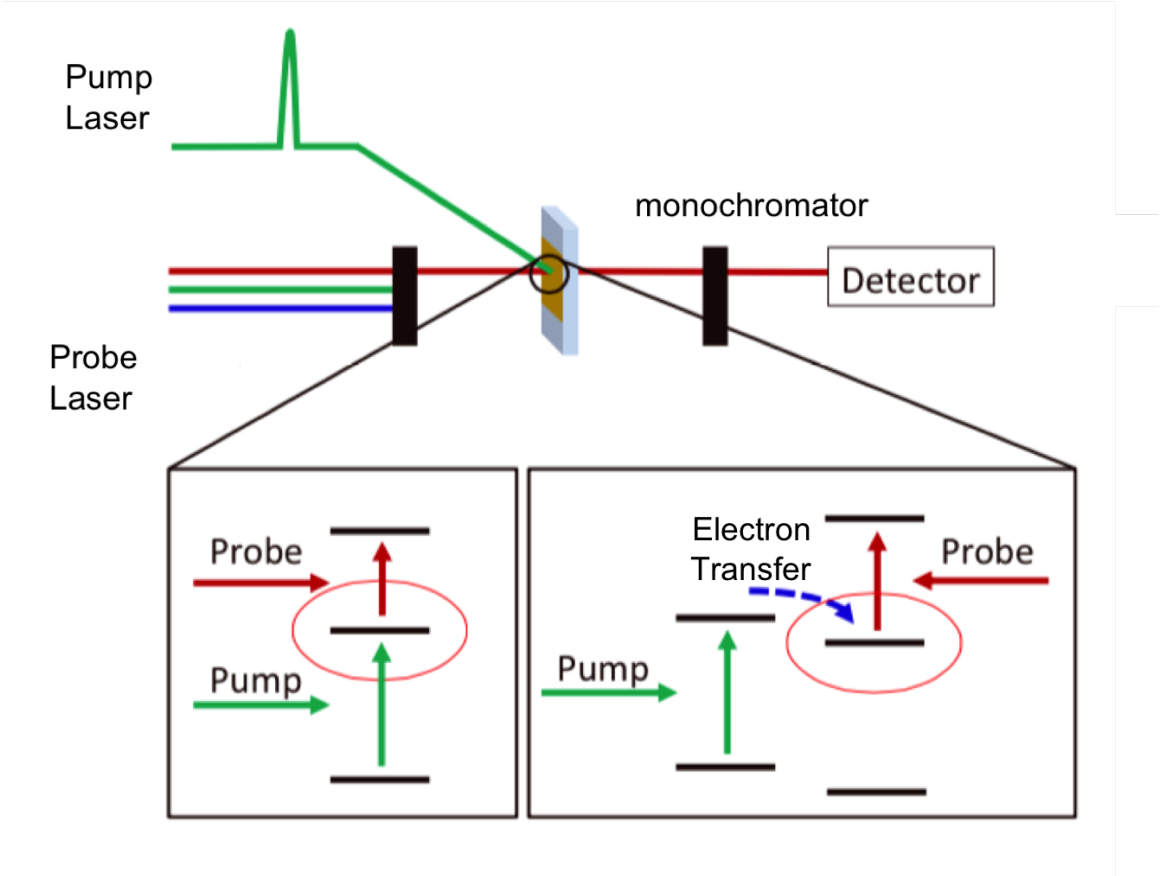


Figure 2.6: TAS experimental apparatus and illustrative representations of the electronic transitions and transfers that can occur within a material and between an interface, respectively.

## 2.3 Inorganic Photovoltaics

For a semiconductor to exhibit photo-conductivity, the promotion of electrons from the valence band to the conduction band must occur. This is realised when photons with energy greater than that of the band gap are absorbed. However, to transform this into electrical energy that can do work, the coulombically bound electron-hole pair must be spatially separated. Special architectures that promote charge separation are necessary, such that charges can be transported through the material(s) and extracted at external contacts before recombination or other loss mechanisms occur. These architectures provide the driving force for separation. In biological systems, for example in photosynthesis a chain of electron transfers are used to spatially separate the charges, which are driven by differences in the free energy of the donor and acceptor species. In solar cells, to efficiently achieve charge separation and transport of the charges, asymmetry is introduced into the device by combining electronically heterogeneous

materials. An electric field across the device is also established as a consequence of this, both factors lead to the creation of the driving force needed for separation. The foundation of this principle was established in crystalline silicone (c-Si) solar cells, which have defined the field of PVs for over 40 years.[11, 12, 13] Generation of asymmetry is established by forming a p-n junction, where the two respective extrinsic semiconductors are joined together. Typically, doping with Boron (an electron poor dopant) in silicon generates p-type, whilst electron rich dopants, such as Phosphorous create n-type silicon. Upon joining these, electrons from the n-type silicon will combine with the holes on the p-type side and balance the Fermi levels of the two materials. Consequently, a space charge layer (SCL) is produced at the interface, where little to no carriers exist and dopant atoms are completely ionised. A contact potential ($\phi$) is now also established, as the n-type side becomes positively charged relative to the p-type side of the device. In turn the band edges of the p-type side shift to a higher energy (e$\phi$) than those of the n-type side. A macroscopic electric field results from this process, which can now cause the splitting of charges generated when a photon of light is absorbed. The exciton must undergo diffusion towards the SCL, where the electrons will then fall down the potential gradient towards the n-type side and the holes will rise up towards the p-type layer. Where the changing free energy of the carriers drives this processes.[14] An illustration of how this process occurs and leads to the charge separation of the electron-hole pair is depicted in Figure 2.7 below.

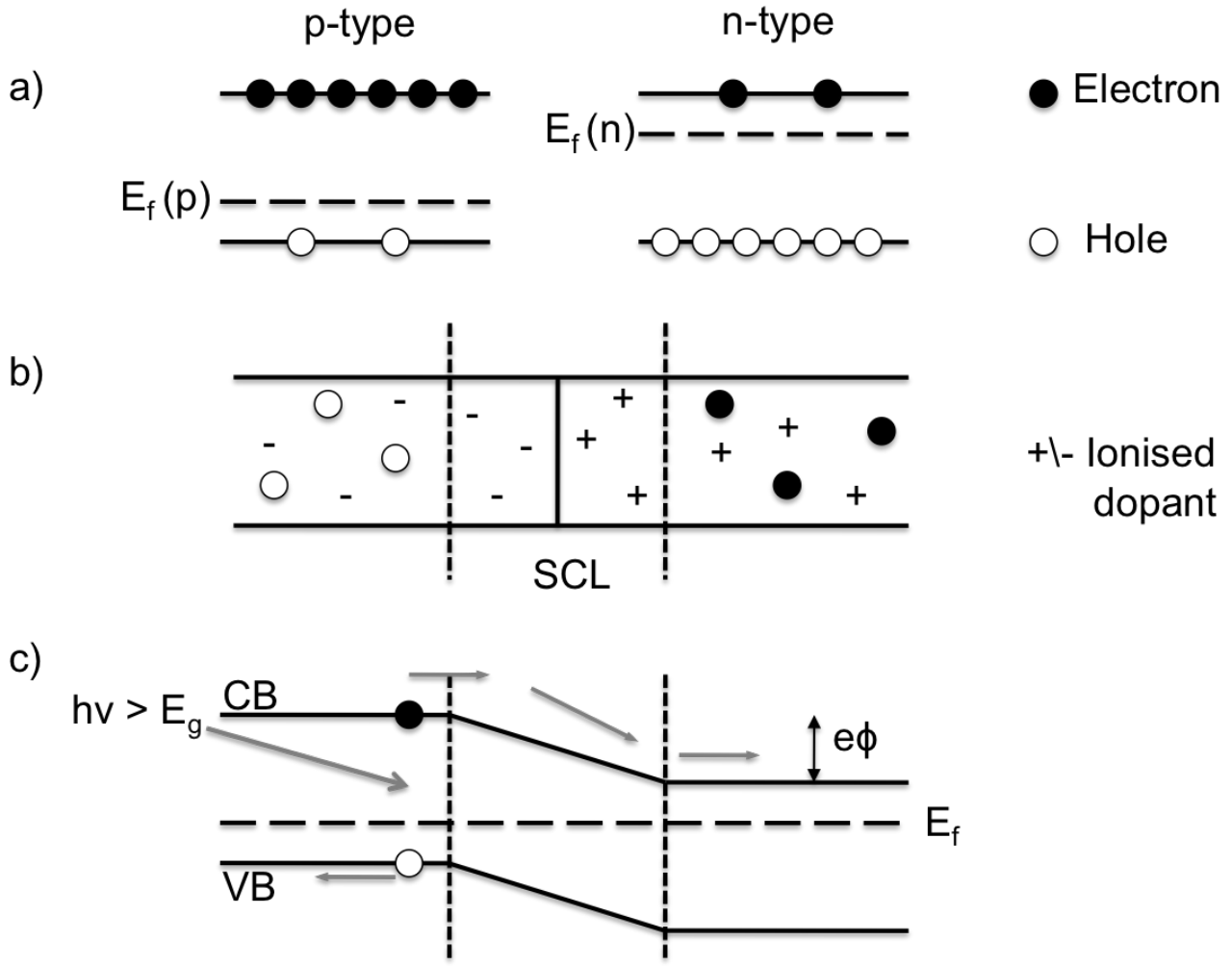


Figure 2.7: Illustration of the formation of a p-n junction at short circuit and it's ability to absorb, split and transport charges. a) Isolated p- and n- type silicon semiconductors, with their respective Fermi levels. b) contact of electronically heterogeneous semiconductors generating the SCL at the interface between the two materials. c) Energy diagram depicting the absorption of a photon and the proceeding ability of the electric field to split the exciton at the SCL for a p-n junction device.

Initially, silicon faced limitations due to being an indirect band gap semiconductor and thus possessing a relatively low extinction coefficient. To negate this issue c-Si SCs are created with thick layers (10$\mu$m) to enhance the number of photons absorbed. Although, this creates more excitons it places strict requirements for the crystallinity of the semiconductor. This is because, the excitons must now travel far greater distances to diffuse to the SCDR to benefit from the interface to promote separation. Hence, the probability for recombination increases and therefore the average distanced traveled before recombination must be maximised through ensuring high silicon crystal purity. This will reduce the number of defects and trap sites at

which recombination can occur. This generated the largest issue with c-Si, high production costs. Fortunately, these issues have been addressed through intelligent architecture design and material optimisation and along with production cost savings. Consequently, the price issue relating to silicon solar cells has been brought down. Combined with remarkable efficiencies exceeding 25% the cost efficiency of silicon solar cell is the benchmark to which all new next generation solar cell technologies must compete.[13, 14, 15]

## 2.4 Excitonic Solar Cells

The inherent limitations that restrict c-Si SCs have afforded the creation of a novel set of PV technologies that aim to overcome these issues. These are classified as excitonic solar cells. Of which, three families of this class of SC have demonstrated efficiencies in excess of 10%. Namely, dye sensitised solar cells (DSSCs), organic solar cells (OPVs) and most prominently perovskite solar cells (PSCs).[16, 17, 18] These solar cells generate excitons that have a lower dielectric constant compared to that of silicon, which produces loosely bound Wannier-Mott charges. In contrast the low dielectric constant creates tighter bound electron-hole pairs, excitons. The binding energy can be extracted from the electrostatic attraction (V), which is derived from the following equation and is a function of the permittivity of free space ($\epsilon_o$), the dielectric constant ($\epsilon_r$) and the spatial separation of the charges (r).

$$V = \frac{e^2}{4\pi\epsilon_o\epsilon_r r} \tag{2.5}$$

The electrostatic attraction lowers the energy and stabilises the exciton such that energy is reduced from that of the semiconductors band gap. Therefore, electrostatic fields invoked by differences in work function are sometimes insufficient to overcome this stabilization energy, generating new issues of fast charge recombination. However, judicious material selection can introduce energy off-sets at hetrojunctions that can provide a sufficient energy difference to overcome the binding energy and cause splitting. The simplest bilayer donor-acceptor interface architecture is illustrated in the figure below. This architecture is required in order to spatially separate the charges and is commonly used in bilayer organic PVs, as shown in Figure 2.8.

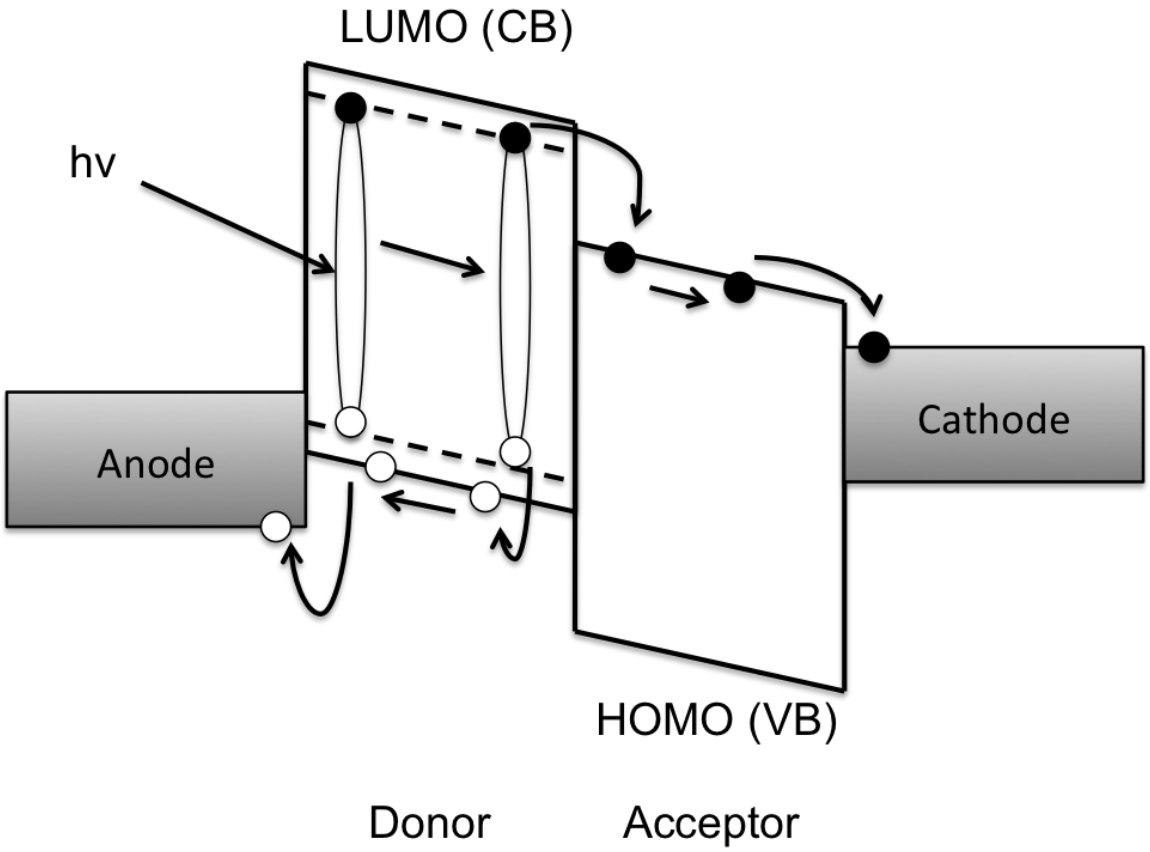


Figure 2.8: Illustration of bilayer excitonic solar cell employing a donor/acceptor interface to facilitate charge separation. Light absorption causes the formation of an exciton that then diffuses to the interface. The energy offset allows the splitting into free charges and transport with the donor or acceptor layer to the anode and cathode for the hole and electron, respectively.

The resulting excitons that form from light absorption, diffuse to the interface and the energy off-set induces spatial separation into free charges. In molecular materials (organic semiconductors or dyes) the highest molecular orbital (HOMO) is equivalent to the VB and conversely, the lowest unoccupied orbital (LUMO) is equivalent to the CB. Upon exciton splitting, charge transport and extraction to the electrodes is driven by an internal electric field that is established by the difference in work functions of the electrodes employed. Critically, the use of direct band gap semiconductors with optical absorption several orders of magnitude lower than c-Si allows thinner layers (10s-100s nm) to be utilised. This reduces the distance excitons and charges must travel, thus alleviating some of the issues of recombination and lowers the constraints of semiconductor mobility and purity. As a result, these materials afford low-cost and scalable solution processing techniques, such as roll-roll printing or spray coating.[19, 20, 21, 22]

### 2.4.1 Dye Sensitized Solar Cells

Although, excitons can diffuse distances of the order of tens of nanometers before recombination, several hundreds of nanometers of material are still required for good light harvesting. Issues of recombination persist in these bilayer systems as the majority of excitons will form at distances greater than the exciton diffusion distance away from the interface and so will more likely undergo recombination than splitting. An intelligent design to navigate this issue is seen in the design architecture of dye-sensitised solar cells (DSSCs). The main principle is to generate excitons in close proximity to donor-acceptor interfaces to increase the yield of charge separation and provide continuous pathways to the electrodes. DSSCs manage this by decoupling light absorption and charge transport. Providing an architecture that enhances splitting of excitons and minimises recombination. In the system, a very thin layer of a light harvesting (photoactive) dye is sandwiched between an electron transport layer (ETL) and a hole transport layer (ETL). Commonly, an n-type metal-oxide semiconductor is employed as the ETL, whilst the HTL is usually a liquid electrolyte (e.g. $I^-/I^{3-}$ redox) or a solid molecular (organic) semiconductor. The major breakthrough for this class of PVs was demonstrated by Gratzel et. al.[23] It was shown that a mesoporous (mp-) scaffold with electrical conductivity, that could be sensitized with a dye, could be created by sintering nanoparticles of $TiO_2$. Advantageously, this provides a high surface area platform to which a dye can be applied to, up to three orders of magnitude larger area than flat glass. Consequently, high optical absorption can be attained from thin layers and ensures the absorption and creation of excitons is then in close proximity to an interface that can split the exciton.[23, 24] This architecture coupled with a solid HTL (solid state DSSC) that can remove the dependency is depicted in the Figure 2.9 below.

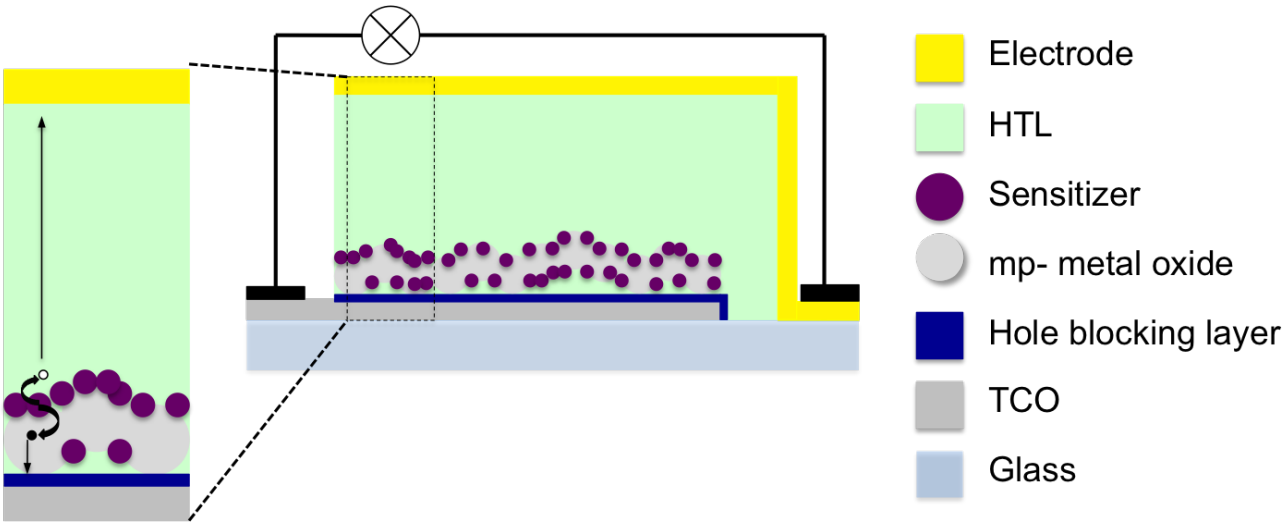


Figure 2.9: Cross section of a solid state DSSC employing a dye sensitized mesoporous metal oxide. Zoomed in profile depicts the charge separation of an exciton into the respective transport layers formed in the dye after light absorption.

Upon light absorption and the formation of the exciton, ultrafast electron extraction into the n-type ETL drives charge separation. The driving force for this derives from differences in electronic energy levels allowing the electron to lower its free energy. On the other side the hole is also driven by similar action into the HTL. This splitting of the exciton from the dye into the ETL and HTL causes the quasi-Fermi levels of the transport layers to split resulting in a photovolatge. The $V_{oc}$ is defined as the difference in energy between the highest Fermi level of the ETL and the potential or HOMO of the HTL depending on the material employed. By transfer of both charges to their respective transport layers regenerates the ground state of the dye, such that no chemical change occurs. Once the charges are in the transport layers, they are transported to the electrodes and extracted, generating current. The efficiency of DSSCs is determined by the kinetic competition of recombination of the charges, either within the dye or across the interface, with the rate of separation and transport.[25] High efficiencies are obtained when the rate of separation and transport dominates the rate of recombination. Electron injection into the ETL and hole injection into the HTL must occur before relaxation to the ground state or recombination across the interface.

In the beginning of DSSCs the HTL predominately used was the electrolyte redox $I^-/I^{3-}$ pair. Unfortunately, issues of toxicity, stability and critically diffusion controlled current led to limited

commercial application despite reported efficiencies of 10%.[26, 27, 28, 29] This caused the evolution of the field towards the use of solid state HTLs as a means of improving stability, power conversion efficiency and versatility owed to less rigid structures being required to encapsulate devices. They also provided the potential for cheaper solution processing and reduced toxicity issues, depending on material selection. Solid state HTLs are wide ranging in design and structure, however the most successfully and widely employed material is spiro-OMeTAD (depicted in the figure below) and has displayed power conversion efficiencies of 7%. [30]. This success is owed to high hole mobilities, long material life-time and its amorphous morphology allowing close contact with the sensitised mesoporous metal-oxide scaffold. Additionally, it possesses a HOMO level of approximately 4.9 eV, which lies above that of many typical dyes used in these systems, ensuring the driving force for separation is efficient and allowing the regeneration of the dye.[31, 32] The full advantages of solid state DSSCs relative to liquid state DSSC are yet to be fully realised and provides a continuing effort in the community to strive towards these goals.

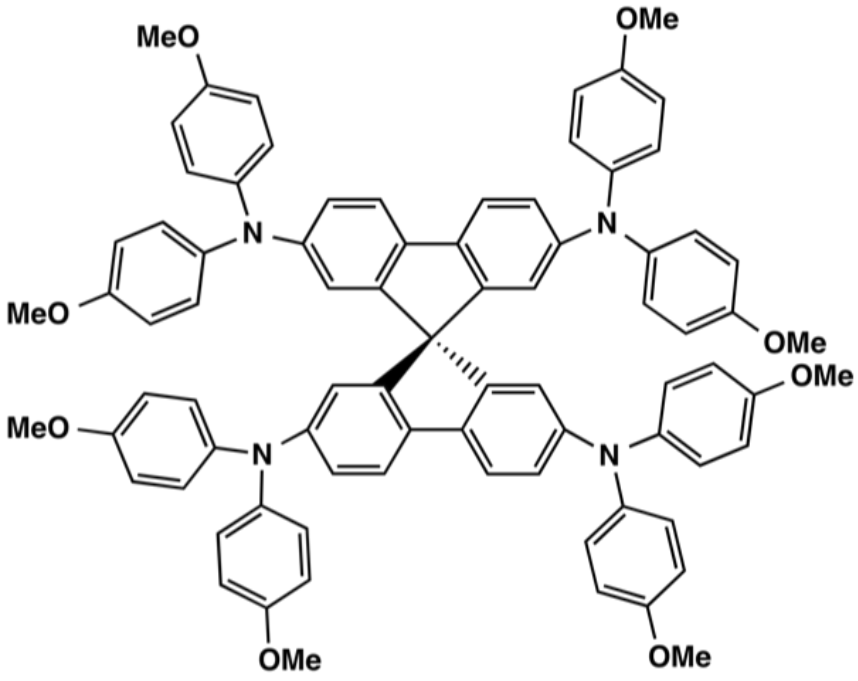


**Spiro-OMeTAD**

Figure 2.10: Illustration of the chemical structure of the commonly employed HTL, Spiro-OMeTAD.

## 2.5 Perovskite Solar cells

Since the development of DSSC the most substantial shift in the field commenced with the employment of organolead halide perovskites as the photoactive layers. Since their first employment in 2009, perovskite absorbers have afforded the greatest rate in change in efficiency and performance, when compared to all other SC technologies.[33] This evolution of performance is depicted in the figure below and highlights how rapid the improvements have been made in contrast to other competing SC technologies.[34] Perovskites are a class of compounds that possesses an $AMX_3$ structure (Figure 2.11b). Where M is typically a metal cation ($Pb^{2+}$ or $Sn^{2+}$), X is a halide ion ($Cl^-$, $Br^-$ or $I^-$) and A is cation that induces charge neutrality. Most commonly A is the Methylammonium cation ($MA^+$, $MeNH_3^+$) but other small cation species can also be employed ($NH_2CH_2N_3^+$, $Cs^+$).[18, 35, 36, 37]

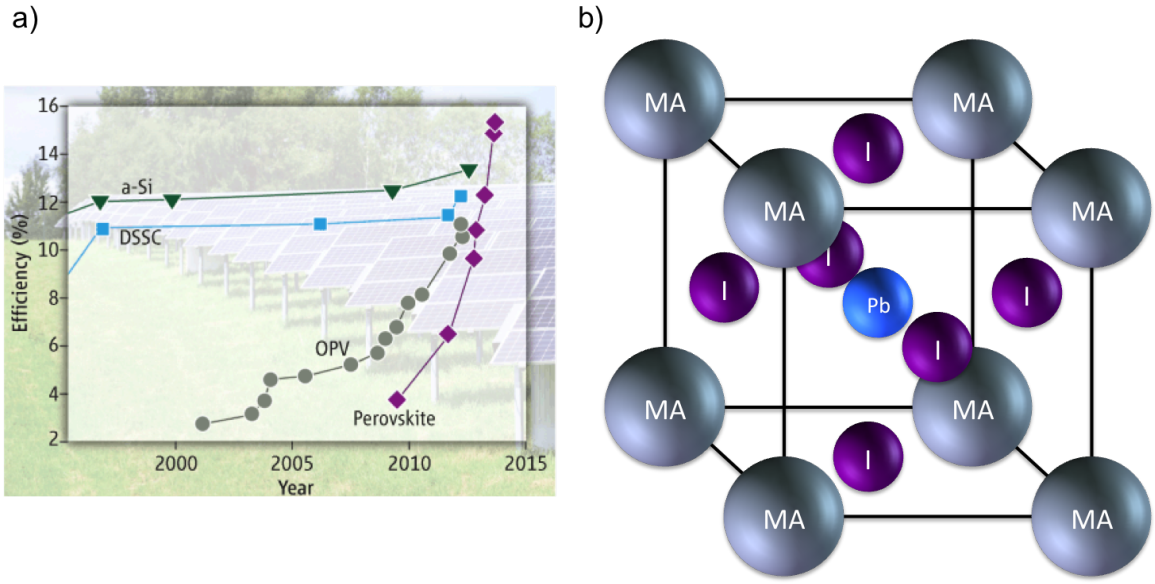


Figure 2.11: a) Illustration of the rate enhancement in performance of perovskite solar cells relative to other competitive technologies.[33] b) Unit cell of the $ABX_3$ perovskite Methylammonium Lead triiodide. M=$Pb^{2+}$, A=$MA^+$ and X=$I^-$

The foundation of perovskite solar cells (PSCs) has been underpinned by the archetypal absorber, Methylammonium lead triiodide (MAPI, $MAPbI_3$, $CH_3NH_3PbI_3$). It posses a vast array of physical properties that make it a very powerful photoactive layer for PV applications. These include its direct band gap of 1.51 eV, causing absorption onset at 800 nm and strong visible light absorption,[38] a small exciton binding energy (ca. 0.03 eV)[39] and high charge

carrier mobilities for both electrons and holes, 7.5 $cm^2$ $V^{-1}$ $s^{-1}$ and 66 $cm^2$ $V^{-1}$ $s^{-1}$ respectively. It is noted that in the literature a range of band gap values and mobilities are reported, due to the dependence of these characteristics on the method of fabrication, device architecture and testing. Mobilities as low as 0.7 $cm^2$ $V^{-1}$ $s^{-1}$ to as high as 600$cm^2$ $V^{-1}$ $s^{-1}$ have been reported in the literature. [40, 41, 42] Furthermore, this perovskite can be fabricated from solution precursors of the salts allowing for low-cost solution processing.[43, 44] This successful implementation into DSSC structures first saw MAPI based PSCs produce efficiencies of 3.8%.[33] This initial finding demonstrated that both high photovoltages and photocurrents could be obtained with large fill factors. Hence, optimisation was quickly achieved and devices with efficiency of 6.54% were realised.[45] However, an instant improvement to these initial devices was made by replacing the problematic liquid electrolyte that dissolved the perovskite phase, with solid hole transport materials. Such as, Spiro-OMeTAD. Consequently, devices now observe efficiencies exceeding 15%.[46, 47, 48, 49, 50, 51]

This rapid development has caused an explosion of research and has seen a wide array of new device architectures and transport layers examined.[48, 49, 51, 52, 53, 54] Although, most successful devices employing MAPI remain close to that of the DSSC and consist of a mesoporous layer intercalated with the perovskite phase. Devices are now exhibiting efficiencies approaching and exceeding 20%.[48, 51] These have been referred to as meso-superstructured solar cells (MSSCs),although architectures are realistically still based on DSSCs. They rely on the mesoporous scaffold and the ambipolar nature of MAPI to provide a high surface area and exciton/charge carrier diffusion to interfaces.[55] They are no longer always required to be n-type and transport electrons, since the electron mobility in the perovskite phase is itself fast. Insulating mesoporous-$Al_2O_3$ posses similar morphology to that of mp-$TiO_2$, but can't conduct electrons and consequently allowed for higher open circuit voltages. Additionally high free charge carrier concentrations and high dielectric constants mean excitons readily dissociate into free charges, which are able to travel through the perovskite phase easily and rapidly. This is also seen by the low binding energy associated with these excitions, with values reported at less than 50 mEv. In contrast Organic solar cells have been reported with exciton binding energies of the order of 0.5 to 1 eV, this significant difference highlights the ability of these

excitons formed in perovskites to want to dissociate into free charges more favourable than in other excitonic systems.[50] Hence, it is common to see in literature the use of both mp-$TiO_2$ and mp-$Al_2O_3$ as they do not rely on interface splitting of excitons as much as other excitonic based solar cells. Typical energy level diagrams for both these mesoporous based architectures are shown below in Figure 2.12.

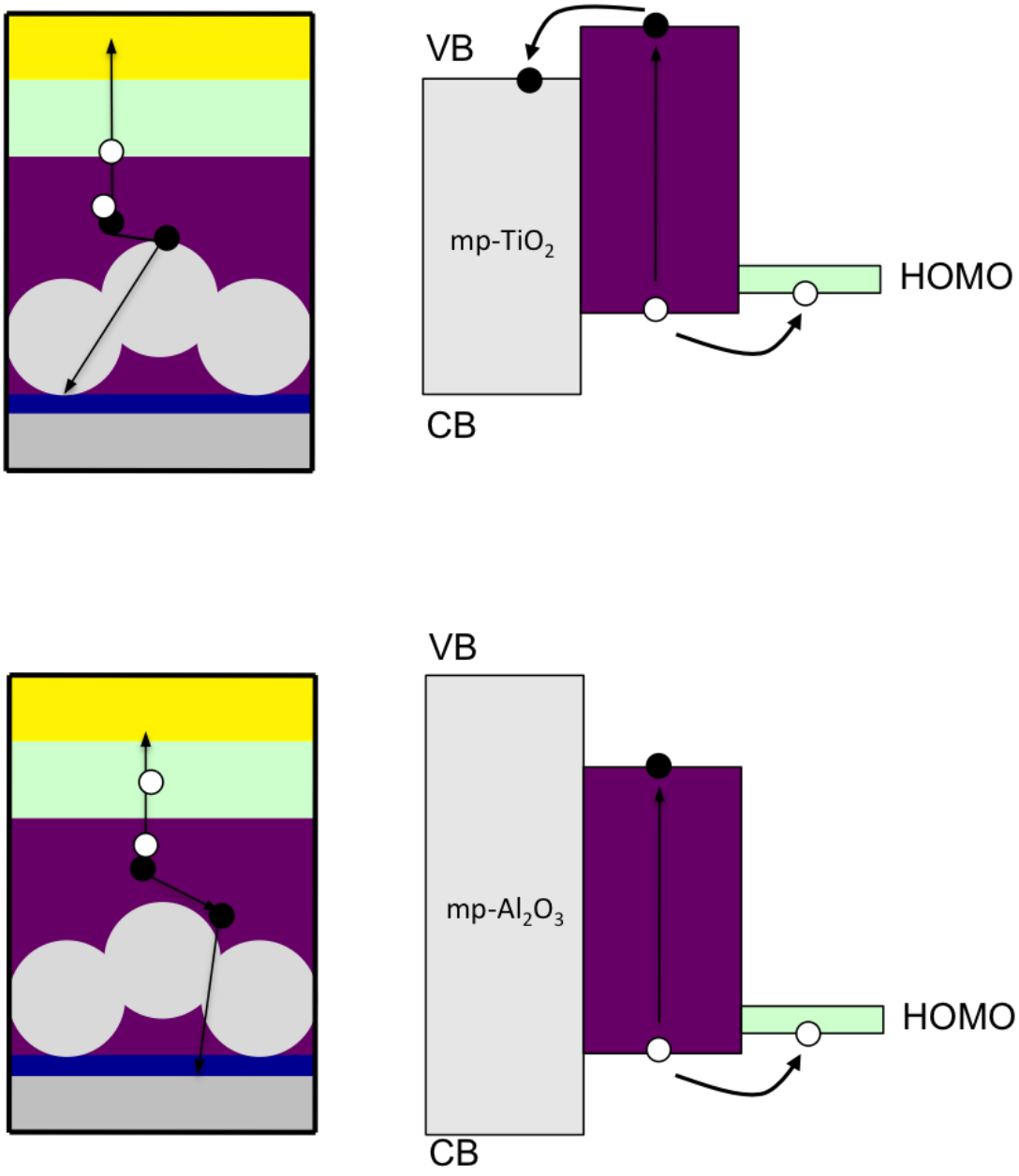


Figure 2.12: Energy level diagrams for a PSC with a mp-$TiO_2$ scaffold and a mp-$Al_2O_3$ scaffold in a DSSC type architecture. Excitons are formed and split into free charge carriers and diffuse to interfaces where they undergo charge extraction, in the mp-$Al_2O_3$ system electron extraction only occurs at the perovskite/electrode interface and the electron is transported through the perovskite phase. mp-$Al_2O_3$ is insulating and only serves to provide a high surface area scaffold for increased photon absorption from thinner layers.

These record efficiencies are far superior to any other next generation SC technology. Especially, in combination with their ability for low-cost scalable production, perovskite absorbers serve to act as the best alternative to harness energy from the sun. Despite this, two key issues exist and need to be addressed so that these materials can become commercially viable. These are, i) Toxicity issues, surrounding the use of lead and ii) Long-term material life-stability.

### 2.5.1 Defect Chemistry

Defects exist in all crystalline semiconductors, their impact affects a range of properties and ultimately performance and stability. There are two main types and they are classified as crystallographic defects (interruptions to the perfect crystal structure) or as impurities, where foreign atoms occupy sites in the lattice. Of these defects numerous studies have explored the impact of crystallographic defects and within this class, defects exist as point defects (atomic vacancies), interstitials (atoms occupying free space between atoms in the lattice) and anti-site substitutions (atoms occupying a different atoms site in the lattice). Higher dimensional point defects also exist, including dislocations and grain boundaries.[56] These point defects impact perovskite crystals and the impact they have on the $AMX_3$ unit cell are demonstrated in the figure below. Defects in perovskites, have been explored through the archetypal methylammonium lead tri-iodide ($MAPbI_3$) species. This material posses 12 native point defects. Three of which are the vacancies, where the atom is missing from the lattice, $V_{MA}$, $V_{Pb}$ and $V_I$. Another three are the interstitials $MA_i$, $Pb_i$ and $I_i$. The remaining defects relate to the anti-site occupations, $MA_{Pb}$, $MA_I$, $Pb_{MA}$, $Pb_I$, $I_{Pb}$ and $I_{MA}$. [57, 58, 59, 60, 61, 62, 63, 64]

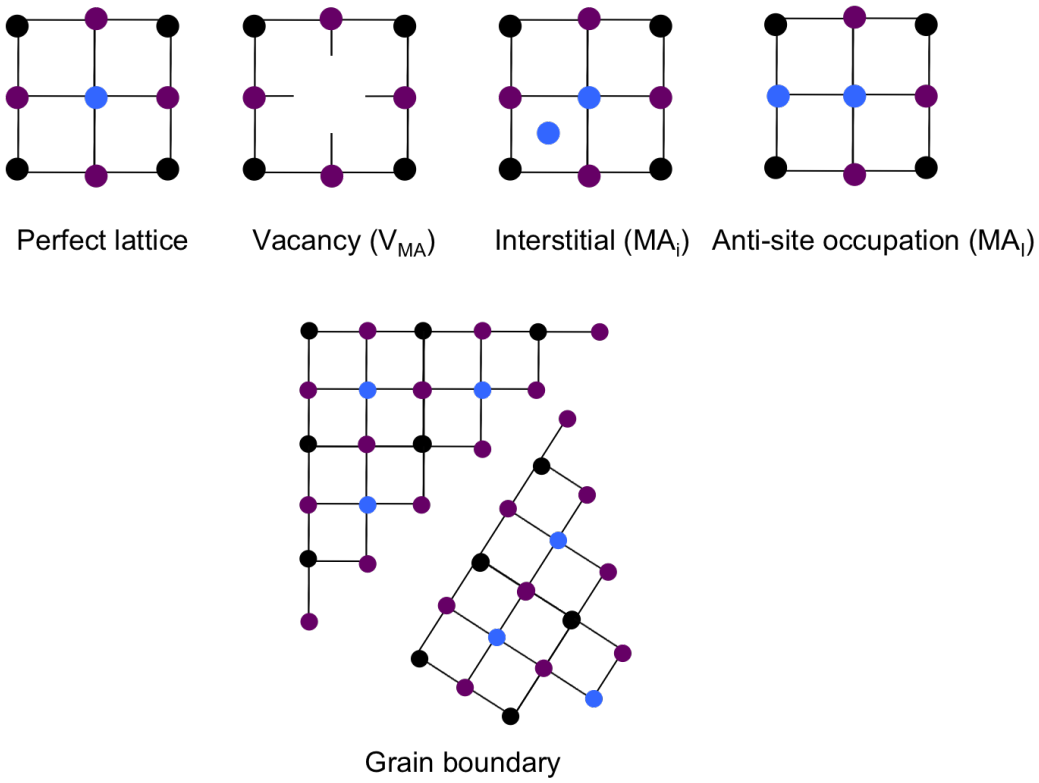


Figure 2.13: Diagrammatic representations of the types of defects in methylammonium lead halide crystal, no defects, a MA vacancy ($V_{MA}$), an extra MA interstitial ($MA_i$) and an anti-site occupation MA cation ($MA_I$). A grain boundary in the crystal is also depicted.

Defects form in a crystal when they have a negative formation energy and are thermodynamically favourable. Here, the formation energy depends on the atomic chemical potential which is related to the concentrations and activity of the reactants, and the electronic chemical potential. As a result growth conditions can greatly impact the internal defect structure and thus the number of defects will be a function of temperature, precursor concentrations, solvent systems, doping and other factors.[65] Traditionally, defects for a particular semiconductor material have been studied using computational methods to calculate the theoretical formation energy. The calculations examine each defect in different charge states, with the lowest formation energy being considered the most stable. The Fermi level, must also be considered though, as the charge state of a defect can alter the electro-chemical potential and ultimately alter the energy of the Fermi-level. This, may mean the most stable charge state of a defect can make a transition for a value of the Fermi level in the band gap. This energy is considered as a state that the charge carriers can interact with, and can lead to changes in recombination rates, charge carrier diffusion and carrier transport velocities. This is because defects can act as trap sites. A trap

restricts the movement of charge carriers, potentially immobilizing the charge carrier and thus increasing the potential for non-radiative recombination pathways to occur. Charges can escape traps, but the rate of transport through the system is consequently reduced too if their is a high density of these trap sites. Trap sites form due to the defect energy levels sitting in the band gap. This phenomenon is depicted in Figure 2.14 [66] In relation to perovskite, DFT calculations have been at the forefront of calculating which defects posses high formation energies and sit deep within the band gap. These include the defects, $I_{MA}$, $I_{Pb}$, $Pb_I$, $I_{MA}$, $Pb_{MA}$. In real terms, this means the defect energy states are so deep in the band gap they have little impact on charge recombination and don't contribute non-radiative processes. In contrast, the acceptor defects ($V_{MA}$, $V_{Pb}$, $I_i$, $MA_{Pb}$, $I_{Pb}$ and $I_{MA}$) and the donor defects ($V_I$, $MA_i$, $Pb_i$, $Pb_{MA}$, $MA_I$ and $Pb_I$) contribute shallow defect energy states with low formation energies leading to n- and p-type doping respectively. These defects can cause high yields of non-radiative charge recombination and reduce the transport velocities of charge carriers.[57, 58, 59, 60, 61, 62]

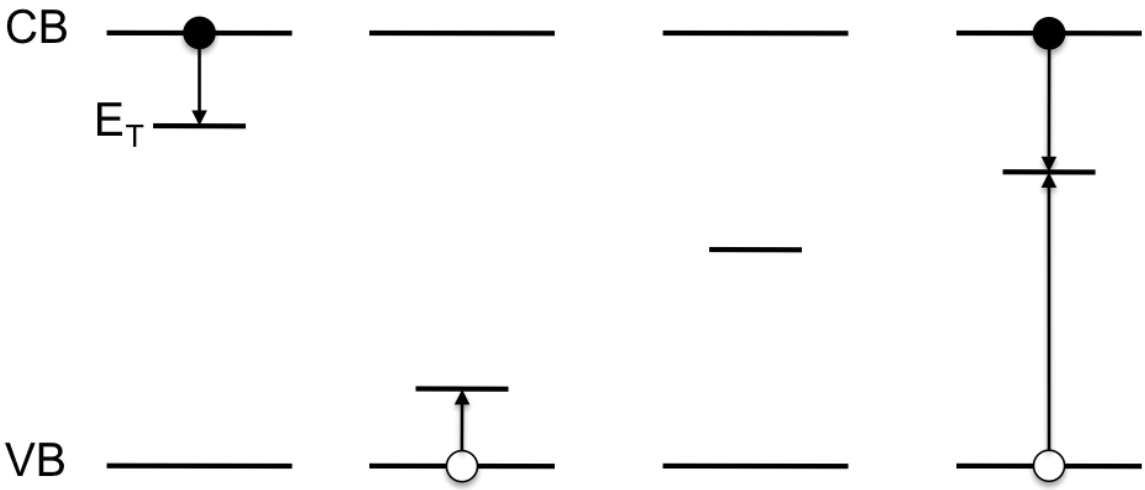


Figure 2.14: Energy level diagram showing the presence of shallow and deep energy trap states. The diagram also represents the impact of defect energy states trapping electrons or holes.

## 2.6 Perovskite Stability

One of the biggest drawbacks to the potential of perovskite photo-absorbers for SC technologies, relates to their inability to retain photo-physical properties over a significant time period. Many environmental factors have been observed to inflict destabilization and performance losses.

Including, thermal degradation, UV degradation and moisture degradation. More importantly though, it has recently emerged that the archetypal MAPI material is highly sensitive to oxygen and light. These conditions are of significant concern as they are harder to eliminate and are present at almost every stage of the production of a solar cell. Furthermore, any system to eliminate oxygen inflicts high production costs and the addition of encapsulation also yields higher costs and they are not always effective at permanently keeping oxygen out of the system for time frames that a solar cell needs to operate in to be viable, tens of years. Understanding the mechanisms and root causes for this sensitivity lie at the heart of improving perovskites such that commercialization can be realised. [67, 68, 69, 70, 71]

### 2.6.1 Phase Stability

The stability of a perovskite phase can be measured via the Goldschmit tolerance factor, t. It is a fundamental physical constant and has no units, that is derived from ratio of the ionic radii of a given set of A, M and X ions in the perovskite $AMX_3$ structure.[72]

$$r = \frac{r_A + r_X}{\sqrt{2}(r_M + r_X)} \tag{2.6}$$

This equation was first developed by Goldschmit for inorganic perovskites, but has crossed over and applies to to hybrid perovskite stability.[72] A stable cubic perovskite structure is observed when t = 0.8 - 1.42. When the ratio of the atomic species causes t to fall outside this limit, the crystal is unstable and the lattice will either crystallise to a distorted structure or form a different structure entirely. For example for a given M ion, an increasing A cation size or decreasing X anion size will manifest in an increasing t value. Here, the large $I^-$ anion in MAPI causes a distorted tetragonal phase to form. This transforms into the cubic phase when it is substituted with smaller anions including $Br^-$ or $Cl^-$ anions[73, 74]. Interestingly though, since organic cations, A, are non-spherical they can adopt different orientations in space in the lattice. So absolute ionic radii and the t factor are more challenging to measure, and more approximate values have to be made relative to the average size of the cation.[75]

### 2.6.2 Thermal Stability

Structural reordering of the MAPI crystal can occur due to environmental factors, namely temperature. It has been observed that a first order phase transition occurs from the tetragonal phase to the cubic phase at 57°C, one sun illumination operating conditions.[76] This process, a symmetry variation, has been linked with changes in optoelectronic performance and material life-time.The material has been shown to undergo rapid degradation to lead iodide ($PbI_2$) within 20 mins at 100°C and at ultra high vacuum. At ambient pressure though, this process is hampered by lower volatilities of methylamine and hydrogen iodide by-products. Even mp-$TiO_2$/MAPI based architectures, subjected to atmospheric pressure and either $N_2$, $O_2$ or ambient air still underwent degradation with constant exposure to temperatures of 85°C. this shows the mechanical stress factor of elevated temperature is sufficient by itself to cause degradation to the perovskite phase.[77] The MAPI crystal structure, has additionally been shown to be a poor thermal conductor in both single crystal and polycrystalline films. This leads to poor dissipation of light-deposited heat and thus heat energy is localized and inflicts high structural stress and limited device life-time.

Degradation has been observed in complete working devices related to elevated temperatures, where mechanical stress caused by thermal expansion inflicts de-lamination in the device layers.[78] This degradation, is of concern as SCs employed in equatorial locations are subjected to persistent elevated operating temperatures. This stresses the need to enhance thermal stability. Of interest though, is the fact that the temperature of the phase transition can be altered by the fabrication process or by using judicious choice of the HTM to invoke an insulating polymer matrix, which protects the perovskite phase from heat related issues.[79, 80]

### 2.6.3 UV stability

Destabilization of the perovskite phase can occur through exposure to UV irradiation. PSCs with a mp-$TiO_2$ scaffold, exhibit rapid photo-current losses and PCE reductions when exposed to air and UV light. These losses are accounted for by the presence of oxygen vacancies at

the surface of the metal oxide nanoparticles, generating oxygen radicals.[81] UV irradiation can generate excitons in the mp-$TiO_2$ nanoparticles, where the hole polaron in the VB reacts with these oxygen radicals. Oxygen then departs from the sites and leaves deep surface traps. Photo-generated electrons in the perovskite can then become immobile by transferring into these trap sites. Trapped electrons are then susceptible to undergo recombination with a hole in the HTM, thereby reducing the probability of photon to electron conversion and reducing the photo-currents. This process is depicted in the figure below.

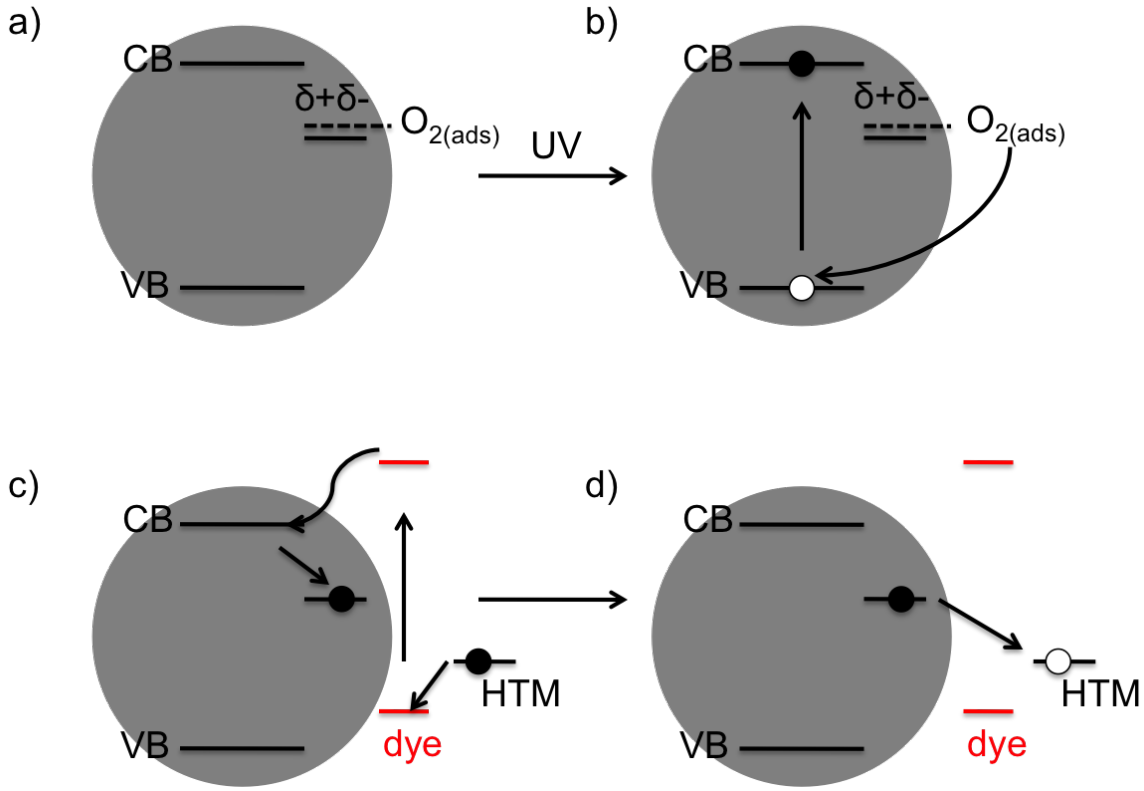


Figure 2.15: Illustration of a PSC degradation and photo-current losses caused by UV irradiation adapted from literature.[81] a) $TiO_2$ nanoparticles with filled surface vacancy sites with oxygen. b) UV excitation forming an exciton in $TiO_2$. The resulting hole recombines with an electron in the oxygen vacancy causing oxygen desorption. c) Photo-excitation in the perovskite (dye) and subsequent trapping of the photo-generated electron. d) Charge recombination of the trapped electron with the hole in the HTM

Further support for this mechanistic action is supported by the substitution of mp-$TiO_2$ for mp-$Al_2O_3$, where increases in UV stability are observed as the electron trapping process can not occur as UV irradiation can not form an exciton in the insulating $Al_2O_3$ material. This substitution can enhance device stability by up 1000 hrs. Additionally, UV filters can be applied

to prevent this issue from occurring.[81, 82, 83] Another approach to mitigate this issue, utilizes a UV absorbing down-shifting layer (DS) for example, $YVO_4$:$Eu^{3+}$. This material can prevent the photo-excitation in the $TiO_2$ layer and enhances red photon flux from the UV photons. This not only improves device life-time it also enhances $J_{sc}$.[84]

### Moisture stability

The impact of moisture on the stability of MAPI and its mixed halide derivatives have been extensively explored. Where below 50% relative humidity (RH), devices are more stable but beyond this significant degradation rates occur. Devices lose over 80% of their performance within 24 hrs.[67, 68, 69, 70] The degradation proceeds via a hydrate intermediate, $(MeNH_3)_4PbI_6.2H_2O$, due to H-bonding between the methylammonium cation and water. Ultimately decomposition into lead iodide results due to moisture exposure. Device life-time can be improved by using blocking layers to prevent water ingress into the system. These are either applied as an encapsulating layer or directly embedded into the structure.[80, 85] These modifications are relatively cheap to implement but do impact the commercial prospects by increasing the complexity of the device architecture.

Water content in hybrid lead halide perovskites has been a specific problem for this class of materials and as such has been the focus of the majority of stability studies.[86, 87, 88, 89, 90, 86] Prolonged exposure of moisture can lead to the permanent degradation of the material.[86, 87] However, other works have also revealed that films of $CH_3NH_3PbI_3$ can have enhanced optoelectronic properties when water is present during the crystallization and annealing processes.[87, 88, 89, 90, 86] This phenomenon has been attributed to the fact that a phase change can occur resulting in the formation of hydrated phases. Humidity controls the crystal growth, with low humidity causing smaller crystallites with large gaps separating them.[86] The research has shown that films exposed to water concentrations below 85% exhibit a reversible phase change into a mono-hydrate phase, whilst at higher concentrations or prolonged exposure an irreversible phase change into the dihydrate phase occurs. It is this research that can account for the differences in stability owed to moisture that have been documented. Additionally, Infrared spectroscopy experiments have highlighted that $CH_3NH_3PbI_3$ films are hygroscopic and

water uptake is rapid. The resulting interaction of water is then with the methylammonium cation component of the perovskite crystal structure. This is reported as an acid-base reaction leading to the breakdown of the crystal. Water has also been found to permeate through perovskite structures to form partly hydrated phases.[88, 91] All these studies highlight factors that are key to understanding the potency of water in determining performance and stability of $CH_3NH_3PbI_3$ films. Consequently, moisture must always be considered in the global picture of $CH_3NH_3PbI_3$ degradation. As such, the work herein starts in an isolated picture where no moisture is present to finally examine the specific degradation considered with the added implications of moisture content within films.

### 2.6.4 Oxygen Stability

A more pertinent issue regarding the environmental stability of methyl-ammonium lead iodide relates to its degradation caused by the combination of both oxygen and light. This photodegradation occurs in moisture free environments at room temperature. The first works reporting this highlighted that the specific conditions of oxygen and light alone could cause the material to show rapid decreases in the yields of photo-induced charge transfer. Where, the yield of long lived charge separation was demonstrated in both bilayer and mp-alumina based architectures to degrade rapidly under these conditions. In contrast, mp-$TiO_2$ exhibited retention of its optoelectronic properties over the time frame examined.[71] My previous research in this field revealed the underlying cause of this degradation and identified the source of the difference in stability between the different architectures towards these conditions. Here, it was shown that the photo-excited electrons (formed from light illumination) can undergo a parasitic electron transfer reaction with molecular oxygen in the atmosphere to form the reactive oxygen species, superoxide ($O_2^{\cdot -}$). This mechanistic understanding provides the origin in the difference in stability between mp-$TiO_2$ and mp-$Al_2O_3$, where the electronically conductive mp-$TiO_2$ can extract the electron from the perovskite phase and compete with the parasitic electron transfer. This deactivation of the photo-excited electron is not possible in the insulating mp-$Al_2O_3$ system and thus the electron has a greater probability of reacting with molecular oxygen to form the reactive oxygen species. This process is demonstrated in an energy level diagram (Figure

2.16 a) of the systems and shows the competing pathways that a photo-excited electron in the perovskite material can undergo. Critically, it was also shown that prolonged exposure not only affected optoelectronic properties, but material decomposition occurs. The work illustrated that the perovskite crystal collapse was due to a reaction with superoxide. An acid-base reaction (deprotonation), between the methylammonium cation and the superoxide species initiates the collapse and results in the formation of iodine, methylammine, water and the yellow lead iodide phase.[92] This reaction scheme along with the generation of superoxide is shown in the Figure 2.16b.

Advancing upon this was the discovery of the impact of these specific conditions on the PCE of devices. The results highlighted and reinforced two key findings. Firstly, that the efficiency of devices was sensitive only towards oxygen and light. In other conditions, where one of these two components was removed degradation in performance was not observed. Furthermore, when both were present and moisture was included into the system, the degradation rate change was minimal. Secondly the results highlight the rapid nature of the degradation with PCE halving within 2hrs of exposure and complete degradation occurring at approximately 6 hours of exposure.[93] Other works have also gone on to show the impact of oxygen and light and the results are all in agreement that these two cause havoc to the performance and life-time of the perovskite phase.[94, 95] The powerful impact of these conditions highlights that both oxygen and light provide the biggest challenge towards creating an environmentally stable perovskite solar cell. These two conditions are extremely difficult to exclude, where light must always be present for a solar cell to operate. On the other hand oxygen, is ever present from the synthesis in the precursor solutions, during the fabrication, on the mesoporous scaffolds, and in the ambient atmosphere to which SCs will operate. Oxygen ingress into solar cells is ultimately a challenge that is almost impossible to prevent and no current polymeric encapsulation exists that can block oxygen,[96] so a greater understanding to improve the perovskite phase tolerance towards oxygen and light is necessary to generate a stable system.

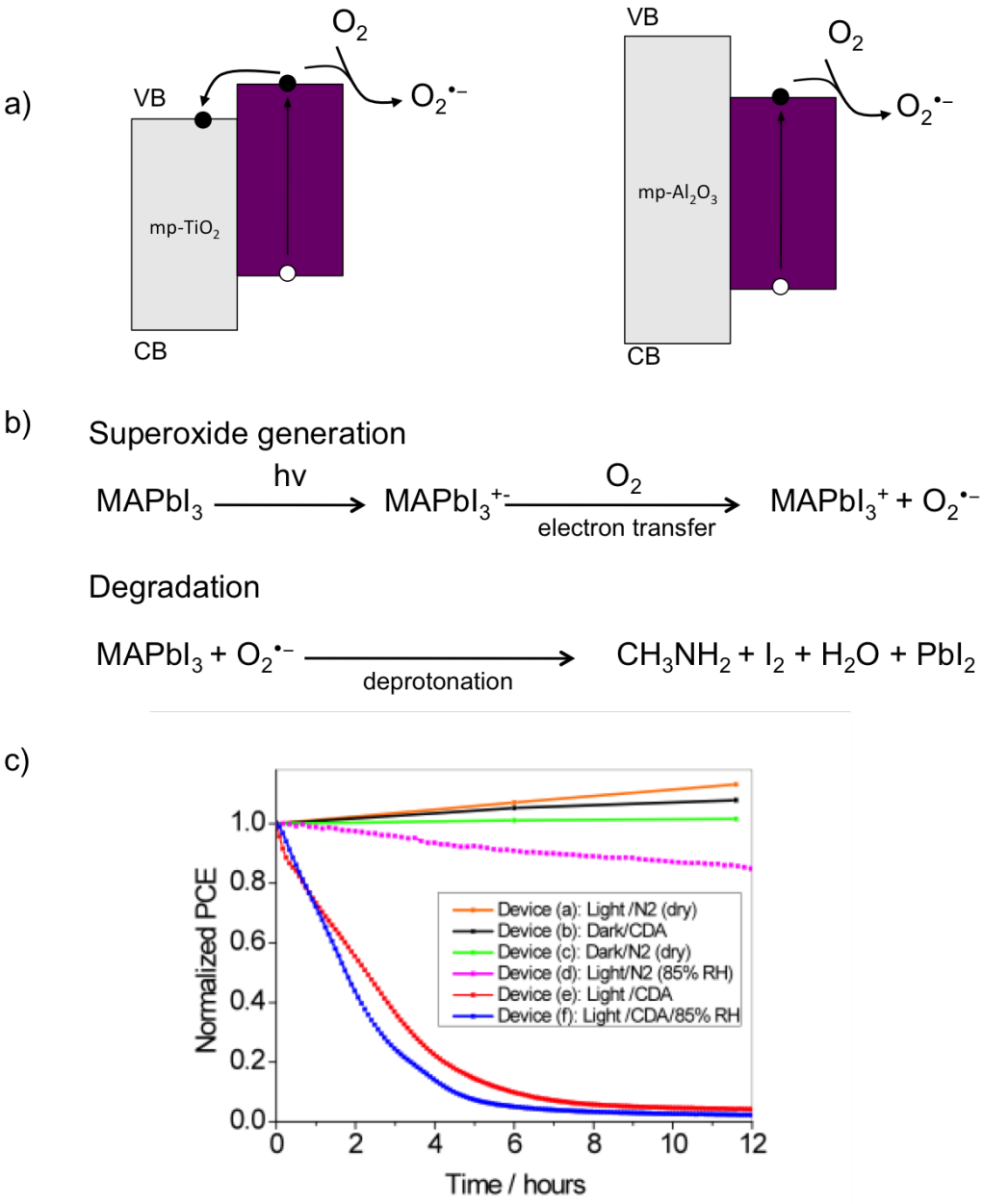


Figure 2.16: a) Energy level diagram depicting the generation of a photo excited electron that can then undergo electron transfer to molecular oxygen to form superoxide. Alternatively, if the mesoporous scaffold is electronically conducting, the photo-electron can be extracted and the pathway competes with the superoxide formation process. This yields more stable films that are better able to retain optoelectronic properties and material stability in comparison to insulating scaffolds that leave the electron active to participate in the parasitic electron transfer reaction. b) Overall degradation mechanism, showing the formation of superoxide via illumination and reaction with oxygen and the subsequent deprotonation of the methylammonium cation leading to the collapse of the crystal structure to lead iodide. c) Data showing the impact of conditions on the PCE of PSCs. Critically both oxygen and light are required and demonstrate rapid degradation to performance. where CDA is compressed dry air.[93]

## 2.7 Current-Voltage Characteristics

A solar cells efficacy to turn solar energy into electrical energy is measured by noting the current (J) passing through the device as a function of an applied voltage (V). The main device parameters allowing characterisation of performance can then be extracted from the resulting current-voltage, J-V, curve. Namely, the power conversion efficiency (PCE, $\eta$), the short circuit current ($J_{sc}$), the open circuit voltage ($V_{oc}$), the Fill factor (FF) and the maximum power output ($P_m$). Identifying these values can yield information regarding major losses and which parameters need to be enhanced to increase efficiency. In the dark a SC device should behave as a diode, only allowing current flow in one direction (forward bias). Illumination, leads to photo-excitation and creates a photo-current/photo-voltage within the device, that scale with light intensity. Typical, J-V curves obtained for a device under illumination and in the dark are presented in the figure below and the key parameters are noted.

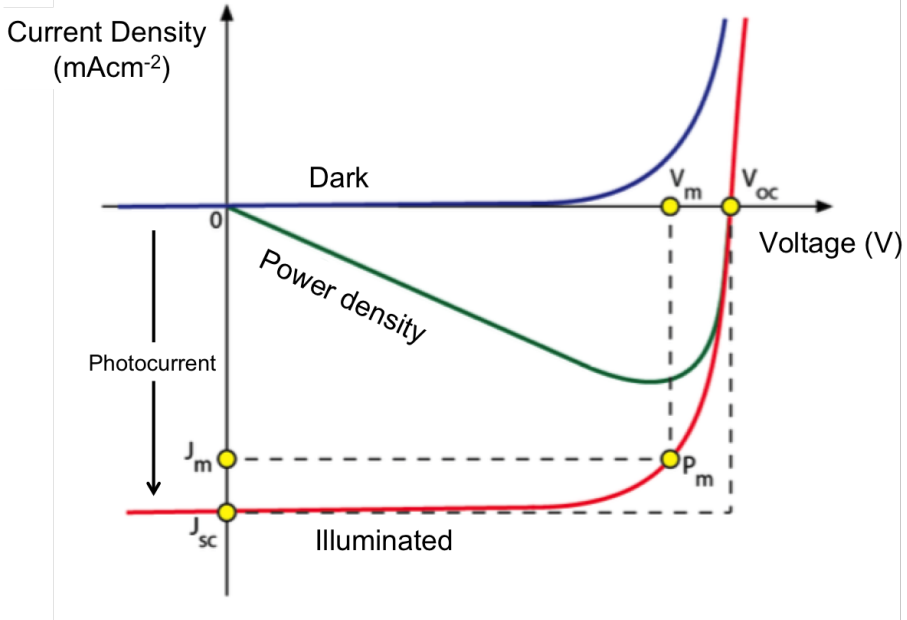


Figure 2.17: J-V curve for a SC highlighting the key device parameters and the profile under illumination and in the dark. The power density (green curve) is the product of the photocurrent and the photovoltage.

**Power Conversion efficiency, PCE**

Power conversion efficiency, $\eta$, is the parameter to which all solar cells are benched marked against. This is the true measure of a SCs ability to turn solar energy into electrical energy. This value is obtained from a number of key device parameters, but is defined as the ratio of the maximum power out ($P_m$) to the incident light power ($P_{In}$). The equation shown illustrates the dependency of the PCE on the parameters shown in the J-V curve figure.

$$\eta = \frac{P_m}{P_{In}} = \frac{V_m.J_m}{P_{In}} = \frac{V_{oc}.J_{sc}.FF}{P_{In}} \tag{2.7}$$

As a standard measurement the conditions to which all SCs PCEs are fixed. This ensures direct comparison is possible. The specific experimental conditions are defined as A.M. 1.5 solar illumination with a power rating of 100 mW/cm$^2$ at 298K.[12] A. M. 1.5 is the air mass factor, that takes into account that sunlight passes through the atmosphere and causes attenuation. As SCs operate at an angle ($\theta \neq 90$) to the sun, the sunlight appears to pass through more than the thickness of the atmosphere. As a result a correction factor of 1.5 is used to increase the attenuation induced by the increased thickness.

### 2.7.1 Open circuit Voltage

Open circuit conditions, deliver a scenario where the rates of charge separation and recombination are equal, such that no net current flows and the voltage is a maximum. The open circuit voltage is this maximum and represents the maximum potential difference between the electron and the hole once they have been extracted into their respective electrodes. This potential difference is also dependent on the energetics of the active layer. In an ideal situation, the $V_{oc}$ would equal the band gap of the absorber. Although, in real devices resistance and energetic losses at interfaces to drive spatial separation lower the $V_{oc}$ obtained. Reducing these losses, while maintaining high levels of charge separation and efficient transport is required for optimal $V_{oc}$ values. For efficient light harvesting the band gap of the absorber needs to be able to absorb

a large percentage of solar radiation. Consequently, small band gaps are desirable but this limits the maximum theoretical value obtainable for the voltage. Hence, a compromise between the current and the voltage is required. The theoretical band gap that generates the optimal balance is around 1.5 eV.[97]

### 2.7.2 Short circuit voltage

Short-circuit conditions provide the picture of when the device is operating with no resistance between the electrodes. Here, charges can flow from the cathode to the anode whilst maintaining the same potential. This yields the maximum obtainable photo-current, $J_{sc}$, and is represented in the following equation:

$$J_{sc} = e \int N_{ph}(E).QE(E).dE \tag{2.8}$$

In the equation, $N_{ph}$ is the incident photon flux (no. of photons in an energy range per unit area per unit time), e is the charge of an electron and QE(E) is the probability of an absorbed photon converting into an electron. QE(E), can be expressed in the following form:

$$QE(E) = P(LH).P(CS).P(1 - CR) \tag{2.9}$$

The probability of conversion is dependent on three variables. First, the probability a photon will be absorbed and depends on the thickness of the active layer and its extinction coefficient. A thicker layer and/or a larger extinction coefficient will cause greater photon absorption and thus increase exciton yields. This dependence is represented by P(LH), and will also depend on other factors such as light scattering and refraction for example. Secondly, the probability an exciton will undergo spatial separation into free charges, the probability of charge separation, P(CS). Ineffective CS causes low current as the majority of excitons will decay back to the ground state rather than split and allow for charge extraction. Thirdly, the probability a charge carrier will undergo transport to the electrodes without undergoing charge recombination (CR). Generated electrons and holes are required to be transported to electrodes without recombining so they can be extracted into an external circuit to perform useful work. This is proportional

to 1 minus the probability of CR. A larger value indicates a low probability of recombination, suggesting the electron and hole are unlikely to come back into contact (within the Coulombic attraction distance) and decay back to the ground state. Therefore, the $J_{sc}$ values of devices compares the ability of system to harvest light energy, split charges and transport them to the electrodes.

An important factor to consider when choosing an active layer is it's light harvesting ability. This is related to it's band gap and dictates how much energy can be absorbed from incident sunlight. Incident photons with energy less than the band gap are wasted and pass through the device without being absorbed. On the other hand, incident photons with energy greater than the band gap waste the excess energy as heat, thermalisation losses. This invokes an optimal balance between these factors and stipulates a band gap that is most efficient for high working currents.[97, 27, 98]

### 2.7.3 Fill Factor, FF

The fill factor is a measure of the "quality" of the SC and is a more sensitive measure than $J_{sc}$ and $V_{oc}$. The FF, is related to factors such as, interface morphology, charge carrier mobility, carrier life-time and material resistance. These factors can dictate the amount of charge recombination or the amount of current leakage. Increasing the FF, causes the $P_m$ to become closer to the theoretical maximum power output, $J_{sc}$*$V_{oc}$. The FF, can be defined as the ratio between the voltage and the current at the maximum power point ($V_m$ and $J_m$) to the the theoretical maximum power.

$$FF = \frac{V_m.J_m}{V_{oc}.J_{sc}} \tag{2.10}$$

Graphically the FF can be represented as the ratio of the areas defined by $V_m$.$J_m$ to the area defined by $J_{sc}$.$V_{oc}$. These areas are depicted in the J-V curve enclosed by the dashed line rectangles. As the property is a ratio the optimal FF is unity. To approach this, losses resulting from CR, current leakage and resistance must be minimised and allow the power output to be maximised.

# References

[1] R. Hoffmann, *Angew. Chem. Int. Ed. Engl.*, 1987, **26**, 846–878.

[2] P. Dirac, *Proceedings of the Royal Society of London A: Mathematical, Physical and Engineering Sciences*, 1926, **112**, 661–677.

[3] A. H. Wilson, *The Theory of Metals*, Cambridge university Press, 1965.

[4] J. Nelson, *The Physics of Solar cells*, Imperial College Press, 2003.

[5] A. Cuevas, *J. App. Phys.*, 1996, **80**, 3370.

[6] H. H. Mohamed, D. W. Bahnemann, *Applied Catalysis B: Environmental*, 2012, **128**, 91 – 104.

[7] R. Murray, D. Granner, P. Mayes, V. Rodwell, *Harper's Illustrated Biochemistry*, Mcgraw-hill, 2003.

[8] R. A. Marcus, *J. Chem. Phys.*, 1956, **24**, 966.

[9] R. A. Marcus, *Discuss Faraday Soc.*, 1960, **29**, 21.

[10] R. A. Marcus, *J. Chem. Phys.*, 1965, **43**, 679.

[11] D. Chapin, C. Fuller, G. Pearson, *J. Appl. Phys.*, 2012, **25**, 676–677.

[12] M. A. Green, K. Emery, Y. Hishikawa, W. Warta, E. D. Dunlop, *Prog. Photo. Res. App.*, 2012, **20**, 606–614.

[13] T. Markvart, L. Castaner, *Solar Cells: Operating Principles, Technology and System Applications*, Prentice-Hall, Inc., 1986.

[14] T. Markvart, L. Castaner, *Practical Handbook of Photovoltaics: Fundamentals and Applications*, Elsevier, 2003.

[15] M. Einzinger, T. Wu, J. F. Kompalla, H. L. Smith, C. F. Perkinson, L. Nienhaus, S. Wieghold, D. N. Congreve, A. Kahn, M. G. Bawendi, M. A. Baldo, *Nature*, 2019, **571**, 90 – 97.

[16] M. K. Nazeeruddin, E. Baranoff, M. Grtzel, *Sol. Energy*, 2011, **85**, 1172–1178.

[17] J. Nelson, *Mater. Today*, 2011, **14**, 462470.

[18] J.-H. Im, I.-H. Jang, N. Pellet, M. Grtzel, N.-G. Park, *Nat. Nanotech.*, 2014, **9**, 927–931.

[19] H. Hoppe, N. S. Sariciftci, *J. Mater. Res.*, 2004, **19**, 19241945.

[20] B. Roth, A. Rudenko, B. Thompson, F. Krebs, *J. Photon. Energy*, 2015, **5**, 1–10.

[21] G. P. Kushto, W. Kim, Z. H. Kafafi, *Appl. Phys. Lett.*, 2004, **86**, 118–125.

[22] S. Lee, Y. Lee, J. Park, D. Choi, *Nano Energy*, 2014, **9**, 88 – 93.

[23] M. Grtzel, *J. Photochem. Photobiol., C: Photochem. Rev.*, 2003, **4**, 145 – 153.

[24] B. O'Regan, M. Gratzel, *Nature*, 1991, **353**, 737–740.

[25] S. E. Koops, B. C. ORegan, P. R. F. Barnes, J. R. Durrant, *J. Am. Chem. Soc.*, 2009, **131**, 4808–4818.

[26] J. R. S. Meng, E. Kaxiras, *Nano Lett.*, 2008, **8**, 3266–3272.

[27] N. Robertson, *Angew. Chem. Int. Ed.*, 2006, **45**, 2338–2345.

[28] A. Yella, H.-W. Lee, H. N. Tsao, C. Yi, A. K. Chandiran, M. Nazeeruddin, E. W.-G. Diau, C.-Y. Yeh, S. M. Zakeeruddin, M. Grtzel, *Science*, 2011, **334**, 629–634.

[29] H. J. Snaith, L. Schmidt-Mende, *Ad. Mater.*, 2007, **19**, 3182–3200.

[30] N. Cai, S.-J. Moon, L. Cevey-Ha, T. Moehl, R. Humphry-Baker, P. Wang, S. M. Zakeeruddin, M. Grtzel, *Nano Lett.*, 2011, **11**, 1452–1456.

[31] U. Bach, D. Lupo, P. Comte, J. Moser, F. Weissortel, *Nature*, 1998, **395**, 583–585.

[32] M. Grtzel, *MRS Bulletin*, 2005, **30**, 23–27.

[33] A. Kojima, K. Teshima, Y. Shirai, T. Miyasaka, *J. Am. Chem. Soc.*, 2009, **131**, 6050–6051, PMID: 19366264.

[34] G. Hodes, *Science*, 2013, **342**, 317–318.

[35] T. Fukumoto, T. Moehl, L. Etgar, *Adv. Energy Mater.*, 2013, **3**, 29–33.

[36] M. Gratzel, *Acc. Chem. Res.*, 2009, **3**, 1788–1798.

[37] I. Borriello, G. Cantele, D. Ninno, *Phys. Rev. B*, 2008, **77**, 235214.

[38] T. Baikie, Y. Fang, T. White, *J. Mater. Chem. A*, 2013, **1**, 5628–5641.

[39] C. P. Jr, T. Pullerits, A. Stepanov, *J. Am. Chem. Soc.*, 2014, **136**, 5189–5192.

[40] D. B. Mitzi, *J. Chem. Soc. Dalt. Trans.*, 2001, **1**, 1–12.

[41] C. C. Stoumpos, C. D. Malliakas, M. G. Kanatzidis, *Inorg. Chem.*, 2013, **52**, 90199038.

[42] L. M. Hertz, *ACS Energy Lett.*, 2017, **2**, 1539–1548.

[43] Z. Cheng, J. Lin, *Cryst. Eng. Comm.*, 2010, **12**, 2646–2662.

[44] D. B. Mitzi, S. Wang, C. A. Feild, C. A. Chess, A. M. Guloy, *Science*, 1995, **267**, 1473–1476.

[45] J.-H. Im, C.-R. Lee, J.-W. Lee, S.-W. Park, N.-G. Park, *Nanoscale*, 2011, **3**, 4088–4093.

[46] H.-S. Kim, J.-W. Lee, N. Yantara, P. P. Boix, S. A. Kulkarni, S. Mhaisalkar, M. Grtzel, N.-G. Park, *Nano Lett.*, 2013, **13**, 2412–2417.

[47] J. H. Heo, S. H. Im, J. H. Noh, T. N. Mandal, C.-S. Lim, J. A. Chang, Y. H. Lee, H.-J. Kim, A. Sarkar, M. K. Nazeeruddin, M. Gratzel, S. I. Seok, *Nat. Photon.*, 2013, **7**, 486–491.

[48] J. Burschka, N. Pellet, S.-J. Moon, R. Humphry-Baker, P. Gao, M. K. Nazeeruddin, M. Gratzel, *Nature*, 2013, **499**, 316–319.

[49] J. M. Ball, M. M. Lee, A. Hey, H. J. Snaith, *Energy Environ. Sci.*, 2013, **6**, 1739–1743.

[50] M. M. Lee, J. Teuscher, T. Miyasaka, T. N. Murakami, H. J. Snaith, *Science*, 2012, **338**, 643–647.

[51] M. Liu, M. B. Johnston, H. J. Snaith, *Nature*, 2013, **501**, 395–398.

[52] J. H. Noh, S. H. Im, J. H. Heo, T. N. Mandal, S. I. Seok, *Nano Lett.*, 2013, **13**, 1764–1769.

[53] L. Etgar, P. Gao, Z. S. Xue, Q. Peng, A. K. Chandiran, B. Liu, M. K. Nazeeruddin, M. Gratzel, *J. Am. Chem. Soc.*, 2012, **134**, 17396–17399.

[54] S. Dharani, H. K. Mulmudi, N. Yantar, P. T. T. Trang, N. G. Park, M. Graetzel, S. Mhaisalkar, N. Mathews, P. P. Boix, *Nanoscale*, 2014, **6**, 1675–1679.

[55] H. J. Snaith, *J. Phys. Chem Lett.*, 2013, **4**, 3623–3630.

[56] H. J. Queisser, E. E. Haller, *Science*, 1998, **281**, 945–950.

[57] J. Kim, S.-H. Lee, J. H. Lee, K.-H. Hong, *The Journal of Physical Chemistry Letters*, 2014, **5**, 1312–1317.

[58] W.-J. Yin, T. Shi, Y. Yan, *Applied Physics Letters*, 2014, **104**, 063903.

[59] M. L. Agiorgousis, Y.-Y. Sun, H. Zeng, S. Zhang, *Journal of the American Chemical Society*, 2014, **136**, 14570–14575.

[60] A. Walsh, D. O. Scanlon, S. Chen, Gong, X. G., S. H. Wei, *Angew. Chem. Int. Ed.*, 2015, **54**, 17911794.

[61] C. Eames, J. M. Frost, P. R. F. Barnes, B. C. ORegan, A. Walsh, M. S. Islam, *Nat. Commun.*, 2015, **6**, 7497–7506.

[62] A. Buin, P. Pietsch, J. Xu, O. Voznyy, A. H. Ip, R. Comin, E. H. Sargent, *Nano Letters*, 2014, **14**, 6281–6286.

[63] J. Xu, A. Buin, A. Ip, W. Li, O. Voznyy, R. Comin, M. Yuan, S. Jeon, Z. Ning, J. McDowell, P. Kanjanaboos, J.-P. Sun, X. Lan, L. N. Quan, D. H. Kim, I. G. Hill, P. M. . E. H. Sargent, *Nat. Commun.*, 2015, **6**, 7081–7089.

[64] A. Buin, R. Comin, J. Xu, A. H. Ip, E. H. Sargent, *Chemistry of Materials*, 2015, **27**, 4405–4412.

[65] S. D. Stranks, P. K. Nayak, W. Zhang, T. Stergiopoulos, H. J. Snaith, *Angewandte Chemie International Edition*, 2015, **54**, 3240–3248.

[66] C. Freysoldt, B. Grabowski, T. Hickel, Neugebauer, G. Kresse, A. Janotti, C. G. Van de Walle, *Rev. Mod. Phys.*, 2014, **86**, 253–305.

[67] H. P. Zhou, Q. Chen, G. Li, S. Luo, T. B. Song, H. S. Duan, Z. R. Hong, J. B. You, Y. S. Liu, Y. Yang, *Science*, 2014, **345**, 542–546.

[68] J. A. Christians, P. M. Herrera, P. V. Kamat, *J. Am. Chem. Soc.*, 2015, **137**, 1530–1538.

[69] G. Niu, W. Li, F. Meng, L.Wang, H. Dong, Y. Qiu, *J. Mater. Chem. A*, 2014, **2**, 705–710.

[70] J. Yang, B. D. Siempelkamp, D. Liu, T. L. Kelly, *ACS Nano*, 2015.

[71] F. T. O'Mahony, Y. H. Lee, C. Jellett, S. Dmitrov, D. T. Bryant, J. R. Durrant, B. C. O'Regan, M. Graetzel, M. K. Nazeeruddin, S. A. Haque, *J. Mater. Chem. A*, 2015.

[72] A. Amat, E. Mosconi, E. Ronca, C. Quarti, P. Umari, M. K. Nazeeruddin, M. Grtzel, F. De Angelis, *Nano Letters*, 2014, **14**, 3608–3616.

[73] A. Poglitsch, D. Weber, *The Journal of Chemical Physics*, 1987, **87**, 6373–6378.

[74] G. Niu, W. Li, F. Meng, L. Wang, H. Dong, Y. Qiu, *J. Mater. Chem. A*, 2014, **2**, 705–710.

[75] M. T. Weller, O. J. Weber, P. F. Henry, A. M. Di Pumpo, T. C. Hansen, *Chem. Commun.*, 2015, **51**, 4180–4183.

[76] G. Niu, X. Guo, L. Wang, *J. Mater. Chem. A*, 2015, **3**, 8970–8980.

[77] B. Philippe, B.-W. Park, R. Lindblad, J. Oscarsson, S. Ahmadi, E. M. J. Johansson, H. Rensmo, *Chemistry of Materials*, 2015, **27**, 1720–1731.

[78] B. Conings, J. Drijkoningen, N. Gauquelin, A. Babayigit, J. DHaen, L. DOlieslaeger, A. Ethirajan, J. Verbeeck, J. Manca, E. Mosconi, F. D. Angelis, H.-G. Boyen, *Adv. Energy Mater.*, 2015, 1–8.

[79] C. C. Stoumpos, C. D. Malliakas, M. G. Kanatzidis, *Inorganic Chemistry*, 2013, **52**, 9019–9038.

[80] S. N. Habisreutinger, T. Leijtens, G. E. Eperon, S. D. Stranks, R. J. Nicholas, H. J. Snaith, *Nano Letters*, 2014, **14**, 5561–5568.

[81] T. Leijtens, G. Eperon, S. Pathak, A. Abate, M. Lee, H. J. Snaith, *Nat. Commun.*, 2013, **4**, 2885–2893.

[82] S. K. Pathak, A. Abate, T. Leijtens, D. J. Hollman, J. Teuscher, L. Pazo, P. Docampo, U. Steiner, H. J. Snaith, *Adv. Energy Mater.*, 2014, **4**, 1301667.

[83] K. Schwanitz, U. Weiler, R. Hunger, T. Mayer, W. Jaegermann, *J. Phys. Chem. C*, 2007, **111**, 849–854.

[84] B. Conings, A. Babayigit, T. Vangerven, J. D'Haen, J. Mancab, H.-G. Boyen, *J. Mater. Chem. A*, 2015, **3**, 1–5.

[85] S. Kundu, T. L. Kelly, *Mater. Chem. Front.*, 2018, **2**, 81–89.

[86] G. E. Eperon, S. N. Habisreutinger, T. Leijtens, B. J. Bruijnaers, J. J. van Franeker, D. W. deQuilettes, S. Pathak, R. J. Sutton, G. Grancini, D. S. Ginger, R. A. J. Janssen, A. Petrozza, H. J. Snaith, *ACS. Nano.*, 2015, **9**, 9380–9393.

[87] C.-J. Tong, W. Geng, Z.-K. Tang, C.-Y. Yam, X.-L. Fan, J. Liu, W.-M. Lau, L.-M. Liu, *The Journal of Physical Chemistry Letters*, 2015, **6**, 3289–3295.

[88] C. Mller, T. Glaser, M. Plogmeyer, M. Sendner, S. Dring, A. A. Bakulin, C. Brzuska, R. Scheer, M. S. Pshenichnikov, W. Kowalsky, A. Pucci, R. Lovrini, *Chem. Mater.*, 2015, **27**, 7835–7841.

[89] G. Grancini, V. D'Innocenzo, E. R. Dohner, N. Martino, A. R. Srimath Kandada, E. Mosconi, F. De Angelis, H. I. Karunadasa, E. T. Hoke, A. Petrozza, *Chem. Sci.*, 2015, **6**, 7305–7310.

[90] J. F. Galisteo-Lpez, M. Anaya, M. E. Calvo, H. Mguez, *J. Phys. Chem. Lett.*, 2015, **6**, 2200–2205.

[91] X. Gong, M. Li, X. Shi, H. Ma, Z. Wang, L. Liao, *Ad. Funct. Mater.*, 2015, **25**, 6671–6678.

[92] N. Aristidou, I. Sanchez-Molina, T. Chotchuangchutchaval, M. Brown, L. Martinez, T. Rath, S. A. Haque, *Angewandte Chemie International Edition*, 2015, **54**, 8208–8212.

[93] D. Bryant, N. Aristidou, S. Pont, I. Sanchez-Molina, T. Chotchunangatchaval, S. Wheeler, J. R. Durrant, S. A. Haque, *Energy Environ. Sci.*, 2016, **9**, 1655–1660.

[94] N. H. Nickel, F. Lang, V. V. Brus, O. Shargaieva, J. Rappich, *Advanced Electronic Materials*, 2017, **3**, 1700158–n/a.

[95] A. J. Pearson, G. E. Eperon, P. E. Hopkinson, S. N. Habisreutinger, J. T.-W. Wang, H. J. Snaith, N. C. Greenham, *Advanced Energy Materials*, 2016, **6**, 1600014–n/a.

[96] G. Strupinsky, A. Brody, *High Barrier Packaging Yesterday, Today and Tomorrow, 1999 Polymers, Laminations and Coatings Conference Proceedings*, TAPPI, 1998.

[97] T. Zdanowicz, T. Rodziewicz, M. Zabkowska-Waclawek, *Sol. Energ. Mat. Sol. Cells*, 2005, **87**, 757 – 769.

[98] P. Vanlaeke, A. Swinnen, I. Haeldermans, G. Vanhoyland, T. Aernouts, D. Cheyns, C. Deibel, J. DHaen, P. Heremans, J. Poortmans, J. Manca, *Sol. Energ. Mat. Sol. Cells*, 2006, **90**, 2150 – 2158.

# Chapter 3

# Experimental

## 3.1 Materials and Processing

In this work, thin films of Hybrid inorganic-organic perovskites are formed from solution by spin coating and deposited on a range of substrates. All chemicals were purchased from Sigma-Aldrich and used as received, except $TiO_2$ nanoparticles and Spiro-OMeTAD from Dyesol and methylammonium iodide (MAI), which were synthesized in the lab. All films were deposited onto clean glass substrates or onto conducting glass substrates with ITO or FTO, of ca. 1 cm by 1 cm size or 4 cm by 4 cm size. The substrates were cleaned by washing sequentially in acetone, deionised water and isopropylalcohol (IPA) under sonication for 10 minutes during each cycle. The slides were then dried using nitrogen flow. A Laurell Technologies WS-650MZ-23NPP Spin Coater was used to fabricate all films. The associated experimental procedures are described herein.

### 3.1.1 Methylammonium Lead Iodide Synthesis

Methylamine 33% wt solution in ethanol (6.2 mL, 0.046 moL) was cooled down in an ice bath. Hy- droiodic acid 55% wt solution in water (10 mL, 0.073 mol) was then added dropwise under vigorous stirring. The reaction was stirred for 1 h at 0°C. The product crashed out from the solution as a white-yellowish solid. Ethanol (5 mL) was added to ensure full precipitation of the solid, which was filtered and washed with cold ethanol. Recrystallization of the product in

chloroform afforded the pure compound as a white crystalline solid (6.4 g, 87%).

### 3.1.2 Phenylethylammonium Iodide

Phenylethylamine was sysnthesised by generating a 33% wt solution in ethanol (6.2ml, 0.046mol) with cooling in an ice bath. Hydroiodic acid 55% wt solution in water (10ml, 0.073mol) was then added dropwise under vigorous stirring. The reaction was stirred for 1hr at 0°C. The product precipitated from the solution as a white-yellowish solid. Ethanol (5ml) was added to ensure full precipitation of the solid, which was filtered and washed with cold ethanol. Recrystallization of the product in ethanol/diethyl ether afforded the pure compound as white crystalline solid.

### 3.1.3 Metal-Oxide Preparation

A mesoporous $Al_2O_3$ layer was fabricated on to the cleaned substrates, by using a 2:1 ratio of $Al_2O_3$ (< 50 nm particle size in IPA solution) to IPA. This solution was pipetted onto the glass slides and spin-coated at 4500 rpm for 45 s. After spin coating, the films were placed on a hotplate at 150°C for 30 minutes.

Mesoporous $TiO_2$ based films were fabricated using a solution of 20 nm $TiO_2$ nanoparticles (Dyesol) in a 1:7 weight ratio with dry Ethanol. This was spin-coated onto glass substrates at 6000 rpm for 30 s. Once spun the films were sintered at 450°C for 1 hour.

Compact $TiO_2$ electron extraction layers were fabricated by mixing 70 $\mu$l of titanium diisopropoxide bis(acetylacetonate), 55 $\mu$l of ethanolamine and 1 ml of 2-methoxythanol. After that, it was left to stir for 30 minutes, and then filtered with a 0.2m PTFE syringe filter. The solution was then deposited onto cleaned glass with spin coating at 6,000 rpm, 2,000 rpm/s for 30 seconds. The films were then heated in a furnace at 500 °C for 30 minutes.

Compact ZnO layers were formed from a solution of anhydrous zinc acetate (0.08 mmol/mL) and 2-ethanolamine (0.08 mmol/mL) in 2-methoxyethanol. The ZnO solution was spin-coated onto cleaned glass substrates. The resulting films were preannealed at 125°C before heating at 500°C for 1 hour. Lithium doping was achieved by using Lithium bis(trifluoromethane sulfonyl) imide (LiTFSI).

Compact $SnO_2$ films were produced by creating a 0.1M solution of $SnCl_2.2H_2O$ in ethanol. This solution was then spin coated onto glass and annealed at 200°C for 1 hour under ambient conditions.[1]

### 3.1.4 Spiro-OMeTAD

Spiro-OMeTAD (2,2,7,7-tetrakis-(N,N-di-p- methoxyphenyl-amine)-9,9- spirobifluorene,) was purchased from SOLARONIX. A solution of 0.17 M spiro-OMeTAD in chlorobenzene was prepared. Additives were introduced by pippeting in 15 L of 86 mg of Lithium bis(trifluoromethane sulfonyl) imide (LiTFSI) in 1 mL acetonitrile and 15 L of 162 mg of 4-tert-butylpyridine (tBP) in 1 mL of acetonitrile. The resulting solution was stirred for two hours prior to use. Deposition was carried out by spin coating at 2000 r.p.m for 1 minute. The resulting film was then oxidized overnight in the dark for 24 hours.

### 3.1.5 Methylammonium Lead Iodide synthesis

A 1M solution of $CH_3NH_3PbI_3$ was formed by adding $PbI_2$ in a 1:1 molar ratio with MAI in a solvent mixture of 7:3 gamma-butyrolactone to DMSO. This solution was then spin-coated onto the selected substrates using a consecutive two-step spin program under a nitrogen atmosphere in a glove box. The first spinning cycle was performed at 1,000 r.p.m. for 10s followed by 5,000r.p.m. for 20s, as reported by Jeon et al.[2] During the second phase, the substrate was treated with toluene (ca. 350ml) drop-casting. The films were then annealed at 100 °C for 10min.

#### Varying Crystal Size

Films were prepared with controlled crystal size in accordance with the two-step deposition method described by Grtzel et al.[3] 20 $\mu$l of a 1M solution of $PbI_2$ in DMF was spin-coated onto glass substrates at 3,000 r.p.m. for 5s and then at 6,000 r.p.m. for another 5s. The films were then annealed at 40°C for 3min followed by heating at 100°C for 5min. Once the films had cooled to room temperature, 200$\mu$l of 0.038M (sample 3), 0.050M (sample 2) and

0.063M (sample 1) MAI in IPA solution were loaded on top of them for 20s, before spinning at 4,000r.p.m. for 20s. Films were then annealed at 100°C for 5min.

**Chlorine Treated**

Chlorine treated $CH_3NH_3PbI_3$: A 1M solution was created by dissolving $PbCl_2$ and MAI in a 1:3 ratio in DMF. The solution was then spin-coated onto substrates at 1,000 r.p.m. for 10 s followed by 5,000 r.p.m. for 20s. Annealing was carried out by leaving the films at room temperature for 30min followed by heating at 100°C for an hour.

### 3.1.6 Synthesis of Mixed Halide Perovskites

Stock solutions of $CH_3NH_3PbI_3$ and $CH_3NH_3PbBr_3$ were prepared by dissolving stoichiometric ratios of $PbX_2$ and $CH_3NH_3X_3$ (X = I, Br) in a DMSO and GBL solution (7:3) at 1.25 M concentration and stirred for 60 minutes at 50°C and room temperature, respectively. To obtain a range of x values in $CH_3NH_3Pb(I_{(1-x)}Br_x)_3$ stock solutions were combined with volumetric ratios. Thin film samples were prepared on glass using the anti-solvent technique adapted from a previously reported method. Glass was washed in soap, acetone, and 2-propanol followed by a 10 min oxygen plasma treatment. The perovskite precursor solution was coated using a spin coating procedure using two speeds where toluene was dripped onto the surface during the second step and then dried at 100°C post deposition.

### 3.1.7 Mixed Cation Derivatives

To generate the mixed cation perovskite species, 1M solutions of MAI, CsI and FAI in DMF were mixed with a 1M solution of Lead Ioidide in DMF to yield $CsPbI_3$, $FAPbI_3$ and $MAPbI_3$. These solutions were then mixed in the desired volume ratios to achieve the following perovskite structures, $Cs_{0.17}FA_{0.83}PbI_3$, $Cs_{0.1}MA_{0.9}PbI_3$ and $FA_{0.4}MA_{0.6}PbI_3$. All solutions were filtered through a 0.45$\mu$m Teflon syringe filters before further use. The resulting species where then spin coated on to cleaned glass substrates where the first spinning cycle was performed at 2,000 r.p.m., 2,000 r.p.m./s for 30 seconds followed by 4,000 r.p.m., 4,000 r.p.m./s for 30 seconds. During the second step, the substrate was treated with dry toluene (approximately 500 ml) drop-casting.

The films were then annealed at 170°C for $Cs_{0.17}FA_{0.83}PbI_3$, 110°C for $Cs_{0.1}MA_{0.9}PbI_3$ and 150°C for $FA_{0.4}MA_{0.6}PbI_3$ for 10 minutes.[4, 5, 6, 7]

### 3.1.8 Salt Coatings

A 0.01M, 0.005M or 0.001M solution was prepared by dissolving the iodide salt (phenylethylammonium iodide, MAI or trimethylsulfonium iodide) in a 1:4 solvent mixture of IPA to chlorobenzene. One hundred microlitres of this solution was then dripped onto pre-deposited perovskite films with a 20s loading time before spinning at 4,000 r.p.m. and annealing at 100°C for 5min. The chloride salt derivatives of the cations phenylethylammonium and methylammonium were prepared using the same protocol.

### 3.1.9 Device Fabrication

FTO-coated glass substrates (100mm by 25mm, 2.3mm thick TEC15, Pilkington) were first etched with Zn power and aqueous hydrochloric acid (37%), and then cut into 25  25mm pieces followed by cleaning sequentially in acetone, distilled water and IPA under sonication for 10min during each washing cycle. A compact $TiO_2$ layer was prepared by spin coating a solution comprised of 350l titanium isopropoxide (Aldrich), 35$\mu$l hydrochloric acid (37%) and 5ml anhydrous ethanol at 5,000r.p.m. for 30s. The $TiO_2$ films were sintered at 160°C for 5min and then at 500°C for 45min. Next, a mesoporous-$TiO_2$ film was deposited onto this using a solution of 20nm particle transparent titania paste (18NR-T, Dyesol). The solution was spin-coated onto the substrates at 5,000r.p.m. for 30s. Once spun, the films were dried on a hotplate at 80°C for 5min, and then sintered at 500°C for 45min. The desired perovskite layer was prepared using a consecutive five-step spin program inside glovebox as previously described.[8] In instances where iodine salt layer were used, 1, 2, 6 and 10mM solution of MAI with IPA were prepared respectively. The solution was then spin-coated onto the perovskite layer. The Spiro-OMeTAD hole conductor layer was spin-coated onto the perovskite films from a solution of 72.3 mg $ml^{-}1$ 2,2,7,7-tetrakis-(N,N-di-p-methoxyphenylamine)9,9-spirobifluorene (spiro-OMeTAD) powder in 1ml anhydrous chlorobenzene. The spiro-OMeTAD solution contained additives including 17.5$\mu$l lithium bis(trifluoromethane) sulfonimide lithium salt (Li-TFSl) and 28.8 $\mu$l 4-tert-butylpyridine

(tBP). Finally, a 100 nm-thick gold contact was evaporated under vacuum (approximately $10^6$ T at a rate of 0.2 nm $s^1$) with an active pixel area of 0.12 $cm^2$.

### 3.1.10 Gold counter Electrode

The counter electrode was deposited by thermal evaporation within the evaporation chamber under a pressure of 5 x $10^{-6}$ Torr. The active area of each cell was 0.25 $cm^2$.

### 3.1.11 *Ab initio* Calculations

All computational simulations and calculations were performed by collaborators at Bath university. Dr Chris Eames offered support for the crystal size and morphology impacts on the degradation of methyl ammonium lead iodide. In addition to performing the calculations for the role of water in the degradation mechanism. Dr Alex Aziz provided computational aid for the understanding of the role of bromide substitution towards stabilizing hybrid halide systems.

DFT calculations were performed using the numeric atom-centered basis set all-electron code FHI-AIMS. Tight basis sets were used with tier 2 basis functions for all species. Electronic exchange and correlation were modeled with the semi-local PBE exchange-correlation functional. For the treatment of spin orbit coupling an atomic zeroth-order regular approximation (ZORA) was used. Van der Waals forces were accounted for by applying a Tkatchenko Sheffler electrodynamic screening scheme. $O_2$ absorption in the bulk was calculated using a 2 x 2 x 1 supercell (giving a tetragonal cell of 192 atoms). A gamma point offset grid at a density of $0.04 Å^{-1}$ was used for k-point sampling. Structures were relaxed with convergence criteria of $10^{-4} eV Å^{-1}$ for forces, $10^{-5}$ electrons for the electron density and $10^{-7}$eV for the total energy. These settings ensured highly converged energies and equilibrium distances.

The CASTEP39 plane wave DFT code, version 16.11, was used for calculations in the role of moisture in the degradation of methylammonium lead iodide. The plane wave cutoff energy was 500 eV and core electrons were represented by ultraso pseudopotentials. Electronic exchange and correlation were modeled with the PBEsol exchange correlation functional. A Monkhorst Pack grid41 with a density of at least 0.04 $Å^{-1}$ was used for k-point sampling. For all compounds the structure was modeled with a supercell with minimum dimensions of 10 Å and the geometry was

optimised until the forces were converged to better than 10 4 eV $Å^{-1}$. For oxygen adsorption and reduction calculations, the charge state of the $O_2$ molecule was controlled by applying bond length and spin constraints to the $O_2$ and $O_2^-$ molecules, using bond lengths determined for isolated molecules in the appropriate charge state.

## 3.2 Physical and Optical Measurements

### 3.2.1 UV/VIS and Photoluminescence Spectroscopy

Steady-state absorbance measurements were performed on a Perkin-Elmer Lambda 25 UV/VIS Spectrometer. Transmission and reflectance spectra used to obtain the % absorption were obtained using a Perkin-Elmer Lambda 750 UV-Vis-n-IR absorption spectrometer fitted with an integrating sphere. $BaSO_4$ was implemented for calibrating for non-absorbing reflectance. Fluorescence spectra were obtained at ambient temperature on a Horiba Jobin Yvon Flourolog-3 Spectrofluorimeter.

### 3.2.2 Raman Spectroscopy

Raman spectroscopy was performed on a Renishaw inVia Raman Microscope using a 532 nm laser.

### 3.2.3 X-Ray Diffraction Spectroscopy

X-ray diffraction patterns were measured on a PANalytical XPert Pro MRD diffractometer using Ni filtered Cu K radiation at 40 kV and 40 mA.

### 3.2.4 Scanning Electron Microscopy

SEM cross sectional images were collected using a Carl Zeiss Ultra Plus Field Emission SEM. SEM- EDX measurements were carried out on a JEOL 6400 scanning electron microscope operated at 20 kV. Prior to measurement all samples were sputter coated with a layer of chromium, ca. 17 nm, to improve conductivity.

### 3.2.5 Nuclear Magnetic Resonance Spectroscopy

$^{1}$H NMR was recorded on a 400MHz Bruker spectrometer. Deuterated acetone was employed as the reference.

### 3.2.6 Energy Dispersive X-Ray Spectroscopy

SEM-EDX measurements were carried out on a JEOL 6400 scanning electron microscope operated at 20kV.

### 3.2.7 Isothermal Gravimetric Analysis

IGA measurements were conducted on a Mettler Toledo TGA spectrometer. Samples were kept under vacuum before exposure to oxygen flux, provided by the spectrometer.

### 3.2.8 Time-of-Flight Secondary Ion Mass Spectrometry

For ToF-Sims measurements samples were firstly soaked under dry flux in the dark for an hour before the ToF-SIMS measurements were recorded. Data were obtained using an IONTOF ToF.SIMS-Qtac LEIS spectrometer employing an Argon sputter gun for oxygen ion detection.

### 3.2.9 Transient Absorption Spectroscopy

Micro and millisecond TAS was performed by exciting films with a dye laser (Photon Technology International GL-301, sub-nanosecond pulse width) and pumped by a pulsed nitrogen laser (Photon Technology International GL-3300). A Bentham IL1 quartz halogen lamp was filtered through a monochromator and used to probe changes in the absorption profile of the film as a function of time after excitation from the pump beam. Probe light was detected using a InxGa1xAs (¿ 1000 nm) photodiode and an oscilloscope. Films were kept under flowing $N_2$ during the measurements.

## 3.3 Degradation Conditions and Measurements

### 3.3.1 Aging Conditions

Films were sealed in a controlled environment, where dry air was gassed through for the duration of the degradation. Illumination was provided by a tungsten lamp of approximately 1.5 $mWcm^{-2}$ power or by a white LED lamp with power of 25 $mWcm^{-2}$ and equipped with a UV-blocking filter.

### 3.3.2 Probe Testing

A stock 31.7 $\mu$M solution of the HE probe was prepared by dissolving 10 mg in 10 ml of dry toluene; sonication was used to facilitate miscibility. Films were then added to 10ml of 0.317 $\mu$M solution created from the stock solution. Photoluminescence spectra were recorded using an excitation wavelength of 520 nm and slit widths of 10 mm on a Horiba Yobin-Ybon Fluorolog-3 spectrofluorometer. Degradation in a moisture free environment was achieved by employing a solution of 10 mL dry toluene to which the films were submerged. Oxygen was continuously gassed through and illumination was provided by a tungsten lamp with a power of approximately 1.5 $mWcm^{-2}$. All data obtained was repeated on several samples and the trends were always observed.

#### Probe tests with different pH

To generate the Nitrobenzoic acid and benzoic acid containing toluene solutions the respective acid was taken and dissolved into the toluene solution to yield a concentration of $110^4$M. The solutions were then used as in the standard protocol described above and the superoxide yields measured.

### 3.3.3 Controlled Moisture Environments

Samples soaked in humid environments were generated via creating a controlled humidity in a small controlled environment. To generate the desired humidities specific Glycerol-Water

solutions were prepared, nitrogen gas was then bubbled through this solution acting as an inert gas carrier for the moisture. This allowed a moisture environment to be transported into a separate inert chamber holding pristine dry perovskite films. For the 85% relative humidity environment a 40% Glycerol (w/w) solution was used and for the 25% environment a 90% Glycerol (w/w) solution was employed. All films were soaked for two hours, after which the chambers were sealed and samples were taken immediately for testing.

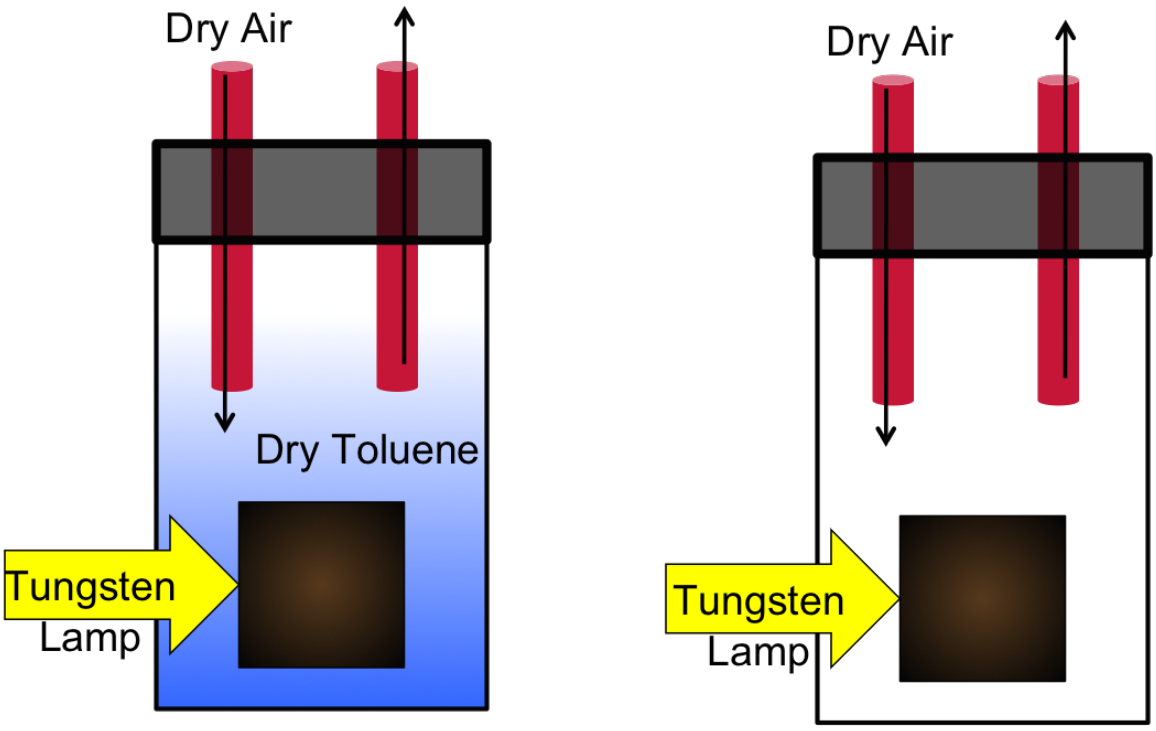


Figure 3.1: Diagramatic representation of the setup used to generate moisture free degradation environments. Left hand side is for superoxide probe studies and the right hand side is the setup used for ageing films

## 3.4 Device Characterisation

### 3.4.1 Current-Voltage Measurements

Current-voltage curves of complete photovoltaic devices were measured on a Keithley 2400 series source meter under illumination using a 150 W Xenon lamp (ScienceTech SS150W solar simulation) with IR filter (Water Filter) and AM 1.5 filter (ScienceTech). Calibration of light intensity to 100 mW cm$^2$ was obtained by using an independently calibrated silicon photodiode.

Scans were performed at a rate of 0.125V/s for forward scan directions, which are used in the results shown herein. Cells were placed unmasked under continuous 1 sun illumination during aging and were masked during each scan to ensure the active area (0.12 $cm^2$) is the same for all measured devices.

# References

[1] W. Ke, G. Fang, Q. Liu, L. Xiong, P. Qin, H. Tao, J. Wang, H. Lei, B. Li, J. Wan, G. Yang, Y. Yan, *Journal of the American Chemical Society*, 2015, **137**, 6730–6733.

[2] N. J. Jeon, J. H. Noh, Y. C. Kim, W. S. Yang, S. Ryu, S. I. Seok, *Nat. Mater.*, 2014, **13**, 897–904.

[3] J.-H. Im, I.-H. Jang, N. Pellet, M. Grtzel, N.-G. Park, *Nat. Nanotech.*, 2014, **9**, 927–931.

[4] Z. Li, M. Yang, J.-S. Park, S.-H. Wei, J. J. Berry, K. Zhu, *Chemistry of Materials*, 2016, **28**, 284–292.

[5] H. Choi, J. Jeong, H.-B. Kim, S. Kim, B. Walker, G.-H. Kim, J. Y. Kim, *Nano Energy*, 2014, **7**, 80 – 85.

[6] N. J. Jeon, J. H. Noh, W. S. Yang, Y. C. Kim, S. Ryu, J. Seo, S. I. Seok, *Nature*, 2015, **517**, 476480.

[7] N. Pellet, P. Gao, G. Gregori, T.-Y. Yang, M. K. Nazeeruddin, J. Maier, M. Grtzel, *Angewandte Chemie International Edition*, 2014, **53**, 3151–3157.

[8] M. Gratzel, *Acc. Chem. Res.*, 2009, **3**, 1788–1798.

# Chapter 4

# The role of metal-oxides and material design on the stability of organolead perovskites

## 4.1 Introduction

Organic lead halide perovskites have been generating enormous interest for application in highly efficient low cost and solution processable optoelectronic applications.[1] However, stability towards environmental conditions remains one of the biggest challenges to successful implementation of perovskite materials into real world devices. There are a number of factors that affect the degradation of perovskite solar cells, namely moisture, temperature and UV illumination.[2, 3, 4, 5] Recent research has identified the role that oxygen and light play in degrading these materials, where it was demonstrated that these two factors alone can degrade films and devices within a remarkably short time period.[6, 7, 8] The cause for this degradation was identified as a photo-degradation, where the highly reactive oxygen species, superoxide, is formed. This arises from photo-excited electrons undergoing an electron transfer reaction to oxygen. On forming superoxide, the species was shown to attack the material by deprotonation of the methylammonium cation leading to the formation of lead iodide ($PbI_2$), iodine ($I_2$) and methylamine (MA). In the previous works it was also demonstrated that in principle the role of

electron extractors could enhance material stability as noted by a decrease in superoxide yields by exchanging the insulating mesoporous-$Al_2O_3$ scaffold to mp-$TiO_2$, which in contrast can extract electrons from the perovskite phase.[7, 9] This electron extraction leads to the removal of the photo-excited electrons from the perovskite phase and acts to compete with the parasitic electron transfer reaction to oxygen.

This original observation suggests that metal-oxide electron extractors could be key to generating stable devices with longer operational lifetimes by deactivating the initial degradation starting point. One of the main aims of this study is therefore to enhance the environmental stability of the perovskite by controlling the electron extraction layer through its ability to extract photo-excited electrons from the perovskite phase, by both optimizing its structure and its deposition. This study seeks to investigate the factors influencing the extraction ability of metal-oxides and present rational design guidelines for achieving a more stable perovskite solar cell. Additionally, material design through exchanging the cation component is explored. This concept originates from the fact that a key step in the collapse of the crystal structure arises from the deprotonation of the methylammonium cation component with the superoxide species. This theoretical hypothesis can explain the observed increased stability towards ambient air in the $CsPbI_3$ perovskite that was explored for performance enhancement.[10, 11] In theory, judicious selection of the cation for systems with less labile protons or none at all could prevent the deprotonation step, leading to the enhanced stability of films.

## 4.2 The effect of electron extraction on stability

To investigate the role of electron extraction on methylammonium lead triodide (MAPI) material stability, the two most common scaffolds are explored as a starting point. Here, MAPI films were fabricated, as described in the experimental section, onto a plain glass substrate with either a mp-$Al_2O_3$ or a mp-$TiO_2$ layer. The main difference between these two materials is their band gap size, where the former has a larger band gap and exhibits insulating character and can not extract electrons from the CB of the perovskite phase. In contrast the latter

has a CB that sits below that of the CB of MAPI, allowing for an energy off-set interface that is conducive for a driving force of charge separation and thus electron extraction from the perovskite. [5, 12, 13] To monitor the impact on stability UV/VIS spectrometry was employed to observe the rate of decomposition from the starting product, a dark brown phase to the degradation products. Where, the key degradation product being examined is the yellow lead iodide phase. Consequently, this colour change between the states allows for the rate of decomposition to be monitored using this spectroscopic technique. Upon synthesis of the films in the glove box, their UV/VIS absorbance was then measured, with this spectrum noted as the fresh sample. To age the films they remained in a dark inert system until compressed dry air flux was used to supply the system with oxygen and a lamp was used for illumination, generating an oxygen and light only degradation environment. The application of a UV filter was implemented and aimed to mitigate any potential superoxide generation that could occur by UV excitation within $TiO_2$.[5, 14, 15] Beyond this point UV/VIS measurements were recorded at set time intervals. The UV/VIS measurements for a fresh and 24 hour aged sample for both mp-$Al_2O_3$/MAPI and mp-$TiO_2$/MAPI are shown in the figure below (Figure 4.1a and 4.1b respectively). The picture insets show the colour change that occurs upon aging, where the left tile is the fresh sample and the right tile is the 24 hour aged sample. To compile all the UV/VIS data obtained and to create an aging with time profile, the spectra are normalized with respect to the magnitude of the absorbance of the fresh sample at 700nm (grey line). This wavelength is specific to absorption from the perovskite phase only, as lead iodide does not absorb at this wavelength.[16, 7] The normalised absorbance at 700 nm for both architectures is displayed in Figure 4.1c below, to demonstrate the rate of degradation over the time period examined.

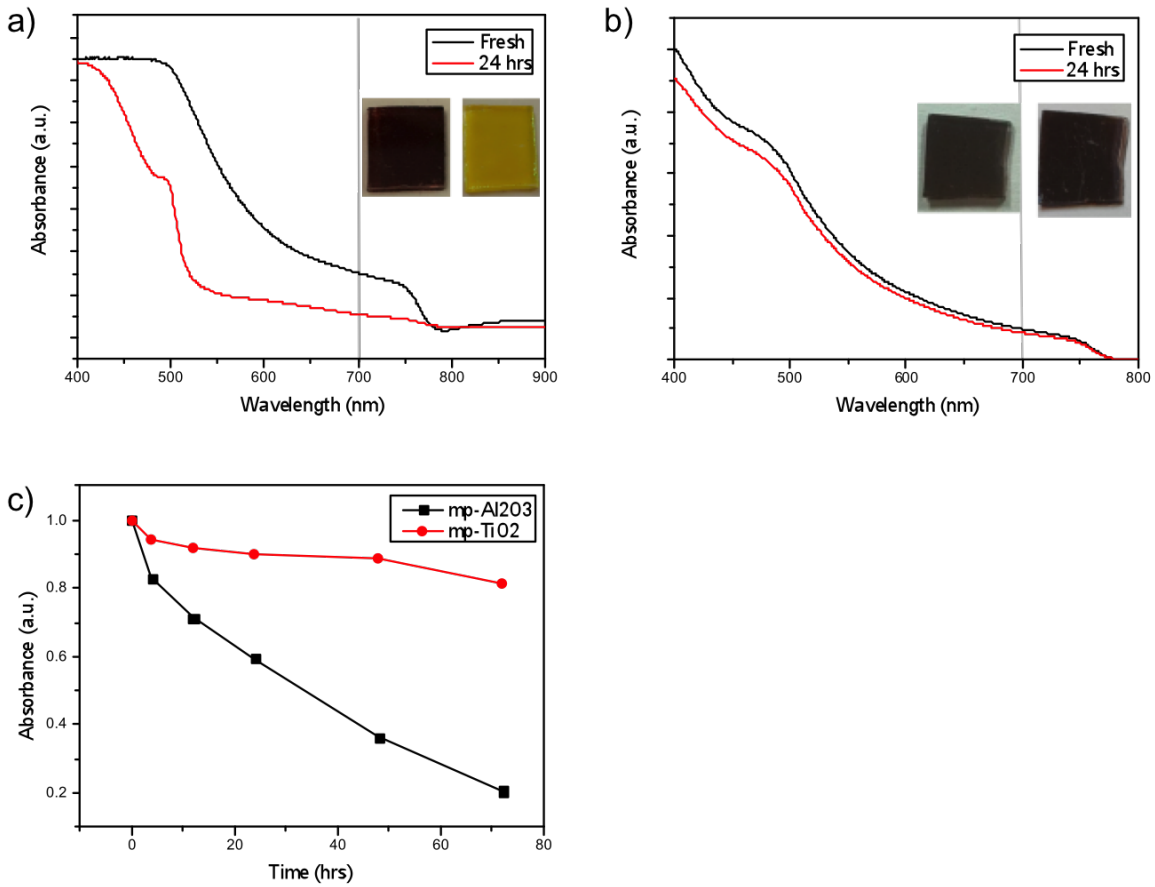


Figure 4.1: a) Absorption spectra of mp-$Al_2O_3$/MAPI before and after 24 hours of oxygen and light aging. b) Absorption spectra of mp-$TiO_2$/MAPI before and after 24 hours of oxygen and light aging. Insets are photos of the samples, left is fresh and right is aged. c) Normalised absorbance at 700 nm for both samples.

From the UV/VIS data it is clear that there is a fundamental stability difference for the perovskite phase when deposited on the different scaffolds. Where, almost complete degradation has occurred in mp-$Al_2O_3$/MAPI films within one day. Whilst, mp-$TiO_2$/MAPI films retain absorbance properties for a longer time. This is graphically demonstrated in the inset images, where the mp-$Al_2O_3$/MAPI has turned yellow in the time frame while the mp-$TiO_2$/MAPI remains dark brown. This indicates that the perovskite material life-time can be affected by the substrate to which it is fabricated on. The impact on device performance is also examined, where devices of the following architectures are explored: Glass/FTO/mp-$Al_2O_3$/MAPI/Spiro-OMeTAD/Au and Glass/FTO/mp-$TiO_2$/MAPI/Spiro-OMeTAD/Au. The PCE of these devices was recorded as fresh and after four hours of exposure to compressed dry air flux and 1 sun illumination. The results of this are shown in the J-V curves in Figure 4.2.

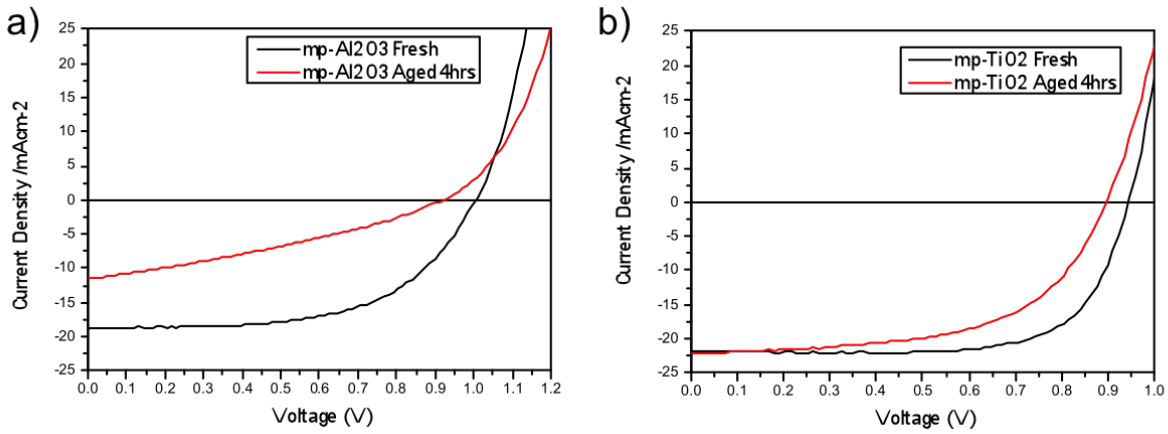


Figure 4.2: J-V curves for Glass/FTO/mp-$Al_2O_3$/MAPI/Spiro-OMeTAD/Au (a) and Glass/FTO/mp-$TiO_2$/MAPI/Spiro-OMeTAD/Au (b) Devices before and after4 hours of exposure to dry air flux and one sun illumination. Device efficiencies decrease from 11.02% to 3.12% and 14.72% to 11.45%, respectively.

Again it is clear that even within this time frame, more notable degradation has occurred in the mp-$Al_2O_3$ architecture, where the PCE has dramatically decreased from 11.02% to 3.12%. While, on the other hand the the device based on mp-$TiO_2$ only demonstrates a decrease in PCE from 14.72% to 11.45% over the same time frame. These findings show the real world implications of the degradation caused by oxygen and light alone. Devices suffer significant performance losses and material life-time is extremely short for any potential real world application. Both of these initial findings suggest the importance of electron extraction on stability. Where it seems that the superior stability of mp-$TiO_2$ based systems is owed to the ability of the metal-oxide to extract electrons from the CB of the perovskite phase. Resulting in the material life-time and device performance becoming more tolerant towards oxygen and light.

Since the key difference between these scaffolds lies in their ability to extract electrons from the perovskite phase. It may therefore be suggested that the electron extraction serves to compete with the parasitic electron transfer reaction, that results in the formation of superoxide. Steady state photoluminesence (PL) quenching experiments and superoxide yield measurements were employed to investigate the origin in the observed enhanced stability of mp-$TiO_2$ architectures. Steady state PL data for bilayer films of mp-$Al_2O_3$/MAPI and mp-$TiO_2$/MAPI are shown in Figure 4.3a. Noted from this data is the fact that the ability to extract electrons leads to reduced

PL intensity, where the mp-$TiO_2$ reduces the PL signal by approximately 40% compared to that of the mp-$Al_2O_3$ bilayer system. As calculated by the change in the area under the spectra. This observation is in agreement with literature, that the efficiency of electron extraction can be determined by the PL.[17] In terms of stability, this suggests that more electrons exist in the MAPI CB in the mp-$Al_2O_3$ architecture that can then undergo the parasitic electron transfer reaction to oxygen. As a direct result of this the number of electrons transferring to molecular oxygen will increase and the yield of superoxide will be greater. More superoxide will in turn lead to faster degradation rates as the number and frequency of deporotonation events will also increase. To test this hypothesis, the correlation between the PL quenching and the superoxide yields from the films is considered. The presence of superoxide was detected by employing the system described in my previous research.[7] The films are immersed in a toluene solution with a superoxide detection probe, dihydroethidiene (DHE), whose emission increases as a function of superoxide presence. The films are subjected again to only oxygen and light during this process. Figure 4.3b, displays the rate of increase in probe emission ($[I_F(t)]/[I_F(t_0)]$ versus ageing time) and consequently shows the superoxide generation yield from the films.

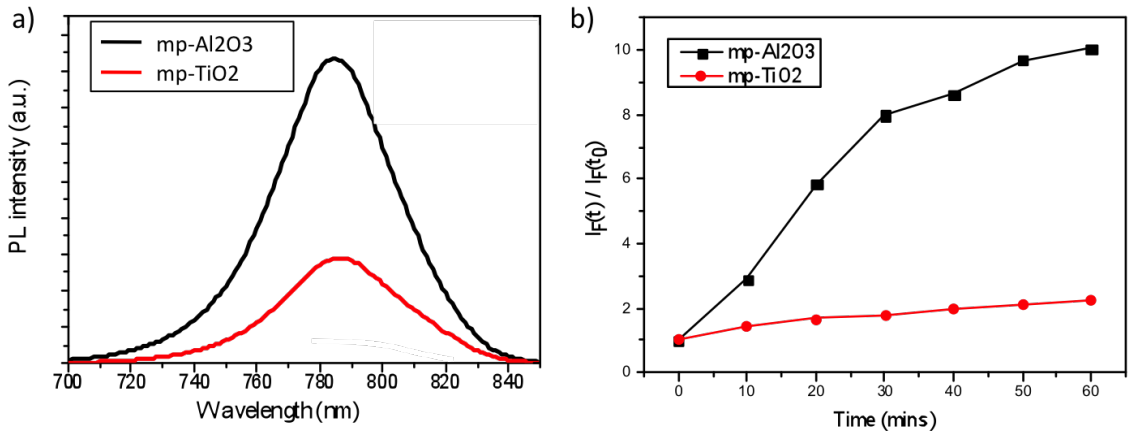


Figure 4.3: a) Steady-state photoluminesence spectra for $MAPbI_3$ fabricated on mp-$TiO_2$ and mp-$Al_2O_3$. b) Superoxide generation yield for mp-$TiO_2$/$MAPbI_3$ and mp-$Al_2O_3$/$MAPbI_3$ systems.

As anticipated, a strong correlation between the PL quenching efficiency and the superoxide generation yield is observed. The superoxide generation yield is far superior in the mp-$Al_2O_3$ architecture, as a result of more of the electrons being able to undergo electron transfer to

oxygen. In the PL measurements, since the environment is inert these electrons can't transfer to oxygen and so undergo charge recombination, leading to higher intensities. In contrast, the mp-$TiO_2$ provides an additional pathway for the electrons that competes with the transfer to oxygen and the radiative charge recombination pathway. Hence, in this bilayer system reduced PL intensities are observed and lower superoxide yields are generated. The data presented indicates that electron extraction improves device and material stability as a consequence of less electrons reacting with oxygen to form superoxide.

## 4.3 Design guidelines for metal-oxide extractors

The previous findings have shown the profound sensitivity of methylammonium lead iodide towards oxygen and light and how that sensitivity can be manipulated through electron extraction. This raises the prospect of creating electron extractor layers that can enhance stability, through deactivating the electron transfer process to oxygen. Achieving enhanced stability, could be managed by increasing the driving force for separation through seeking extractors with a more favourable energy off-set to increase the rate of electron transfer from the perovskite CB, in accordance with Fermi's golden rule.[18, 19, 20] It is also rational to suspect that the surface area to which the extractors operate will impact the stability enhancement achieved from extraction layers, where higher surface areas should remove more electrons thus reducing yields of superoxide. Additionally, as noted from the instability of electron transport within the CB, electron mobility may also be a factor that can be exploited to enhance stability. Faster electron mobility, should allow for more electrons to be extracted per unit time and again reduce the yields of superoxide. These principles are explored and the yields of superoxide are noted as a function of these factors. If superoxide yields can be decreased, stability will be enhanced.

### 4.3.1 Increasing the driving force for charge separation

To examine the effect of changing the energy-off set between the CBs of the extractor and methylammonium lead iodide, a selection of metal-oxides with different CB energies are considered. These include, $TiO_2$, ZnO and $SnO_2$. Figure 4.4 illustrates the energy off-set between these

extractors and the perovskite phase, where the CB energies are -4.0eV, -3.8eV and -4.5eV, respectively for the electron extractors and -3.9eV for ethylammonium lead iodide.[21, 22, 23, 24, 25, 26] From the previous results it is hypothesised that this is the driving force for charge separation increase, the free energy change increases, the number of photo-excited electrons undergoing transfer into the extractor will increase. In turn, this will result in a reduction in the number of electrons reacting with oxygen and thereby reduce the yields of superoxide. Therefore, the superoxide production and stability should be a function of the energy off-set. Lower superoxide yields will result in a more stable perovskite phase.

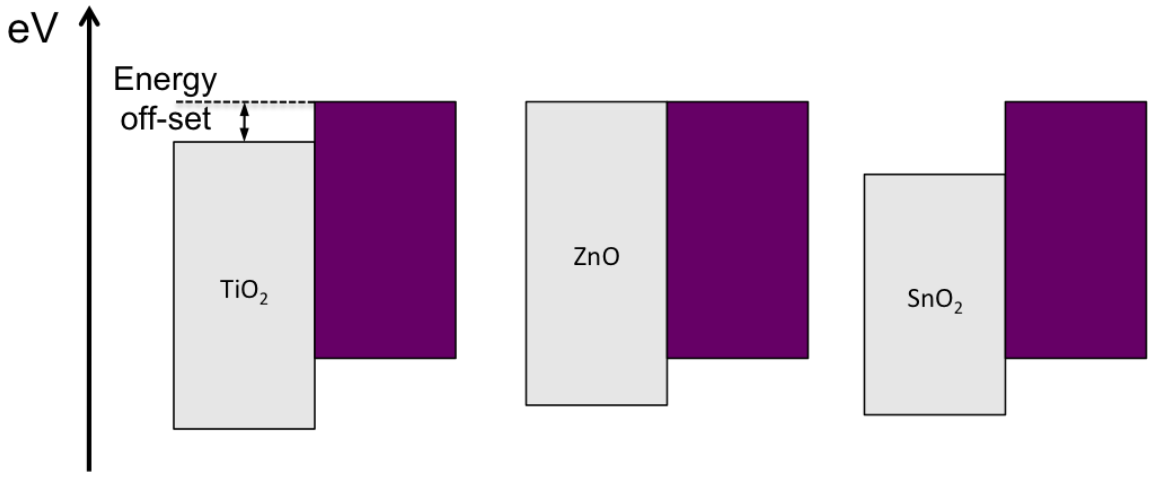


Figure 4.4: Diagrammatic illustration of the energy off-set across the metal-oxide/perovskite interface as a function of the CB. The CB for the metal oxides explored is lowered relative to the CB of $MAPbI_3$ from ZnO, $TiO_2$ to $SnO_2$.

As a starting point photoluminescence (PL) experiments were conducted to probe if lowering the conduction band does in fact lead to greater extraction. Films of Methylammonium lead triiodide were fabricated on top of compact layers of the chosen metal-oxides and PL measurements were recorded. The data was obtained under a nitrogen environment and were kept in the dark, with samples only being exposed to the pump and probe beam. Figure 4.5a, indicates that lowering the CB does give rise to greater extraction, as the PL intensity is increasingly quenched as the energy off-set increases. This corresponds to the photo-excited electrons undergoing a transfer process from the perovskite to the metal-oxide, thus reducing the number of electrons available to participate in radiative recombination, thereby reducing the PL intensity. To confirm if this process could compete with the parasitic electron transfer reaction the yield

of superoxide from perovskite fabricated on these metal-oxide films was tested employing the method described in previous studies.[7, 8] Figure 4.5b, shows that c-$SnO_2$ based films yield the least amount of superoxide, whilst c-ZnO ones yield the largest. The data also shows that in the control sample where no extraction layer is present (glass/$CH_3NH_3PbI_3$) exhibits the highest PL intensity. Corresponding to the fact no electrons can be extracted, and so more photo-excited electrons can participate in radiative recombination. This coincides with the PL measurements and the trend of lowering the CB for enhanced extraction. As a result, less photo-excited electrons undergo the parasitic electron transfer reaction with oxygen. As predicted, when the CB is lowered there is a greater driving force for the electron to be transferred into the CB of the metal-oxide and thus more electrons undergo this transfer process instead of transferring to oxygen. Again, in the control sample the highest superoxide yields are observed as a result that no extraction of photo-excited electrons can occur and therefore more electrons can react with oxygen to form superoxide. To note the impact of this reduction in the yield of superoxide by lowering the CB, and increasing the energy off-set, UV/VIS measurements were utilised (Figure 4.5c) to probe the resulting perovskite material stability and track its transformation into lead iodide as a function of time. By plotting the normalized absorbance at a specific wavelength ( 700 nm ) the rate of degradation can be compared. From the normalised data plot it can be seen that the material stability is enhanced and two factors accounting for this are observed. Firstly, on comparing the architectures glass/$CH_3NH_3PbI_3$ and compact-MO/$CH_3NH_3PbI_3$ the UV/VIS data shows a stability enhancement with respect to the latter (a longer time period to convert to lead iodide) due to removal of photo-excited electrons from $CH_3NH_3PbI_3$. This coincides with previous studies and reinstates the initial findings (Figure 4.5a and 4.5b) that removal of photo-excited electrons from the perovskite layer leads to enhanced stability by lowering superoxide yields. Moreover the data highlights that by utilizing a more efficient extraction layer greater stability can be achieved as the absorbance retains the perovskite profile over a longer time frame before converting to the $PbI_2$ phase. Both facts combined reinforces the theory that removal of photo-excited electrons leads to enhanced stability and that enhancing the driving force for extraction can generate further stability enhancement by decreasing the number of electrons available to react with oxygen to form superoxide.

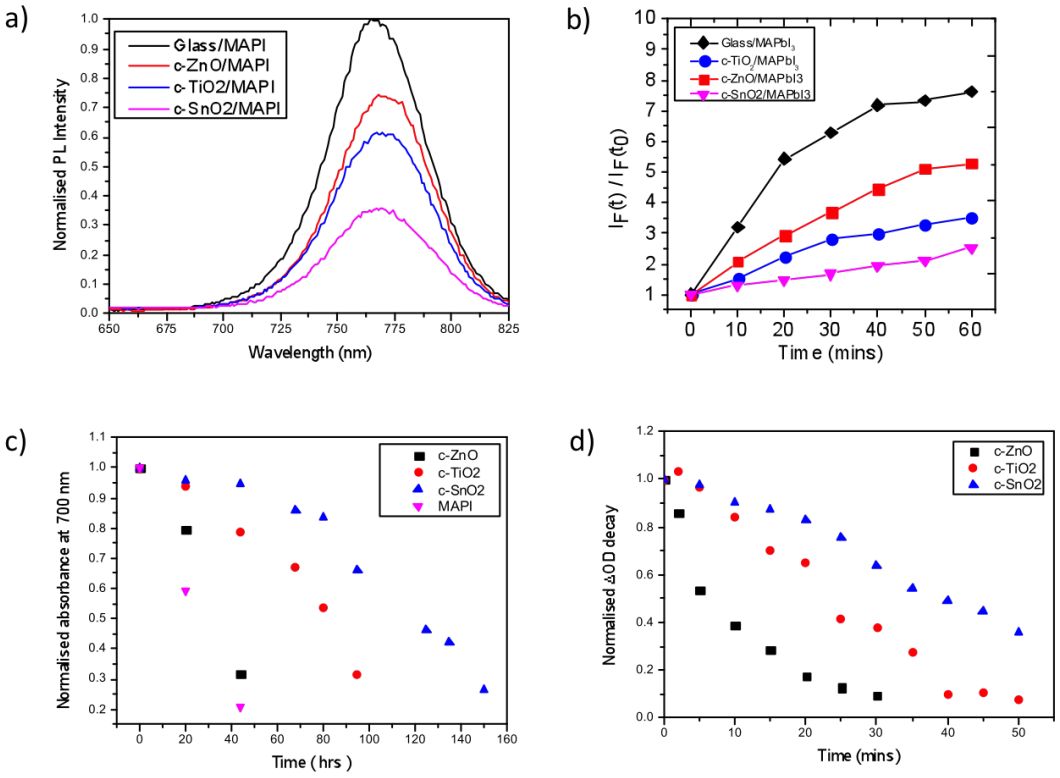


Figure 4.5: a) Steady state photoluminescence spectra for glass/$MAPbI_3$, c-ZnO/$MAPbI_3$, c-$TiO_2$/$MAPbI_3$ and c-$SnO_2$/$MAPbI_3$. Data was obtained under nitrogen and samples were stored in the dark. b) Superoxide generation yields for the control and the metal oxide samples. c) Normalised absorbance degradation plot for the samples and d) Normalised transient absorption decay for the samples with a spiro-OMeTAD hole transport layer, charge yield was taken at 1$\mu$s with a 1600nm probe wavelength and a 560nm pump wavelength.

Finally, the relative yield of charge separation (i.e. long-lived spiro-$OMeTAD^+$) is considered. Here, the compact based bilayer architectures have the spiro-OMeTAD hole transporting layer added to them and the yield of charge separation is measured as a function of exposure to ambient air and light.[6] In these studies, Figure 4.5d, the transient absorption signal at 1600 nm is obtained at regular time intervals over the course of an hour. Each transient absorption measurement was recorded under a nitrogen environment. The collected data shows that the transient absorption signal decays with exposure to oxygen and light. The rate of this degradation in charge separation yields increases as the metal oxide layer used changes from c-$SnO_2$ to c-$TiO_2$ to c-ZnO. This suggests that hole transfer is inhibited by exposure to these conditions and that the degradation rate is dependent on the ability of the extraction layer to extract electrons from the perovskite phase. It is worth noting that these changes in separation

yield for all samples are not accompanied by any noticeable decrease in steady-state absorption. Consequently, this data demonstrates that the parasitic electron transfer reaction to oxygen impacts the hole transfer to the HTM and implies that superoxide inhibits this process and could account for the rapid decay in device performance observed when these conditions are applied. The trend of increasing the energy-off set increasing stability is observed and further supports the rationale that increasing the electron extraction enhances film stability and performance. This can be attributed to the reduced superoxide yields, through the extraction layers decreasing the number of electrons reacting with oxygen and reducing the yields of superoxide.

### 4.3.2 Electron-extraction surface area

Another design factor that could be key to generating longer material life-time comes from not only the ability of the electron extraction of the metal oxide, but from the area to which extraction can occur from. A larger area should allow for more excited electrons to be removed from the perovskite. Again, leading to fewer electrons transferring to oxygen and thus reducing superoxide yields and increasing stability. The surface area for extraction will not only be impacted by the surface area of the extractor, but by the presence of an overlayer. This is an amount of perovskite that extends beyond the mesoporous extraction layer and acts like perovskite fabricated in a bilayer configuration. Therefore, the amount of MAPI protruding from the an increased surface area extractor needs to be minimised, such that optimal transfer can occur. In a similar approach PL measurements and superoxide yields were calculated for a perovskite film fabricated on to compact-$TiO_2$, mesoporous-$TiO_2$ and mp-$TiO_2$ with no perovskite overlayer capping the mesoporous layer. This sample will be referred to as optimal mp-$TiO_2$. The two configurations for the mp-$TiO_2$ systems with and without the perovskite overlayer are shown in the following SEM images, Figure 4.6.

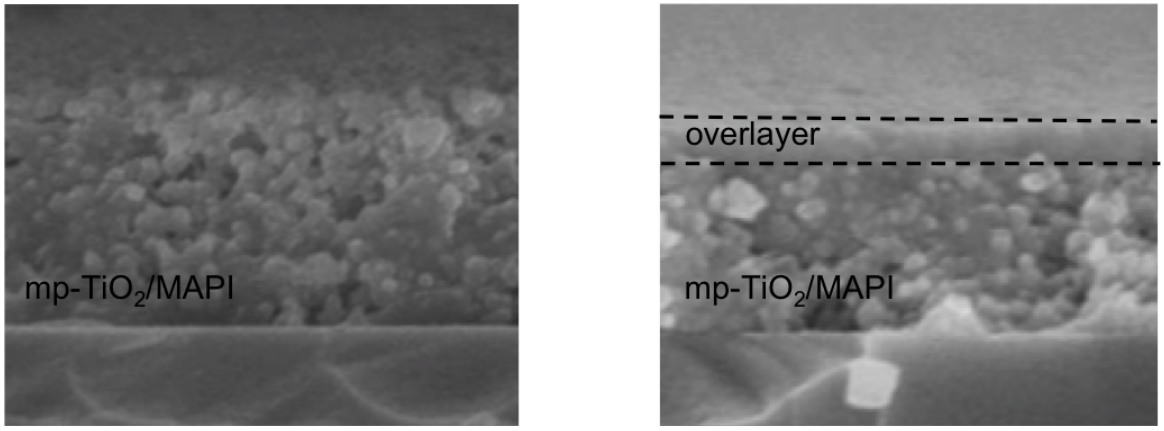


Figure 4.6: SEM images for the mp-$TiO_2$/$MAPbI_3$ architecture, without and with a perovskite capping (overlayer) over the mp-$TiO_2$. Optimal contact interface area is achieved where no overlayer is present.

The PL data for these systems, Figure 4.7a, show that the $TiO_2$ layers give increased PL quenching on transformation from a compact layer to a mesoporous one. This indicates that increasing the surface area could in fact increase the number of electrons being extracted from the perovskite phase. This enhancement of removing photo-excited electrons from the perovskite leads to reduced superoxide yields, as shown in Figure 4.7b. It is also possible the $TiO_2$ could act as a site for charge recombination leading to lower PL yields, but ultimately still reduces the number of electrons available to react with molecular oxygen and form superoxide. This data thus highlights the need to optimise the area of extraction, so that more electrons can be removed from the perovskite again to alleviate the electron transfer process to oxygen, such that the yields of superoxide are lowered. The impact on stability is once more demonstrated through UV/VIS as a method to indicate the stability enhancement associated with increasing surface area, Figure 4.7a. This shows that an increase in material stability is observed with increasing extraction surface area. From the initial research work on these degradation conditions it was noted that the presence of an overlayer may contribute to superoxide generation, due to the fact there is perovskite material where the photo-excited electrons cant be extracted from to the metal-oxide layer readily before the transfer to oxygen occurs. Developing on this, a system was designed to create a scaffold where no such overlayer is present, so that in theory the generation of excited electrons will transfer primarily into the metal-oxide layer before being able to undergo the transfer process to oxygen and again as a consequence reduce superoxide

generation. To do this a perovskite film was fabricated onto a mp-$TiO_2$ layer, such that no perovskite extruded the layer and this was confirmed by SEM imaging (Figure 4.6). PL data (Figure 4.7a) obtained from this sample shows that almost complete quenching is observed, this further supports the need for optimal surface area coverage so that the most amount of electrons can be extracted. It could also be suggested that the diffusion length in these samples is short, since this small distance (nano-meter sized overlayer) should be negligible compared to the reported micron distances that have been reported for charge diffusion lengths in MAPI. Hence, any electrons formed in the overlayer should easily reach the extractor layer. If the diffusion distances are not short, it may be that there are extraction issues from the overlayer to the metal-oxide and hence the observed increased probability of electrons to react with oxygen from this area. In any case reducing the presence of the overlayer leads to better stability via reducing the yields of superoxide (Figure 4.7b) and observed in the longer material stability from the UV/VIS measurements (Figure 4.7c).

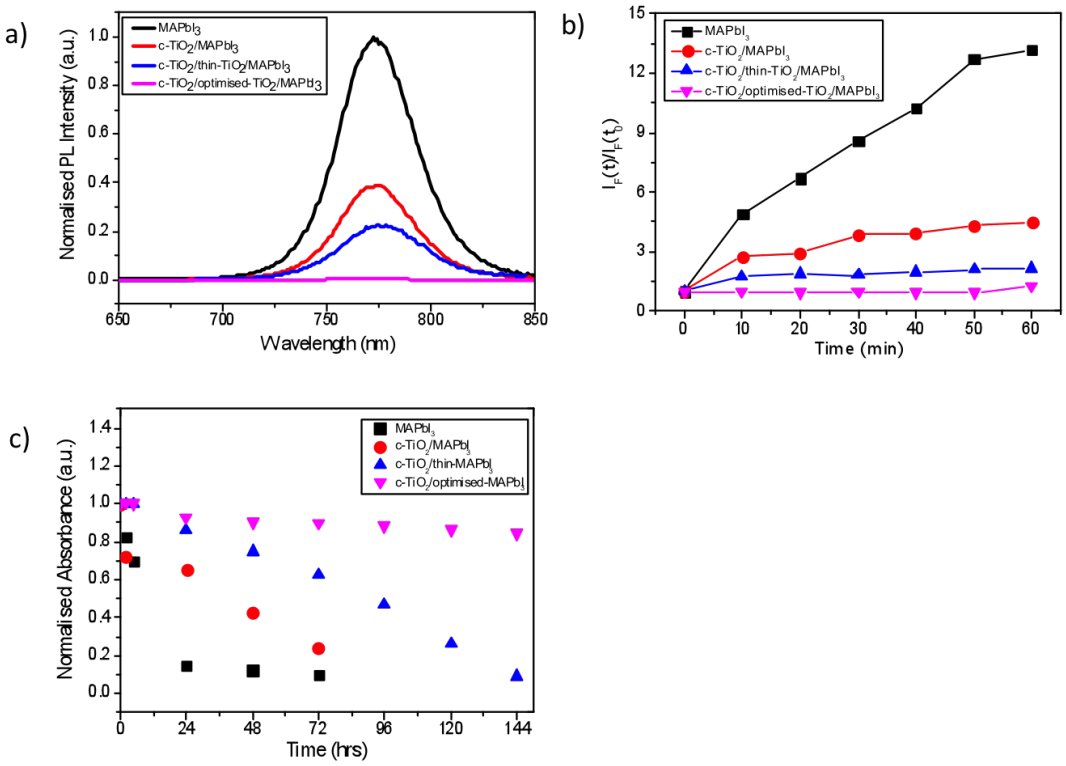


Figure 4.7: a) Steady state photoluminescence spectra for increasing surface area of $TiO_2$ and optimising the contact surface between the phases. b) Superoxide generation for the same samples along with the (c) Normalised aborsbance decay.

The design concept is also explored in ZnO, as this system is poor at extracting electrons when in a compact layer. In a similar approach the PL, Superoxide generation yields and the material life-time measurements were recorded for a c-ZnO and mp-ZnO based systems. Figures 4.8a-c, depict the same trends observed in that increasing the surface area reduces the number of electrons available to react with oxygen, the PL intensity increases with surface area. In turn, this reduces superoxide yields (Figure 4.8b) and generates longer material life-time stability (Figure 4.8c).

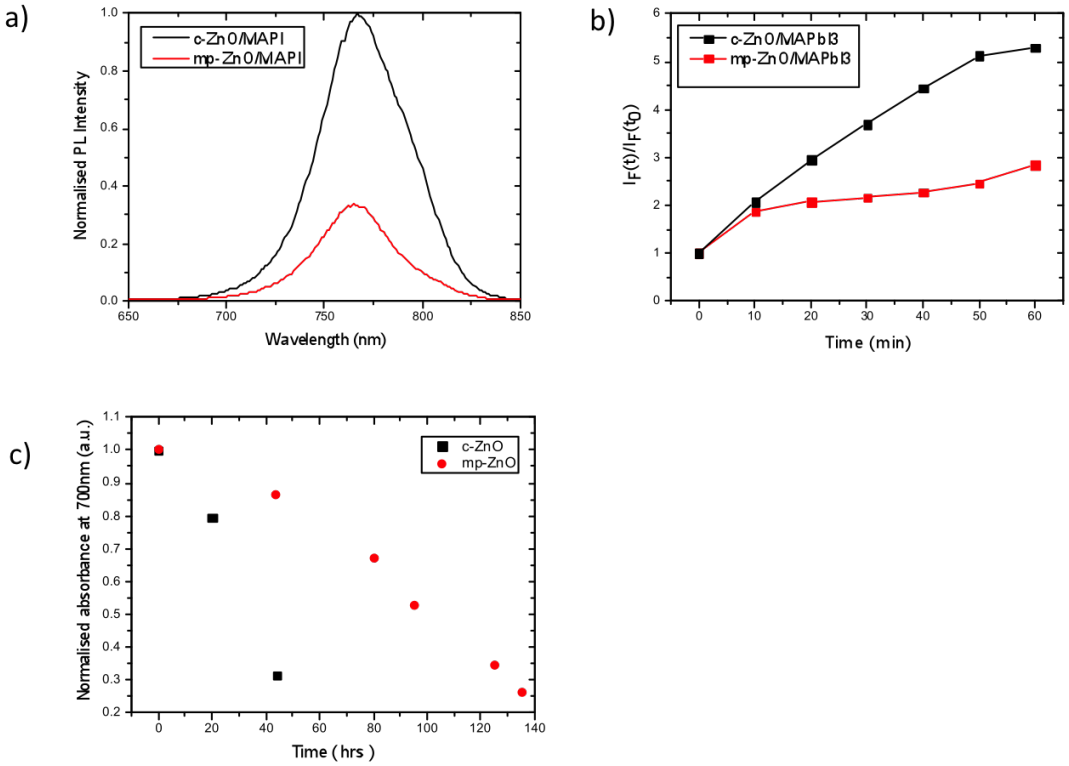


Figure 4.8: a) Steady state photoluminescence spectra for increasing surface area of ZnO, via changing the structure from a planar compact film to a mesoporous scaffold. b) Superoxide generation for the same samples along with the (c) normalised aborsbance decay.

In review of these findings, it is clear that the surface area for extraction can serve to increase film stability of methyl ammonium lead iodide. Additionally, the contact area of the interface between the extractor and the perovskite phase is critical for extraction of photo-excited electrons, and when maximized the number of electrons participating in the electron transfer reaction decreases. Therefore from these results it can be suggested that for enhanced stability a design guideline for electron extractors must be that the surface area and the contact area

of the interface must be increased. Resulting in the reduced yield of superoxide and longer material life-time.

## 4.4 Mixed cation perovskites and electron extraction

In addition to methylammonium lead iodide, an alternative leading perovskite structure (Caesium formidinium lead iodide, $Cs_{0.17}FA_{0.83}PbI_3$) was investigated to note if the effects of increased stabilization resulting from extraction layers can also be applied. This composition was selected as it has been shown to demonstrate both high efficiencies and stability for photovoltaic applications.[27] Absorbance measurements and superoxide yields were conducted for three $Cs_{0.17}FA_{0.83}PbI_3$ films, where the perovskite was fabricated on plain glass, c-$TiO_2$ and mp-$TiO_2$. Furthermore, this material has also been shown by our group to exhibit light and oxygen induced degradation, critically needing both components before degradation will occur. Figure 4.9a, shows the normalized absorbance degradation when the films have been exposed to oxygen and light and indicates that both including an extractor and increasing its active area generate films with a greater resistance to the degradation conditions. This again results from the ability of the extractor to reduce the yields of superoxide generated under these conditions as demonstrated in Figure 4.9b, where the yield of superoxide decreases as a metal-oxide extractor is introduced and decreased even further when the area of extraction is increased (c-$TiO_2$ to mp-$TiO_2$).

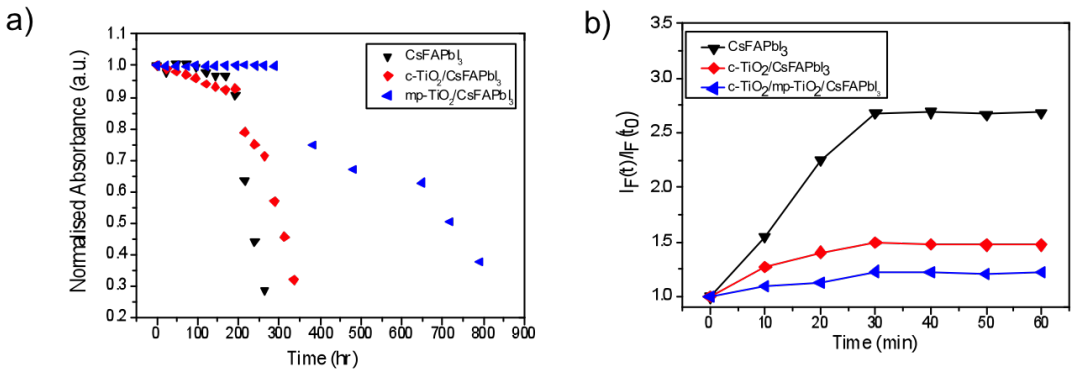


Figure 4.9: a) Normalised absorbance degradation for $Cs_{0.17}FA_{0.83}PbI_3$, fabricated on plain glass, c-$TiO_2$ and mp-$TiO_2$ substrates. Raw absorbance data was obtained in collaboration with Thana Chotchuangchutchaval b) Superoxide generation yields for the same architectures.

An important point to note from this experiment, is that generation of superoxide is also

possible from another perovskite species. This is the first study to prove that this reactive species can also be produced by an alternative system and has impacts that could apply to all perovskite systems. It is clear, that again the yield of superoxide is directly proportional to the overall stability of the perovskite film and the methods explored earlier can be utilised to enhance stability by manipulating the yield of superoxide. Promisingly, noted from a comparison between the two perovskite materials is that the $Cs_{0.17}FA_{0.83}PbI_3$ species has a greater intrinsic stability with respect to oxygen and light degradation. The degradation rate even when on plain glass is slower than that of a methylammonium lead iodide film fabricated on the same substrate. This poses an interesting question as to why the material exhibits enhanced stability.

### 4.4.1 Cation exchange effects

To understand this fundamental increased oxygen and light resistance a series of perovskite materials with modified intrinsic compositions are examined. The cation species is exchanged/-substituted by changing/substituting the organic cation MA- with Cs and/or FA- in the chemical structure of the perovskite. The impact of the superoxide generation and degradation rate are compared to illuminate the origins of the enhanced stability. It is hypothesised that the intrinsic stability of mixed cation perovskites originates from the increased tolerance of the cations towards superoxide. Where, they are able to reduce the deprotonation rate or in the case of the Cs cation not participate in this reaction. This leads to a block in the degradation reaction mechanism that either stops or slows the process down. Hence, greater film life-times are observed. Figure 4.10a shows the UV/VIS stability measurements for three state of the art alternatives to methylammonium lead iodide, which are $Cs_{0.17}FA_{0.83}PbI_3$, $Cs_{0.1}MA_{0.9}PbI_3$ and $FA_{0.4}MA_{0.6}PbI_3$.[28, 11, 1, 29] In all cases the amount of the problematic methylammonium cation is reduced and as a result increased stabilities are observed with respect to $MAPbI_3$, in particular where full substitution occurs the oxygen and light stability of the $Cs_{0.17}FA_{0.83}PbI_3$ film was enhanced by approximately 4 times more than the $MAPbI_3$ perovskite film. Especially, within the first 5 days after exposure to dry air and light for the $Cs_{0.17}FA_{0.83}PbI_3$ film, where its absorbance trace showed a limited reduction in this time period. Interestingly, superoxide measurements (Figure 4.10b) indicate that changing the cation composition does not result in a

change in the yield of superoxide and suggests that the effect of changing the cation introduces a greater tolerance to the reactive oxygen species.

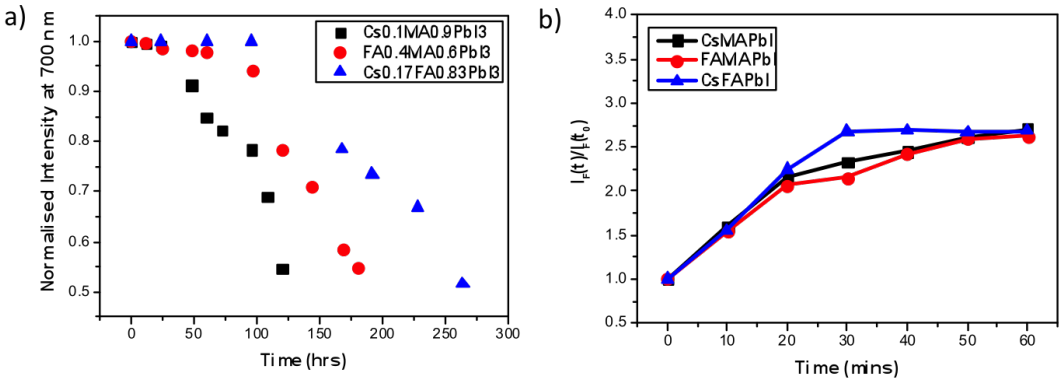


Figure 4.10: Normalised absorbance degradation for $Cs_{0.17}FA_{0.83}PbI_3$, $Cs_{0.1}MA_{0.9}PbI_3$ and $FA_{0.4}MA_{0.6}PbI_3$ fabricated on plain glass substrate. b) Superoxide generation yields for the same perovskite compositions.

Having identified a potential cause for this enhanced stability as an increased tolerance of the cation species to the superoxide deprotonation reaction, NMR experiments were employed. $^1$H NMR tests were conducted in the same approach as in previous studies, that first showed the deprotonation step of superoxide with the methylammonium cation. Here, the authors reacted methylammonium iodide (MAI) with potassium superoxide ($KO_2$), showing conversion to methylamine (MA). NMR depicts this process by the up field shift of the proton environments of the N-H and C-H groups in MAI once converted to MA.[7] In a similar approach the experiments carried out tested the deprotonation yield of formamidinium (Figure 4.11) by $KO_2$, with the top spectra corresponding to the starting materials, whilst the bottom one is the spectra after addition of $KO_2$. Estimated reaction yields were obtained by integration of the signals. In the case of methylammonium iodide, as stated in the previous work, upfield shifts of the signals were observed, which is consistent with deprotonation of the ammonium group by the superoxide species.[7] The product of the reaction is, therefore, methylamine. In the case of formamidinium iodide the scenario is more complex. There is a significant amount of deprotonation (76%), observed from the small shift of the signal of the C-H group to a lower chemical shift and the remnants of some unreacted FA cation. The N-H protons appear as a broad signal at around 5 ppm. Additionally, a singlet at 9.33 ppm is also observed, which corresponds to the formation

of 1,3,5-triazine (17%). It is known that this compound can be obtained by condensation of formamidine hydrochloride, either thermally or initiated by a base.[30] The formation of this product requires $NH_3$ to be released as the leaving group during the cyclization, whose protons may also be contained in the broad signal around 5ppm although the majority should be released as gas. Finally, a small amount of unreacted formamidinium (6%) was detected in the NMR spectra.

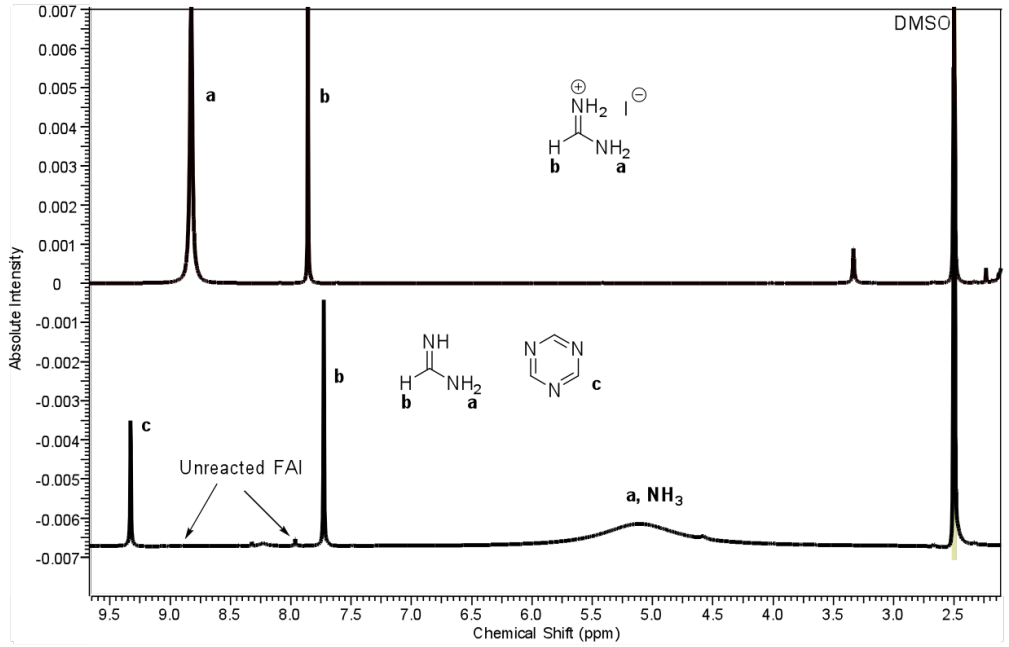


Figure 4.11: $^1$H NMR for the model reaction of $KO_2$ with FAI. Top spectrum corresponds to the proton NMR for unreacted FAI. Bottom spectrum is the NMR after the reaction.

In the proton NMR experiments of both formamidinium and methylamonnium, practically all the starting material is consumed during the reaction. However, the deprotonation yield, obtained from integration of the $^1$H-NMR signals and taking into account the stoichiometry of the two reactions, is 76% for formamidinium versus a quantitative reaction for methylamonnium. This is consistent with the pKa values described for these compounds ($MeNH_3^+$ pKa=10.62; Formamidinium, pKa=12.40).[31] Consequently, the difference in pKa demonstrates that the protons will be harder to liberate in the FA cation, leading to slower degradation rates. Furthermore, the second reaction pathway of formamidinium (17% yield in the NMR experiment) with superoxide is likely to be inhibited in the perovskite crystal structure. As in the solid state, it should be more difficult than in solution to get three molecules of formamidinium to

collide in the same location and react to form the 1,3,5-triazine. Consequently, the further stability enhancement is attributed to the reduced acidity of the protons and more complex decomposition pathway reducing the rate of deprotonation and thus the rate of degradation. For the cesium cation, no deprotonation reaction is possible, hence complete tolerance towards superoxide was observed and no reaction occurred. Combining this result with the previous data (Figure 4.10) the stability of the films tested can be rationalised. Where the combination of cation compositions with the least amount of the methylammonium lead iodide generates the most stable perovskite system towards oxygen and light. Critically, this defines that the methylammonium cation is the most sensitive component in the degradation and it's easily liberated protons contribute to the rapid conversion of methylammonium lead iodide into lead iodide.

## 4.5 Conclusions

From the data collected it is apparent that the tolerance of $MAPbI_3$ perovskite films to oxygen and light induced degradation can be enhanced by electron extraction. Three key parameters have been found to result in further stability enhancements and have led to the creation of design guidelines for generating films with longer life-times. These factors are: i) the ability of the metal oxide to extract photo-excited electrons from the perovskite phase, and ii) the surface area to which the extractor can remove electrons These guidelines translate into the fact that to achieve a highly stable perovskite, the electron extraction layer needs to maximise the energy off-set to increase charge separation across the interface, increase the surface area to increase the number of electrons extracted. Further to these findings, it has also been shown that the generation of superoxide is possible from alternative cation composition lead halide perovskites. The yield of superoxide was independent of the composition, with all films generating similar amounts of the reactive oxygen species. However, different relative stabilities were observed. Accounting for this was the ability of the cation to participate in the deprotonation reaction with the generated superoxide. In systems with harder to abstract protons (less acidic) or no protons at all, the perovskite becomes more tolerant towards oxygen and light conditions.

Resulting from a reduced degradation reaction rate. All in all, metal oxide fabrication and morphology can generate stability enhancements. However, it is important to note from all the data presented that degradation still occurs. The role of electron extraction partially passivates the degradation and the material still produces superoxide. It is then of concern as to why the material still produces this problematic species and can the root cause of its production be identified. The proceeding chapters set out to address this and search for the fundamental property of methylammonium lead iodide that is responsible. Achieving this will allow for a greater understanding of the degradation and hopefully lead to the generation of methods to prevent the degradation from occurring.

# References

[1] N. J. Jeon, J. H. Noh, W. S. Yang, Y. C. Kim, S. Ryu, J. Seo, S. I. Seok, *Nature*, 2015, **517**, 476480.

[2] H. P. Zhou, Q. Chen, G. Li, S. Luo, T. B. Song, H. S. Duan, Z. R. Hong, J. B. You, Y. S. Liu, Y. Yang, *Science*, 2014, **345**, 542–546.

[3] J. A. Christians, P. M. Herrera, P. V. Kamat, *J. Am. Chem. Soc.*, 2015, **137**, 1530–1538.

[4] G. Niu, X. Guo, L. Wang, *J. Mater. Chem. A*, 2015, **3**, 8970–8980.

[5] T. Leijtens, G. Eperon, S. Pathak, A. Abate, M. Lee, H. J. Snaith, *Nat. Commun.*, 2013, **4**, 2885–2893.

[6] F. T. O'Mahony, Y. H. Lee, C. Jellett, S. Dmitrov, D. T. Bryant, J. R. Durrant, B. C. O'Regan, M. Graetzel, M. K. Nazeeruddin, S. A. Haque, *J. Mater. Chem. A*, 2015.

[7] N. Aristidou, I. Sanchez-Molina, T. Chotchuangchutchaval, M. Brown, L. Martinez, T. Rath, S. A. Haque, *Angewandte Chemie International Edition*, 2015, **54**, 8208–8212.

[8] D. Bryant, N. Aristidou, S. Pont, I. Sanchez-Molina, T. Chotchunangatchaval, S. Wheeler, J. R. Durrant, S. A. Haque, *Energy Environ. Sci.*, 2016, **9**, 1655–1660.

[9] G. Niu, W. Li, F. Meng, L. Wang, H. Dong, Y. Qiu, *J. Mater. Chem. A*, 2014, **2**, 705–710.

[10] G. E. Eperon, S. D. Stranks, C. Menelaou, M. B. Johnston, L. M. Herz, H. J. Snaith, *Energy Environ. Sci.*, 2014, **7**, 982–988.

[11] H. Choi, J. Jeong, H.-B. Kim, S. Kim, B. Walker, G.-H. Kim, J. Y. Kim, *Nano Energy*, 2014, **7**, 80 – 85.

[12] J. M. Ball, M. M. Lee, A. Hey, H. J. Snaith, *Energy Environ. Sci.*, 2013, **6**, 1739–1743.

[13] T. Leijtens, B. Lauber, G. E. Eperon, S. D. Stranks, H. J. Snaith, *The Journal of Physical Chemistry Letters*, 2014, **5**, 1096–1102.

[14] S. K. Pathak, A. Abate, T. Leijtens, D. J. Hollman, J. Teuscher, L. Pazo, P. Docampo, U. Steiner, H. J. Snaith, *Adv. Energy Mater.*, 2014, **4**, 1301667.

[15] K. Schwanitz, U. Weiler, R. Hunger, T. Mayer, W. Jaegermann, *J. Phys. Chem. C*, 2007, **111**, 849–854.

[16] A. Aslani, M. Arefi, K. Beyki-Shuraki, A. Babapoor, *Journal of Saudi Chemical Society*, 2013, **17**, 403 – 407.

[17] M. Anaya, W. Zhang, B. C. Hames, Y. Li, F. Fabregat-Santiago, M. E. Calvo, H. J. Snaith, H. Miguez, I. Mora-Sero, *J. Mater. Chem. C*, 2017, **5**, 634–644.

[18] R. A. Marcus, *J. Chem. Phys.*, 1956, **24**, 966.

[19] R. A. Marcus, *Discuss Faraday Soc.*, 1960, **29**, 21.

[20] R. A. Marcus, *J. Chem. Phys.*, 1965, **43**, 679.

[21] Y. Chergui, N. Nehaoua, D. E. Mekki, *InTech*, 2011.

[22] R. Jose, V. Thavasi, S. Ramakrishna, *Journal of the American Ceramic Society*, 2009, **92**, 289–301.

[23] K.E.Jasim, *DyeSensitizedSolarCells-Working Principles , Challenges and Opportunities*, InTechOpen, 2007.

[24] N. G. Park, *Journal of Electrochemical Science and Technology*, 2010, **1**, 69–74.

[25] P. Tiwana, P. Docampo, M. B. Johnston, H. J. Snaith, L. M. Herz, *ACS Nano.*, 2011, **5**, 51585166.

[26] H. A. Harms, N. Tetreault, N. Pellet, M. Bensimon, M. Gratzel, *Faraday Discuss.*, 2014, **176**, 251–269.

[27] D. P. McMeekin, G. Sadoughi, W. Rehman, G. E. Eperon, M. Saliba, M. T. Hörantner, A. Haghighirad, N. Sakai, L. Korte, B. Rech, M. B. Johnston, L. M. Herz, H. J. Snaith, *Science*, 2016, **351**, 151–155.

[28] Z. Li, M. Yang, J.-S. Park, S.-H. Wei, J. J. Berry, K. Zhu, *Chemistry of Materials*, 2016, **28**, 284–292.

[29] N. Pellet, P. Gao, G. Gregori, T.-Y. Yang, M. K. Nazeeruddin, J. Maier, M. Grtzel, *Angewandte Chemie International Edition*, 2014, **53**, 3151–3157.

[30] C. Grundmann, A. Kreutzberger, *Journal of the American Chemical Society*, 1954, **76**, 5646–5650.

[31] T. Ishikawa, *Superbases for Organic Synthesis*, John Wiley and Sons Ltd., 2009.

# Chapter 5

# Fast oxygen diffusion and iodide defects mediate oxygen-induced degradation of perovskite solar cells

## 5.1 Introduction

Despite the remarkable progress in organolead halide perovskites, the serious issues related to the long-term stability of perovskite halides towards oxygen and light needs to be addressed. Although, our understanding has improved and the ability to enhance stability has been achieved through electron extraction, leading to the increased competition with the electron transfer reaction to oxygen reducing yields of superoxide. The degradation of hybrid perovskite materials and device instability is still significant and generally at higher rates than those typically observed in polymer and dye-sensitized photovoltaics. [1, 2, 3, 4, 5]

The oxygen-induced degradation pathway has been shown to affect the stability of both $CH_3NH_3PbI_3$ photoactive layers and solar cell devices.[6] Transient absorption spectroscopy studies of interfacial charge transfer in $CH_3NH_3PbI_3$-based films revealed that such oxygen-induced degradation results in a large decrease in the yield of photo-induced charge carriers.[7] While the work reported earlier has demonstrated the importance of electron extraction in reducing the

severity of this degradation pathway along with other studies that have been conducted.[3, 8, 6, 7] It is highly unlikely that charge extraction alone will completely solve this problem. Hybrid lead halide layers deposited from solution typically produce polycrystalline films with varied micro-structure and particle morphologies. The impact of film micro-structure on charge carrier transport, photoluminescence, device performance parameters (for example, $J_{sc}$, $V_{oc}$, fill factor) and tolerance to moisture has been reported.[9, 10, 11, 12, 13, 14, 15, 16, 17, 18, 19] It is reasonable to suppose that the particle size and defect chemistry of the films may also influence oxygen diffusion into the perovskite layer and its susceptibility to oxidative reactions.

Studies on $CH_3NH_3PbI_3$ suggest a significant equilibrium defect concentration of $I^-$, $Pb^{2+}$ and $CH_3NH_3^+$ vacancies at room temperature, which could provide vacancy-mediated pathways for ion transport.[20] Other notable studies[21, 22, 23, 24, 25, 26, 27, 28] indicate that these hybrid perovskites are mixed ionic-electronic conductors, and also implicate vacancy-mediated iodide ion diffusion as being responsible for the observed hysteresis effects. Recent studies have also investigated the role of ion migration in perovskite degradation.[29] Ionic defect and transport phenomena in hybrid perovskites thus have important implications in terms of the long-term stability and performance of perovskite solar cell devices. However, the exact mechanism of oxygen diffusion and the defect species associated with oxygen and light-induced degradation are poorly understood. Additionally, these stability issues raise important questions that have not been fully addressed. Specifically, these questions relate to: (i) the origin of the observed fast rate of oxygen-induced degradation of $CH_3NH_3PbI_3$ films and (ii) the relationship between the film particle size, oxygen transport, intrinsic vacancies and the mechanism of oxygen-induced degradation. A schematic representation of the potential degradation pathway and the role vacancies could play is provided below.

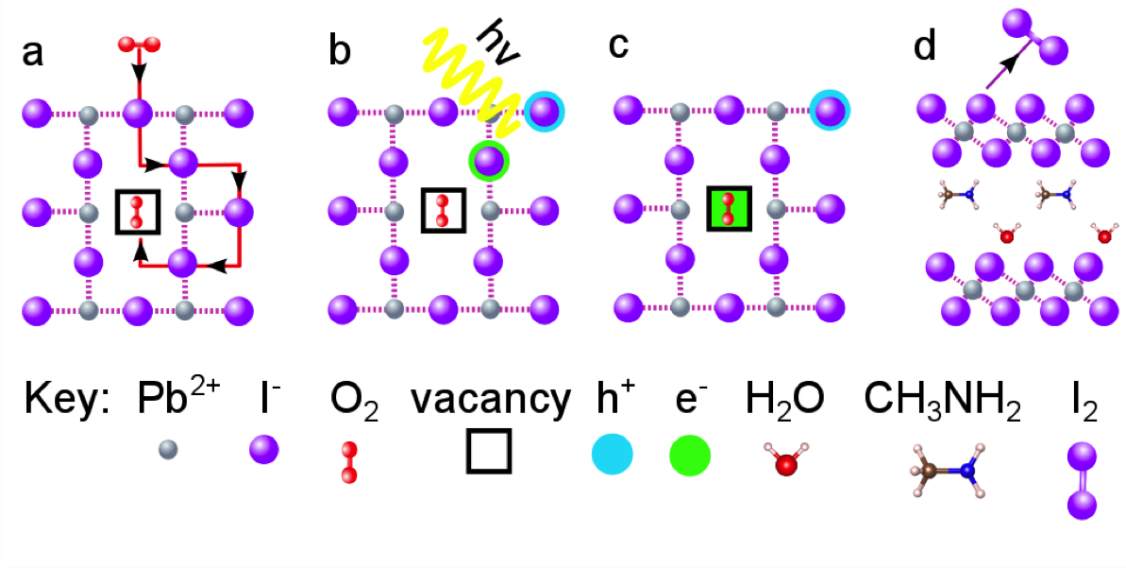


Figure 5.1: Schematic representation of the proposed reaction steps of $O_2$ with $CH_3NH_3PbI_3$. (a) Oxygen diffusion and incorporation into the lattice, (b) photoexcitation of CH3NH3PbI3 to create electrons and holes (c) superoxide formation from O2, and (d) reaction and degradation to layered $PbI_2$, $H_2O$, $I_2$ and $CH_3NH_2$

Herein a combination of experimental and computational methods to address these important questions at the microscopic level and extended upon the previous work on hybrid perovskites is presented.[8, 6, 22] Specifically, the dynamics of oxygen diffusion in perovskite films have been probed and investigations into how the film morphology influences reactivity to molecular oxygen have been pursued. Oxygen diffusion into perovskite films is observed to occur remarkably fast with, for example, a typical film (500nm thick) reaching complete saturation within 10min. Density functional theory (DFT) calculations also reveal the importance of iodide vacancies as reaction mediators to form superoxide species. The results provide valuable insights for the design of perovskite devices exhibiting improved environmental stability.

## 5.2 Oxygen Diffusion

First the dynamics of oxygen diffusion in hybrid perovskite films is considered. $CH_3NH_3PbI_3$ and $CH_3NH_3PbI_3$(Cl) were chosen for a comparative study, since both have been widely tested in photovoltaic devices. Here, the perovskite that has the formula $CH_3NH_3PbI_3$(Cl) refers to a perovskite material fabricated from a combination of iodide and chloride precursors ($PbI_2$

and $PbCl_2$). Of the two systems, $CH_3NH_3PbI_3(Cl)$ films are reported to be more stable but the origin(s) of this superior stability remains unclear. In this study, films were fabricated as described in the experimental section onto clean glass substrates.[30, 31] X-ray diffraction (XRD) was used to characterize both materials, and confirmed that in both cases $CH_3NH_3PbI_3$ is the compound formed (Figure 5.2a). Additionally, the XRD (Figure 5.2b) of a fully oxygen and light degraded $CH_3NH_3PbI_3(Cl)$ sample is provided and shows that the major degradation product is $PbI_2$. Where the peaks correspond to the same degradation product ($PbI_2$) as reported in the previous literature.[8] It is, however, possible that the concentration of chlorine and $PbCl_2$ within the $CH_3NH_3PbI_3(Cl)$ film and the degraded film respectively, may be too low to determine through XRD. The presence of any chlorine may give rise to differences in charge carrier recombination, which could influence stability, but the low Cl levels mean this is unlikely to be the dominant effect. Chlorine substitution is thus unlikely to be responsible for the improved stability of the material.

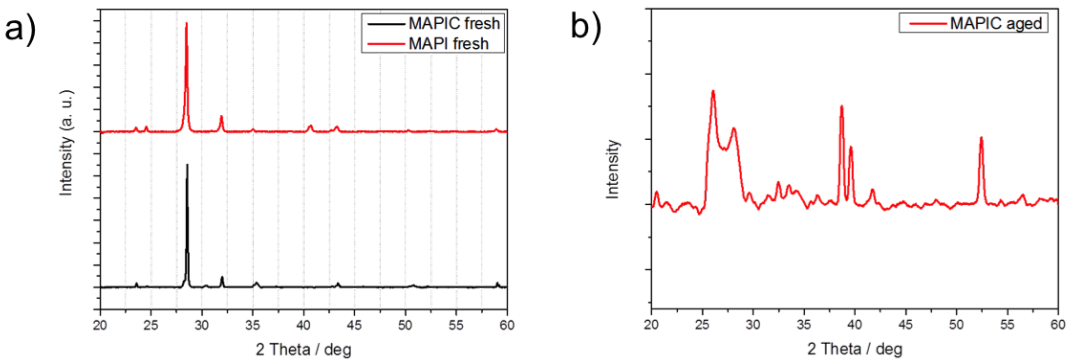


Figure 5.2: a) XRD patterns of $CH_3NH_3PbI_3$ and $CH_3NH_3PbI_3(Cl)$ films. b) XRD pattern of a degraded $CH_3NH_3PbI_3(Cl)$ film

For the first time, Isothermal gravimetric analysis (IGA) was used to probe the dynamics of oxygen diffusion in these perovskite samples and the results are illustrated in Figure 5.3a. In a typical experiment, the sample chamber with the perovskite film was first flushed with He gas for 30 min. Next, the weight of the perovskite sample was recorded as a function of exposure to dry air ($N_2$=80%, $O_2$=20%) over the course of 20 min at room temperature (25°C). As can be seen from the IGA traces in Figure 5.3a, oxygen diffusion into both $CH_3NH_3PbI_3$ and $CH_3NH_3PbI_3(Cl)$ films is rapid, with saturation being achieved within 5 to 10 minutes.

This observation is supported by the rate of photo-luminescence quenching (Figure 5.3b) upon exposure to oxygen for the samples. In this experiment, steady state PL of the films was measured first under nitrogen and then at subsequent time intervals after the introduction of oxygen into the environment. Again, the signal has plateaued after 10 minuets of exposure to oxygen, suggesting that oxygen has saturated the film within this time frame and no further quenching by oxygen occurs. The incoming oxygen quenches the PL signal by an electron transfer reaction, where the photo-excited electron generated from the pump pulse transfers to the molecular oxygen. This decreases the number of electrons available to under go radiative recombination, hence as the content of oxygen increases with time the PL intensity decreases. Further evidence for the fast rate of oxygen diffusion in these two materials was obtained from time-of-flight secondary ion mass spectrometry (ToF-SIMS) measurements, in which the depth profile of oxygen throughout the films was determined. In these experiments, films of both $CH_3NH_3PbI_3$ and $CH_3NH_3PbI_3$(Cl) were soaked in dry air in the absence of light and ToF-SIMS data collected. The ToF-SIMS images shown in Figure 5.3b and c represent slices through $CH_3NH_3PbI_3$ and $CH_3NH_3PbI_3$(Cl) layers at a depth of approximately 200 nm in the films, after soaking for 30 min (Figure 5.3c and d respectively). 3D profiles (raw data) showing oxygen concentration as a function of film depth are also provided, Figure 5.3e and 5.3f respectively. The data depicts that oxygen is ubiquitously present throughout the samples and films have a high oxygen content, after soaking in a dry air environment even after half an hour.

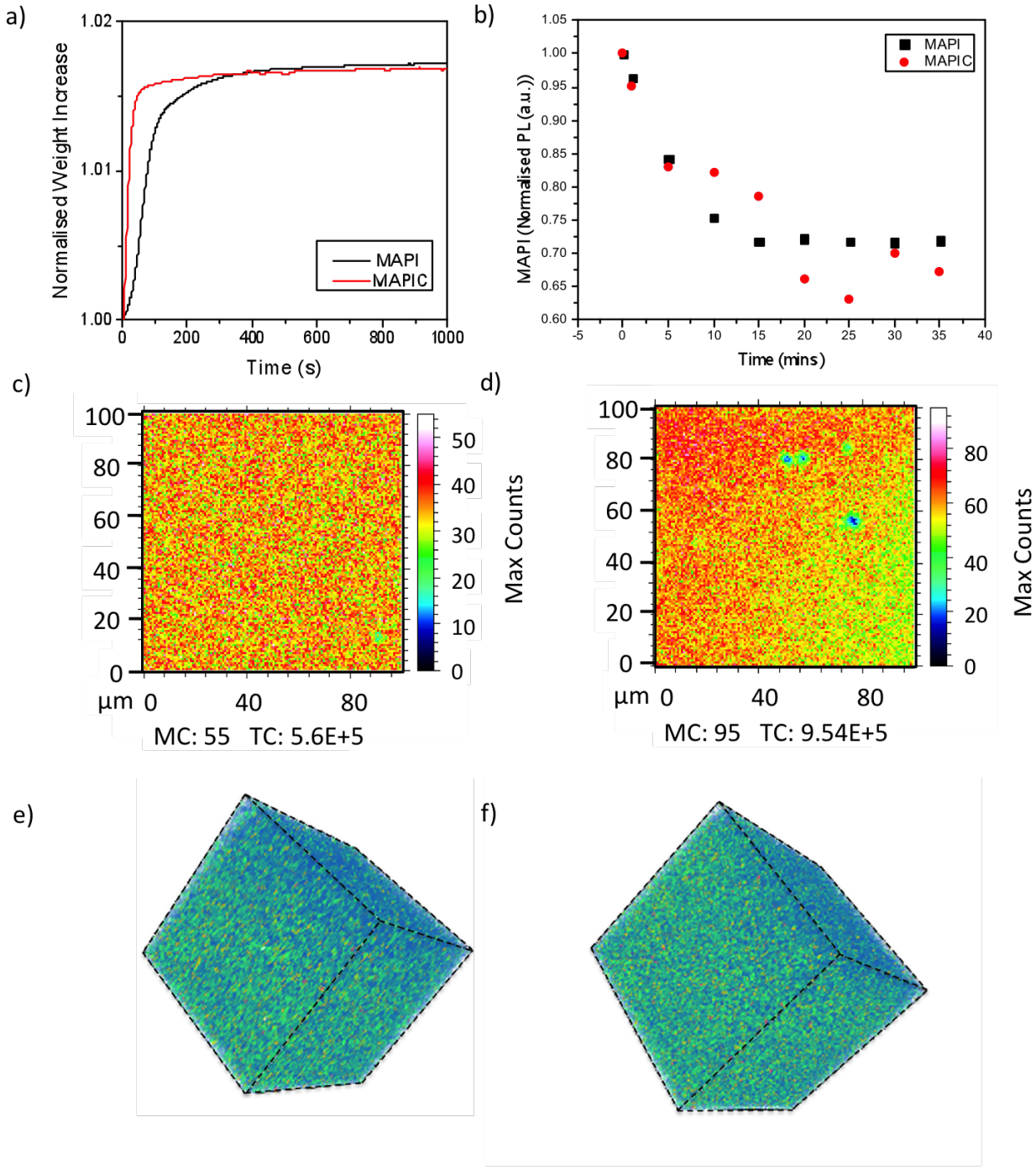


Figure 5.3: a) Isothermal gravimetric analysis plot (IGA) of $CH_3NH_3PbI_3$ (MAPI) and $CH_3NH_3PbI_3$(Cl) (MAPIC) thin films coated on non-conductive cleaned glass with 30 min of Helium soaking before oxygen exposure, where t=0 corresponds to the time at which oxygen was introduced into the system. b) Normalised photoluminescence decay after exposure to oxygen for both $CH_3NH_3PbI_3$ and $CH_3NH_3PbI_3$(Cl) films. c,d) ToF-SIMS surface images(100 100mm) of $CH_3NH_3PbI_3$ and $CH_3NH_3PbI_3$(Cl) respectively after exposure to dry air flow with no illumination, where the maximum counts (MC) and the total number of secondary oxygen ion counts (TC) are shown with the colour scales corresponding to the interval [0, MC]. e) ToF-SIMS 3D Oxygen ion plot of a MAPI film. f) ToF-SIMS 3D Oxygen ion plot of a MAPIC film.

Taken together, these findings demonstrate that oxygen enters the perovskite samples and is uniformly distributed throughout the films. As the time period for oxygen uptake to reach saturation is in agreement with the fast degradation rate previously observed in $CH_3NH_3PbI_3$ photoactive layers and devices,[8, 6, 7] it can therefore be concluded that the high sensitivity of $CH_3NH_3PbI_3$ devices to oxygen is owed, in part, to the rapid rate at which oxygen can diffuse into the films. From the IGA data it is also possible to estimate the air (80% $N_2$ and 20% $O_2$) diffusion coefficient, $D_a$, to be in the range $10^{-7}$ to $10^{-9}$ $cm^2$ $s^{-1}$ for the $CH_3NH_3PbI_3$ perovskite material. This value is comparable to the fast diffusion of gases into polymer thin films where, for example, the diffusion coefficient in poly-(3-hexylthiophene-2,5-diyl) (P3HT) thin films is of the order of $10^{-8}$ $cm^2$ $s^{-1}$.[32] It is widely accepted that these fast diffusion kinetics are responsible for the relatively low stability of semiconducting polymer films to molecular oxygen.[33, 34, 35] As such, it is proposed that the fast oxygen diffusion kinetics are critical to the observed oxygen- and light-induced degradation rates seen in perovskite-based optoelectronic devices.

## 5.3 Particle Size and Morphology

Next, the effect of visible light and oxygen on the relative stability of $CH_3NH_3PbI_3$ and $CH_3NH_3PbI_3$(Cl) films and devices is explored through UV/VIS, superoxide generation and PCE degradation experiments. Figure 5.4a,b shows the absorption spectra of $CH_3NH_3PbI_3$ and $CH_3NH_3PbI_3$(Cl) films on glass substrates measured as a function of aging under illumination in dry air. Figure 5.4a,b reveals that both perovskite materials rapidly degrade under these conditions. However, it is apparent that $CH_3NH_3PbI_3$(Cl) films degrade at a significantly slower rate than $CH_3NH_3PbI_3$ films. With complete degradation taking approximately three days for $CH_3NH_3PbI_3$ compared to 12 days for $CH_3NH_3PbI_3$(Cl). Figure 5.4c shows the power conversion efficiency (PCE) versus time profile for $CH_3NH_3PbI_3$ and $CH_3NH_3PbI_3$(Cl)-based solar cells, with the devices being continuously aged in dry air under one sun illumination light. For these studies, a solar cell architecture of the type [FTO/compact-TiO2/mesoporous-TiO2/perovskite/spiro-OMeTAD/Au] was employed and all PCE measurements were performed on un-encapsulated devices as in previous work.[12] The PCEs of the solar cells were determined

from current-voltage characteristics ascertained at regular time intervals over the course of 4 hours. In Figure 5.4c, $CH_3NH_3PbI_3(Cl)$ devices show a relatively small 10% drop in PCE over the 4 hr aging period whereas the $CH_3NH_3PbI_3$ devices display a more substantial ($\approx 80\%$) drop in PCE under the same aging conditions. The better stability of the $CH_3NH_3PbI_3(Cl)$ solar cells (compared to $CH_3NH_3PbI_3$) is consistent with the absorption data in Figure 5.4a,b, as well as other recent reports.[30] The difference in stability between $CH_3NH_3PbI_3$ and $CH_3NH_3PbI_3(Cl)$ observed here may be related to the smaller size of the particles.

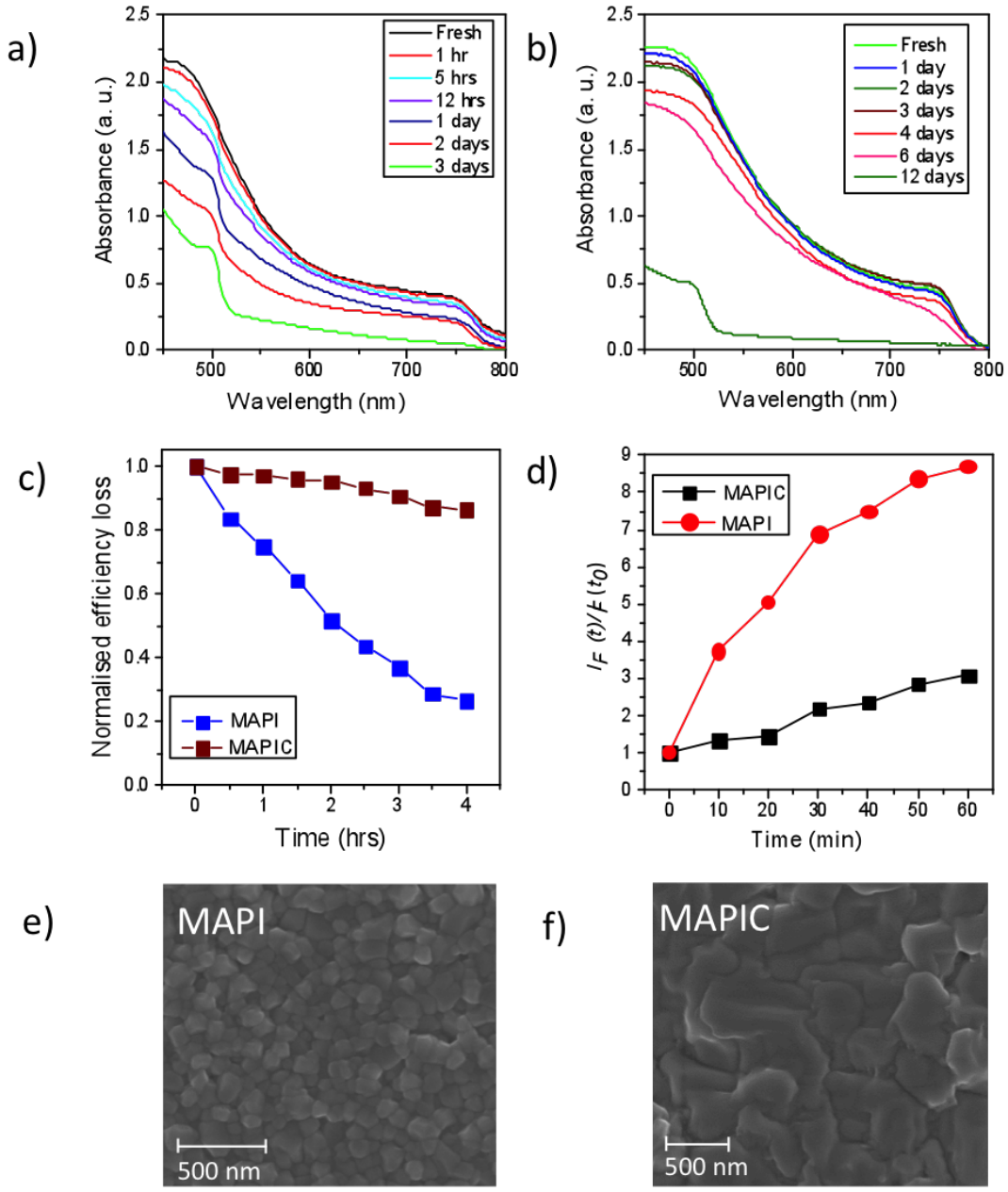


Figure 5.4: a,b) Light absorption spectrum for ageing $CH_3NH_3PbI_3$ and $CH_3NH_3PbI_3(Cl)$ under dry air and illumination ($25mWcm^{-2}$) respectively. (c) Normalized power conversion efficiency loss for photovoltaic devices employing $CH_3NH_3PbI_3$ and $CH_3NH_3PbI_3(Cl)$ as the light harvesting materials in an [FTO/planar-$TiO_2$/mesoporous-$TiO_2$/perovskite/spiro-OMeTAD/Au] architecture. Raw device data was obtained in collaboration with Xiangnan Bu d) Normalized fluorescence intensity increase of the HE probe at 610 nm (excitation at 520 nm). $I_F(t)$ is the fluorescence maximum at time t, while $I_F(t_0)$ is the background fluorescence intensity. $I_F(t)/I_F(t_0)$ ratio corresponds to the yield of superoxide generation for the perovskite films. e,f) Surface SEM images of $CH_3NH_3PbI_3$ and $CH_3NH_3PbI_3(Cl)$ films deposited on cleaned glass substrates.

The next question that arises relates to the origin of the difference in stability observed be-

tween $CH_3NH_3PbI_3$ and $CH_3NH_3PbI_3(Cl)$. To identify the cause(s) for this difference, the yield of photo-induced superoxide formation for the two perovskites was determined. As previously established, superoxide is the key reactive species responsible for the hybrid perovskite and device degradation.[8, 6] Here the yield of superoxide was determined for both $CH_3NH_3PbI_3$ and $CH_3NH_3PbI_3(Cl)$ films using a hydroethidine (HE) fluorescent probe (as described in the Methods section). As detailed in previous literature, the degradation effect observed cannot be ascribed to degradation of the hole transporting material Spiro-OMeTAD since this HTM has not been employed in these experiments.[8] Figure 5.4d, shows the rate of increase in HE emission and, accordingly, the superoxide generation yield. The data in Figure 5.4d show that $CH_3NH_3PbI_3$ produces a significantly higher yield of superoxide than $CH_3NH_3PbI_3(Cl)$, consistent with the film and device stability data in Figure 5.4ac. It is reasonable to propose that this difference in reactivity stems from differences in the particle sizes within the films. For example, the presence of chloride ions in the precursor mixture is known to slow down the rate of crystal formation, leading to larger crystals.[5, 36] This hypothesis was confirmed by taking scanning electron microscopy (SEM) images of the $CH_3NH_3PbI_3$ and $CH_3NH_3PbI_3(Cl)$ films. Figure 5.4e and f shows that the $CH_3NH_3PbI_3(Cl)$ film consists of crystal domains that are several hundreds of nanometres in diameter, considerably larger than those observed in the $CH_3NH_3PbI_3$ sample. This strongly suggests that crystal size plays a crucial role in determining the stability.

In order to test this hypothesis, in a systematic manner the stability of $CH_3NH_3PbI_3$ films composed of different crystal sizes were created and compared. The controlled growth of $CH_3NH_3PbI_3$ crystals was achieved following the method previously reported by Gratzel and co-workers.[18] In this way, samples with perovskite crystal sizes defined as small (100 nm), medium (160 nm) and large (250nm) were synthesized and confirmed by SEM imaging. Representative SEM images are shown in Figure 5.5a to 5.5c. In Figure 5.5d the magnitude of the absorbance at 750nm is plotted against aging time, with black, red and blue curves corresponding to films composed of small (sample 1), medium (sample 2) and large (sample 3) $CH_3NH_3PbI_3$ crystallites, respectively. These absorbance measurements were recorded until the

$CH_3NH_3PbI_3$ film had turned completely yellow, indicating full conversion of the perovskite to the degradation product, $PbI_2$. It is apparent from the data in Figure 5.5d that the films with large $CH_3NH_3PbI_3$ crystals are considerably more stable than the films composed of small $CH_3NH_3PbI_3$ crystals. It is noted that all three samples showed similar rates of oxygen uptake, with all the films reaching saturation within 10min, as determined by IGA experiments, Figure 5.4e. Next, the possible correlation between $CH_3NH_3PbI_3$ crystal size, materials stability and superoxide generation yield is explored. The results are displayed in Figure 5.5f.

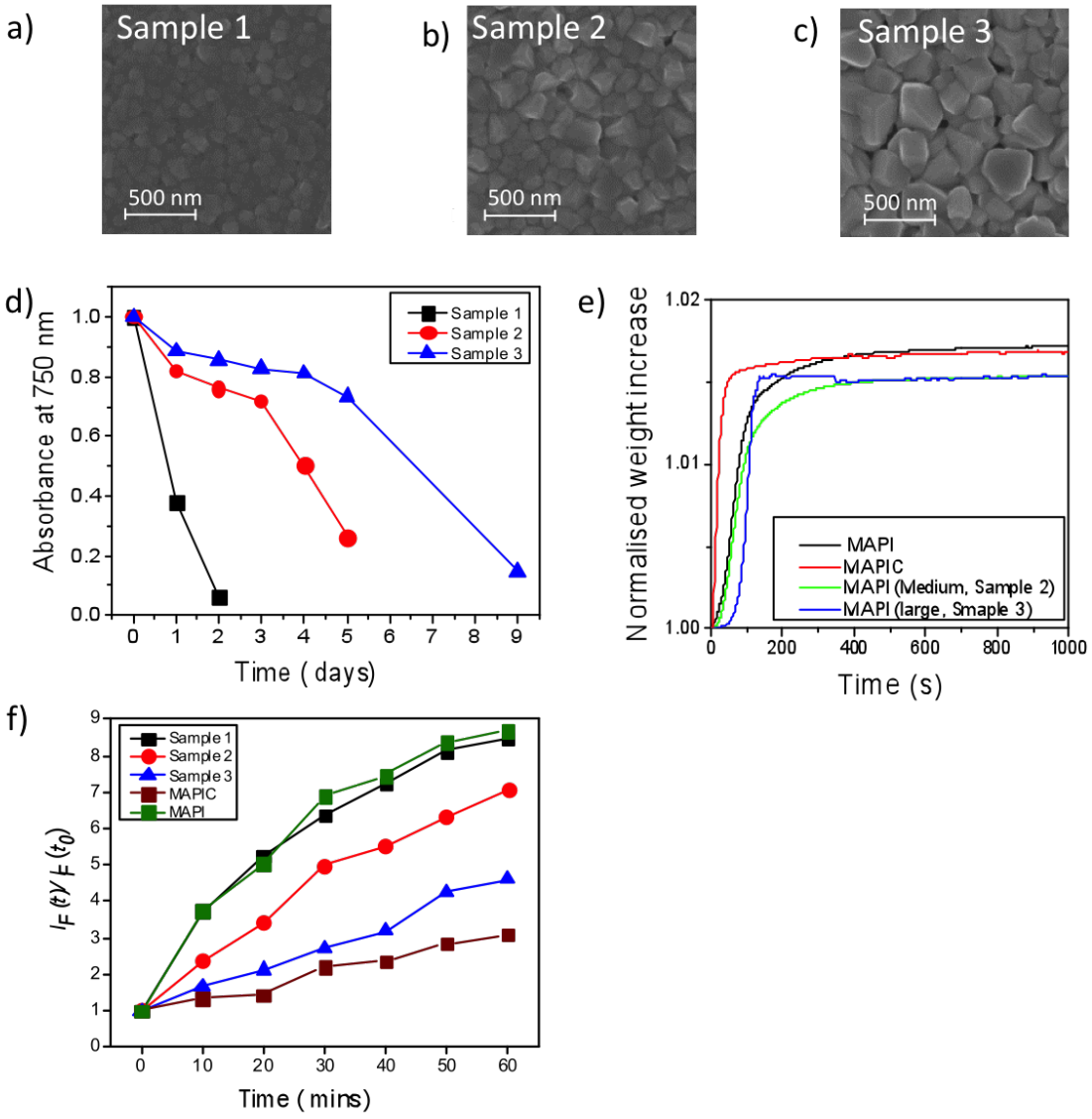


Figure 5.5: a to c) Surface SEM images of small (sample 1), medium (sample 2) and large (sample 3) crystal sizes of $CH_3NH_3PbI_3$. d) Normalized absorbance decay at 750 nm for methylammonium lead iodide of sample 1 (small crystals, 100 nm), sample 2 (medium crystals, 150 nm) and sample 3 (large crystals, 250nm) with degradation conditions of illumination ($25mWcm^2$) and dry air. e) IGA data displaying the oxygen diffusion into all three crystal sizes. f) Superoxide yield plot for $CH_3NH_3PbI_3$ (with small (black), medium (red), large (blue) crystal sizes and a toluene dripped prepared sample (green) and $CH_3NH_3PbI_3$(Cl) (brown).

Figure 5.5f shows the measured rate of increase of superoxide species in these three samples; a correlation is observed between the $CH_3NH_3PbI_3$ crystallite size, stability (that is, tolerance to visible light and oxygen stress) and superoxide yield. It is evident that the $CH_3NH_3PbI_3$ films with large crystallites show a relatively low yield of superoxide formation and display better stability. Conversely, the $CH_3NH_3PbI_3$ films composed of smaller crystallites show a

higher yield of superoxide generation and rapidly degrade within 2 days. The impact on device stability is once again monitored through the degradation of the PCE of devices utilizing the different crystal size perovskites. In a similar manner the devices are aged under dry air flux and continuous one sun illumination for the duration of the aging time. The normalised PCE vs time plot is displayed in Figure 5.6a. The data reinforces the previous findings and shows that the stability of devices towards the aging conditions decreases with decreasing crystal size. That is, the device with small crystals observes approximately a 70% decrease in PCE compared to that of a 30% PCE decrease from the larger crystal sample over the course of four hours. This data thus states a correlation between crystal size and device stability that is ultimately underpinned by the yield of superoxide generated from the crystals. Moreover, steady state PL experiments, Figure 5.6b, reveal that the emission intensity is dependent on crystallite size. Where the smaller crystals, have a lower intensity emission compared to that of the medium and larger crystal sizes. Inferred from this, is that there could be a correlation between the number of defects present and the stability. Where defects, could dictate the yield of superoxide this is because defects have been shown to cause non-radiative recombination pathways leading to lower emission intensities.[37, 38, 39, 40] Hence, if the sample posses more defects lower PL signals are observed and these could also cause increased superoxide generation. Small crystallites have been shown from the experiments to have higher superoxide yields and lower PL intensities, suggesting this correlation between defect density, superoxide yield and thus stability could be the factor that determines tolerance towards oxygen and light degradation.

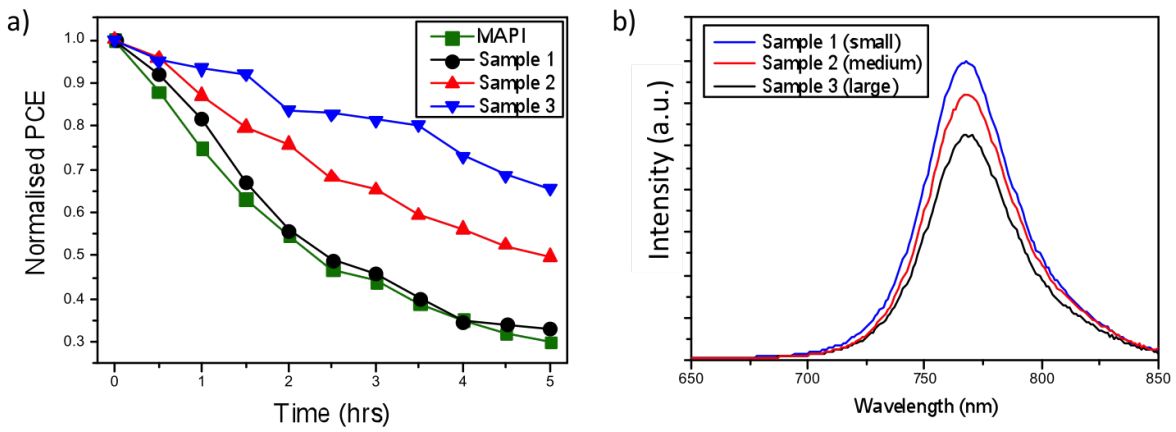


Figure 5.6: a) Normalised PCE loss for small (sample 1), medium (sample 2) and large (sample 3) crystal sizes of $CH_3NH_3PbI_3$ in devices as the light harvesting materials in an [FTO/planar-$TiO_2$/mesoporous-$TiO_2$/perovskite/spiro-OMeTAD/Au] architecture. b) Steady state photoluminescence for the same crystal size sample but in a plain glass/perovskite bilayer system.

There then appears to be a direct correlation between the yield of superoxide generation (and subsequently degradation rate) and perovskite crystallite size, whilst no difference in oxygen uptake is observed. Consequently, there must be an intrinsic factor that is dictated by the crystal formation/size/morphology that controls the formation of superoxide from oxygen. From the data collected, it is suggested that defects may be accountable for this observed trend. Where smaller crystals with a higher defect density leads to greater superoxide formation.

### 5.3.1 Changing Morphology

The impact of changing morphology from cubic to needle-like nano-crystals on the stability is explored. Additionally, a combination of the morphologies with the cubic perovskite fabricated onto the needle crystallite structure are examined with varying cubic crystal size. The samples were prepared according to the methods section and as reported in the literature using a combination of 1-step and 2-step deposition methods.[41] SEM images are presented below, Figure 5.7, showing the fabricated morphologies and their corresponding labels. The samples are labeled A-E representing film morphologies of needles, needles with small cuboids, needles with medium cuboids

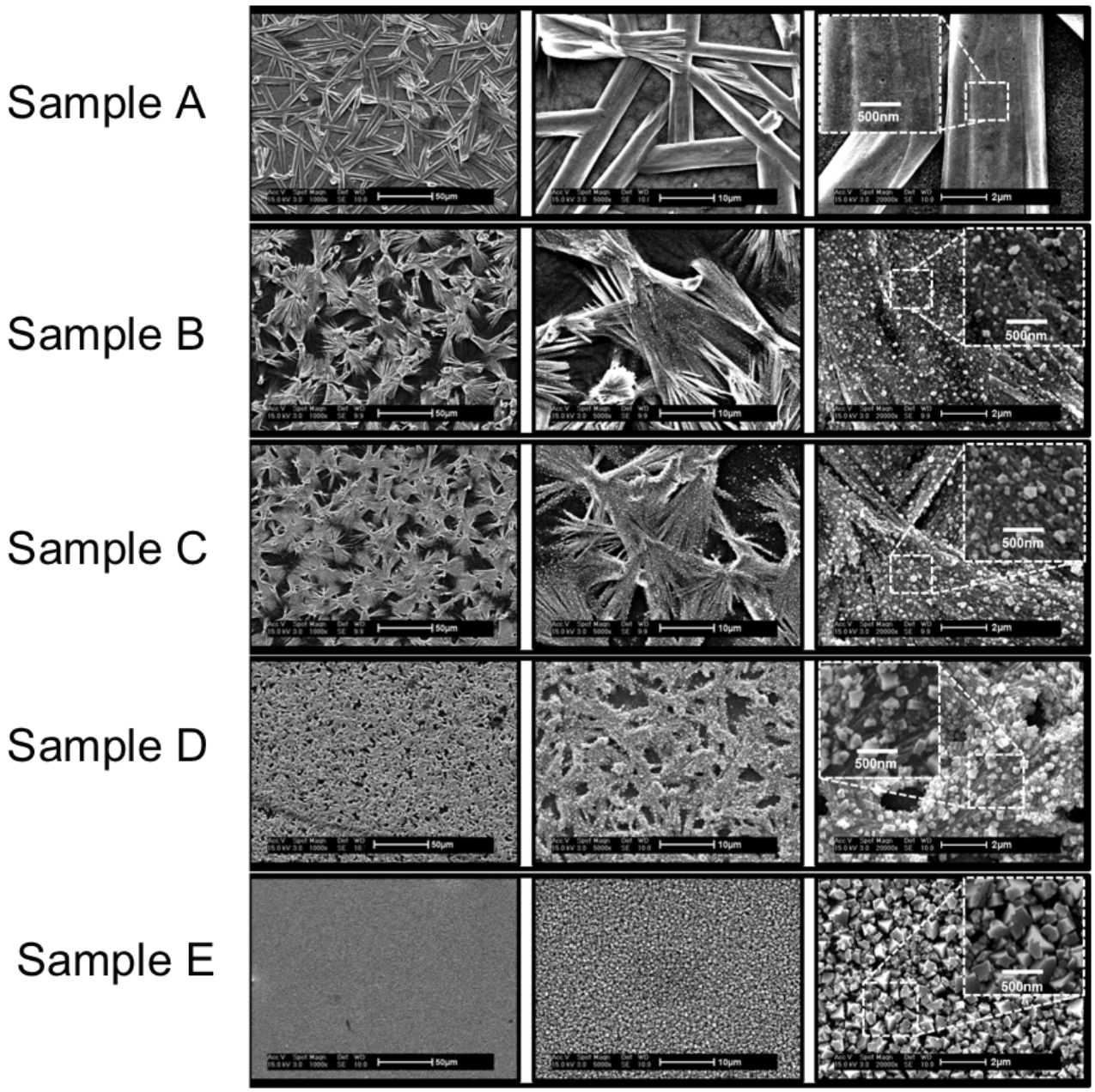


Figure 5.7: SEM images of increasing magnification from left to right for the different samples A-E top to bottom. Images were collected at Manchester University by Muhammad Mokhtar.

In order to ascertain a correlation between morphology and stability, the samples A-E were degraded under dry air and light and their absorbance data and superoxide generation yields were collected at regular time intervals. Figure 5.8a and b, demonstrate that again film life-time correlates to superoxide yields. Here if we compare only sample A and sample E as these represent the extremes, i.e cuboids vs needles, sample A shows the longest material life-time and lowest superoxide yields. In contrast sample E, degrades the fastest and generates the most amount of superoxide. The difference in stability between samples B-D, can be rationalised in

a similar manner to the samples explored earlier, where the increasing cuboid size generates more stable films. Interestingly, the difference in stability between the morphologies of sample A and sample E, suggest that again size dictates the relative stability towards the degradation environment. Larger structures are more tolerant to oxygen and light. This is hypothesised to be due to the difference in surface area and consequently the surface reactivity. Crystal surfaces are commonly known to be more defect rich.[37, 38, 21, 27, 24, 40] Changing the surface area of the samples in all cases results in a change in stability. Once more steady state PL is employed to observe if changing the morphology and crystal size causes a difference in sample emission intensity. The PL experiment results are shown in Figure 5.8c.

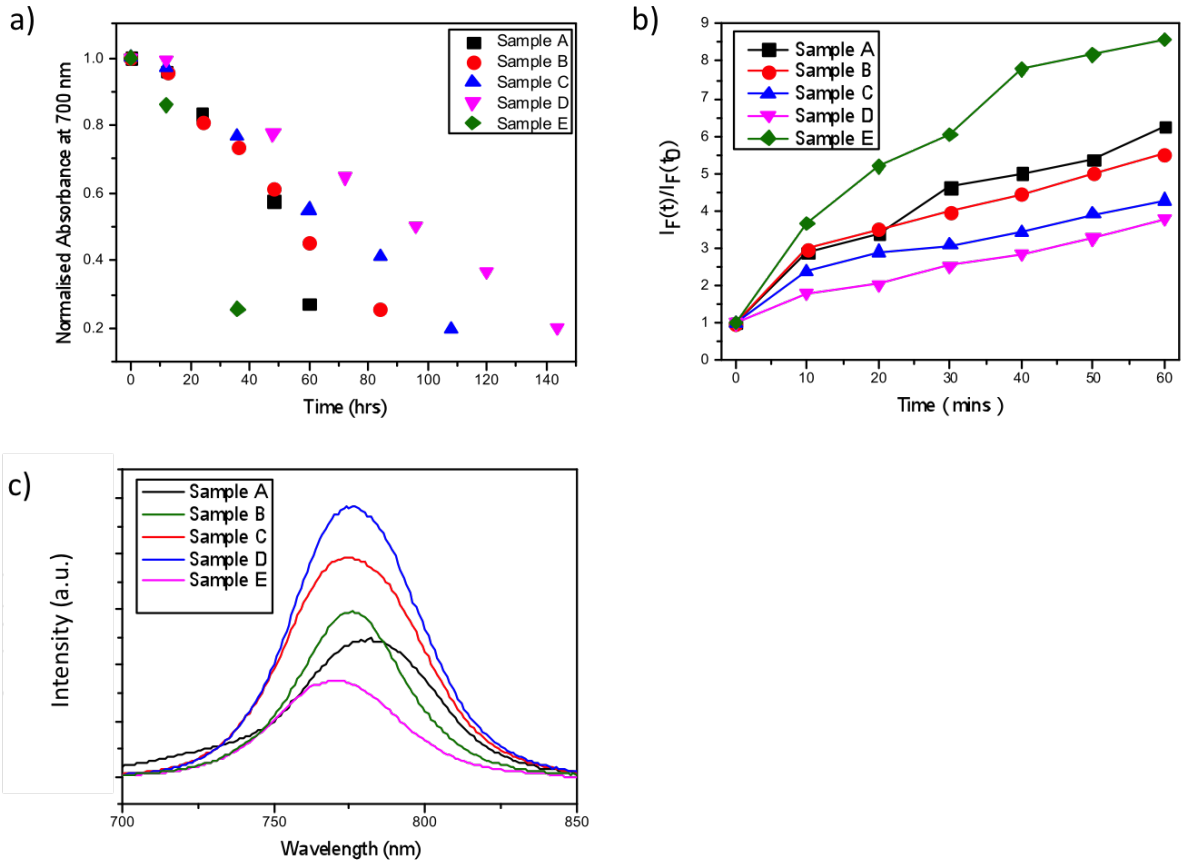


Figure 5.8: a) Nomralised absorbance at 700 nm as a function of time under oxygen and light stress for samples A-E. b) Superoxide yield plot for the 5 samples and c) their steady state photoluminescence.

Figure 5.8c, confirms that increasing crystal size does increase emission intensity. This reinforces the suggestion that crystal size impacts the defect density, be it surface or bulk defects,

which in turn influences the rate of superoxide generation and the material film stability. From the samples tested and the experiments conducted it is not possible to determine if surface or bulk defects are more influential. Since, increasing the crystal size could also influence the time dynamics of the oxygen reaction. Where larger crystals increase the time taken for oxygen to reach the defects in the bulk of the crystal before reacting to form superoxide. Comparing the time-resolved photoluminescence of samples A and E, Figure 5.9a, further reinforces the concept that the origin of the difference in superoxide production lies in the defect density. The data shows that the smaller higher surface area cuboids, sample E, have faster decay dynamics and lose emission intensity quicker. This results from more defects acting as trap sites, which mediate non-radiative recombination. Faster emission decay is known to be correlated to defect density and trap sites within crystal structures.[22, 40] However, further experiments are required to identify which defect and which location are more accountable for the generation of superoxide. These factors will be explored later. However, a clear trend of crystal size, defect density and material stability is observed. The impact on device performance is demonstrated again by monitoring the PCE degradation with time after exposure to dry air flux and one sun illumination. The data, Figure 5.9b, as predicted shows that increasing crystal size, via changing the morphology leads to prolonged retention of device performance under oxygen and light conditions.

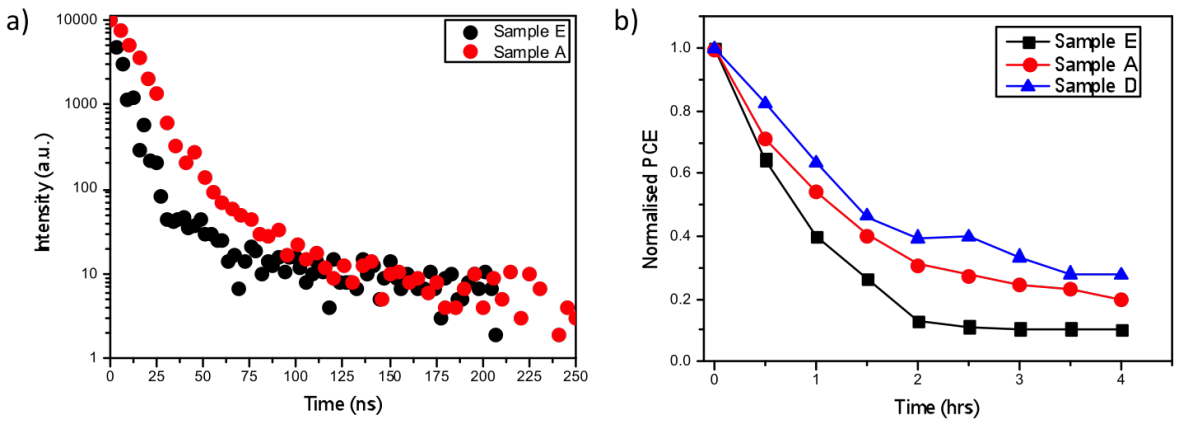


Figure 5.9: a) Time resolved photoluminescence for samples A and E, comparing the different morphologies of needles and cubic $CH_3NH_3PbI_3$. b) Normalised PCE loss for perovskite samples A, D and E in the device architecture: [FTO/planar-$TiO_2$/mesoporous-$TiO_2$/perovskite/spiro-OMeTAD/Au]

## 5.4 Superoxide formation sites

To explore the potential role of defects and to gain atomic-scale insights into the energetics and defect mechanisms of the degradation process ab initio simulations based on DFT have been harnessed. These calculations were conducted by Chris Eames. The use of these computational simulations to help identify the most probable sites for superoxide formation are deigned to approximate the energies of formation and identify the key issue in the perovskite crystal responsible for the sensitivity towards oxygen and light. As a starting point, the reaction with oxygen (with no photo-generated electrons in the perovskite lattice), described by the following equation was probed:

$$4CH_3NH_3PbI_3 + O_2 \longrightarrow 4PbI_2 + 2I_2 + 2H_2O + 4CH_3NH_3 \tag{5.1}$$

The enthalpy of the reaction was calculated to be +1.60 eV per $O_2$ molecule, indicating that the reaction in the absence of light is unfavourable, which is consistent with observation.[8, 6] Where it has already been shown that in order for the overall degradation reaction to occur, the film must be exposed to both $O_2$ and light in order for superoxide species to form.[8, 6, 3, 7] The implication as defined earlier is that $O_2$ acts as an electron scavenger and absorbs electrons generated by light or an external electrical bias. The next step in the reaction sequence is for superoxide $O_2$ to react with photo-oxidized $CH_3NH_3PbI_3$* to produce $PbI_2$, $I_2$, $H_2O$ and $CH_3NH_2$ according to the following reaction (illustrated in Figure 5.1)

$$4CH_3NH_3PbI_3^* + O_2^- \longrightarrow 4PbI_2 + 2I_2 + 2H_2O + 4CH_3NH_3 \tag{5.2}$$

In contrast to the first reaction, the calculated enthalpy for this reaction is negative ($-1.40$ eV per $O_2$ molecule), indicating that the degradation reaction is now highly favourable, again in agreement with observation. This indicates that both the photo-oxidized $CH_3NH_3PbI_3$ and the superoxide species are unstable with respect to the reaction products. A key step in the degradation reaction is the formation of the superoxide species according to the reaction $O_2 + e^- = O_2^-$. This raises the important question of where the superoxide forms in the crystal lattice. It is plausible that ionic defects such as iodide vacancies play a key role in mediating superoxide

formation from $O_2$ and hence the degradation reaction. As noted, recent work indicates a significant population of intrinsic Schottky-type defects leading to the favourable formation of ion vacancies in the crystal lattice.[20, 40] Such vacancy defects may act as molecular or charge traps which in turn could mediate the electron transfer reaction with oxygen. It is known that the anion vacancy in binary lead halides can trap a photoelectron to form an Farbe center, where an anion vacancy (an iodide vacancy in perovskite) is occupied by an electron.[42, 43] To investigate this process and the potential role of vacancies in mediating superoxide formation, the energetics for superoxide formation from $O_2$ molecules on various lattice and vacancy sites in the $CH_3NH_3PbI_3$ perovskite structure were calculated; the most favourable configurations and the corresponding superoxide formation energies are summarized in Figure 5.10. Two main findings emerge. First, superoxide formation by direct electron transfer from the perovskite to oxygen is energetically favourable, a negative formation energy is obtained. Analysis of the electron density and bond lengths shows that the photo-generated electron resides on the $O_2$ molecule; upon adsorption the $O_2$ bond length increases from 1.22 to 1.33$\mathring{A}$ and the species becomes spin polarized. Second, superoxide formation energies indicate that vacant iodine ($V_I$) sites are the preferred location for the reduction process in the crystal bulk. Interestingly, an iodide ion is of similar size to the superoxide species Figure 5.11, and in occupying an iodide vacancy, the superoxide ion restores the full octahedral coordination of $Pb^{2+}$.

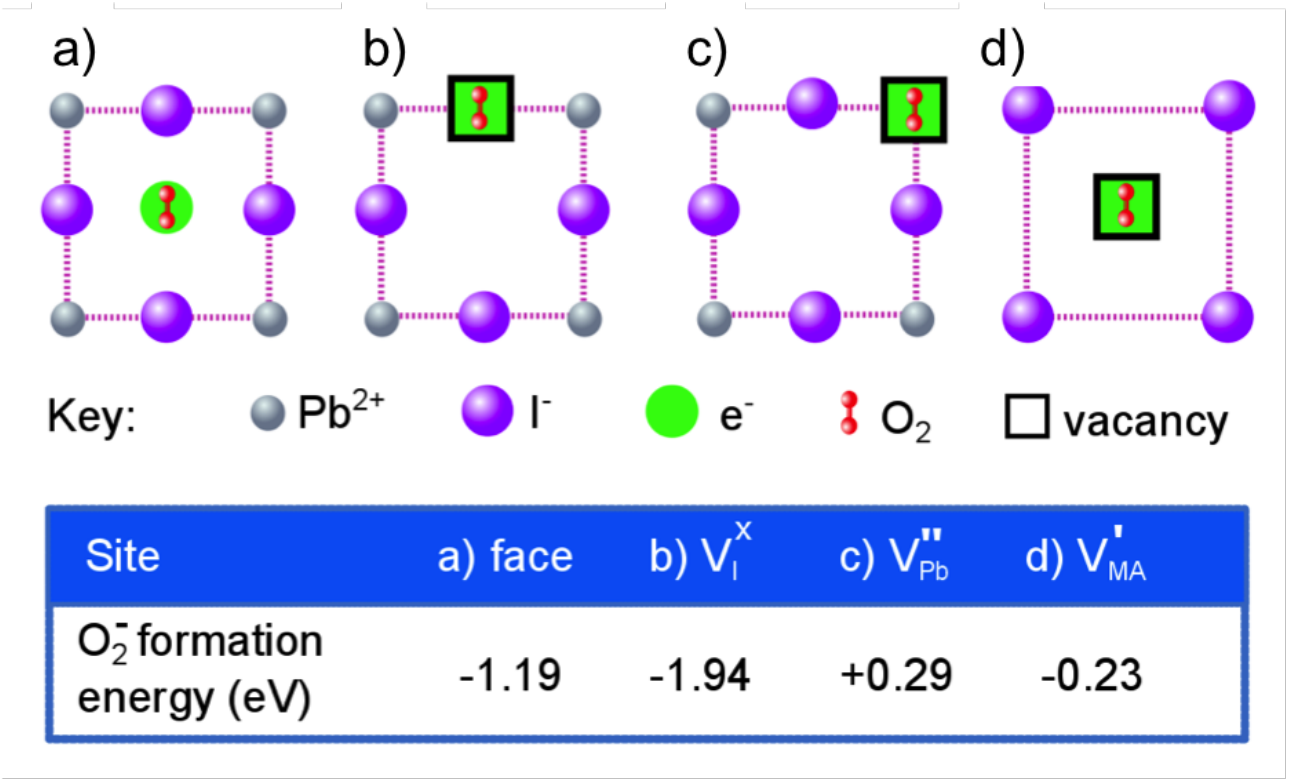


| Site | a) face | b) $V_I^x$ | c) $V_{Pb}''$ | d) $V_{MA}'$ |
|---|---|---|---|---|
| $O_2^-$ formation energy (eV) | -1.19 | -1.94 | +0.29 | -0.23 |

Figure 5.10: Schematic representation of possible $O_2$ binding and reduction sites in $CH_3NH_3PbI_3$ ([001] plane) and corresponding superoxide formation energy: (a) face site neighbouring four iodide ions, (b) neutral iodide vacancy (with a photoelectron on the defect site) and negatively charged lead (c) and methylammonium (d) vacancies (with no photoelectron on them since this was found to be unphysical). Computational data was helped obtained by Dr Chris Eames.

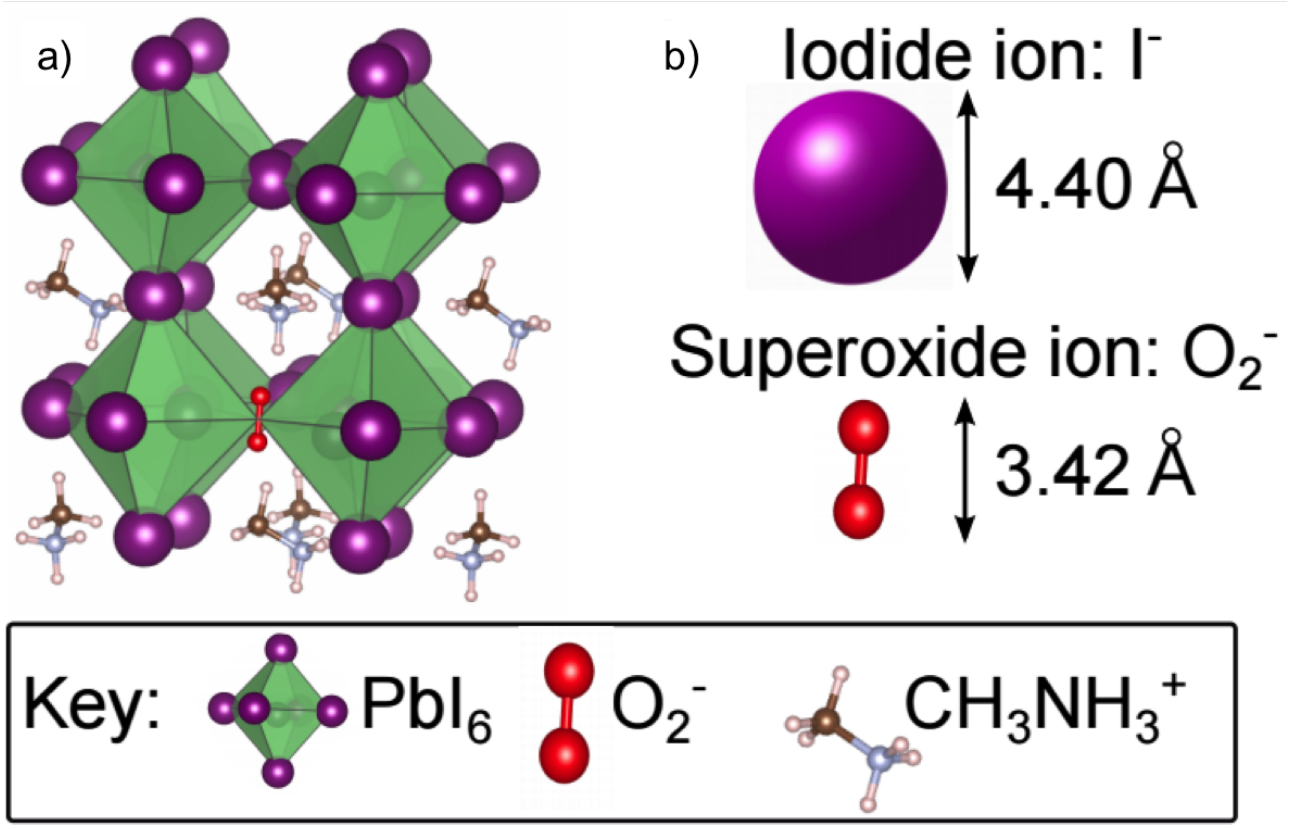


Figure 5.11: Atomic structure of $CH_3NH_3PbI_3$ showing a) superoxide ion, $O_2^-$, occupying an iodide vacancy, $V_I^x$ (for clarity, a pseudo-cubic sub-region of the structure is shown and not the full tetragonal supercell used in the calculations). b) Comparison of relative size of iodide and superoxide anions (using ionic radius of $I^-$ and, for the superoxide ion, interpolation between covalent radius in $O_2$ and ionic radius of $O_2^-$).

Further evidence for the favourable energetics of $O_2$ reduction is given by the calculated band structures for $O_2$ incorporation into $CH_3NH_3PbI_3$ reported in Figure 5.12. In Figure 5.12a it can be seen that the unoccupied oxygen $\pi^*$ anti-bonding orbital is located in the middle of the $CH_3NH_3PbI_3$ band gap where it can readily act as an acceptor state for photo-excited electrons in the conduction band. Moreover, when the $O_2$ superoxide species occupies an iodide vacancy (Figure 5.12b), the oxygen states are shifted down into the valence band as a result of changes in bonding interactions, clearly indicating that it is even more energetically favourable for $O_2$ to be reduced by photo-excited electrons in the conduction band.

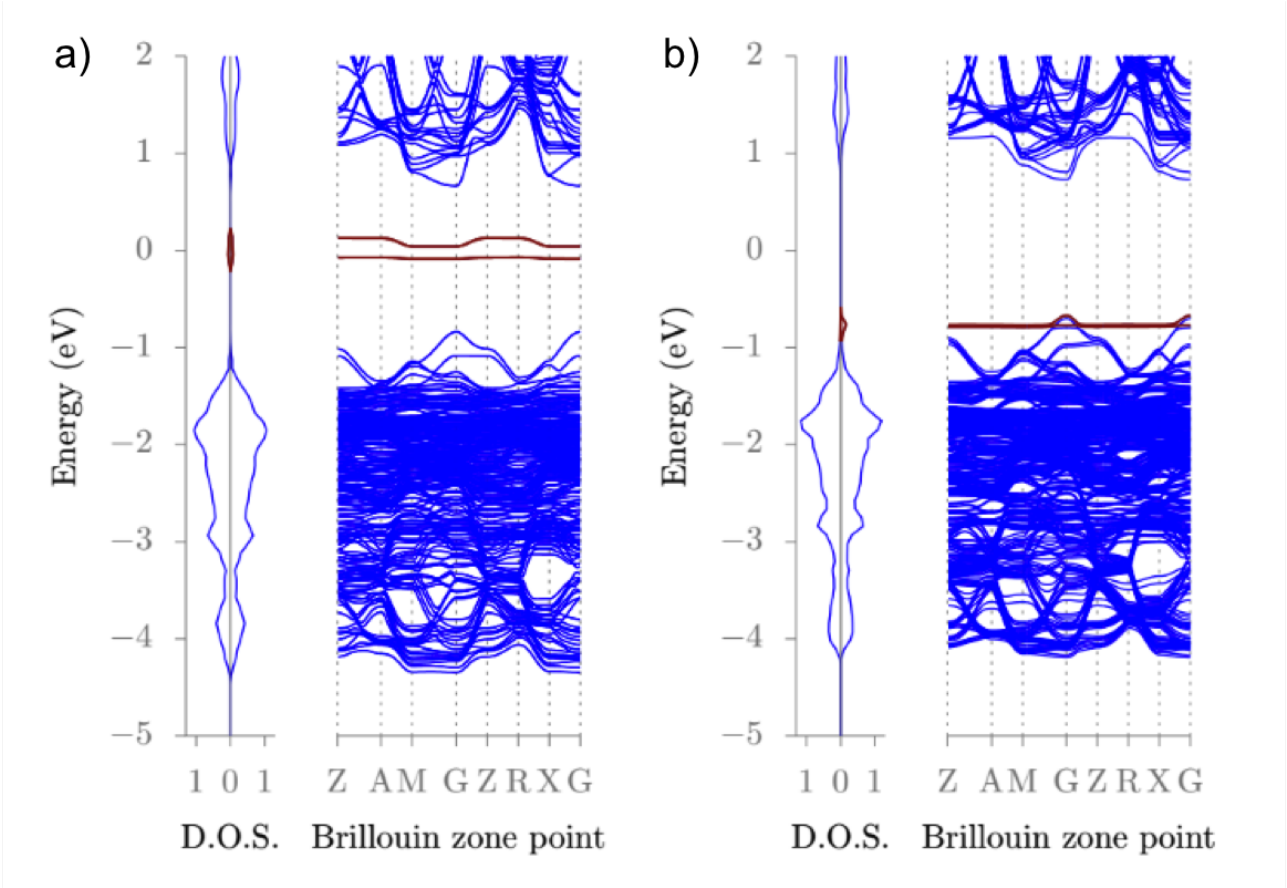


Figure 5.12: a) $O_2$ in defect-free $CH_3NH_3PbI_3$ and b) $O_2$ at iodide vacancy in $CH_3NH_3PbI_3$. Key: blue $CH_3NH_3PbI_3$, red $O_2$. Note the band structure is folded due to the use of a large supercell. Computational data was helped obtained by Dr Chris Eames.

## 5.5 Degradation mechanism - Surface vs bulk defects

The data obtained presents four key observations: (i) photo-induced oxygen degradation of $CH_3NH_3PbI_3$ shows a strong particle size dependence, (ii) structural degradation from the black perovskite phase to the yellow lead $PbI_2$ phase occurs on a timescale of days, whilst the device performance degrades in a matter of hours, (iii) rapid oxygen uptake occurs on a timescale of less than 1 hour and results in superoxide generation, and (iv) superoxide formation is always associated with degradation and is facilitated by iodide vacancies. To rationalize these findings, a mechanism that is summarized schematically in Figure 5.13 is presented. The scheme depicts a $CH_3NH_3PbI_3$ sample under illumination throughout this process to provide a constant source of photo-excited electrons in the bulk and surface regions. Oxygen is admitted to the sample and diffuses between the particles and within an hour permeates the inter-particle regions (Figure

5.13a). Superoxide species immediately begin to form at the particle surfaces as $O_2$ is reduced while occupying surface iodide vacancies. Over the first few hours there is an initial reaction between these superoxide species and the particle surfaces, leading to their passivation. The degradation of the particle surfaces prevents the extraction of the photo-current,[44] causing the device properties such as efficiency (PCE) to decline rapidly. On a timescale of days (Figure 5.13b) oxygen diffuses into the interior of the particles where it occupies bulk iodide vacancies while being reduced, leading to full structural degradation of the material.

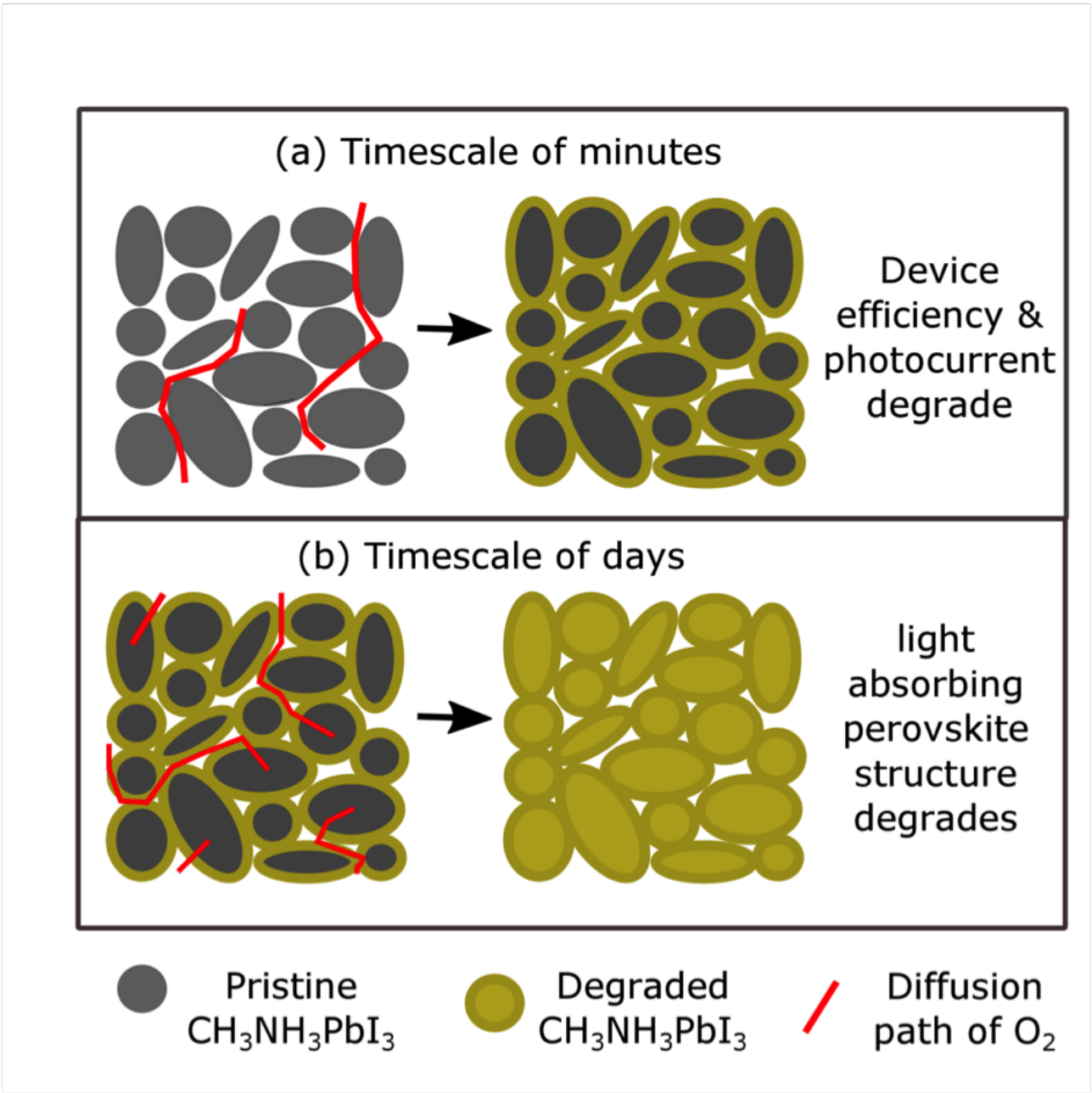


Figure 5.13: a) $O_2$ diffusion in inter-particle regions and initial reaction with particle surfaces over a timescale of hours leading to reduction in device efficiency, open circuit voltage and photo-current and b) $O_2$ diffusion into particle bulk regions over a time scale of days leading to a phase change from the photo-absorbing perovskite phase into the non-absorbing lead iodide phase (yellow).

For both the surface and bulk reactions it would be expected that the particle size and iodide vacancy levels will influence the rate of reaction. It is well known that particle surfaces are normally much more reactive than the bulk; in the halide perovskites it has been shown that different particle facets can display markedly different photovoltaic behaviour.[45] Furthermore, Haruyama et al.[46] have shown that in $CH_3NH_3PbI_3$ the most prominent surfaces are vacancy

rich with defect concentrations of $10^{12}$ $cm^{-2}$, and the data shows that oxygen reduction occurs most readily at the iodide vacancies. Thus, the increased initial degradation rate for smaller crystallites may be directly related to the surface vacancy concentration. Figures 5.5a and 5.5c, show the SEM micrographs of large crystallites with typical sizes of ca. 250 nm and small crystallites of ca. 100nm. Based on these average values, the number density of surface vacancies can be approximately calculated to be around 2.4x$10^{17}$ $cm^{-3}$ in the large crystallites and around 6.0x$10^{17}$ $cm^{-3}$ in the small crystallites. The small crystallites thus provide more than twice as many surface adsorption/ reaction sites per unit volume as the large crystallites. This is experimentally explored through comparative rates of degradation of $CH_3NH_3PbI_3$ films fabricated on low surface area plain glass and on high surface area area mp-$Al_2O_3$ substrates. SEM images shown in the proceeding figure, show the surface area differences of the substrates and show the fabricated perovskite crystals are of the same order of magnitude and morphology. This then allows for a direct comparison of the surface area of the perovskite and its degradation rate in oxygen and light environments.

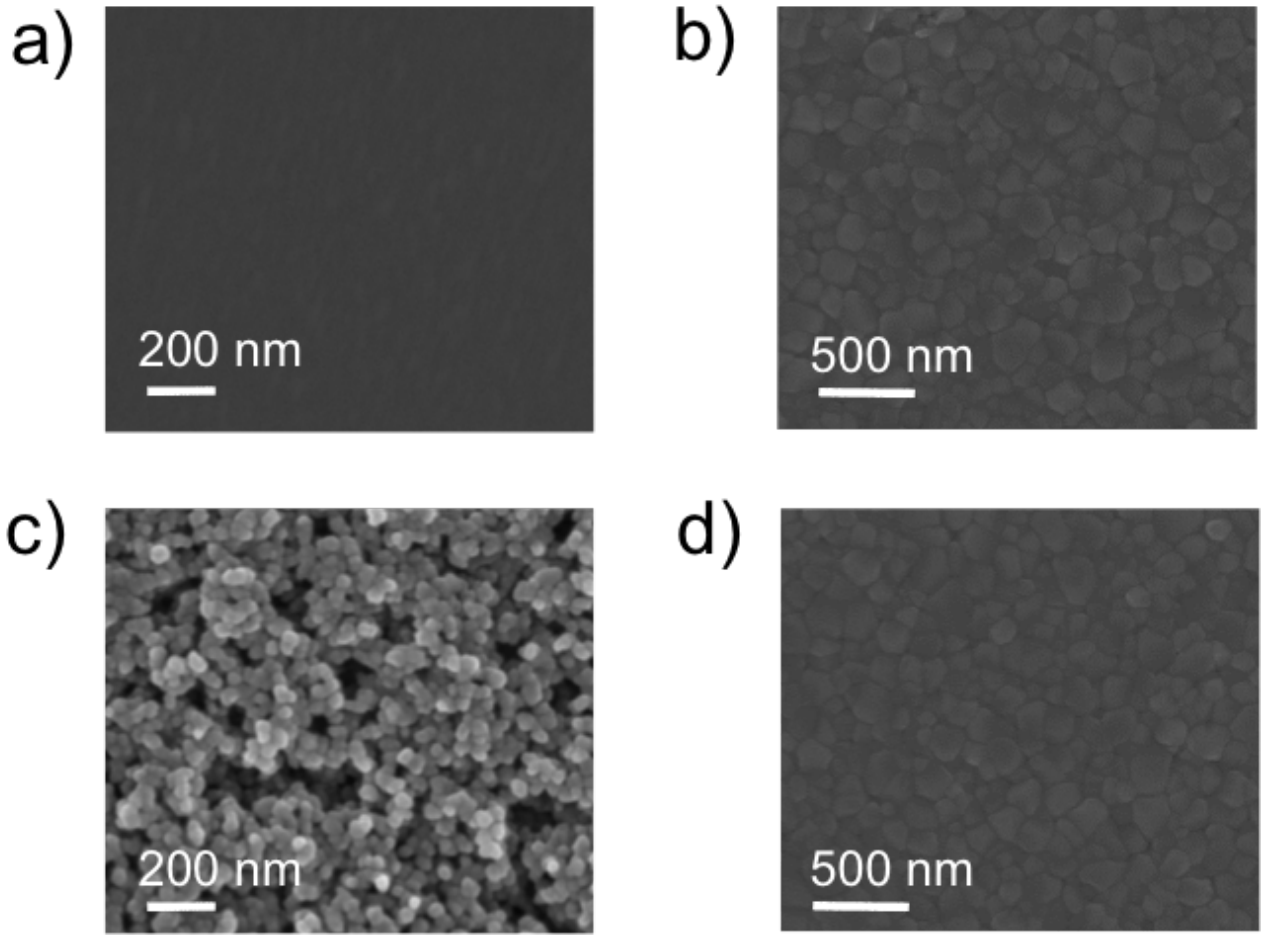


Figure 5.14: Surface SEM images for a) plain glass b) glass/$CH_3NH_3PbI_3$ c) glass/mp-$Al_2O_3$ and d) glass/mp-$Al_2O_3$/$CH_3NH_3PbI_3$

The resulting $CH_3NH_3PbI_3$ films have the same crystallite size, but however have different active surface areas. Consequently, the higher active surface area should generate more unstable films as oxygen will be able to react with more surface $V_I$ sites leading to greater superoxide generation and faster degradation rates. Whilst both substrates are electrically inert no competing electron extraction processes can occur so any differences in stability should be owed to the change in active surface area. To probe this, absorbance measurements are correlated to superoxide generation, time-resolved photoluminescence and PCE losses. These experiments were conducted in the same manner as previously and the results are shown in Figure 5.15a-d respectively.

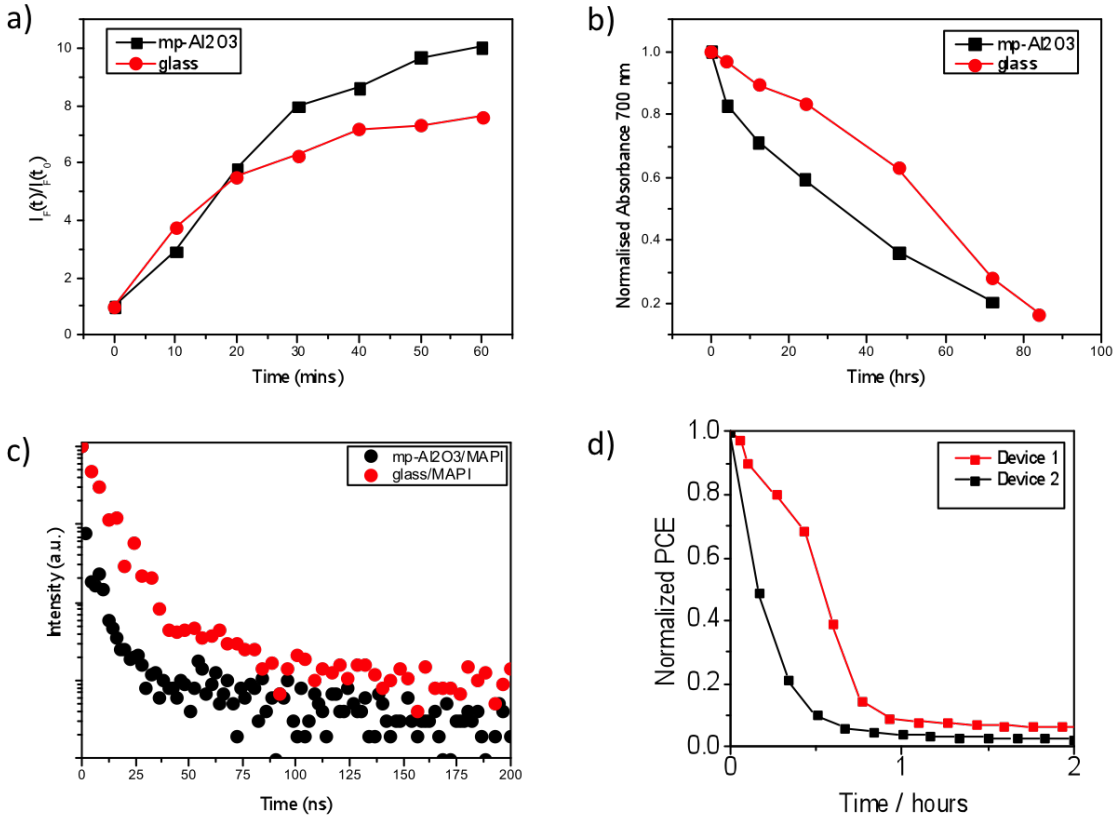


Figure 5.15: a) Superoxide yield plot for glass/$CH_3NH_3PbI_3$ and glass/mp-$Al_2O_3$/$CH_3NH_3PbI_3$. b) Normalised absorbance as a function of time under oxygen and light stress for $CH_3NH_3PbI_3$ films fabricated on glass and mp-$Al_2O_3$. c) Time resolved photoluminescence for glass/$CH_3NH_3PbI_3$ and glass/mp-$Al_2O_3$/$CH_3NH_3PbI_3$ systems and d) Normalised PCE loss for devices of the architectures: [FTO/planar-$TiO_2$/perovskite/spiro-OMeTAD/Au] and [FTO/planar-$TiO_2$/mesoporous-$Al_2O_3$/ perovskite/spiro-OMeTAD/Au]

From Figure 5.15, the data shows that the higher active surface area mp-$Al_2O_3$ substrate does in fact generate more unstable $CH_3NH_3PbI_3$ films. That correlates with a greater yield in superoxide generation from these samples. The increased surface area is therefore allowing for improved reaction kinetics of the iodide vacancy with oxygen in forming the superoxide species. Further evidence for the role of the increased active surface area altering the kinetics and increasing the surface vacancies, is shown in Figure 5.15c. The TRPL data, shows that the emission intensity has faster decay dynamics in the higher active surface area sample. Here, the surface sites are more reactive with oxygen creating faster pathways that result in non-radiative recombination. Additionally this finding supports previous literature, in that the surface sites are more active and impact the performance of $CH_3NH_3PbI_3$ optoelectronics.[45, 46, 40] Moreover, the PCE degradation provides reinforcement for this, where devices of FTO/c-$TiO_2$/

$CH_3NH_3PbI_3$/Spiro-OMeTAD/Au [Device1] and FTO/c-$TiO_2$/mp-$Al_2O_3$/ $CH_3NH_3PbI_3$/Spiro-OMeTAD/Au [Device2] display different degradation rates upon exposure to dry air flux and one sun illumination. These findings confirm that surface sites are key to the initial stage of degradation and surface $V_I$ sites are the most serious cause of optoelectronic performance decay in $CH_3NH_3PbI_3$ systems. However, after this bulk adsorption/reaction sites will contribute significantly to the rate of degradation over long time-scales. Iodide vacancy concentrations in the bulk have been estimated at $10^{22}$ $cm^{-3}$,[20] which suggests that in a typical particle, bulk vacancies will be five orders of magnitude more numerous than surface vacancies. Although it is noted that a wider range of values have also been reported in the literature. Since, the ToF-SIMS data showed that $O_2$ can diffuse into the bulk, the increased degradation rate for smaller crystallites over longer time periods may be due to the shorter $O_2$ diffusion path lengths to the particle interiors. In general, the characteristic time constant, t, for ion diffusion is given by $t = L^2/D$, where L is the diffusion path length and D is the diffusion coefficient. The rate of oxygen permeation into the bulk of $CH_3NH_3PbI_3$ can be expected to drop by a factor of four for every doubling of the particle size. This model can thus account for the observations in the experimental data obtained.

## 5.6 Conclusions

The findings presented suggest that iodide defects (specifically, $V_I$) in the $CH_3NH_3PbI_3$ structure are key sites for superoxide formation. Where, a combination of IGA, photoluminescence, ToF-SIMS and ab initio simulation techniques have provided mechanistic insights into the oxygen- and light-induced degradation of perovskite solar cells. The experiments and calculations have highlighted that fast oxygen diffusion into $CH_3NH_3PbI_3$ films is accompanied by the formation of the superoxide species, which is critical to oxygen-induced degradation. The yield of the superoxide species and thus the degradation rate are dependent on crystallite size when exposed to light and oxygen: perovskite films composed of small crystallites show high yields of photo-induced superoxide formation and therefore low stability. Ab initio simulations indicate that iodide vacancies are the preferred sites in mediating the photo-induced formation of

superoxide species from $O_2$. Further experimental evidence, has shown that the initial fast decay (within hours) in optoelectronic properties is likely due to the higher reactivity of surface iodide vacancies, resulting in a passivating $PbI_2$ layer. whilst the complete degradation (of the order of days) is due to the reaction of oxygen with vacancies in the bulk. Hence, small crystallites with larger surfaces area and short diffusion distances to the bulk, generate more inherently unstable films towards oxygen and light. On the short time scale they degrade faster due to higher surface areas, and the smaller crystallite size means oxygen has a shorter distance to travel before finding a bulk $V_I$ site causing faster degradation over a longer time frame. In contrast larger crystallites have lower surface areas, fewer surface vacancies, and have larger distances for oxygen to diffuse in order to reach bulk vacancies. Consequently, increasing crystallite size generates more stable films.

# References

[1] Y. W. Soon, H. Cho, J. Low, H. Bronstein, I. McCulloch, J. R. Durrant, *Chem. Commun.*, 2013, **49**, 1291–1293.

[2] T. A. Berhe, W.-N. Su, C.-H. Chen, C.-J. Pan, J.-H. Cheng, H.-M. Chen, M.-C. Tsai, L.-Y. Chen, A. A. Dubale, B.-J. Hwang, *Energy Environ. Sci.*, 2016, **9**, 323–356.

[3] A. J. Pearson, G. E. Eperon, P. E. Hopkinson, S. N. Habisreutinger, J. T.-W. Wang, H. J. Snaith, N. C. Greenham, *Advanced Energy Materials*, 2016, **6**, 1600014–n/a.

[4] J. A. Christians, P. A. Miranda Herrera, P. V. Kamat, *Journal of the American Chemical Society*, 2015, **137**, 1530–1538.

[5] L. Zhang, P. H.-L. Sit, *The Journal of Physical Chemistry C*, 2015, **119**, 22370–22378.

[6] D. Bryant, N. Aristidou, S. Pont, I. Sanchez-Molina, T. Chotchunangatchaval, S. Wheeler, J. R. Durrant, S. A. Haque, *Energy Environ. Sci.*, 2016, **9**, 1655–1660.

[7] F. T. O'Mahony, Y. H. Lee, C. Jellett, S. Dmitrov, D. T. Bryant, J. R. Durrant, B. C. O'Regan, M. Graetzel, M. K. Nazeeruddin, S. A. Haque, *J. Mater. Chem. A*, 2015.

[8] N. Aristidou, I. Sanchez-Molina, T. Chotchuangchutchaval, M. Brown, L. Martinez, T. Rath, S. A. Haque, *Angewandte Chemie International Edition*, 2015, **54**, 8208–8212.

[9] J. M. Ball, M. M. Lee, A. Hey, H. J. Snaith, *Energy Environ. Sci.*, 2013, **6**, 1739–1743.

[10] M. D. Bastiani, V. DInnocenzo, S. D. Stranks, H. J. Snaith, A. Petrozza, *APL Materials*, 2014, **2**, 081509.

[11] G. Grancini, S. Marras, M. Prato, C. Giannini, C. Quarti, F. De Angelis, M. De Bastiani, G. E. Eperon, H. J. Snaith, L. Manna, A. Petrozza, *The Journal of Physical Chemistry Letters*, 2014, **5**, 3836–3842.

[12] W. Nie, H. Tsai, R. Asadpour, J.-C. Blancon, A. J. Neukirch, G. Gupta, J. J. Crochet, M. Chhowalla, S. Tretiak, M. A. Alam, H.-L. Wang, A. D. Mohite, *Science*, 2015, **347**, 522–525.

[13] D. W. de Quilettes, S. M. Vorpahl, S. D. Stranks, H. Nagaoka, G. E. Eperon, M. E. Ziffer, H. J. Snaith, D. S. Ginger, *Science*, 2015, **348**, 683–686.

[14] S. Kandada, A. Ram, A. Petrozza, *Accounts of Chemical Research*, 2016, **49**, 536–544.

[15] A. Sharenko, M. F. Toney, *Journal of the American Chemical Society*, 2016, **138**, 463–470.

[16] W. Zhang, S. Pathak, N. Sakai, T. Stergiopoulos, P. K. Nayak, N. K. Noel, A. A. Haghighirad, V. M. Burlakov, D. W. deQuilettes, A. Sadhanala, W. Li, L. Wang, D. S. Ginger, R. H. Friend, H. J. Snaith, *Nat. Commun.*, 2016, **6**, 10030.

[17] T. Salim, S. Sun, Y. Abe, A. Krishna, A. C. Grimsdale, Y. M. Lam, *J. Mater. Chem. A*, 2015, **3**, 8943–8969.

[18] J.-H. Im, I.-H. Jang, N. Pellet, M. Grtzel, N.-G. Park, *Nat. Nanotech.*, 2014, **9**, 927–931.

[19] L. X., M. I. Dar, C. Yi, J. Luo, M. Tschumi, S. M. Zakeeruddin, M. K. Nazeeruddin, H. Han, M. Grtzel, *Nat. Chem.*, 2015, **7**, 703–711.

[20] A. Walsh, D. O. Scanlon, S. Chen, X. G. Gong, S.-H. Wei, *Angew. Chem. Int. Ed.*, 2015, **54**, 17911794.

[21] A. Walsh, D. O. Scanlon, S. Chen, Gong, X. G., S. H. Wei, *Angew. Chem. Int. Ed.*, 2015, **54**, 17911794.

[22] C. Eames, J. M. Frost, P. R. F. Barnes, B. C. ORegan, A. Walsh, M. S. Islam, *Nat. Commun.*, 2015, **6**, 7497–7506.

[23] A. Buin, P. Pietsch, J. Xu, O. Voznyy, A. H. Ip, R. Comin, E. H. Sargent, *Nano Letters*, 2014, **14**, 6281–6286.

[24] J. Xu, A. Buin, A. Ip, W. Li, O. Voznyy, R. Comin, M. Yuan, S. Jeon, Z. Ning, J. McDowell, P. Kanjanaboos, J.-P. Sun, X. Lan, L. N. Quan, D. H. Kim, I. G. Hill, P. M. . E. H. Sargent, *Nat. Commun.*, 2015, **6**, 7081–7089.

[25] A. Buin, R. Comin, J. Xu, A. H. Ip, E. H. Sargent, *Chemistry of Materials*, 2015, **27**, 4405–4412.

[26] S. D. Stranks, P. K. Nayak, W. Zhang, T. Stergiopoulos, H. J. Snaith, *Angewandte Chemie International Edition*, 2015, **54**, 3240–3248.

[27] C. Freysoldt, B. Grabowski, T. Hickel, Neugebauer, G. Kresse, A. Janotti, C. G. Van de Walle, *Rev. Mod. Phys.*, 2014, **86**, 253–305.

[28] J. M. Azpiroz, E. Mosconi, J. Bisquert, F. De Angelis, *Energy Environ. Sci.*, 2015, **8**, 2118–2127.

[29] H. Yuan, E. Debroye, K. Janssen, H. Naiki, C. Steuwe, G. Lu, M. Moris, E. Orgiu, H. Uji-i, F. De Schryver, P. Samor, J. Hofkens, M. Roeffaers, *J. Phys. Chem. Lett.*, 2016, **7**, 561–566.

[30] S. Colella, E. Mosconi, P. Fedeli, A. Listorti, F. Gazza, F. Orlandi, P. Ferro, T. Besagni, A. Rizzo, G. Calestani, G. Gigli, F. De Angelis, R. Mosca, *Chemistry of Materials*, 2013, **25**, 4613–4618.

[31] F. K. Aldibaja, L. Badia, E. Mas-Marza, R. S. Sanchez, E. M. Barea, I. Mora-Sero, *J. Mater. Chem. A*, 2015, **3**, 9194–9200.

[32] H. Hintz, H.-J. Egelhaaf, L. Ler, J. Hauch, H. Peisert, T. Chass, *Chemistry of Materials*, 2011, **23**, 145–154.

[33] L. Ler, H.-J. Egelhaaf, D. Oelkrug, G. Cerullo, G. Lanzani, B.-H. Huisman, D. de Leeuw, *Organic Electronics*, 2004, **5**, 83–89.

[34] M. Jrgensen, K. Norrman, S. A. Gevorgyan, T. Tromholt, B. Andreasen, F. C. Krebs, *Advanced Materials*, 2011, **24**, 580–612.

[35] S. Beaupre, M. Leclerc, *J. Mater. Chem. A*, 2013, **1**, 11097–11105.

[36] R. K. Misra, S. Aharon, B. Li, D. Mogilyansky, I. Visoly-Fisher, L. Etgar, E. A. Katz, *J. Phys. Chem. Lett.*, 2015, **6**, 326–330.

[37] H. J. Queisser, E. E. Haller, *Science*, 1998, **281**, 945–950.

[38] J. Kim, S.-H. Lee, J. H. Lee, K.-H. Hong, *The Journal of Physical Chemistry Letters*, 2014, **5**, 1312–1317.

[39] W.-J. Yin, T. Shi, Y. Yan, *Applied Physics Letters*, 2014, **104**, 063903.

[40] J. M. Ball, A. Petrozza, *Nature Energy*, 2016, **1**, 16149.

[41] M. Z. Mokhtar, M. Chen, E. Whittaker, B. Hamilton, N. Aristidou, S. Ramadan, A. Gholinia, S. A. Haque, P. O'Brien, B. R. Saunders, *Phys. Chem. Chem. Phys.*, 2017, **19**, 7204–7214.

[42] W. Hayes, A. M. Stoneham, *Defect and Defect Processes in Nonmetallic Solids*, Wiley, 1985.

[43] J. Schoonman, *Chem. Phys. Lett.*, 2015, **619**, 193–195.

[44] A. Calloni, A. Abate, G. Bussetti, G. Berti, R. Yivlialin, F. Ciccacci, L. Du, *J. Phys. Chem. C.*, 2015, **119**, 21329–21335.

[45] S. Y. Leblebici, L. Leppert, Y. Li, E. Reyes-Lillo, Sebastian, S. Wickenburg, E. Wong, J. Lee, M. Melli, D. Ziegler, K. Angell, Daniel, D. F. Ogletree, D. Ashby, Paul, M. Toma, Francesca, B. Neaton, Jeffrey, D. Sharp, Ian, A. Weber-Bargioni, *Nat. Energy*, 2016, **1**, 16093.

[46] J. Haruyama, K. Sodeyama, L. Han, Y. Tateyama, *J. Phys. Chem. Lett.*, 2014, **5**, 2903–2909.

# Chapter 6

# Iodide vacancy passivation and radical quenching

## 6.1 Introduction

The previous findings in combination with other initial observations in the literature have started to highlight the key role defects play in the properties observed in perovskite solar cells, especially with explaining parameters related to performance.[1, 2, 3, 4, 5, 6, 7, 8, 9, 10, 11] It has become clear that the role of vacancies is of critical importance and the effect they may have on stability has begun to be explored. The first insights into defect mediated degradation were reported by Hoke et. al.[2] within mixed halide perovskites and were shown to mediate degradation to light exposure. Where upon white light illumination, emissive sub-bandgap states are formed and that photo-excitation is hypothesized to result in photo-induced segregation generating iodine rich and bromine rich phases. What is important to note is that when the optical properties of several films were studied it was shown that crystals with fewer defects and thus higher photoluminescence were less susceptible to photo-degradation. It may be suggested that due to the mobility of vacancies that this phase segregation can occur and result in the observed photo-induced degradation. It is thus of importance to improve crystal quality not only for optoelectronic performance but also for long-term material stability.

Beyond this initial study, the role of vacancies has emerged as one of the fundamental flaws in perovskite crystal stability. It has been shown that sensitivity of $MAPbI_3$ towards oxygen and light is due to a photo-degradation process mediated by the electron transfer of a photo-excited electron to molecular oxygen generating superoxide. Where, this reactive oxygen species initiates the breakdown of the crystal by an acid-base reaction with the methylammonium cation component.[12, 13] This work has been complemented by the previous studies reported herein, that has provided the identification that crystal structure/morphology impacts the susceptibility to degradation upon exposure to both oxygen and light. The evidence showed that stability could be enhanced in larger crystals with more uniform grain boundaries and with lower defect density. Here, larger crystals showed slower rates of degradation compared to thin-films composed of smaller and higher defect density crystallites. These observations led to the exploration of the role that point defects play in the degradation via a combination of experimental techniques and computational calculations. The obtained results showed that oxygen diffusion into perovskite crystals is rapid and ubiquitous and the formation of the superoxide species is proportional to defect density. This also showed the relation of defect density determining the sensitivity of perovskite towards oxygen and light. Critically, it was shown that the superoxide species is preferentially formed within the $V_I$ defect (-1.94 eV) and the resulting superoxide radical ion is of the correct size to satisfy the vacancy and restore the full octahedral co-ordination of $Pb^{2+}$ before going on to react with the methylammonium cation.[12, 13, 14] The evidence provided by these findings highlights that photo-oxidation degradation is mediated most importantly by the presence of Iodine vacancies. It has also been shown for $CH_3NH_3PbI_3$ that the most prominent type of point defect on the surface are vacancies, especially Iodine.[15] Combining these two findings demonstrates that controlling Iodide vacancy is critical to obtaining more intrinsically stable perovskite films towards oxygen and light. Here, a general approaches to reducing iodide vacancies are presented, leading to enhanced stability of perovskite films. In addition to this a method to prevent the degradation mechanism through radical scavenging is proposed and provides another route to enhance film stability.

## 6.2 Film passivation using salt additives

The previous data reported in Chapter 5 raises a key question that relates to whether the stability of $CH_3NH_3PbI_3$ films can be improved by inhibiting superoxide formation at iodide vacancies, for example, by defect passivation. To investigate this, a new experimental method was developed were a solution of either a chloride or iodide salt was used in a post treatment to $CH_3NH_3PbI_3$ fabricated on glass substrates. The salts were dissolved in a 1:4 solvent mixture of isopropanol to chlorobenzene and spin coated onto the perovskite films after a 20s loading time. Allowing the salt solution to permeate through the entire film. After this the films were spin dried and annealed at 100°C for 10 minuets. The procedure is depicted in Figure 6.1 below.

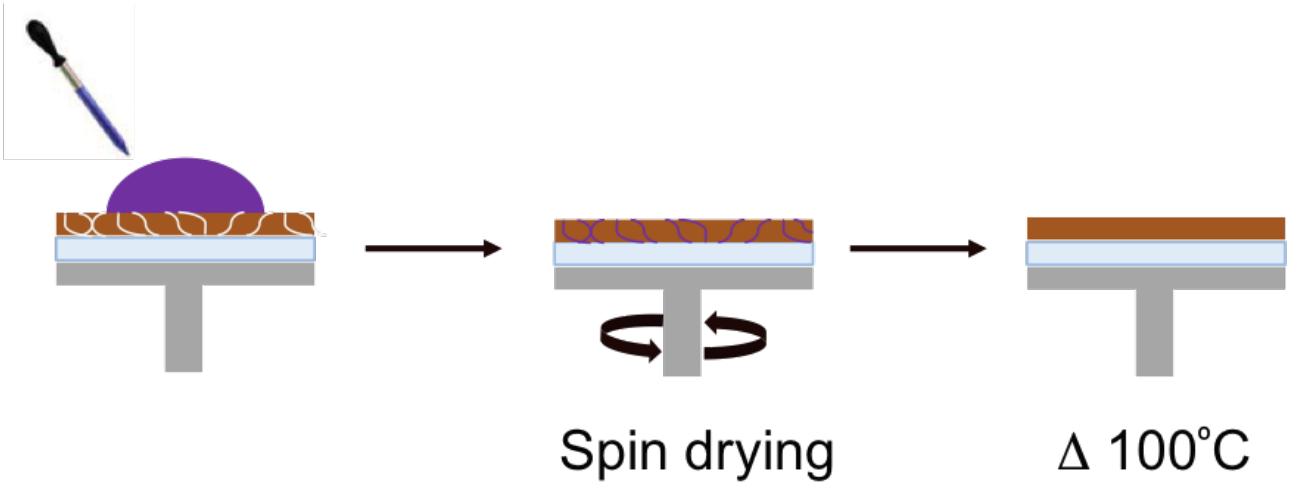


Figure 6.1: Diagrammatic representation of the experimental procedure to treat perovskite films with salt coatings.

The counter cations chosen were: phenylethylammoniun (PEA), methylammonium (MA) and trimethlsulfonium (S). Ionic passivating agents carrying bulky cations were chosen to ensure that substitution with methylammonium cations in the perovskite was unfavourable. The successful preparation of the films was confirmed by XRD analysis presented in the following Figure 6.2. Where the collected spectrums for the iodide based solutions show no change in crystal structure after treatment with the salt solutions. The key diffraction peaks at 14.2°, 28.5° and 43.3° correspond to the (110), (220) and (330) lattice orientations of orthorhombic halide perovskite respectively. This demonstrates that the passivated films exhibit a pure crystal structure akin to that for the pristine perovskite, which crystallizes in the expected orthorhombic

Pan21 space group.[16] Furthermore, the peak intensity of the perovskite films passivated with iodide salts did not change in comparison to the un-passivated perovskite film, implying that the salt passivation does not damage or structurally alter the film.

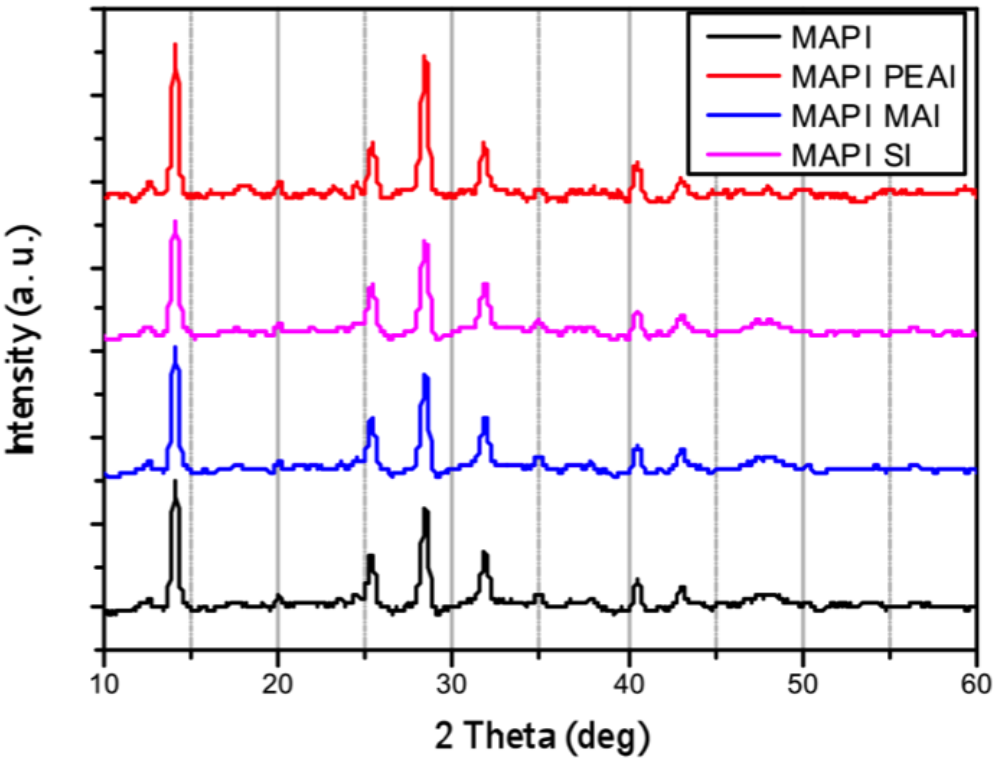


Figure 6.2: XRD spectra for perovskite films with no salt treatment and with treatments of 0.01M MAI, PEAI and SI.

In a similar approach to the studies before, the stabilities of the coated films were then examined after exposure to light and oxygen through the use of UV/VIS absorbance measurements and superoxide yield tests. Both the chloride and iodide salts of all cations were examined and the impact on stability was correlated through the ability of the film to retain its optical properties as a function of superoxide generation. As can be seen in Figure 6.3a, all the iodide salt- coated samples display an enhanced tolerance to light and oxygen (relative to the uncoated control sample), showing little or no degradation over the ageing time period. In contrast, the chloride salt derivatives showed no stability enhancement, exhibiting a comparable rate of degradation as that of an uncoated perovskite sample. It is noted that the iodide treated films

showed no sign of any degradation over 3 weeks of ageing under light and oxygen. Furthermore, the enhanced stability of the coated samples is consistent with the superoxide generation data shown in Figure 6.3b. In particular, it can be seen that all the iodide salt coated samples show a significantly lower yield of the superoxide species than the uncoated sample and the chloride salt-treated samples.

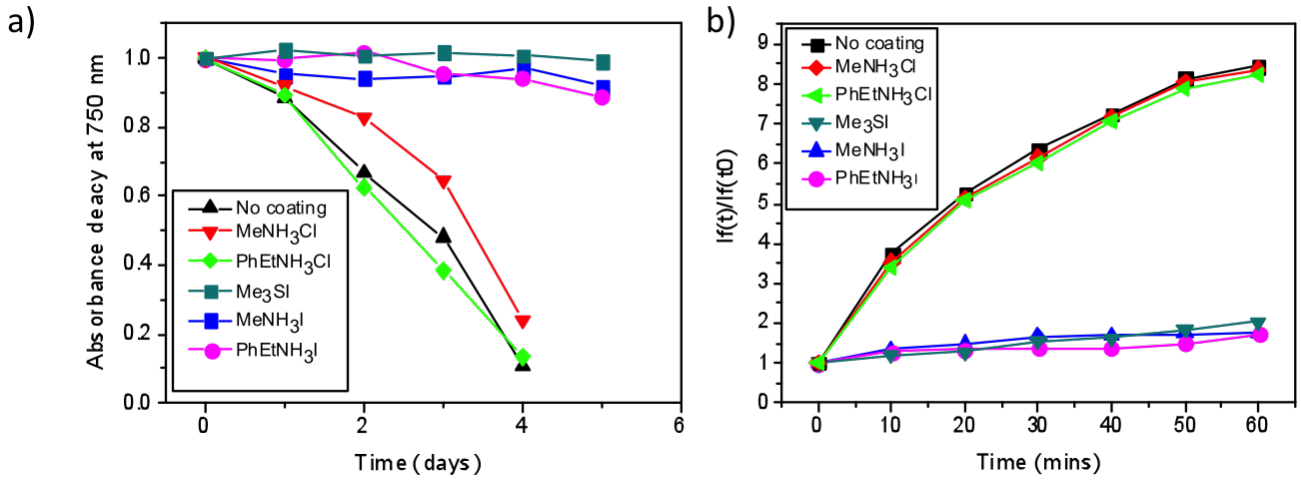


Figure 6.3: a) Normalized absorbance decay at 750 nm under illumination (25 mWcm$^{-2}$) and dry air flow for a pristine $CH_3NH_3PbI_3$ and $CH_3NH_3PbI_3$ coated with phenylethylammonium iodide ($PhEtNH_3I$), methylammonium iodide ($MeNH_3I$), trimethylsulfonium iodide ($Me_3SI$), phenylethylammonium chloride ($PhEtNH_3Cl$) and methylammonium chloride ($MeNH_3Cl$) as described in the experimental section. b) Superoxide yield plot comparing the generation of superoxide for $CH_3NH_3PbI_3$ treated with the coatings and without.

These findings suggest that the key component in the salt solutions, is the iodide anion. Where the relative change in stability enhancement is minimal when the cation is changed, implying that the cation bears little to no impact on the stability. Likewise, the chloride anion does not affect stability and leads to treated $CH_3NH_3PbI_3$ films degrading in the same time period as the uncoated sample. However, to confirm that the iodide salt treatments are indeed passivating iodide defects rather than some other effect, for example acting as an oxygen blocking layer, time-resolved photoluminescence, IGA, SEM and superoxide yield measurements are harnessed to reveal the operating mechanism of the stability enhancement. Since, no stability enhancement was observed in the chloride salt derivatives, these solutions were removed from the investigation. Furthermore, transient absorption data collected for all the iodide salt coated treatments, Figure 6.4, demonstrates that the normalised decay in charge separation yield is

prevented by the salt coatings where in the time frame explored no relative change in the yield is observed. In contrast and in agreement with previous literature the uncoated sample suffers severe charge losses upon exposure to oxygen and light in the course of minutes. From here onwards, only the methylammonium cation derivative is explored. As from the previous data the cation has no impact on the stability, the superoxide yield or the charge separation decay dynamics. In a sensible approach if the technique is to be employed in real-world operating systems, additionally MAI, in the fabrication process would have the smallest impact on the cost of production as it is already a necessary component in the crystal structure. However, any of the other cations could have been used.

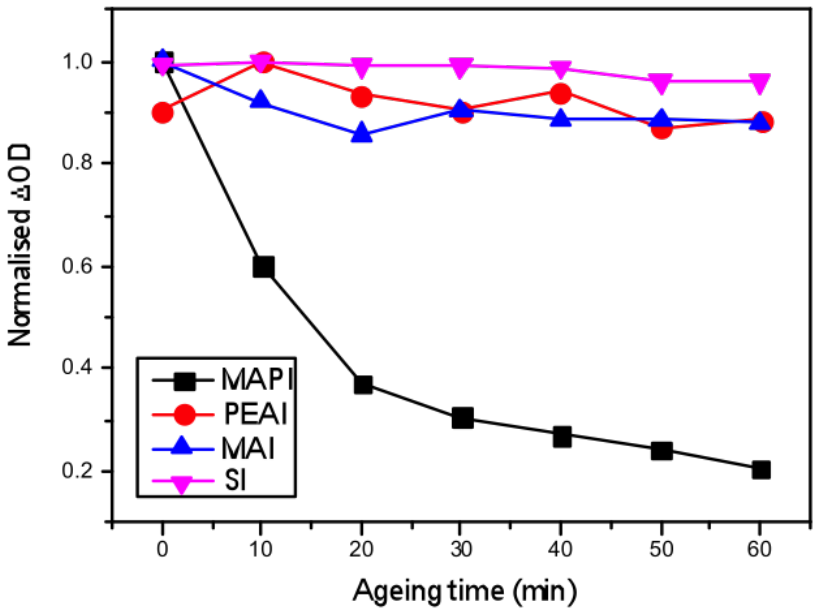


Figure 6.4: Normalised TAS decay taken at 1$\mu$s as a function of exposure time to oxygen and light stress for a pristine $CH_3NH_3PbI_3$ and $CH_3NH_3PbI_3$ coated with phenylethylammonium iodide ($PhEtNH_3I$), methylammonium iodide ($MeNH_3I$) and trimethylsulfonium iodide ($Me_3SI$)

IGA data was collected for three samples, an uncoated $CH_3NH_3PbI_3$ film, a MAI coated film and a control film that was encapsulated in a glass blocking layer. Blocking layers are currently employed to prevent oxygen entering solar cells and should in theory result in no weight increase in the $CH_3NH_3PbI_3$ film that is encapsulated. Figure 6.5 indicates similar fast oxygen diffusion kinetics in both $CH_3NH_3I$ treated and untreated films. In contrast, the control sample comprising a $CH_3NH_3PbI_3$ film encapsulated in glass does in fact show little or no weight

increase upon exposure to oxygen; in this instance the glass layer does function as an oxygen blocking layer.

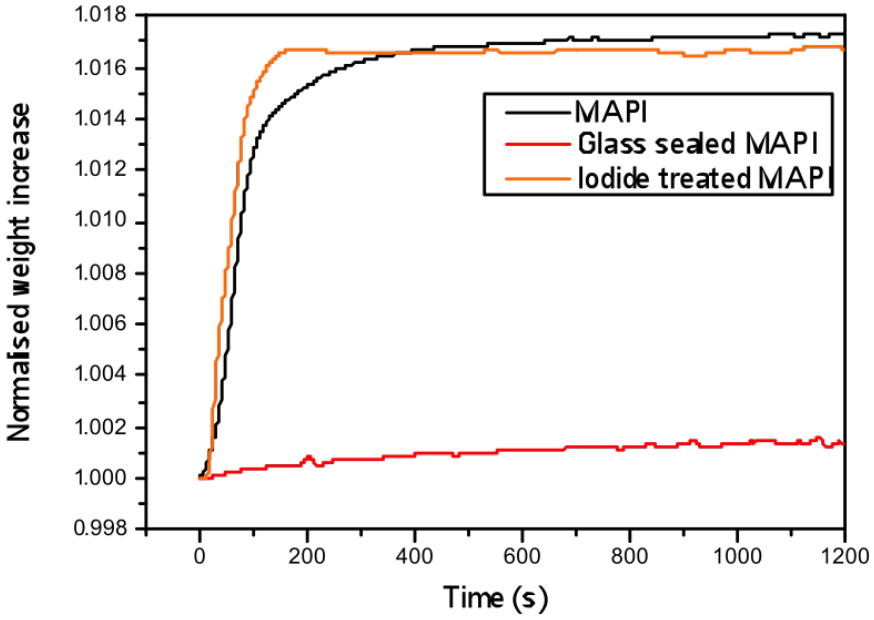


Figure 6.5: IGA results for MAI coated and uncoated $MAPbI_3$ films. Also shown is the IGA data for a $MAPbI_3$ film encapsulated in glass.

Further to this, SEM images and ToF-SIMS for the both a $CH_3NH_3PbI_3$ film with and without the MAI coating were collected. These experiments reinforce the previous two statements. First through the SEM images, Figure 6.6, it can be seen that the crystal size and morphology does not change as a result of the salt coating. This is important as it eliminates any potential stability enhancement being owed in part to the a changing morphology, which has been shown to influence stability. Secondly, the ToF-Sims data, Figure 6.6, for the samples, again shows that after 30 mins of exposure to dry air flux that both the systems are saturated with oxygen and that it is ubiquitously present throughout the sample. The ToF-Sims, shown represents slices half-way through the films. Once more this shows that the salt treatment is not blocking oxygen and any stability enhancement observed by the salt treated $CH_3NH_3PbI_3$ film is not as a result of less oxygen reacting with photo-excited electrons. Consequently, the salt treatment must be enhancing stability through changing the iodide vacancy mediated generation of superoxide, since the yield of superoxide is reduced when the coatings are applied and that the iodide

component is most critical in achieving this.

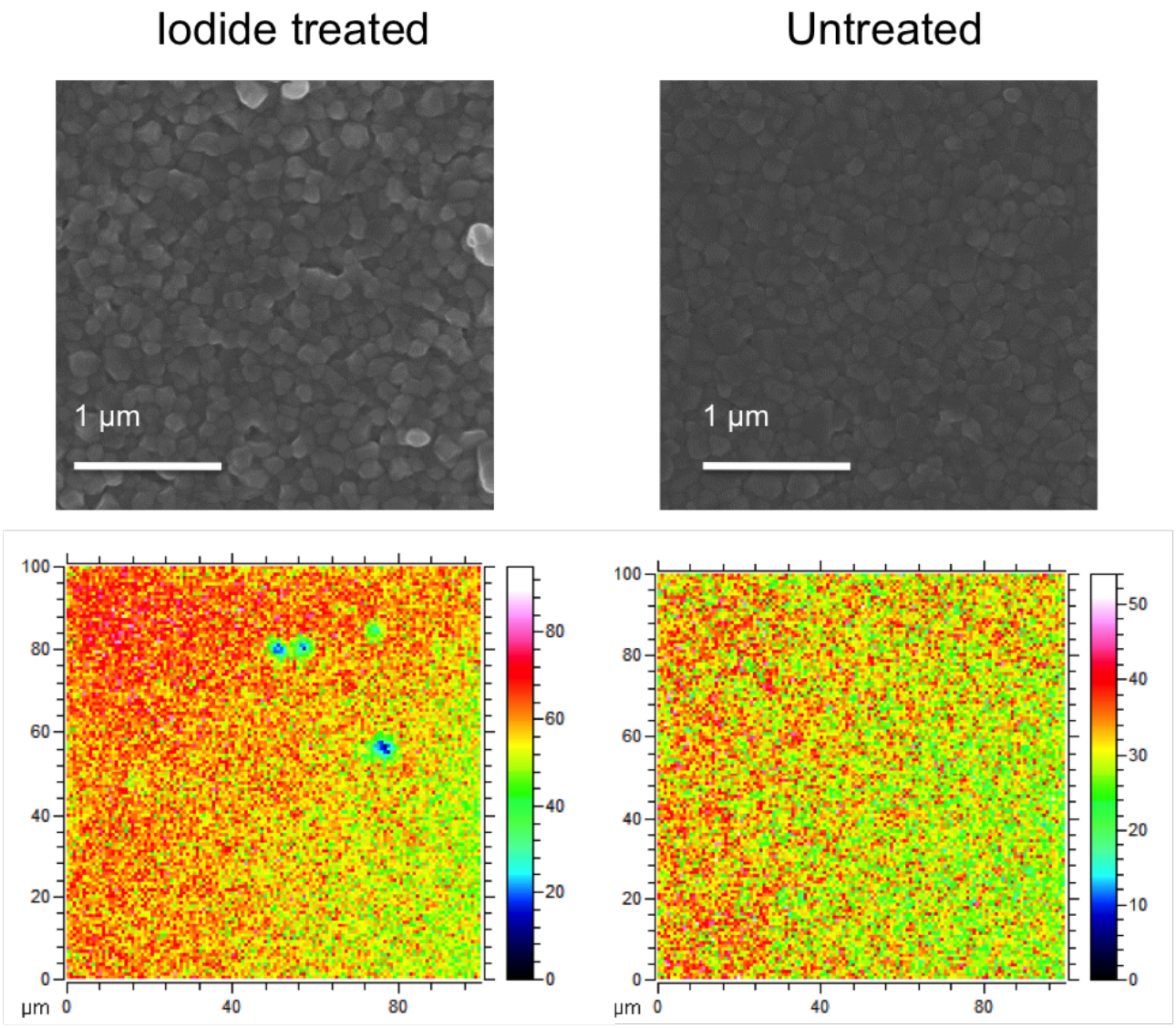


Figure 6.6: Scanning electron microscopy studies and TOF-SIMS imaging of oxygen ions for MAI coated (left column) and uncoated (right column) $MAPbI_3$ films.

Since the MAI salt treatment does not alter the oxygen content within $CH_3NH_3PbI_3$ films, stability enhancement may be occuring through the iodide anion passivating iodide vacancies. The data so far suggests this may be the situation, however to reinforce this a concentration study was implemented. Here, the concentration of the salt coating should be proportional to the stability if it is serving as a $V_I$ passivating agent. As the number of defects filled (removed) should be proportional to the amount of iodide anion added. First, Time-resolved photoluminescence measurements were performed on perovskite films treated with different concentrations (0.001 M, 0.005 M and 0.01 M) of $CH_3NH_3I$. As can be seen from the data,

Figure 6.7a, increasing the iodide salt concentration leads to an increased photoluminescence lifetime. Moreover, this observation is consistent with the iodide salt treatment reducing the number of defects and therefore the number of trap states for non-radiative recombination, resulting in longer emission lifetimes. Recent studies[17, 18] have found that alkali metal halide salts introduced at the perovskite interface can decrease halide vacancy levels, resulting in improved device performance. Next, the relative stability and charge separation yield decay of $CH_3NH_3PbI_3$ films treated with different concentrations of $CH_3NH_3I$ were investigated. Figure 6.7b, shows that the rate of decay upon exposure to oxygen and light is concentration dependent and the sensitivity of charge separation is impacted by vacancy filling. This highlights that increasing the iodide anion concentration alleviates more $V_I$ defects and leads to more stable films. Since, the charge separation yield becomes more stable as the MAI concentration increases, this may be owed to two factors. Firstly, since the time-resolved data, Figure 6.7a, suggests that number of defects has decreased the number of trap sites is reduced so there are fewer sites for charge recombination losses. Secondly, the yield of superoxide my be impacted and thus less crystal is degraded and so the optoelectronic properties can be retained as no $PbI_2$ blocking layer is formed. To test this the superoxide yield as a function of the concentration of the MAI coating is explored.

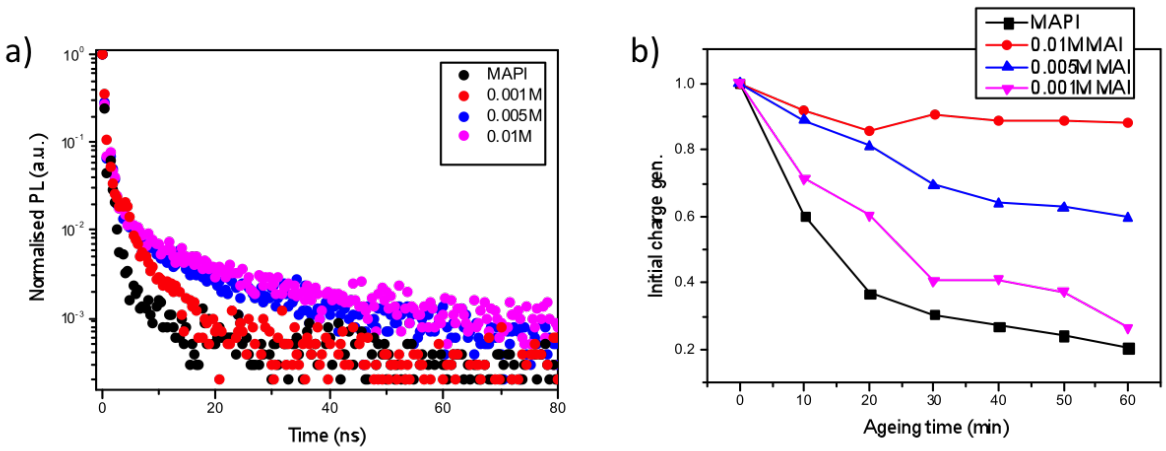


Figure 6.7: a) Time resolved photoluminescence data as a function of concentration of MAI coating solution. Also shown are emission kinetics for an uncoated control sample (black decay). b) Normalised TAS decay at 1$\mu$s as a function of aging time for a pristine $CH_3NH_3PbI_3$ film and films treated with MAI of concentrations: 0.01M, 0.005M and 0.001M.

The relationship between $CH_3NH_3I$ concentration, stability and superoxide yield is explored

again through UV/VIS and superoxide generation experiments. The normalised absorbance at 750nm and the superoxide yields for the samples are presented in Figure 6.8a and b, respectively. The data lays out that increasing the concentration of $CH_3NH_3I$ salt does lead to lower yields of superoxide generation and consequently better stability. Noted by the fact that increasing the MAI concentration leads to greater retention in absorbance at 750nm. In combination with the IGA and the SEM images taken of the treated and an untreated $CH_3NH_3PbI_3$ film (Figure 6.5 and 6.6 respectively) that showed the treatment does not induce any significant morphological changes to the films surface infers that salt treatments passivate the crystal defects. Rather than providing a physical barrier layer to oxygen diffusion. Passivation of crystal defects using iodide salts reduces superoxide yields and enhances film stabilities, and in addition leads to retention of not only the absorbance properties but also charge separation yields. These are critical to device performance, as greater yields of charge separation will generate better performing devices when exposed to oxygen and light.

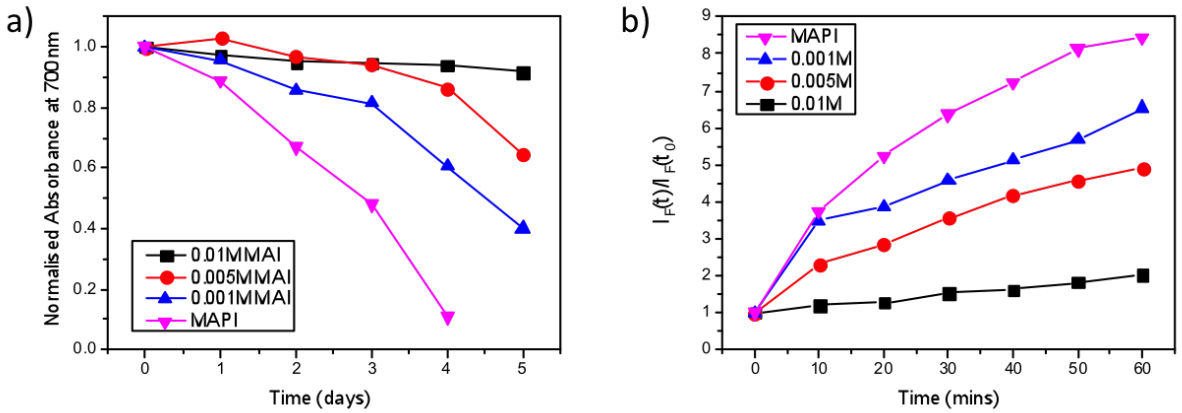


Figure 6.8: a) Normalised absorbance degradation plot indicating that increasing the concentration of MAI salt treatment leads to an enhanced stability (longer retention of absorption at 700 nm). b) Superoxide generation plot as a function of MAI concentration. Indicates that increasing superoxide is observed for reduced salt concentrations.

To confirm the potential impact of enhancing device stability, solar cells were fabricated and the PCE monitored as a function of time under different dry air flux and one sun illumination. A range of MAI salt concentrations from 1mM to 10mM, were employed before the next layers were fabricated in the architecture. The results, shown in Figure 6.9 indicate solar cells that use $CH_3NH_3I$-coated $CH_3NH_3PbI_3$ films exhibit better stability than those that use uncoated

perovskite layers. More specifically, exposure of devices using uncoated perovskite layers to light and dry air for just 2.5 h leads to nearly a 50% drop in the PCE (11.4% to 5.9%). In contrast, the device containing 10mM $CH_3NH_3I$ coated layer exhibits a significantly smaller 10% drop in efficiency (9.1% to 8.19%) over the same ageing period. Once more the concentration dependence of the salt coating impacting stability, superoxide yield and charge separation yield is observed and manifests itself in an increasing PCE stability. It is clear from these results that increasing the concentration of $CH_3NH_3I$ salt leads to progressively higher stability and tolerance towards oxygen and light conditions. These results further confirm that the iodide anion from the salt passivates the iodide vacancies in the crystal, and by occupying the otherwise vacant iodide sites leads to increased stability by suppressing superoxide formation. It is noted that degradation of the coated devices is not halted completely, which suggests that other factors also influence overall device stability. For example, it is possible that iodide vacancies in the bulk are not filled by iodide ions from the coating and these can still act as sites for superoxide generation. It is also possible that even if all sites are occupied some superoxide can still be generated from the pristine perovskite surface, this is possible since the superoxide formation energy is favourable albeit small relative to the energy of formation from the $V_I$ defect site. Nevertheless, it is clear from the present findings that the iodide salt coatings lead to significant improvements in device stability.

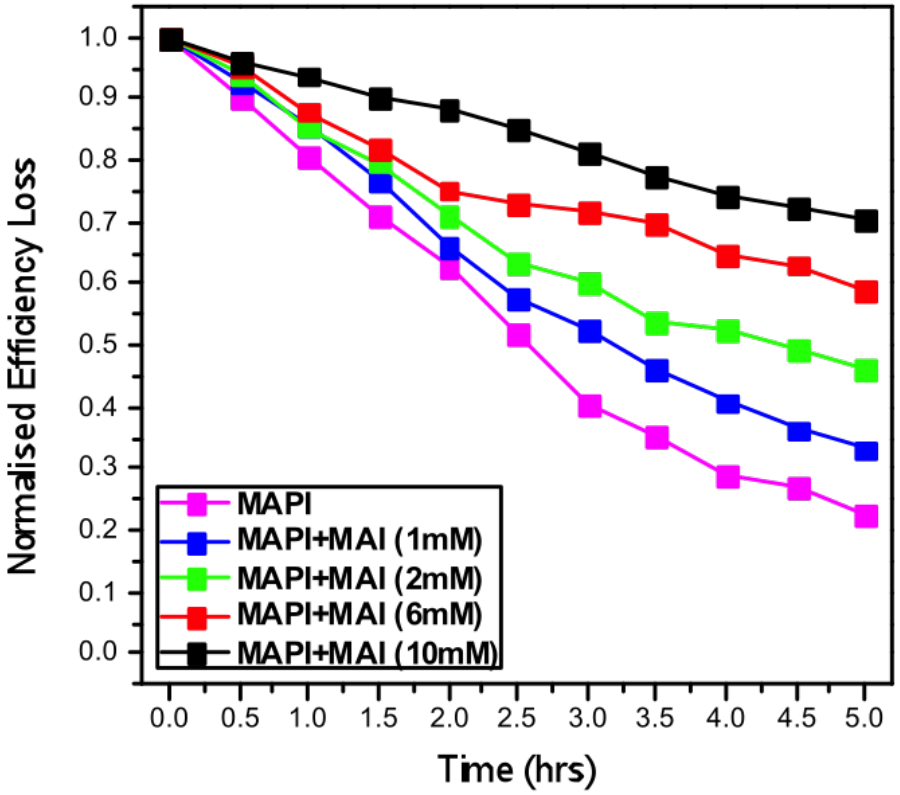


Figure 6.9: Normalised PCE loss as a function of ageing time under 1 sun illumination with dry air flux, for MAPI films with no coating, 1mM, 2mM, 6mM and 10mM of methylammonium iodide salt coating. Raw device data was obtained in collaboration with Xiangnan Bu.

## 6.3 Impact of Iodide reagent concentration

The previous results have shown that iodide defects in the $CH_3NH_3PbI_3$ structure are key sites for superoxide formation. In addition, the results demonstrate that an iodide salt treatment can be employed to reduce the number of problematic iodide vacancies ($V_I$), thereby hindering the electron transfer reaction that generates the superoxide species. However, recent literature has shown that in the preparation of $CH_3NH_3PbI_3$ films an excess of either one of the starting reagents, MAI or $PbI_2$, can generate perovskite systems with enhanced optoelectronic properties.[19, 20, 21, 22, 23] It has been demonstrated that $CH_3NH_3PbI_3$ films generated with an excess of MAI can lead to reduced non-radiative recombination and enhanced device efficiency.[11, 24, 25, 26] However, it must be noted that too much excess MAI can hinder performance.[19] It is suspected that in a similar approach to using a iodide salt post treat-

ment, using an excess of the starting reagents reduces the quantity of halide vacancies in the $CH_3NH_3PbI_3$ structure. Since, in the fabrication there ultimately will always be an excess of iodide present that can be used to fill in any vacancies that form. When too much reagent is in excess the remaining material will provide no benefit and may generate trap sites and electronically inert layers that will hamper optoelectronic properties.

To investigate the potential impact of excess reagents on the stability and vacancy concentration in $CH_3NH_3PbI_3$ films, three perovskite samples were generated using different molar ratios of the starting materials. The samples were fabricated onto clean glass. Here, an equimolar ratio of MAI:$PbI_2$ (1:1) is donated as sample 1, whilst the ratios of 0.9:1 and 1:0.9 of the starting reagents are labeled as sample 2 and sample 3, respectively. To ensure the crystal size was the same, all deposition parameters were kept identical for all samples. This then eliminates any stability enhancement owed to changing crystal morphology, surface area and thus defect concentration as a result of those parameters. SEM, Figure 6.10, was employed to confirm that the crystal size, uniformity and distribution was approximately equal between all three samples.

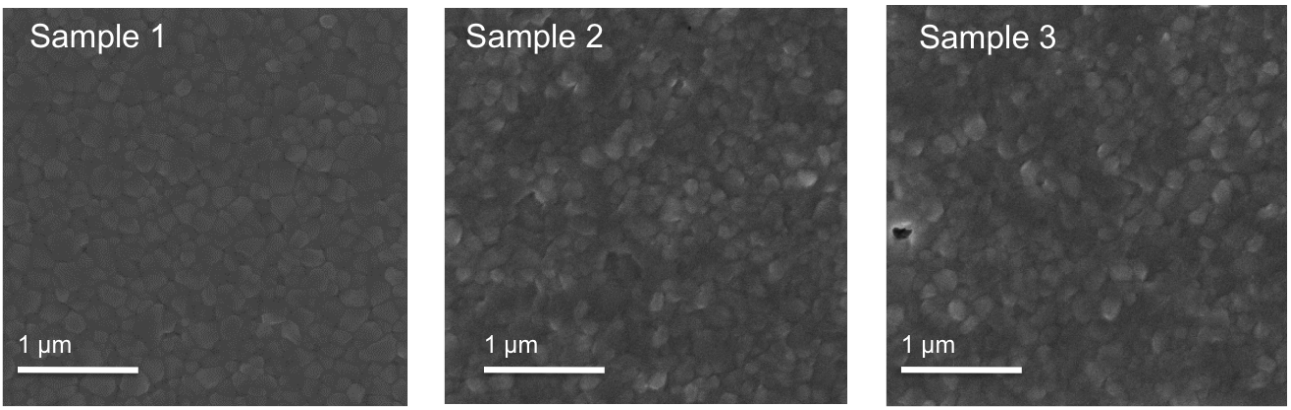


Figure 6.10: Scanning electron microscopy studies for $CH_3NH_3PbI_3$ films created from different reagent ratios, MAI:$PbI_2$. Sample 1 (equimolar, (1:1)), Sample 2 (0.9:1) and sample 3 (1:0.9)

Figure 6.10, illustrates that all three samples have similar crystal size, uniformity and distribution. Additionally, it shows that at these ratios no other layers are forming as a result of the excess reagents. This allows for any morphological impacts to be dismissed and any change in stability between samples should be owed to the presence of excess iodide. Next, to confirm that there is a difference in stability between samples, UV/VIS spectroscopy was employed to

monitor the degradation. The normalised absorbance magnitude at 700 nm is plotted against ageing time under dry air flux and ambient illumination. The results are shown in Figure 6.11.

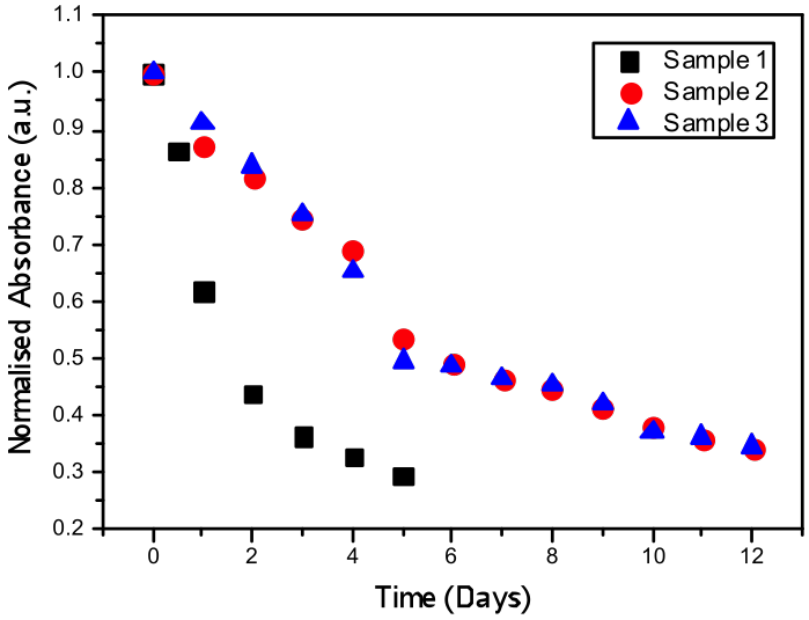


Figure 6.11: Normalised absorbance as a function of aging time for the three samples with varying reagent ratios compositions.

The normalised absorbance data, Figure 6.11, shows that upon exposure to oxygen and light conditions there exists a difference in stability between the samples. Critically, in both samples (2 and 3) where an excess of reagent is used, enhanced material life-time relative to the system composed of equimolar ratios (sample 1) is observed. This implies that inducing an excess of iodide ions in the synthesis protocol can induce stability enhancements. Where either biasing with MAI or $PbI_2$ leads to the total time taken to completely degrade to approximately double. Having confirmed no effect from a change in crystal morphology, this supports the hypothesis that the introduction of excess iodide in the synthesis can, like the salt solution post treatment, decrease the quantity of the problematic iodide vacancies. In this scenario, the excess iodide is provided by the starting reagents and ensures that less vacancies are formed in the process. It may have been anticipated that using an excess of $PbI_2$ could lead to an increase in iodide vacancies due to incomplete regions of the crystal structure that are lead rich. However, these findings combined with the fact that enhanced photoluminescence and device efficiencies have

been observed in perovskite films created from using an excess of either reagent suggests that this bias reduces the $V_I$ defect concentration.[19, 21, 20] To confirm if the excess iodide provided by either reagents is operating by alleviating iodide vacancies the absorbance measurements are correlated to superoxide generation yields and steady state PL measurements, Figure 6.12a and 6.12b respectively. The measurements were conducted in accordance with the previous protocols described.

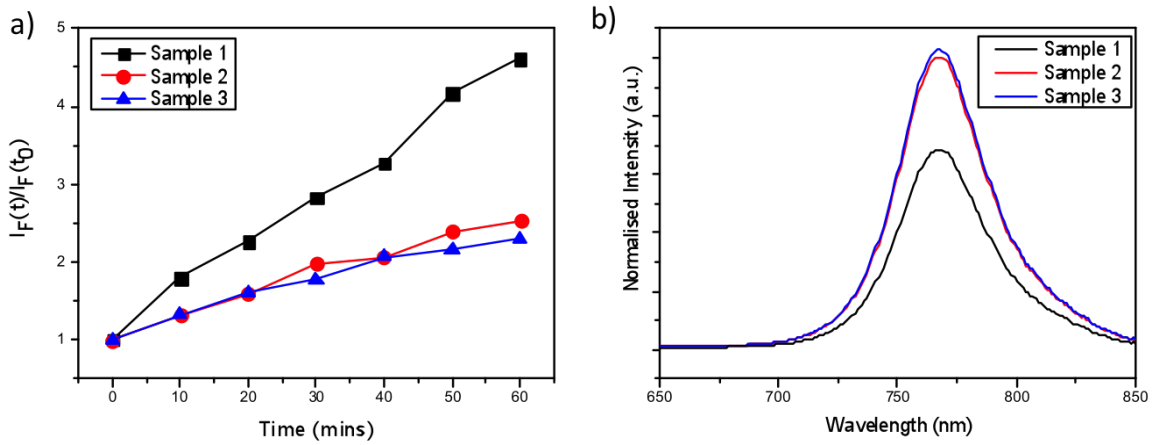


Figure 6.12: a) Superoxide yield plot for samples 1-3 and b) their steady state photoluminescence.

Figure 6.12a, depicts the superoxide yield generation and the results correlate with the observed stability of the samples. Both samples 2 and 3, with excess iodide present in the synthesis display reduced superoxide yields with respect to sample 1. This is in accordance with the previous understanding that increased stability is accompanied by a decrease in superoxide generation. Interestingly, it has emerged that the results show that using either an excess of MAI or $PbI_2$, does not influence the stability enhancement or the reduction in superoxide. This finding reinstates the importance of the iodide component and further supports the assertion that the excess iodide in the fabrication leads to reduced halide vacancy $CH_3NH_3PbI_3$ films. Corroborating this hypothesis, is the steady state PL data, Figure 6.12b, that shows sample 2 and 3 have higher emission intensities compared to sample 1. From this, sample 2 and 3, must have fewer defects or trap sites that promote non-radiative recombination. Hence, with fewer defects, in this situation iodide vacancies, the perovskite samples with excess iodide in the fabrication protocol generate higher emission intensities as a result of fewer photo-excited

electrons and holes undergoing non-radiative recombination. Again, the observation that the impact on the parameter under investigation is independent of the reagent used in excess is noted. Both samples 2 and 3, exhibit similar increases in emission magnitude relative to sample 1. Taken with all the previous findings, namely the same crystal morphology, implies that the excess iodide is the key component in the use of a reagent excess and this results in fewer halide vacancies in $CH_3NH_3PbI_3$ films. This not only highlights the key role iodide vacancies impart on stability of $CH_3NH_3PbI_3$ films, but also on their optoelectronic properties. Where literature has shown that increasing either reagent (MAI or $PbI_2$) can induce favourable increases in device performance. [19, 20, 21] Of particular interest is the fact that it has also now been observed in the literature that using potassium iodide treatments enhances perovskite life-time.[27, 28] It could be suggested that this observation can also be rationalised by the work conducted herein, where the presence of the Iodide in the salt passivates the $V_I$ defects and in turn leads to reduced superoxide formation.

## 6.4 Radical Quenching

So far, the impact of iodide salt additives and iodide reagent bias in the starting materials have demonstrated an ability to enhance material life-time. This has been attributed to the ability of the methods to passivate/reduce the number of iodide vacancy defects in the perovskite crystal. The defects are critical in the generation of superoxide, as they allow molecular oxygen in the atmosphere to insert in the crystal and accept photo-excited electrons. This process has been shown to be facile and energetically favourable. The generation of superoxide is detrimental to the longevity of the perovskite phase as it rapidly acts to break the crystal down via a deprotonation reaction with the organic cation component, methyalammonium. However, even in a completely defect free system superoxide can still be generated from the pristine surface of methylammonium lead iodide, and as such film and device life-times of all systems, even those treated with iodide salts still degrade eventually upon exposure to both oxygen and light. Furthermore, radical species have been identified as plaguing organic solar cells and novel methods to employ radical quenchers has helped improve material tolerance

towards this reactive species and hence increase material life-time.[29, 30, 31, 32] In review of this, a method to protect the perovskite crystal from the action of superoxide could solve the stability issues. In nature, radicals are a potent issue leading to cell destruction and aging. To circumvent these issues, chemical species exist to inhibit and deactivate radicals. A prime example of this is Ascorbic acid (AA), Vitamin C, as an anti-oxidant it has a primary role of defending cellular membranes from free radicals.[33] In light of this, the application of Ascorbic acid doped within the perovskite crystal is explored as method of inhibiting the destruction of the crystal from superoxide. It is hypothesised that the superoxide species will react with the Ascorbic acid as the reaction will be more favourable. Where, the reaction may occur via more stable intermediates and therefore create a more favourable pathway. Consequently, this should reduce the amount of superoxide that is able to react with the cation component and thus generate longer material life-times.

To examine the effect of anti-oxidant doping, Ascorbic acid was doped into the starting solution as a weight percentage of the perovskite (Methylammonium lead iodide). Here, 1% and 10% by weight quantities were utilised. The resulting solutions were employed as per the standard fabrication procedure and films were deposited onto plain cleaned glass substrates. These films were then compared against an undoped methylammonium lead iodide film. As a starting point, the optical degradation of the film compositions was examined using UV/VIS spectroscopy. The effect on the normalised absorbance at 700 nm after exposing these films to oxygen and light are shown in Figure 6.13.

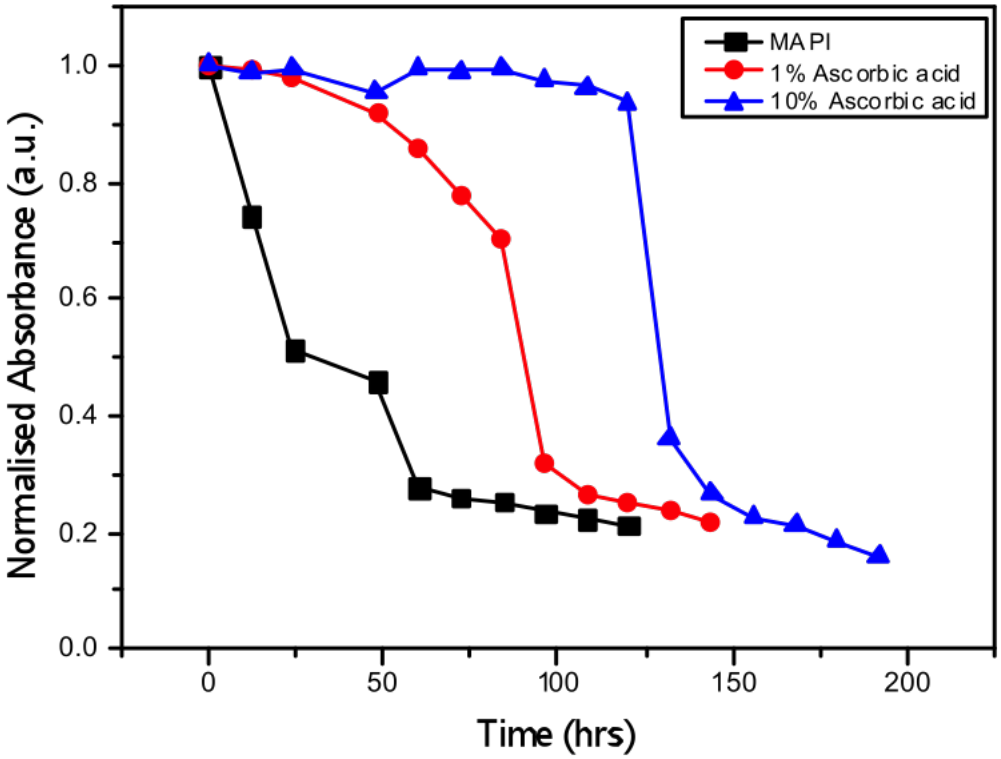


Figure 6.13: Normalised absorbance as a function of aging time for a pristine $CH_3NH_3PbI_3$ film, and for films doped with 1% and 10% by weight quantities of Ascorbic acid (AA).

From the normalised absorbance, it is observed that the addition of Ascorbic acid delays the onset of degradation. Where critically, the optical absorbance is retained over a longer time-frame as the content of the Ascorbic acid is increased. In contrast to the other methods implemented to enhance stability, the Ascorbic acid doping prevents the degradation for a set amount of time depending on the dopant quantity. Then after this time the film degrades with similar kinetics as that of the undoped sample. In the iodide salt treatments, the degradation kinetics were altered and the rate of reaction slowed as function of a reduced rate of superoxide production. In these samples examined there appears to be little to no degradation until a certain point and then after this the films are completely degraded within 50 hours. For the 1% sample the film lasts until 50 hours of exposure and is then fully decomposed by 100 hours, whilst the 10% sample retains it's optical properties until approximately 110 hours of exposure to oxygen and light and is then completely degraded by 160 hours. This suggests that the Ascorbic acid may be serving to react with the generated superoxide rather than decreasing the

generation of the reactive species. As if the same yield is being generated the rate of decay will be similar between all samples once the Ascorbic acid dopant has been used. To understand if this is the case, the superoxide test is employed on all three samples and the results of which are displayed in Figure 6.14.

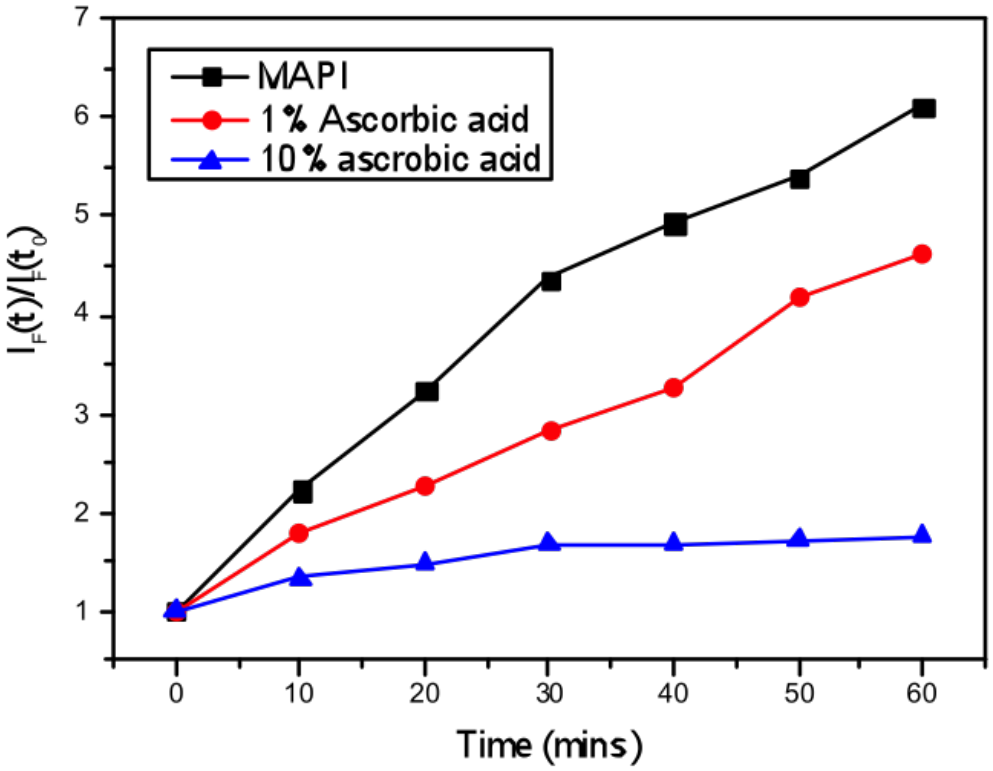


Figure 6.14: Superoxide yield plot for a pristine $CH_3NH_3PbI_3$ film, and for films doped with 1% and 10% by weight quantities of Ascorbic acid

Interestingly, the superoxide yields decrease as function of increasing Ascorbic acid concentration within the film. This observation is in contrast to the expected result, where there would be little to no difference in the yield between films. However, since the films contain Ascorbic acid the generated superoxide can react with this species before leaving the film and reacting with the probe in the solution. This may account for why the increase in fluorescence of the detection probe decreases as a function of Ascorbic acid content. Less superoxide leaves the film to react with the probe. It is therefore, still anticipated that all films generate similar yields of superoxide. While the difference in stability is accounted for by the ability of Ascorbic acid to

react with superoxide in favour of the cation component of the perovskite crystal. The reaction of AA with superoxide mediated through methylammonium lead iodide, is a radical quenching mechanism. A potential mechanism is presented in the figure below.

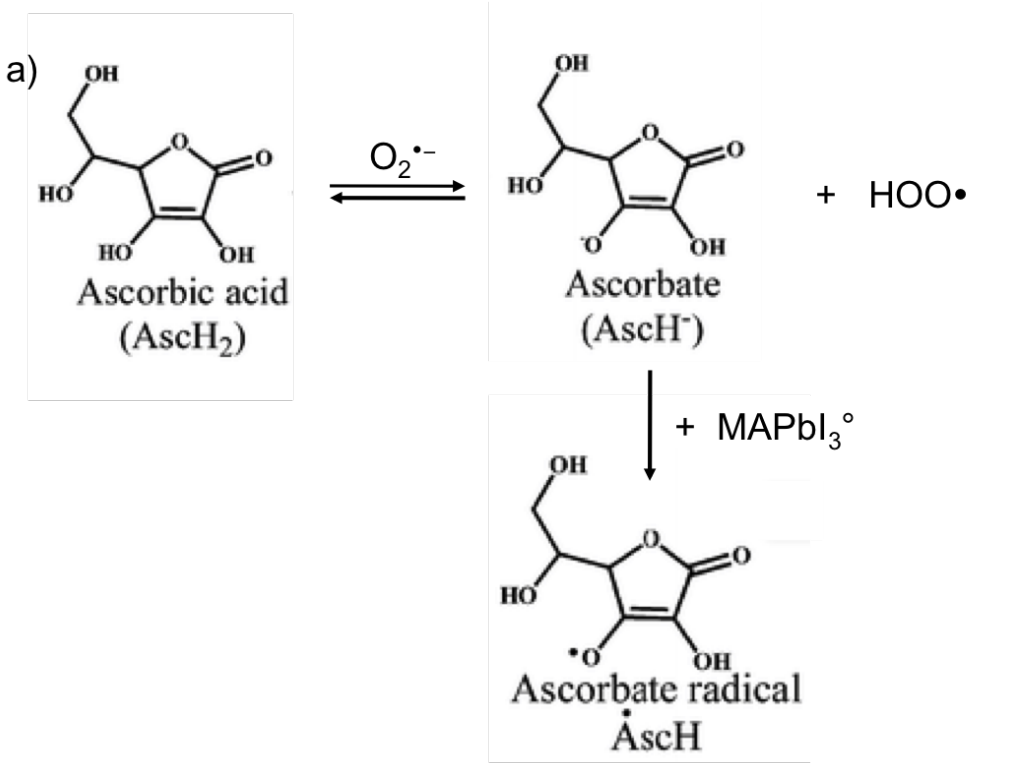


b) $O_2^{\bullet-} + HOO\bullet \rightarrow O_2 + HOO^-$

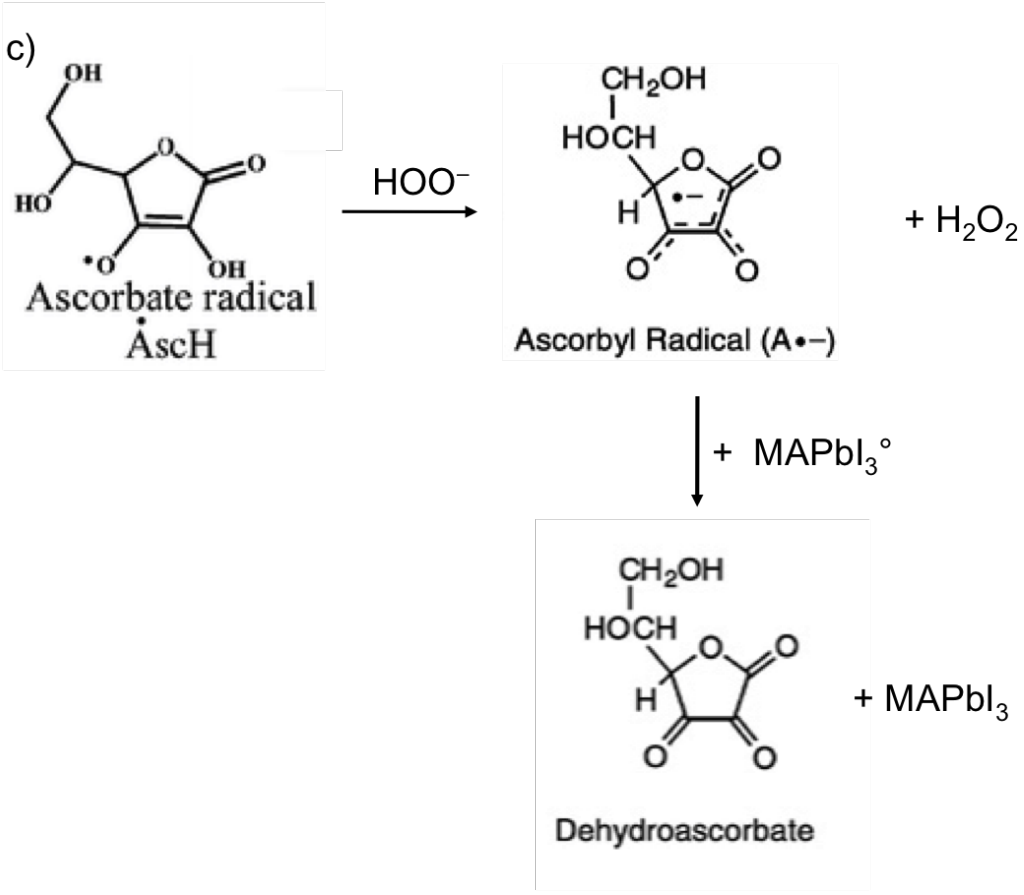


Figure 6.15: Mechanistic proposal of the action of Ascorbic acid to stabilise perovskite films by deactivating the superoxide radical.

The mechanism is split into three major components. First, the reaction of AA with superoxide, generates the Ascorbate and the hydroperoxyl radical. The Ascorbate species can then quench the hole that is left in the perovskite crystal ($MAPbI_3^{\circ}$), leading to the formation of the Ascorbate radical. This species is very stable, due to the resonance structures allowing the electron to be delocalised across the structure. This low energy system stabilizes the radical and reduces its potency. It also accounts for the reason why superoxide prefers to react with Ascorbic acid over the methylammonium cation. More stable intermediates lead to a more energetically and kinetically favourable pathway. Next, the hydroperoxyl radical that was also formed reacts with another superoxide anion, generating hydroperoxyl anion. This new species can now react with the Ascorbate radical forming Ascorbyl radical. This is another stable system due to resonance structures allowing the stabilisation and delocalisation of the charge across the structure. Hydrogen peroxide is formed as a by product. Again the hole left in the perovskite crystal after the formation of superoxide can react with the Ascorbyl radical. The resulting species are Dehydroascorbate and Methylammonium lead iodide in its ground state. Overall, the mechanism proposed leads to the consumption of the Ascorbic acid species and the protection of methylammonium lead iodide. This, ties in with the observed optical spectroscopy data, where the Ascorbic acid will protect the perovskite crystal until it is consumed by the superoxide species. After this point the crystal will degrade as the radical quencher is no longer present and the radical oxygen species will attack the organic cation component leading to the breakdown of the crystal. Hence when more quencher is doped into the structure, the longer the film will last as there is more Ascorbic acid to react with more superoxide species before it can begin to react with the crystal. Furthermore, this mechanism also supports the observed superoxide yields. Where increasing the quencher concentration leads to reduced observed superoxide yields, as less superoxide can leave the film to react with the probe as it reacts with Ascorbic acid before it can diffuse out of the film and react with the probe.

### 6.4.1 Impact on Charge Separation

Next, the impact of the addition of a radical quencher is considered with respect to optoelectronic properties. The previous results have shown that the optical absorption life time can be enhanced

by doping the perovskite crystal with Ascorbic acid. However, the addition of foreign species in a crystal can cause issues of non-radiative recombination by providing trap sites and centers that encourage the recombination of electrons and holes.[34] To investigate this, the three samples with no AA, 1% and 10% were fabricated and the photoluminescence of the films was recorded. Figure 6.16a, shows the steady state PL emission intensity for these three samples and clearly shows that the intensity decreases as the content of Ascorbic acid is increased in the film. From this, it can be rationalised that the Ascorbic acid is causing issues of non-radiative recombination and leading to losses that waste the photo-generated electrons and hole pairs within methylammonium lead iodide. Charges couples are unable to travel as effectively within the perovskite structure and more polarons are lost, thus less charges will be able to be extracted in working devices. Time resolved PL experiments on these samples, Figure 6.16b, confirms this.

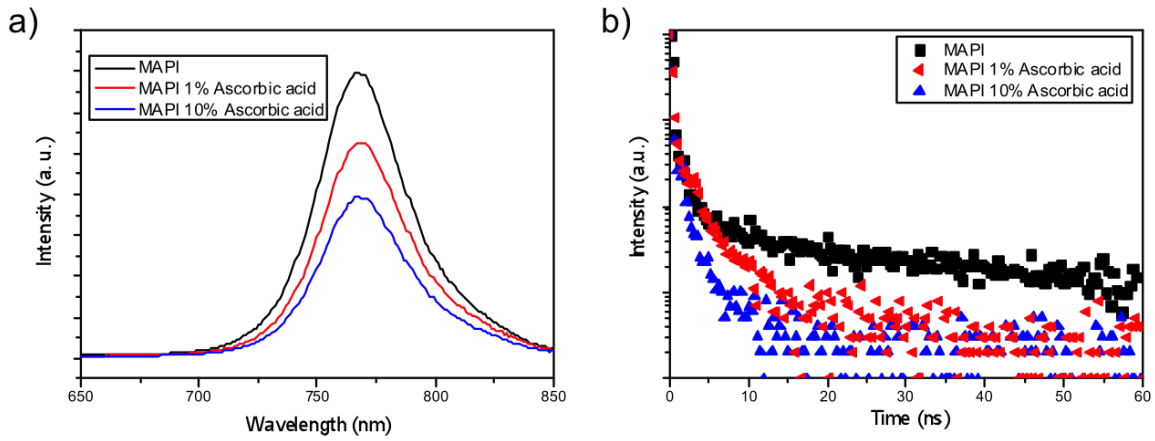


Figure 6.16: a) Steady state photoluminescence for the three samples with no Ascorbic acid and with 1% and 10%. b) Time resolved photoluminescence for the films with and without doping of Ascorbic acid.

The TRPL data, reveals that the emission life time also decreases as AA content is increased. A decrease in emission life-time identifies that the polarons are recombining quicker and will have a reduced ability to do useful work in a device. Where, charge transport will be reduced and less charges will be able to be extracted and separated. Time resolved transient absorption spectroscopy (TAS), is now employed to demonstrate the potential impact that increasing recombination will have on charge separation across the perovskite/HTM interface. This will provide the first insights into the impact on device performance. There is a strong correlation

between charge separation yields and device efficiency. For these experiments $CH_3NH_3PbI_3$ was fabricated on mesoporous-$Al_2O_3$, with no doping, 1% and 10% AA doping. After the fabrication of the perovskite phase the hole transporting layer spiro-OMeTAD was deposited on top by spin coating. The resulting thin-film architectures with varying moisture content of glass/mp-$Al_2O_3$/$CH_3NH_3PbI_3$(xAA)/spiro-OMeTAD were then probed at 1600 nm to obtain the yield of charge separation and the kinetic decay. Measurements were obtained under a nitrogen atmosphere. The TAS kinetic decay curves for the three samples are displayed in Figure 6.17 below.

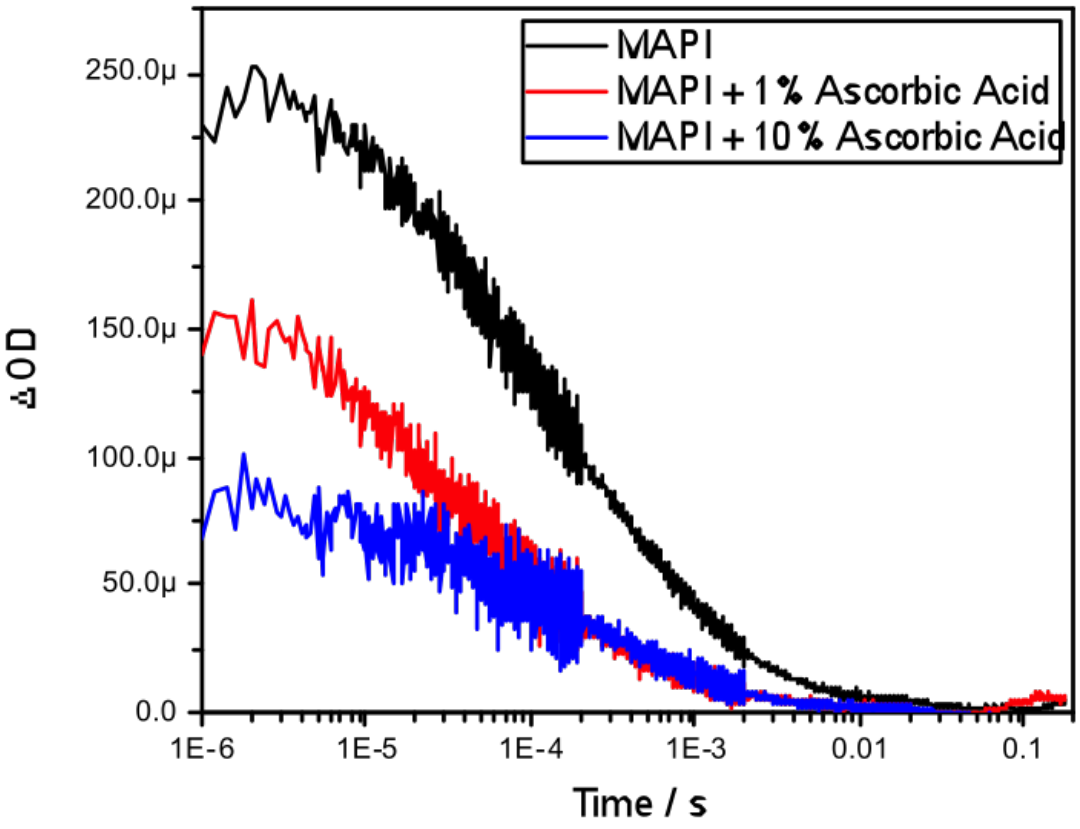


Figure 6.17: TAS kinetic decay traces for the three samples with no Ascorbic acid and with 1% and 10%. highlighting the impact on the yield of charge separation as the Ascorbic acid concentration is increased.

In accordance with both the steady state and time-resolved PL experiments the TAS investigation highlights that Ascorbic acid reduces the yield of charge separation. This is a

consequence of the fact that less electron-hole pairs reach the interface as they non-radiatively recombine at AA sites or defect sites generated by the addition of AA into the crystal structure. However, the half-life of charge separated across the interface increases indicating that once the electron-hole pair is split interfacial recombination becomes less favourable. This is most likely due to the reduced yields of charges reaching the interface and so the frequency of recombination events is reduced. Taken together the data confirms that the role Ascorbic acid plays in enhancing stability is through a reaction mechanism with superoxide, at the expense of optoelectronic performance. Doping the crystal with a radical quencher causes increased non-radiative recombination, where the dopant either facilitates this through collisions with the electron hole-pair or through increasing the defect density in the crystal structure.

### 6.4.2 Implications for device efficiency and stability

Finally, devices employing the three perovskite layers, with 1%, 10% and no AA were fabricated to monitor the impact on both device performance and stability. Devices of the architecture FTO/c-$TiO_2$/mp-$TiO_2$/$CH_3NH_3PbI_3$/Spiro-OMeTAD/Au were created using the methods described in the experimental section. These devices were then recorded as fresh and then the efficiency was recorded as a function of aging time under dry air flux and one sun illumination. The J-V curves obtained for the samples as fresh and the normalised efficiency decay are shown in Figure 6.18 a and b respectively.

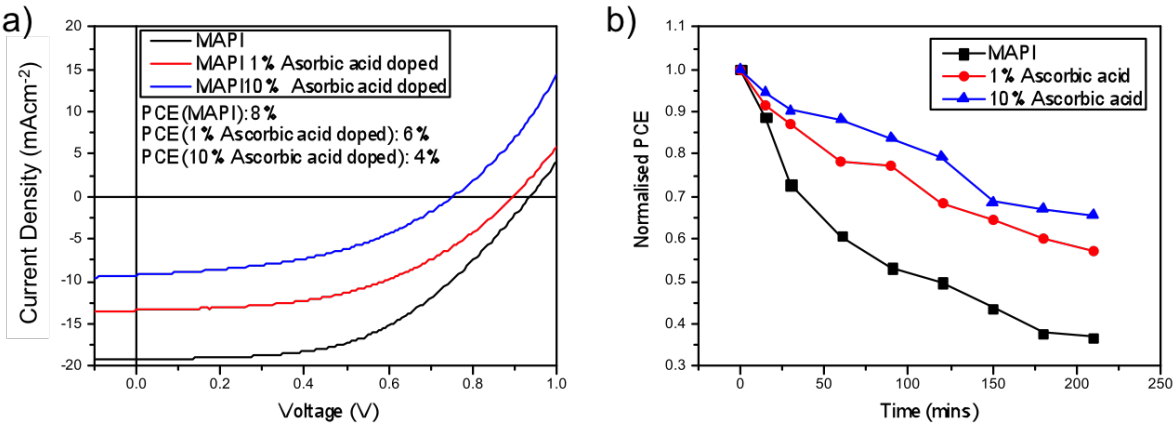


Figure 6.18: a) J-V curves obtained for devices comprising a pristine $CH_3NH_3PbI_3$ film and films containing 1% and 10% by weight content of Ascorbic acid. b) The normalised efficiency loss for these devices as a function of exposure to oxygen and one sun illumination. The device architecture employed was: FTO/c-$TiO_2$/mp-$TiO_2$/Perovskite/Spiro-OMeTAD/Au

The fresh J-V curves, Figure 6.18a, confirm that the addition of Ascorbic acid into the perovskite phase reduces the efficiency. Most significantly, the current is most affected which is to be expected from the previous data showing the impact on charge separation and life-time. Fewer charges are able to be extracted, due to increased recombination rates. The open circuit voltage is also reduced with increasing AA doping most likely due to an increased resistance within the perovskite phase due to the presence of the dopant. The efficiency for the pristine solar cells, approximately halves from no AA to 10% doped. Despite these issues regarding performance, PSC employing a radical quencher demonstrate increased resistance to oxygen and light stress. Where both the 1% and 10% doped samples exhibit greater retention of device efficiency when exposed to dry air flux and illumination. The devices with 1% and 10% AA only lose 10% and 20% respectively, in the same time frame that the undoped sample losses over 50% of its starting efficiency. Within these samples, in agreement with the optical degradation measurements, the increased AA content causes increased stability.

## 6.5 Conclusions

In conclusion, the experiments conducted have shown that thin-film passivation with iodide salts leads to reduced superoxide formation, and consequently enhanced film and device stabilities. It

has been clearly demonstrated that the role of iodide is key in this passivation, where exchange for alternative halides leads to no enhancement in stability. Likewise, the role of the counter cation bears no impact on the magnitude of stability towards oxygen and light. This reinforces the identification of iodide vacancies within the methylammonium lead iodide crystal as one of the intrinsic flaws in its instability towards this degradation stress. Moreover, it has provided a method to enhance stability by reducing defect densities and ultimately the ability of the film to yield superoxide. In line with this finding, is the fact that increasing either the MAI or $PBI_2$ starting reagent concentration generates films with fewer iodide vacancy defects. The increased iodide content in the film preparation ensures more uniform and pristine films are formed in the fabrication process. Consequently, this also allows the perovskite films to yield lower quantities of superoxide and enhance film life-time. Again the importance of iodide and its vacancy sites has been highlighted as the fundamental issue of instability towards oxygen and light.

Additionally, the role of doping films with a radical quencher, Ascorbic acid, has proven the degradation mechanism acts through the generation of the reactive radical species, superoxide. The addition of Ascorbic acid can be deployed to enhance stability via reacting with the superoxide in favour of the perovskite crystal. However, this comes at two detrimental costs. First the degradation is not completely stopped as once the radical quencher is consumed the crystal begins to breakdown. Where the quantity of dopant is correlated to the longevity of the crystal. More dopant gives rise to more stable films. Secondly, and more detrimentally, the addition of the dopant results in performance losses. This was noted by a reduction in starting efficiency in devices and reduced PL intensities and life-times in addition to reduced charge separation yields and life-times. This was attributed to the fact that the Ascorbic acid species, increases non-radiative charge recombination and hampers charge transport within the perovskite phase, by inducing defects and traps. These combined results improve our fundamental understanding of degradation phenomena in perovskite solar cells, and provide strategies for greatly improving their long-term stability.

# References

[1] J. M. Ball, M. M. Lee, A. Hey, H. J. Snaith, *Energy Environ. Sci.*, 2013, **6**, 1739–1743.

[2] E. T. Hoke, D. J. Slotcavage, E. R. Dohner, A. R. Bowring, H. I. Karunadasa, M. D. McGehee, *Chem. Sci.*, 2015, **6**, 613–617.

[3] A. Walsh, D. O. Scanlon, S. Chen, X. G. Gong, S.-H. Wei, *Angew. Chem. Int. Ed.*, 2015, **54**, 17911794.

[4] L. Etgar, P. Gao, P. Qin, M. Graetzel, M. K. Nazeeruddin, *J. Mater. Chem. A*, 2014, **2**, 11586–11590.

[5] J. Kim, S.-H. Lee, J. H. Lee, K.-H. Hong, *J. Phys. Chem. Lett*, 2014, **5**, 1312–1317.

[6] W.-J. Yin, T. Shi, Y. Yan, *Applied Physics Letters*, 2014, **104**, 063903.

[7] M. L. Agiorgousis, Y.-Y. Sun, H. Zeng, S. Zhang, *Journal of the American Chemical Society*, 2014, **136**, 14570–14575.

[8] A. Walsh, D. O. Scanlon, S. Chen, Gong, X. G., S. H. Wei, *Angew. Chem. Int. Ed.*, 2015, **54**, 17911794.

[9] C. Eames, J. M. Frost, P. R. F. Barnes, B. C. ORegan, A. Walsh, M. S. Islam, *Nat. Commun.*, 2015, **6**, 7497–7506.

[10] A. Buin, P. Pietsch, J. Xu, O. Voznyy, A. H. Ip, R. Comin, E. H. Sargent, *Nano Letters*, 2014, **14**, 6281–6286.

[11] J. Xu, A. Buin, A. Ip, W. Li, O. Voznyy, R. Comin, M. Yuan, S. Jeon, Z. Ning, J. McDowell, P. Kanjanaboos, J.-P. Sun, X. Lan, L. N. Quan, D. H. Kim, I. G. Hill, P. M. . E. H. Sargent, *Nat. Commun.*, 2015, **6**, 7081–7089.

[12] N. Aristidou, I. Sanchez-Molina, T. Chotchuangchutchaval, M. Brown, L. Martinez, T. Rath, S. A. Haque, *Angewandte Chemie International Edition*, 2015, **54**, 8208–8212.

[13] D. Bryant, N. Aristidou, S. Pont, I. Sanchez-Molina, T. Chotchunangatchaval, S. Wheeler, J. R. Durrant, S. A. Haque, *Energy Environ. Sci.*, 2016, **9**, 1655–1660.

[14] N. Aristidou, C. Eames, I. Sanchez-Molina, X. Bu, J. Kosco, M. S. Islam, S. A. Haque, *Nat. Comm.*, 2017, **8**, 15218.

[15] J. Haruyama, K. Sodeyama, L. Han, Y. Tateyama, *J. Phys. Chem. Lett.*, 2014, **5**, 2903–2909.

[16] A. Poglitsch, D. Weber, *The Journal of Chemical Physics*, 1987, **87**, 6373–6378.

[17] H.-J. Yen, P.-W. Liang, C.-C. Chueh, Z. Yang, A. K.-Y. Jen, H.-L. Wang, *ACS Appl. Mater. Interfaces*, 2016, **8**, 1451314520.

[18] K. M. Boopathi, R. Mohan, T.-Y. Huang, W. Budiawan, M.-Y. Lin, C.-H. Lee, K.-C. Ho, C.-W. Chu, *J. Mater. Chem. A*, 2016, **4**, 1591–1597.

[19] B.-E. Cohen, S. Gamliel, L. Etgar, *APL Mater.*, 2014, **2**, 081502.

[20] Y. Zhang, H. Lv, C. Cui, L. Xu, P. Wang, H. Wang, X. Yu, J. Xie, J. Huang, Z. Tang, D. Yang, *Nanotech.*, 2017, **28**, 205401.

[21] T. J. Jacobsson, J.-P. Correa-Baena, E. Halvani Anaraki, B. Philippe, S. D. Stranks, M. E. F. Bouduban, W. Tress, K. Schenk, J. Teuscher, J.-E. Moser, H. Rensmo, A. Hagfeldt, *J. Am. Chem. Soc.*, 2016, **138**, 10331–10343.

[22] N. Guo, T. Zhang, G. Li, F. Xu, X. Qian, Y. Zhao, *J. Semiconductors*, 2017, **38**, 014004.

[23] F. Liu, Q. Dong, M. K. Wong, A. B. Djurii, A. Ng, Z. Ren, Q. Shen, C. Surya, W. K. Chan, J. Wang, A. M. C. Ng, C. Liao, H. Li, K. Shih, C. Wei, H. Su, J. Dai, 2016.

[24] A. Buin, R. Comin, J. Xu, A. H. Ip, E. H. Sargent, *Chemistry of Materials*, 2015, **27**, 4405–4412.

[25] S. D. Stranks, P. K. Nayak, W. Zhang, T. Stergiopoulos, H. J. Snaith, *Angewandte Chemie International Edition*, 2015, **54**, 3240–3248.

[26] C. Freysoldt, B. Grabowski, T. Hickel, Neugebauer, G. Kresse, A. Janotti, C. G. Van de Walle, *Rev. Mod. Phys.*, 2014, **86**, 253–305.

[27] D. J. Kubicki, D. Prochowicz, A. Hofstetter, S. M. Zakeeruddin, M. Grtzel, L. Emsley, *J. Am. Chem. Soc*, 2018, **23**, 7232–7238.

[28] M. Abdi-Jalebi, Z. Andaji-Garmaroudi, S. Cacovich, C. Stavrakas, B. Philippe, J. M. Richter, M. Alsari, E. P. Booker, E. M. Hutter, A. J. Pearson, S. Lilliu, T. J. Savenije, H. Rensmo, G. Divitini, C. Ducati, R. H. Friend, S. D. Stranks, *Nature*, 2018, **555**, 497501.

[29] I. F. Domnguez, A. Distler, L. Ler, *Adv. Energy Mater.*, 2017, **7**, 1601320.

[30] Q. Xue, M. Liu, Z. Li, L. Yan, Z. Hu, J. Zhou, W. Li, X. Jiang, B. Xu, F. Huang, Y. Li, H. Yip, Y. Cao, *Adv. Func. Mater.*, 2018, 1707444.

[31] V. I. Madogni, B. Kounouhwa, A. Akpo, M. Agbomahna, S. A. Hounkpatin, C. N. Awanou, *Chem. Phys. Lett.*, 2015, **640**, 201 – 214.

[32] V. Turkovic, S. Engmann, N. Tsierkezos, H. Hoppe, U. Ritter, G. Gobsch, *ACS App. Mater. Inter.*, 2014, **6**, 18525–18537.

[33] R. E. Beyer, *Journal of Bioenergetics and Biomembranes*, 1994, **26**, 349–358.

[34] A. L. Tchebotareva, M. J. de Dood, J. S. Biteen, H. A. Atwater, A. Polman, *Journal of Luminescence*, 2005, **114**, 137 – 144.

# Chapter 7

# Insights into the increased degradation rate of $CH_3NH_3PbI_3$ solar cells in combined water and $O_2$ environments

## 7.1 Introduction

Despite developing new methods to enhance stability towards oxygen and light conditions, degradation issues still plague devices. Problematic iodide vacancies can be quenched, but the PCE of devices can still decrease with exposure to these conditions. Resulting from superoxide being able to form from vacancies that are still unsatisfied. These persistent fundamental issues of operational and material stability,[1, 2, 3, 4] along with the associated toxicity of lead, restrict the commercial possibilities of devices employing these materials. A greater understanding of the conditions that impact material life-time is warranted if commercial employment is to be realised. A number of studies have reported the effects of moisture, UV and temperature on the archetypal material, methylammonium lead iodide ($CH_3NH_3PbI_3$).[5, 6, 7, 8, 9, 10, 11, 12, 13, 14, 15, 16, 17, 18, 19, 20, 21, 22, 23, 24, 25, 26, 27, 28, 29] Moisture has been identified as a particular problem for this material leading to its permanent degradation after prolonged exposure. However, previous studies have also shown that when films of $CH_3NH_3PbI_3$ are exposed to water during crystallization and annealing an enhancement in its optoelectronic

properties is observed.[19, 30, 31, 32, 33] This is partly due to a phase change that occurs in which hydrated phases are formed and the fact that humidity controls the crystal growth, where low humidity leads to smaller crystallites with large gaps between them.[33] When films are exposed to water concentrations below 85% a reversible phase change into a monohydrate phase occurs, but higher concentrations or prolonged exposure causes an irreversible phase change into a dihydrate phase. Moreover, IR spectroscopy studies have shown that $CH_3NH_3PbI_3$ films are hygroscopic and water uptake is rapid where the resulting interaction of water is with the methyl ammonium cation component in the crystal structure. In addition, water has been shown to permeate across perovskite structures to form partly hydrated phases. These factors demonstrate the potency of water in determining the performance and stability of $CH_3NH_3PbI_3$ films.[30, 34] Separate studies have shown oxygen to be an even more aggressive degradation agent, where exposure to oxygen and light leads to rapid and permanent degradation of device performances.[35, 36, 37, 38] The previous chapters have shown that the combined action of oxygen and light can significantly affect the device efficiencies within a matter of hours, and identified the active species, superoxide, as the key component in the oxygen and light mediated degradation of $CH_3NH_3PbI_3$. The generation of this reactive oxygen species is the origin of the degradation process that initiates the breakdown of the crystal structure by an acidbase reaction with the methylammonium cation, as shown in previous works.[35] More recently, the understanding of the degradation mechanism has evolved to indicate that iodide vacancies are key to the generation of superoxide species and that oxygen diffusion into perovskite films is rapid, which contributes to the fast degradation noted in films and devices.[37] In technologically relevant conditions the ambient environment may contain both oxygen and moisture as degradation agents. Whilst it is true that in many applications device encapsulation will be commonplace, this will restrict the use of flexible covers. Moreover, the oxygen diffusion into films has been shown to be extremely rapid and any barrier must be guaranteed to hold an inert atmosphere, otherwise the system will rapidly fail.

As discussed above, superoxide has been identified as the active species causing degradation. Previous research from Sawyer et al.[39] investigated the mechanisms of superoxide as a reactive

species and showed that in protic solvents or in the presence of water, the solvation is very strong and accelerates hydrolysis and disproportionation reactions. As such, water may facilitate the degradation pathway as the reaction between the superoxide and the methylammonium cation becomes even more favourable. Consequently, this work aims to test this hypothesis and identify the impact water has on the light and oxygen mediated degradation in an attempt to explore the effect of real world conditions on solar cells that employ $CH_3NH_3PbI_3$ as the photoactive layer. To achieve this, UV-vis spectrometry will be employed to monitor the time taken for degradation to occur in combination with the previously reported superoxide tests that will reveal differences in the production of superoxide species between samples. Additionally, ab initio simulations will examine reaction energetics and transient absorption spectroscopy (TAS) and device performance measurements will demonstrate if there could be any impact on the device functionality under this combined oxygen and water photo-degradation conditions.[35, 36, 37]

## 7.2 Effect of $H_2O$ on light and oxygen induced degradation

First the influence of moisture on light and oxygen induced degradation of $CH_3NH_3PbI_3$ films is considered. Stability studies were performed on $CH_3NH_3PbI_3$ films pre-soaked with water in humid environments. Thin films of $CH_3NH_3PbI_3$ on cleaned plain glass substrates were soaked in the dark for two hours by bubbling dry nitrogen through a specific water/glycerol mix to obtain a selected humidity of 0%, 25% or 85% RH (sample 1, sample 2 and sample 3, respectively). The exact protocol for sample preparation is described in the Methods section and according to the protocol set out by Forney et.al.[40] As a result of this pre-treatment the $CH_3NH_3PbI_3$ crystal is hydrated with different amounts of water contained within the film.[9] X-ray diffraction was employed to show that there was no resulting impact on the crystal structure among all three samples, as shown in Figure 7.1. This observed through the fact all samples have overlapping spectral peaks, and no additional peaks emerge or any existing peaks are removed from the humid atmosphere treatment. Having similar crystal structures, eliminates any stability effects arising from morphology.

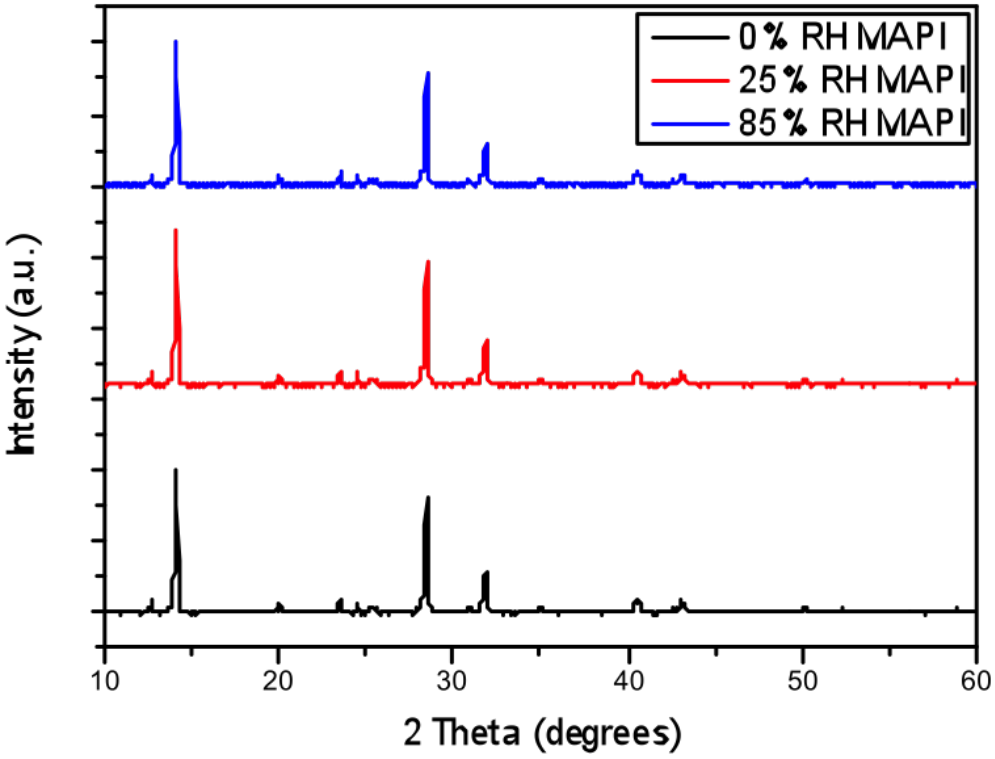


Figure 7.1: X-Ray diffraction patterns of Methylammonium lead iodide after synthesis and exposure to: i) no moisture (Black trace) ii) 25% RH (Red trace) and iii) 85% RH (Blue trace)

To image the dispersion of water through the crystal arising from the humid environments, isotopic labeling combined with ToF-SIMS measurements was employed. Isotopically labeled perovskite films were prepared by replacing $H_2O$ with deuterated-water ($D_2O$) in the moisture pre-soaking step. Slices of the $CH_3NH_3PbI_3$ films at approximately halfway through the crystal (200 nm) and the 3D plots obtained from the experiment are displayed in Figure 7.2. The data indicates that increasing the humidity of the soaking environment leads to a greater water content within the thin-film structure. As noted by an increased presence of deuterated water contained within the film, where sample 2 has less water distributed throughout the crystal compared to sample 3. Here the total count (TC) and maximum count (MC) of deuterated water in sample 3 exceeds that of those in sample 2, MC=3 TC=4.0E$^3$ and MC=5 TC=7.6E$^3$ respectively. Sample 1 had no water content and as such only blank results were obtained (TC=0 and MC=0). In addition, it is worth noting that the apparent diffusion of water into films is facile, akin to oxygen diffusion into the perovskite structure and in agreement with

previous reports of the hygroscopic nature of $CH_3NH_3PbI_3$ films. Since, both samples 2 and 3 appear to have a significant water content within the two soaking time frame.[30, 37]

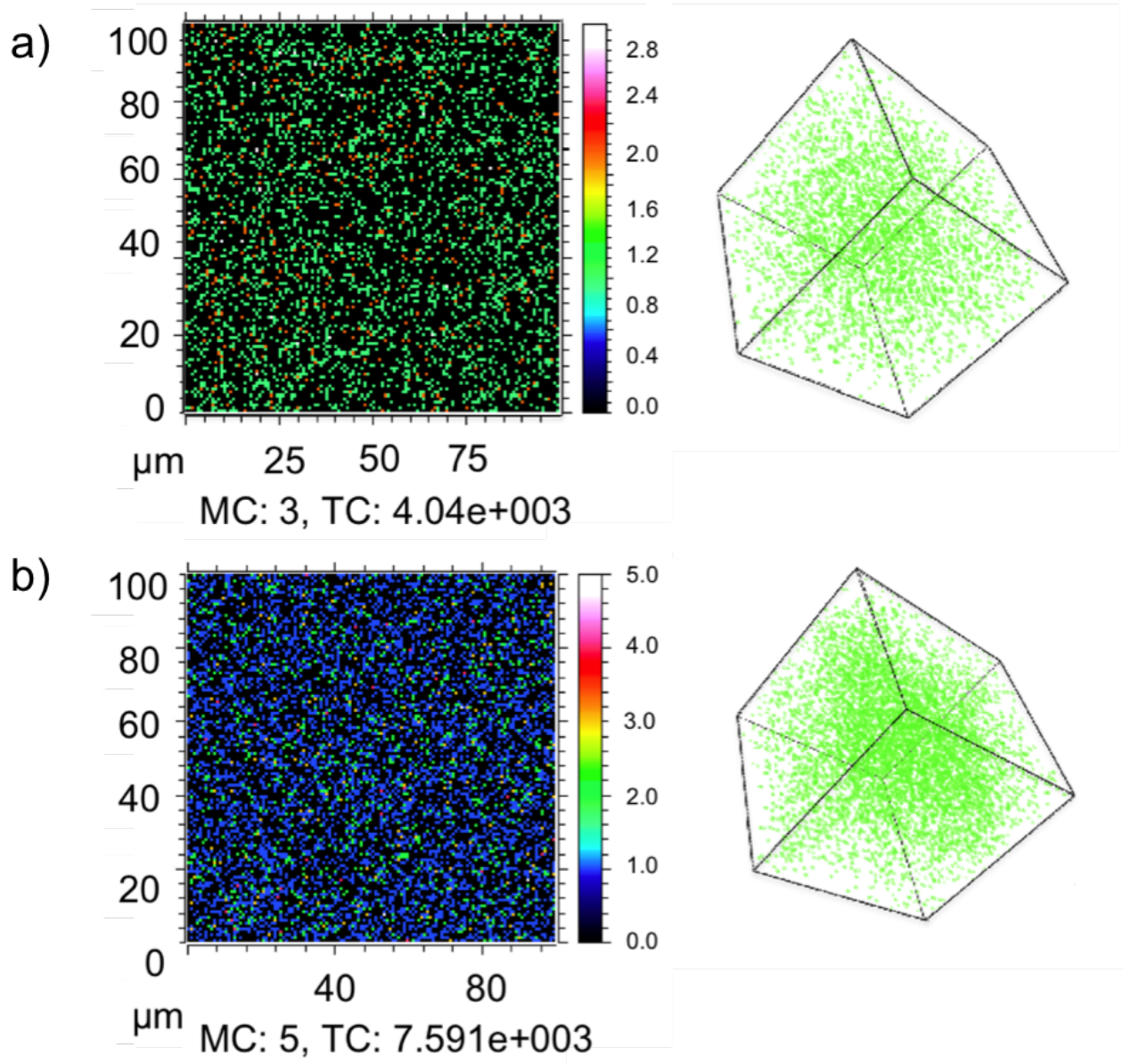


Figure 7.2: ToF-SIMS surface imaging of $D_2O$ at an approximately 150 nm depth in thin films and 3D depth profile plots of glass/$CH_3NH_3PbI_3$ films pre-treated with (top) 25% and (bottom) 85% deuterated water in humid environments. MC is the maximum count and TC is the total number of $D_2O$ counts.

Next, as a control experiment, the resulting moisture loaded films were isolated and subjected to illumination under an inert nitrogen atmosphere. UV-vis measurements were employed to monitor the degradation of the perovskite material upon exposure to light. It is important to highlight that the $CH_3NH_3PbI_3$ samples were prepared purposefully with a higher ratio of lead

iodide, as iodide defects have been shown to increase degradation rates.[37] The increased iodide content allows for both enhanced stability and a more observable trend between samples on a detectable time-scale. In these experiments, the absorbance value at 700 nm was selected and the magnitude was normalised with respect to the starting value (fresh), where subsequent values lead towards the complete conversion of the film into the degradation product lead iodide, $PbI_2$. The UV data (Figure 7.3) shows that the combination of moisture and light under nitrogen (i.e. no oxygen) has little impact on the material stability over the period of investigation (85 hrs). This is noted in the photos presented in Figure 7.3a, where the pre-soaked film subjected to nitrogen and illumination shows no decolouration and remains dark brown for the duration of the investigation and the magnitude of the absorbance remains constant. The profile of the spectrum also remains constant for this sample, suggesting no structural changes are occurring either. As such, the effect of moisture in the films can then be ruled out from causing any alternative degradation pathways independent from oxygen. In contrast, as soon as the pre-soaked films are subjected to dry air flux under illumination, degradation begins to occur. This is drastically noted in the photos of the samples, where decolouration from dark brown to yellow is observed. The time frame for this conversion is accelerated as a function of the water content in the film. Sample 3 degrades the fastest, followed by sample 2 and then sample 1 degrades the slowest with no water content. This reinforces the previous chapters findings of the critical importance of oxygen in the degradation of $CH_3NH_3PbI_3$.[37] It is also apparent from the data in Figure 7.3a and b that, for samples exposed to oxygen, the rate of degradation is higher when the concentration of water is increased. For example, the rate of light and oxygen induced degradation in the 85% RH sample is higher than that in the 50% RH sample, which is in turn higher than that observed in the 25% RH sample. In particular, the complete material degradation time reduces from around 85 hours for the sample with no water to approximately 60 hrs for the sample that has been exposed to 85% RH, and therefore the sample with highest water content. Moreover, this result confirms that moisture present in the hydrated crystals leads to faster, more facile oxygen and light mediated degradation.

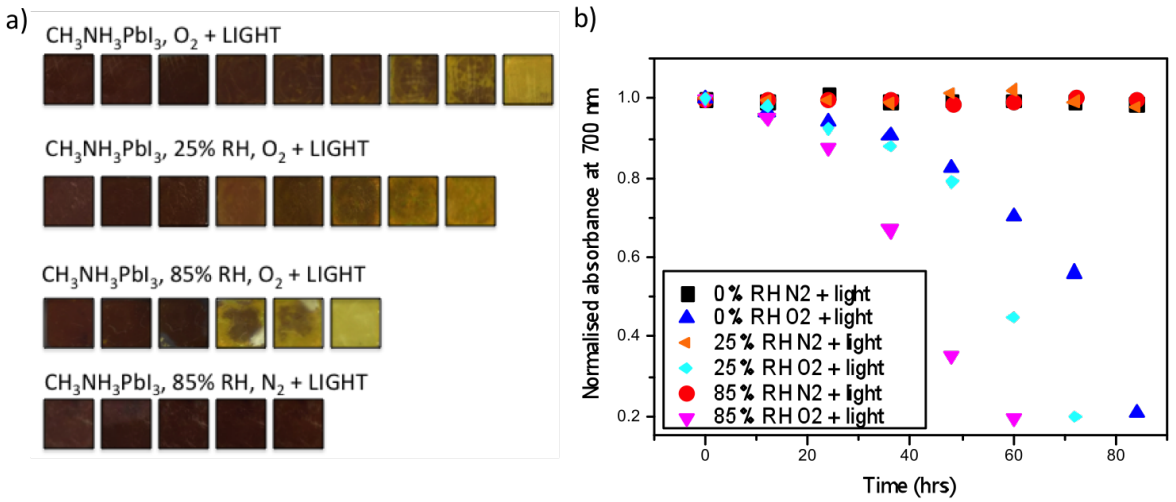


Figure 7.3: a) Photo images of the degradation process of films with no treatment and pre-treated films at relative humidity levels of 25% and 85%. b) Normalised absorbance decay of $CH_3NH_3PbI_3$ at 700 nm. Where conversion to lead iodide is tracked under a range of conditions, including (i) no moisture, $N_2$ and light; (ii) no moisture, $O_2$ and light; (iii) pre-treated under 25% RH, $N_2$ and light; (iv) pre-treated under 25% RH, O2 and light; (v) pre-treated under 85% RH, $N_2$ and light; and (vi) pre-treated under 85% RH, $O_2$ and light.

To further quantify the degradation of photo-excited $CH_3NH_3PbI_3$, DFT methods are used to calculate the enthalpy of reaction for degradation pathways in a number of different ambient environments and these are displayed in the following equations 7.1 to 7.5. A few features are apparent in these reaction energies. First, degradation reactions which involve oxygen and light are the most favourable in accord with observation. For example, degradation under light alone (eqn 7.1) releases -54 kJ $mol^{-1}$ whereas in contrast reaction with $O_2$ and light (eqn 7.5) releases -74 kJ $mol^{-1}$. Such reactions involve the highly reactive superoxide species and allow the deprotonation of $CH_3NH_3^+$. Second, reaction with water (eqn 7.4) is slightly less favourable than the reaction with light (eqn 7.1). This may explain the reported observations that sometimes $CH_3NH_3PbI_3$ exposed to moisture and light does not form hydrated phases and instead directly decomposes to $PbI_2$. These preliminary calculations on reactions involving light, water and oxygen indicate very similar energies to reaction (eqn 7.5), which are consistent with the experimental observations that indicate enhanced reactivity when both water and oxygen are present. However,the potential for any catalytic intermediate states involving water have not been investigated, and is an area for future investigation. Computational results were obtained in collaboration with Bath university and in particular Dr Chris Eames. In the

following equations 'light' represents the generation of an electron and hole within the perovskite crystal.

$$CH_3NH_3PbI_3(s) + light \longrightarrow PbI_2(s) + CH_3NH_3I(s), \Delta E = -54kJmol^{-1} \tag{7.1}$$

$$CH_3NH_3PbI_3(s) + light \longrightarrow PbI_2(s) + CH_3NH_2(g) + HI(g), \Delta E = +153kJmol^{-1} \tag{7.2}$$

$$CH_3NH_3PbI_3(s) + H_2O \rightleftharpoons CH_3NH_3PbI_3.H_2O(s), \Delta E = -16kJmol^{-1} \tag{7.3}$$

$$4CH_3NH_3PbI_3(s) + 2H_2O(g) \longrightarrow 3PbI_2(s) + (CH_3NH_3)_4PbI_6.2H_2O(s), \Delta E = -49kJmol^{-1} \tag{7.4}$$

$$4CH_3NH_3PbI_3(s)+O_2(g)+Light \longrightarrow 4PbI2+4CH_3NH_2(g)+2H_2O(g)+2I_2(G), \Delta E = -74kJmol^{-1} \tag{7.5}$$

## 7.3 Effect of $H_2O$ on superoxide formation

Moving forward, the effect of moisture on the yield of superoxide formation is investigated herein. The relationship between stability and superoxide generation has been well established by the data presented prior to this, where increasing superoxide yields generate films with shorter material life-time. The role of water in the generation of superoxide has not been previously considered, however water may play a crucial role as either a catalyst or it may even serve to stabilise transition states in the degradation mechanism. Since, increasing moisture content in $CH_3NH_3PbI_3$ films leads to faster degradation, the increasing moisture content will be impacting either the yield or the potency of superoxide (namely, its ability to deprotonate

the methylammonium cation). For this purpose, the fluorescent probe, hydroethidine (HE) is employed to detect the generation of superoxide as previously reported,[35] in which superoxide can react with probe forming a species that is luminescent. This hypothesis was tested by monitoring the superoxide generated in films pre-soaked with water. The second possibility is that water may stabilise superoxide after it has formed, increasing its yield and reactivity. To test this hypothesis perovskite films were exposed to $O_2$ and water at the same time. To achieve this the superoxide probe was dissolved in a solvent (toluene) to form a probe solution, like before. However, to vary the water content, a low moisture toluene sample was prepared by drying a portion of toluene over activated molecular sieves. Whilst a high moisture toluene solution saturated with water was generated by simple liquid - liquid extraction; different ratios of these two toluene samples were then mixed when preparing the probe solution. The perovskite films were then exposed to the probe solution with the superoxide yield and the subsequent degradation monitored. The results from these tests are shown in Figure 7.4 a and b.

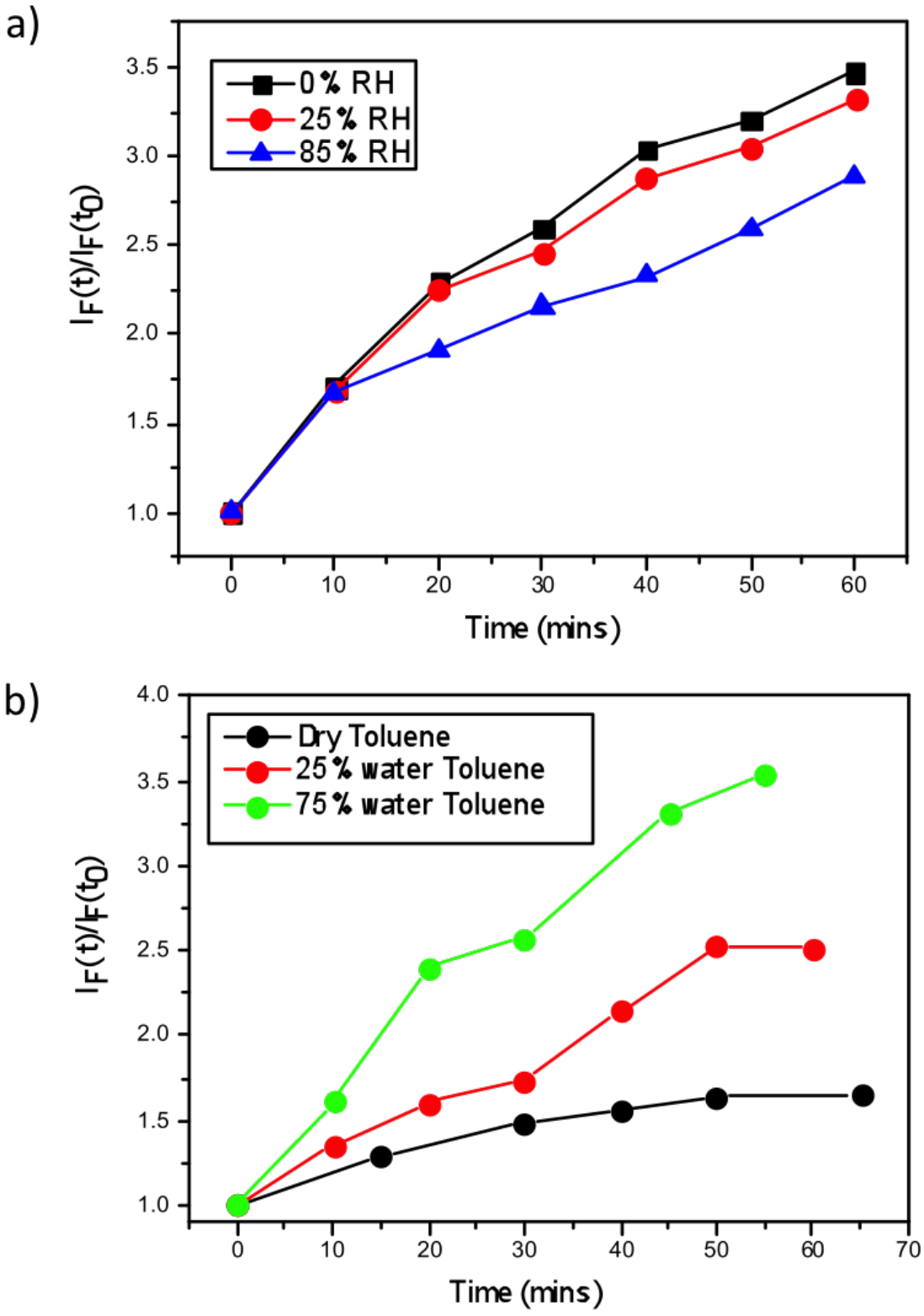


Figure 7.4: Superoxide yield plots for $CH_3NH_3PbI_3$ where (a) demonstrates the effect on the yield via pre-treating the film under no moisture, 25% RH and 85% RH and b) demonstrates the effect of increasing water content in the toluene solution that houses the superoxide reactive probe

The data collected, Figure 7.4a and b, clearly depicts that the yield of superoxide increases when water is added to the probe solution (Fig. 7.4b) but it decreases (Fig. 4.7a) when water is pre-loaded into the films. Moreover, these findings support the second of the two possible effects of water; i.e. water serves to enhance the reactivity, since within these samples the superoxide is more likely to start reacting with the methyl ammonium cation in the crystal rather than be extracted from the film and react with the probe. To further understand the observation that the degradation rate is enhanced when water is added at the same time as $O_2$ than when water is added first, the enthalpies of $O_2$ adsorption and reduction in $CH_3NH_3PbI_3$, and in the monohydrate $CH_3NH_3PbI_3.H_2O$ and dihydrate $(CH_3\ NH_3)_4PbI_6.2H_2O$ phases are calculated computationally; the results are shown in Table 7.1. The enthalpies reveal that it is favourable for $O_2$ to be adsorbed into all phases (apart from the dihydrate). However, it is only in the photoreduced (electron polaron) regions of $CH_3NH_3PbI_3$ that it is favourable for superoxide to form. It is noteworthy that the band gap of the hydrated phases is much larger (>3 eV) than that of $CH_3NH_3PbI_3$ (1.6 eV), and hence visible light cannot generate free carriers which can reduce $O_2$. This is a key result and helps to explain why the superoxide yield is reduced if the films are pre-soaked with water since superoxide cannot be generated in any regions of the perovskite film that become hydrated.

Table 7.1: Calculated energies for $O_2$ adsorption and reduction in methylammonium lead iodide solar cell materials in their ground state, photo-excited state and hydrated phases (in the excited state the weakly bound exciton is considered as being decomposed into two components, a hole polaron and an electron polaron). Results presented in the table were obtained by Dr Chris Eames of Bath university.

| Compound | $O_2$ adsorption energy kJ $mol^{-1}$ | $O_2$ reduction energy kJ $mol^{-1}$ |
|---|---|---|
| $CH_3NH_3PbI_3$ | -14.5 | +8.7 |
| $CH_3NH_3PbI_3 + h^+$ | -35.5 | +9.6 |
| $CH_3NH_3PbI_3 + e^-$ | -88.2 | -32.8 |
| $CH_3NH_3PbI_3.H_2O$ | -31.8 | +15.6 |
| $(CH_3NH_3)_4PbI_6.2H_2O$ | +65.1 | - |

An important question is then raised; why does the presence of water alter the superoxide yield and increase reactivity? When superoxide acts as a base, the overall reaction can be divided into two steps, deprotonation and disproportionation, of which the first one is an equilibrium process.[39] Therefore, increasing the proton concentration in the medium should shift this equilibrium towards the products. This would quickly reduce the concentration of superoxide near the surface of the crystals and leave the sites where it is formed free for another oxygen molecule to react with the photo-excited electrons on the perovskite, thus resulting in a larger increase of the fluorescence of the probe. A further consideration arises from the fact that the superoxide species itself acts in an acidbase reaction with the probe and thus a protic environment in the medium would lead to a more facile reaction between the two species. Hence, a greater fluorescence would be observed. To further demonstrate this point, the same experiment in dry toluene was repeated but other protic sources such as benzoic and nitrobenzoic acid were added, shown in Figure 7.5.

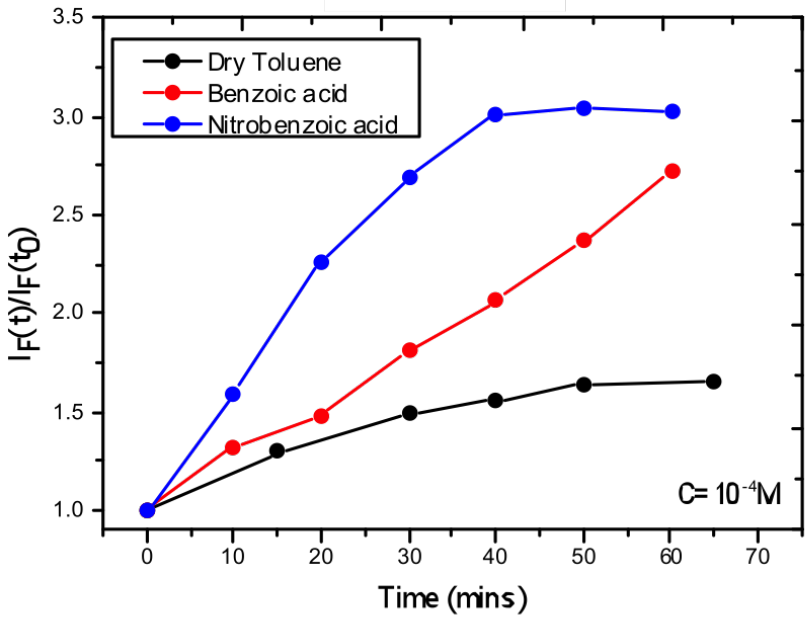


Figure 7.5: Superoxide yield plot for $CH_3NH_3PbI_3$ films submerged in toluene probe solution with different protic solvents. The figure illustrates the impact of acid strength on the superoxide yield, where benzoic acid and nitrobenzoic acid are doped into the toluene solution, with increasing acidity and superoxide generation observed respectively.

In both cases, the superoxide generation yield increases, and it does so in such a way that it

correlates with the $pK_a$; the more acidic species (nitrobenzoic acid) gives rise to more superoxide. The value of the $pK_a$ shifts from 4.19 to 3.43, via addition of the nitro group.[41] Consequently, this points to the fact that the role of moisture within perovskite structures is to enhance the reactivity of the superoxide species and hence increases the degradation rate of perovskite solar cells. The energetics and kinetics of the separate steps and pathways of the overall degradation reactions requires further investigation; such processes would include the deprotonation of the methylammonium cation by the superoxide species and the reaction of water with the superoxide species to generate hydroxyl ions.

## 7.4 Implications for device performance

Finally, the impact of these earlier findings is considered with respect to device function under combined oxygen, water and light conditions. Firstly, by exploring the effect on the yield of charge separation between the perovskite phase and the hole transporting layer, spiro-OMeTAD and secondly on the rate of decay of the PCE of devices composed of films subjected to the pre-soaking treatments. Time resolved transient absorption spectroscopy (TAS) has been previously employed to show the impact of oxygen and light, where it was shown that $CH_3NH_3PbI_3$ fabricated on mesoporous-$Al_2O_3$ suffered significant losses in charge separation within 510 minutes.[38] Correspondingly, $CH_3NH_3PbI_3$ films were fabricated onto this mesoporous scaffold and again subjected to the same pre-soaking treatment with the same selected humidity levels of 0%, 25% and 85% RH. After soaking the hole transporting layer spiro-OMeTAD was deposited on top by spin coating. Exposing the samples to humidity prior to the HTL being deposited aimed to eliminate moisture affecting the HTL phase, which could be encountered if the layer was present during the treatment, and ensure that the film is homogeneously hydrated throughout the whole surface and the bulk. The resulting thin-film architectures with varying moisture content of glass/mp-$Al_2O_3$/$CH_3NH_3PbI_3$/spiro-OMeTAD were then probed at 1600 nm to obtain the yield of charge separation. Decays were collected at regular time intervals over a 20 minute period with exposure to a dry air flow and ambient illumination. Measurements were obtained under a nitrogen atmosphere. The value of $\Delta$OD at 1 $\mu$s was taken as indicative of

the yield of charge separation. These values obtained were then normalised with respect to the starting value (the yield of charge separation at exposure t=0). The normalised decay of the charge separation yield is presented in Figure 7.6a.

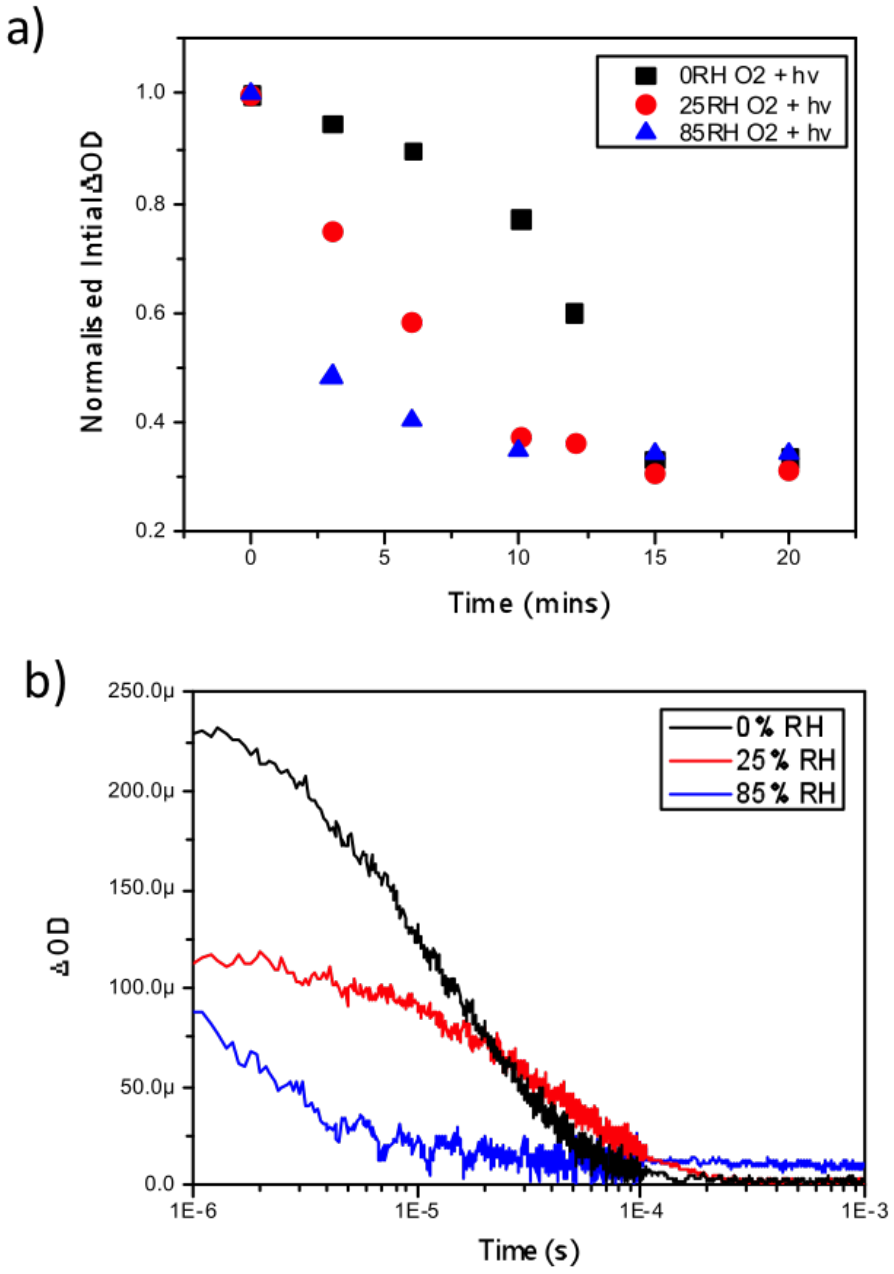


Figure 7.6: a) Normalised transient absorption spectroscopy yield values obtained at 1 $\mu$s highlighting the degradation rate differences between $CH_3NH_3PbI_3$ pre-treated under no moisture, 25% RH and 85% RH upon exposure to both oxygen and light at t=0. b) Kinetic decays obtained after five minutes of exposure to oxygen and light for all three samples. All films were excited with a pump wavelength of 567 nm and an average power of 23 $\mu$J cm$^{-2}$ and a probe wavelength of 1600 nm was employed to probe the resulting holes in spiro-OMeTAD.

In accordance with the UV-vis data presented in Figure 7.3b, it is observed that films loaded with increasing moisture content show an increased rate of loss in the yield of charge separation. When no moisture is present (black trace in Fig. 7.6a) it takes approximately 13 minutes of exposure to oxygen and light for the yield to drop by 50%, and in comparison it takes approximately 3 minutes for the same level of loss to occur in the film soaked in the 85% RH environment (blue trace in Fig. 7.6a) prior to exposure to oxygen and light. In real terms this means that the number of holes being transferred to the hole transporting layer is critically hampered by oxygen and light, but even more so when water is introduced into the system. It is generally accepted that a good yield of charge separation is a pre-requisite for optimal device functionality. Consequently these findings would suggest that introducing water into functioning devices could lead to significant performance losses. In the event of exposure to ambient conditions devices would fail rapidly due to the fast diffusion kinetics of oxygen and the presence of water that accelerates the degradation mechanism. It is also worth noting that in the control experiments where the pre-soaked films were subjected to nitrogen and illumination, no losses in the yield of charge separation were observed. This clearly demonstrates the significant role oxygen still plays within this degradation mechanism and in the time frame of these experimental conditions the impact of moisture on optoelectronic properties is negligible. The obtained TAS spectrum's for the systems exposed to nitrogen and light are displayed in Figures 7.7a-c, for the 0%, 25% and the 85% RH samples respectively.

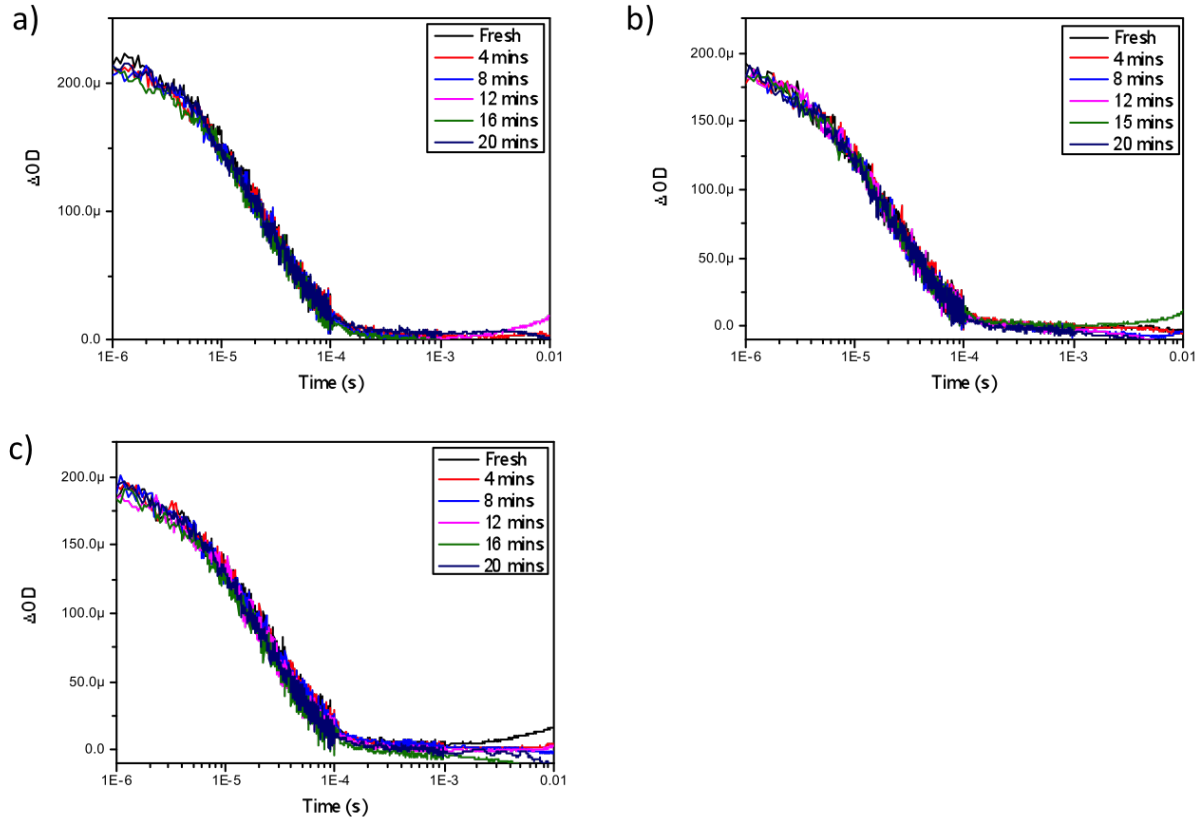


Figure 7.7: Transient absorption spectroscopy charge separation lifetime decay spectrums highlighting the degradation rate differences between $CH_3NH_3PbI_3$ pre-treated under a) no moisture 0% , b) 25% RH and c) 85% RH upon exposure to nitrogen and light at t=0. All films were excited with a pump wavelength of 567 nm and an average power of 23 $\mu$J cm$^{-2}$ and a probe wavelength of 1600 nm was employed to probe the resulting holes in spiro-OMeTAD.

So far the data collected indicates that device performance will be impacted by the presence and quantity of water contained within perovskite films. To probe this, functioning devices were created based on the following architecture: FTO/c-$TiO_2$/mp-$TiO_2$/ $CH_3NH_3PbI_3$/Spiro-OMeTAD/Au. Three systems within this architecture were created, where a device with a perovskite exposed to no moisture, 25% RH and 85% RH were fabricated. Again the water soaking treatment occurred once the perovskite layer was fabricated and before the subsequent layers were added to the configuration. The aim of this was once again to ensure minimal effect of water on any other layers and to ensure complete soaking of the perovskite layer occurred. The resulting devices were then exposed to dry air flow and one sun illumination and their PCE was recorded as a function of time exposed to the degradation conditions. The obtained J-V curves for this process are shown in Figures 7.8a to 7.8c. The rate of PCE decay as a function

of time for all three samples is displayed in Figure 7.8d.

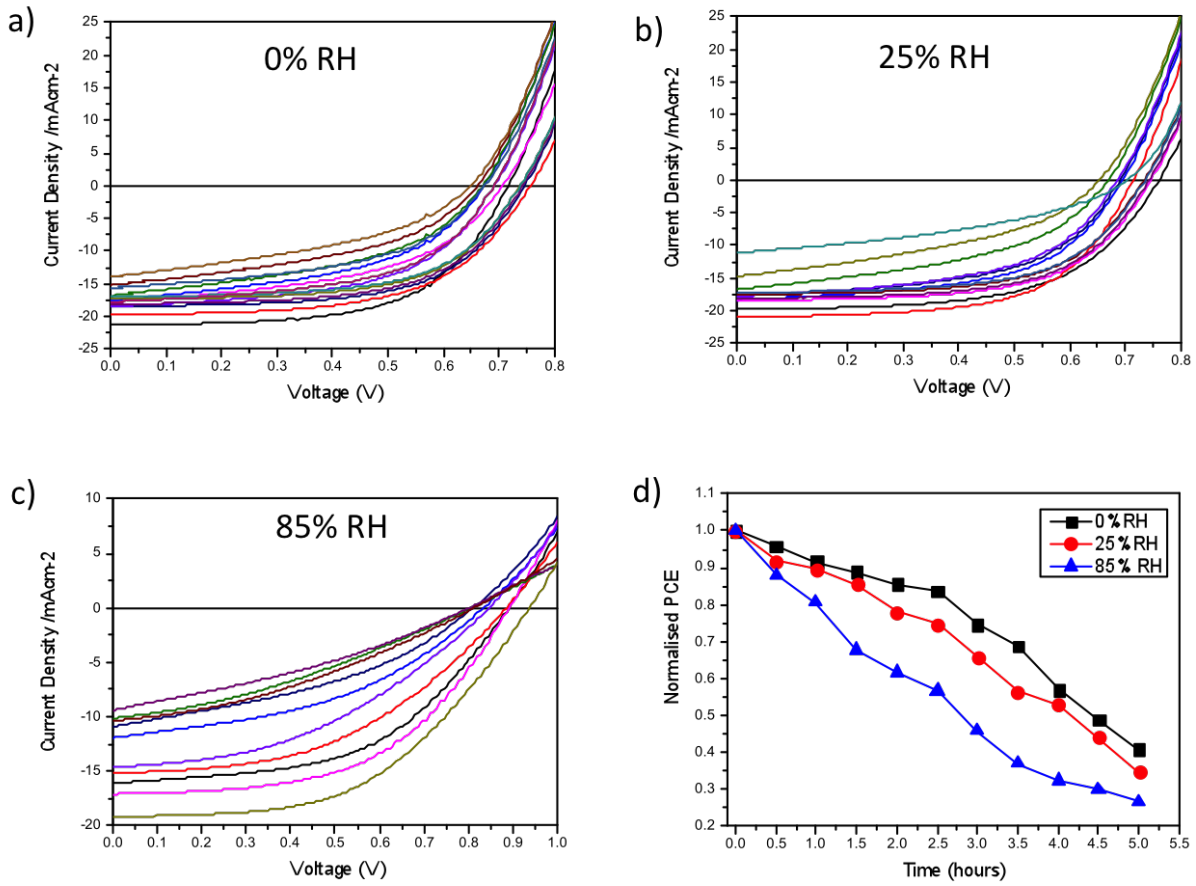


Figure 7.8: a-c) J-V curves obtained for perovskite films soaked in 0%, 25% and 85% RH respectively, in device architectures of the type: FTO/c-$TiO_2$/mp-$TiO_2$/ $CH_3NH_3PbI_3$/Spiro-OMeTAD/Au. d) Normalised PCE loss for the same device architecture and perovskite samples with varying levels of water content.

Figure 7.8d, clearly demonstrates that the rate of PCE decay of devices is impacted by the water content of perovskite films. Here the data shows that the film pre-soaked in an 85% RH (Blue trace) prior to exposure to oxygen and light suffers a 40% loss in device performance after 2 hours of exposure. In contrast the device that was subjected to a 25% RH (Red trace) environment only losses approximately 20% in performance. Further reducing the water content to no soaking (Black trace), shows that the device only suffers a 10% loss in efficiency over the same time period of exposure to oxygen flux and illumination. Consequently, this data supports the findings from the TAS data, suggesting that water enhances the degradation rate of oxygen and light breakdown of $CH_3NH_3PbI_3$. The impact of water enhances losses in charge

separation yield, leading to fewer excitons leading to current being extracted from devices. This then translates to losses in current in functioning devices, whilst the breakdown of the crystal into the degradation product changes the resistance and the electronic structure of the film leading to voltage losses. These features are observed in all the systems, Figure 7.8a-c. The consequence of both the current and the voltage reducing with time leads to efficiency losses in the devices and the rate at which this occurs is directly impacted by the water content in $CH_3NH_3PbI_3$ films. Overall, this further suggests that water enhances and accelerates the mode of superoxide degradation leading to faster decays in optoelectronic properties and ultimately device efficiencies.

## 7.5 Conclusions

A strong mix of photoluminescence, SIMS and ab initio simulation techniques has provided insights into combined humidity, oxygen and light-induced degradation of perovskite solar cells. The data presented has found that the rate of degradation is significantly increased when both oxygen and moisture are present in comparison to when just air or moisture is present alone. In addition is has shown that the yield of the reactive superoxide species is increased in the presence of moisture, and that this process cannot occur in the hydrated phases of $CH_3NH_3PbI_3$. All of this suggests that water stabilises the superoxide species and aids in their reduction via protonation, which enhances the overall degradation of the perovskite lattice. Finally, the impact on the device function was also assessed and both the yield of charge separation and the PCE were found to rapidly decline in combined air and moisture environments. Where a strong dependence on the water content was observed. Higher water content increased the rate of losses in these optoelectronic properties. In general, these findings suggest that other hybrid perovskites that are shown to yield superoxide species through the action of light and oxygen would also undergo accelerated degradation upon increased moisture content. Consequently, the ability to prevent not only oxygen but also moisture from entering these systems will be of utmost importance in designing optoelectronics with sufficient stability for real world function.

# References

[1] T. Leijtens, G. E. Eperon, N. K. Noel, S. N. Habisreutinger, A. Petrozza, H. J. Snaith, *Advanced Energy Materials*, 2015, **5**, 1500963.

[2] G. Niu, X. Guo, L. Wang, *J. Mater. Chem. A*, 2015, **3**, 8970–8980.

[3] T. A. Berhe, W.-N. Su, C.-H. Chen, C.-J. Pan, J.-H. Cheng, H.-M. Chen, M.-C. Tsai, L.-Y. Chen, A. A. Dubale, B.-J. Hwang, *Energy Environ. Sci.*, 2016, **9**, 323–356.

[4] Z. Li, M. Yang, J.-S. Park, S.-H. Wei, J. J. Berry, K. Zhu, *Chemistry of Materials*, 2016, **28**, 284–292.

[5] J. A. Christians, P. A. Miranda Herrera, P. V. Kamat, *Journal of the American Chemical Society*, 2015, **137**, 1530–1538.

[6] S. De Wolf, J. Holovsky, S.-J. Moon, P. Lper, B. Niesen, M. Ledinsky, F.-J. Haug, J.-H. Yum, C. Ballif, *The Journal of Physical Chemistry Letters*, 2014, **5**, 1035–1039.

[7] I. Deretzis, A. Alberti, G. Pellegrino, E. Smecca, F. Giannazzo, N. Sakai, T. Miyasaka, A. L. Magna, *Applied Physics Letters*, 2015, **106**, 131904.

[8] Y. Han, S. Meyer, Y. Dkhissi, K. Weber, J. M. Pringle, U. Bach, L. Spiccia, Y.-B. Cheng, *J. Mater. Chem. A*, 2015, **3**, 8139–8147.

[9] A. M. A. Leguy, Y. Hu, M. Campoy-Quiles, M. I. Alonso, O. J. Weber, P. Azarhoosh, M. van Schilfgaarde, M. T. Weller, T. Bein, J. Nelson, P. Docampo, P. R. F. Barnes, *Chemistry of Materials*, 2015, **27**, 3397–3407.

[10] E. Mosconi, J. M. Azpiroz, F. De Angelis, *Chemistry of Materials*, 2015, **27**, 4885–4892.

[11] G. Murugadoss, S. Tanaka, G. Mizuta, S. Kanaya, H. Nishino, T. Umeyama, H. Imahori, J. S. Ito, *J. Appl. Phys.*, 2015, **54**, 08KF08.

[12] G. Niu, W. Li, F. Meng, L. Wang, H. Dong, Y. Qiu, *J. Mater. Chem. A*, 2014, **2**, 705–710.

[13] J. H. Noh, S. H. Im, J. H. Heo, T. N. Mandal, S. I. Seok, *Nano Lett.*, 2013, **13**, 1764–1769.

[14] B. Philippe, B.-W. Park, R. Lindblad, J. Oscarsson, S. Ahmadi, E. M. J. Johansson, H. Rensmo, *Chemistry of Materials*, 2015, **27**, 1720–1731.

[15] M. Shirayama, M. Kato, T. Miyadera, T. Sugita, T. Fujiseki, S. Hara, H. Kadowaki, D. Murata, M. Chikamatsu, H. Fujiwara, *Journal of Applied Physics*, 2016, **119**, 115501.

[16] C. C. Stoumpos, C. D. Malliakas, M. G. Kanatzidis, *Inorg. Chem.*, 2013, **52**, 90199038.

[17] I. C. Smith, E. T. Hoke, D. SolisIbarra, M. D. McGehee, H. I. Karunadasa, *Angew. Chem. Intern. Ed.*, 2014, **53**, 11232–11235.

[18] E. Tenuta, C. Zheng, O. Rubel, H. Suga, H. J. Snaith, *Sci. Rep.*, 2016, **6**, 37654.

[19] C.-J. Tong, W. Geng, Z.-K. Tang, C.-Y. Yam, X.-L. Fan, J. Liu, W.-M. Lau, L.-M. Liu, *The Journal of Physical Chemistry Letters*, 2015, **6**, 3289–3295.

[20] J. Yang, B. D. Siempelkamp, D. Liu, T. L. Kelly, *ACS Nano*, 2015.

[21] H. Yuan, E. Debroye, K. Janssen, H. Naiki, C. Steuwe, G. Lu, M. Moris, E. Orgiu, H. Uji-i, F. De Schryver, P. Samor, J. Hofkens, M. Roeffaers, *J. Phys. Chem. Lett.*, 2016, **7**, 561–566.

[22] W. Zhang, S. Pathak, N. Sakai, T. Stergiopoulos, P. K. Nayak, N. K. Noel, A. A. Haghighirad, V. M. Burlakov, D. W. deQuilettes, A. Sadhanala, W. Li, L. Wang, D. S. Ginger, R. H. Friend, H. J. Snaith, *Nat. Commun.*, 2016, **6**, 10030.

[23] J. Chun-Ren Ke, A. S. Walton, D. J. Lewis, A. Tedstone, P. O'Brien, A. G. Thomas, W. R. Flavell, *Chem. Commun.*, 2017, **53**, 5231–5234.

[24] W. Hao, X. Chen, S. Li, *The Journal of Physical Chemistry C*, 2016, **120**, 28448–28455.

[25] M. L. Petrus, Y. Hu, D. Moia, P. Calado, A. M. A. Leguy, P. R. F. Barnes, P. Docampo, *ChemSusChem*, 2016, **9**, 2699–2707.

[26] C. Clegg, I. G. Hill, *RSC Adv.*, 2016, **6**, 5244852458.

[27] A. Alberti, I. Deretzis, G. Mannino, E. Smecca, S. Sanzaro, Y. Numata, T. Miyasaka, A. La Magna, *J. Phys. Chem. C.*, 2017, **121**, 13577–13585.

[28] T. Zhang, X. Meng, Y. Bai, S. Xiao, C. Hu, Y. Yang, H. Chen, S. Yang, *J. Mater. Chem. A*, 2017, **5**, 1103–1111.

[29] N.-K. Kim, Y. H. Min, S. Noh, E. Cho, G. Jeong, M. Joo, S.-W. Ahn, J. S. Lee, S. Kim, K. Ihm, H. Ahn, Y. Kang, H.-S. Lee, D. Kim, *J. Phys. Chem. Lett.*, 2017, **7**, 4645.

[30] C. Mller, T. Glaser, M. Plogmeyer, M. Sendner, S. Dring, A. A. Bakulin, C. Brzuska, R. Scheer, M. S. Pshenichnikov, W. Kowalsky, A. Pucci, R. Lovrini, *Chem. Mater.*, 2015, **27**, 7835–7841.

[31] G. Grancini, V. D'Innocenzo, E. R. Dohner, N. Martino, A. R. Srimath Kandada, E. Mosconi, F. De Angelis, H. I. Karunadasa, E. T. Hoke, A. Petrozza, *Chem. Sci.*, 2015, **6**, 7305–7310.

[32] J. F. Galisteo-Lpez, M. Anaya, M. E. Calvo, H. Mguez, *J. Phys. Chem. Lett.*, 2015, **6**, 2200–2205.

[33] G. E. Eperon, S. N. Habisreutinger, T. Leijtens, B. J. Bruijnaers, J. J. van Franeker, D. W. deQuilettes, S. Pathak, R. J. Sutton, G. Grancini, D. S. Ginger, R. A. J. Janssen, A. Petrozza, H. J. Snaith, *ACS. Nano.*, 2015, **9**, 9380–9393.

[34] X. Gong, M. Li, X. Shi, H. Ma, Z. Wang, L. Liao, *Ad. Funct. Mater.*, 2015, **25**, 6671–6678.

[35] N. Aristidou, I. Sanchez-Molina, T. Chotchuangchutchaval, M. Brown, L. Martinez, T. Rath, S. A. Haque, *Angewandte Chemie International Edition*, 2015, **54**, 8208–8212.

[36] D. Bryant, N. Aristidou, S. Pont, I. Sanchez-Molina, T. Chotchunangatchaval, S. Wheeler, J. R. Durrant, S. A. Haque, *Energy Environ. Sci.*, 2016, **9**, 1655–1660.

[37] N. Aristidou, C. Eames, I. Sanchez-Molina, X. Bu, J. Kosco, M. S. Islam, S. A. Haque, *Nat. Comm.*, 2017, **8**, 15218.

[38] F. T. O'Mahony, Y. H. Lee, C. Jellett, S. Dmitrov, D. T. Bryant, J. R. Durrant, B. C. O'Regan, M. Graetzel, M. K. Nazeeruddin, S. A. Haque, *J. Mater. Chem. A*, 2015.

[39] D. T. Sawyer, J. S. Valentinel, *Acc. Chem. Res.*, 1981, **14**, 393400.

[40] C. F. Forney, D. G. Brandl, *Technology and Product Reports*, 1992, **2**, 52–54.

[41] C. A. Hollingsworth, P. G. Seybold, C. M. Hadad, *J. Quantum Chem.*, 2002, **90**, 1396–1403.

# Chapter 8

# Understanding the enhanced stability of bromide substitution in Methyl ammonium lead halide perovskite films.

## 8.1 Introduction

The previous chapters have highlighted the susceptibility of the archetypal $CH_3NH_3PbI_3$ to degrade under both dry and humid environments when illuminated with oxygen present. In the investigations the experiments have identified that iodide vacancies, $V_I$, have been vital in generating the problematic reactive oxygen species, superoxide. Having previously shown that iodide defect passivation through salt treatment can increase material tolerance towards environmental stress, the generation of more intrinsically stable films coupled with salt coatings could be key to generating a material with real commercial viability. In Chapter 4, the impact of changing the cation revealed that stability could be enhanced through deactivating the deprotonation reaction. However, superoxide is still formed as a result of the persistent iodide defects. Although the perovskite layer could tolerate the superoxide stress, other layers in a device may begin to suffer, especially if organic layers are used, namely as the hole transporting layer. Since, these layers are adjacent to the superoxide formed from the perovskite phase could cause a range of interfacial separation issues leading to performance breakdown of an operating

device. To reduce the generation of superoxide, it is clear that iodide vacancies need to be removed. A potential method to achieve this may be possible through anion substitution.

Recent publications have observed that anion substitution (bromide for iodide) to create mixed anion perovskite films has generated longer operational lifetimes and higher power conversion efficiencies.[1, 2, 3, 4, 5, 6, 7, 8, 9, 10, 11, 12, 13, 14, 15] In particular, $CH_3NH_3Pb(I_{(1-x)}Br_x)_3$ has been reported to show enhanced stability towards ambient conditions and increased moisture tolerance when the bromide content is increased.[4, 16] However, research investigating oxygen and light degradation in mixed bromide/iodide perovskites has been absent from the literature. The origin of enhanced stability with increased bromide substitution is not fully understood and therefore remains unclear. It is reasonable to suppose that this stability enhancement could originate as a result of reducing the number of iodide vacancies within the structure, thereby reducing the number of active sites that can yield superoxide. In this study, this potential phenomenon is examined by exploiting a range of computational and experimental techniques, such as Ab-initio DFT, UV/VIS, Fluorescence, Time-resolved Photoluminescence (TRPL) and Transient absorption spectroscopy (TAS). These techniques were selected as they have previously been shown to help identify the rate of degradation and the yield of superoxide along with the impact on charge separation.[17, 18, 19, 20, 21, 22, 23] First examined is the correlation between superoxide generation yield and material stability as a function of bromide substitution using these techniques. Beyond this, the work investigates the potential role that iodide salt coatings can play in obtaining a more stable film composition as well as using it to support the hypothesis of reduced iodide defects for increasing bromide substitution. This will be achieved through simultaneously varying the concentration of salt coating deposited and the bromide composition of the films.

## 8.2 Thin film stability and superoxide characterisation

To first assess the stability of $CH_3NH_3Pb(I_{(1-x)}Br_x)_3$ perovskite films towards dry air (oxygen) and light films were deposited on cleaned plain glass. Following this UV/VIS spectroscopy

was employed to monitor the degradation. The method used is in accordance to the work set out in the previous chapters and studies, where a selected wavelength is used to monitor the transformation from the starting material to the degradation products.[17, 19] This is possible as the degradation mechanism results in a colour change from the dark perovskite phase to a yellow lead iodide phase. The degradation products have been identified and reported in the previous findings.[17] A range of values from x=0-1, were selected to explore the impact of bromide substitution on stability towards the degradation conditions. The results of this are presented in Figure 8.1a. The optical degradation measurement highlights that in all cases where iodide is present degradation occurs. Importantly though, the time taken to degrade decreases with increasing bromide content. To emphasize this, the pristine methyl ammonium lead iodide film (x=0) completely degrades within 100 hours whilst when 75% bromide (x=0.75) substitution has occurred degradation takes over 400 hours. Continuing the substitution to the point when no iodide is present, $MAPbBr_3$ films, exhibits little to no observable degradation under the time frame investigated. This infers that enhanced stability can be brought about by bromide substitution. Hypothesized from this, is that the observed enhanced stability is induced by a reduction in the number of iodide vacancies present. Since, these vacancies have been shown to be the most favourable site for superoxide production (Chapter 5)[19], thus if they are reduced the yield of superoxide will also decrease leading to enhanced stability of films. To probe this, the previously reported superoxide yield test was used to measure the yields from films and confirm if there was a trend between increasing bromide content and decreased superoxide generation. Figure 8.1b, shows the obtained superoxide yields for the same film compositions explored in Figure 8.1a. The data collected confirms our original hypothesis and illustrates that increasing bromide content reduces superoxide yields and enhances stability towards oxygen and light.

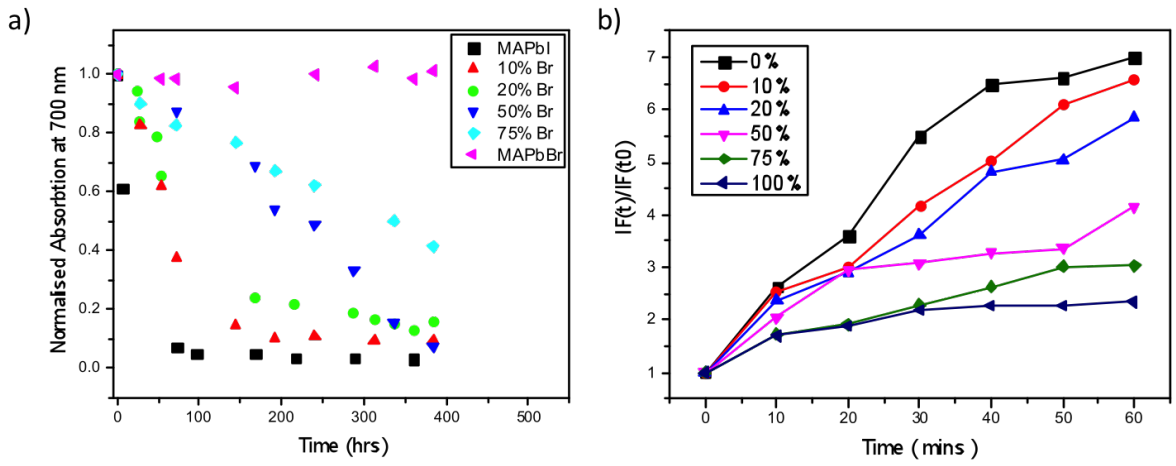


Figure 8.1: a) Normalised absorbance decays as a function of aging under oxygen and light conditions for $CH_3NH_3Pb(I_{(1-x)}Br_x)_3$ where x = 0, 0.1, 0.2, 0.5, 0.75 and 1. Films become more stable as the Bromine content increases. b) Superoxide yield generation for the same films compositions. Superoxide yields increase as the Iodide content increase

To probe the degradation in more detail, XRD characterisation of the degradation was conducted. Here, pristine mixed halide films were measured and the XRD for films after 6 hours of exposure to oxygen and light conditions were also recorded. Figure 8.2a-b, shows the spectral analysis of the crystal lattice before (black traces) and after exposure (red traces). The data in Figure 8.2a indicates a shift from the tetragonal $CH_3NH_3PbI_3$ peak ($2\theta = 14.2°$) to the cubic $CH_3NH_3PbBr_3$ peak ($2\theta = 15.05°$) with increasing bromide concentrations. Indicating that these films form intermixed structures on the X-ray length scale, approximately 75-100nm. Upon exposure to light and dry air flux degradation occurs, and consequently the crystal lattice peak of the mixed halide films (x= 0.25,0.5 and 0.75) shifts towards higher angles. This translates into a reduction in the iodide content in the perovskite regions of the films. Interestingly, the data (Figure 8.2b) clearly shows that the XRD peak of lead iodide is observed in all films that contain iodide, but no peak corresponding to lead bromide is observed. A peak at 12.2-12.4° should be observed if lead bromide was formed.[24] It is also important to highlight that at low iodide concentrations a larger full width at half maximum of the lead iodide peak is noted demonstrating a more amorphous structure. These findings, suggest that for the mixed halide systems a reduction in the iodide content of the perovskite phase occurs upon exposure to light and oxygen and results in the formation of lead iodide.

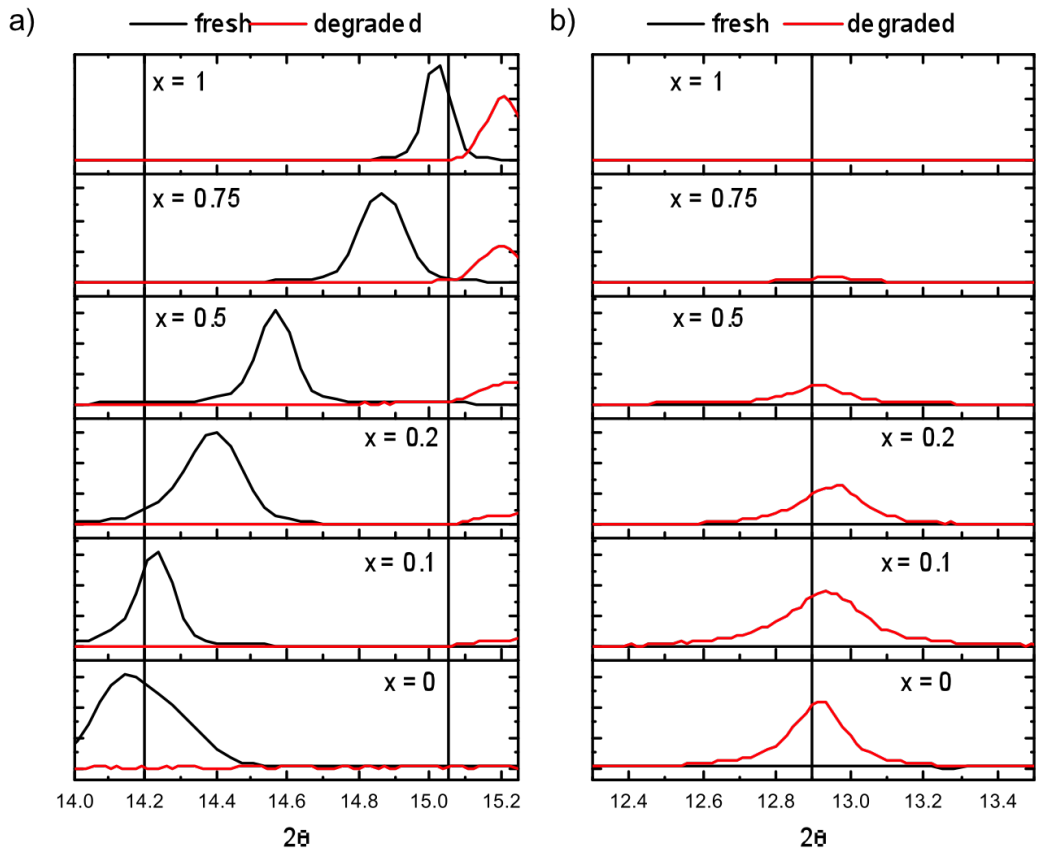


Figure 8.2: XRD spectrums of $CH_3NH_3Pb(I_{(1-x)}Br_x)_3$ films before and after exposure to light and dry air for 6 hrs where, x = 0.0, 0.2, 0.5, 0.75, 1.0. a) showing the region of the tetragonal (220) and cubic (200) peaks. Degraded films show a shift to the bromide, cubic structure indicating a loss of the iodide perovskite phase. At x = 1.0, the peak is shown to be very stable. b) XRD analysis focusing on the lead iodide peak showing the formation of lead iodide in all halide ratios, but not lead bromide. At lower iodide ratios, the FWHM greatly increases due to the formation being more amorphous.

In combination, these findings so far demonstrate that increasing bromide content does induce enhanced stability, through reducing superoxide yields. Critically though, in the mixed halide systems only the formation of lead iodide occurs, leading to reduced iodide content perovskite phases being produced. From this, it could be suggested that only the iodide rich phases are degrading. Literature has shown that under illumination phase segregation can occur,[13, 15] applying this to the data obtained herein leads to the concept that illumination separates the phases and only the $CH_3NH_3PbI_3$ phase degrades whilst the $CH_3NH_3PbBr_3$ remains. Superoxide yields can then be rationalised as there will be less iodide rich phases as bromide content increases and so there is less material that can produce superoxide as efficiently.

Since some superoxide is produced even from the pure bromide sample, superoxide may still form from bromide defects but there may be fewer defects present or it breaks down the crystal with less efficacy as the bromide structure is more resistant to superoxide. This phenomenon will be explored later on. This hypothesis, attains support from the extreme cases where only one anion is present. In the iodide only system degradation occurs whilst in contrast no degradation occurs in the bromide only system.

Computational calculations have been conducted by Bath university to calculate the energy of the reaction of the mixed halide perovskites with oxygen and with superoxide. The energies were calculated for the following reactions:

$$CH_3NH_3Pb(I_{1-x}Br_x)_3 + O_2 \longrightarrow PbX_2 + CH_3NH_3X + H_2O + X_2 \tag{8.1}$$

$$CH_3NH_3Pb(I_{1-x}Br_x)_3 + O_2^- \longrightarrow PbX_2 + CH_3NH_3X + H_2O + X_2 \tag{8.2}$$

The energies, Figure 8.3, show that the in all halide compositions that the reaction energy is positive and therefore unfavourable with oxygen. When superoxide is used the degradation of the crystal occurs as the reaction energy becomes negative, the energies shift downward (red line to blue line). This is in-line with previous calculations and experimental observations seen in pristine iodide perovskite samples and mixed cation perovskites. Critically, only low bromide composition films, x is less than 1.0, exhibit negative reaction energies. This reveals that the reaction with superoxide becomes less favourable as the bromide content increases. Since the reaction is less favourable, this may account for the enhanced stability observed by bromide samples even though superoxide is generated. This further raises the question of whether fewer defects are present in bromide samples or if higher bromide content samples have an inherently more stable crystal structure towards superoxide.

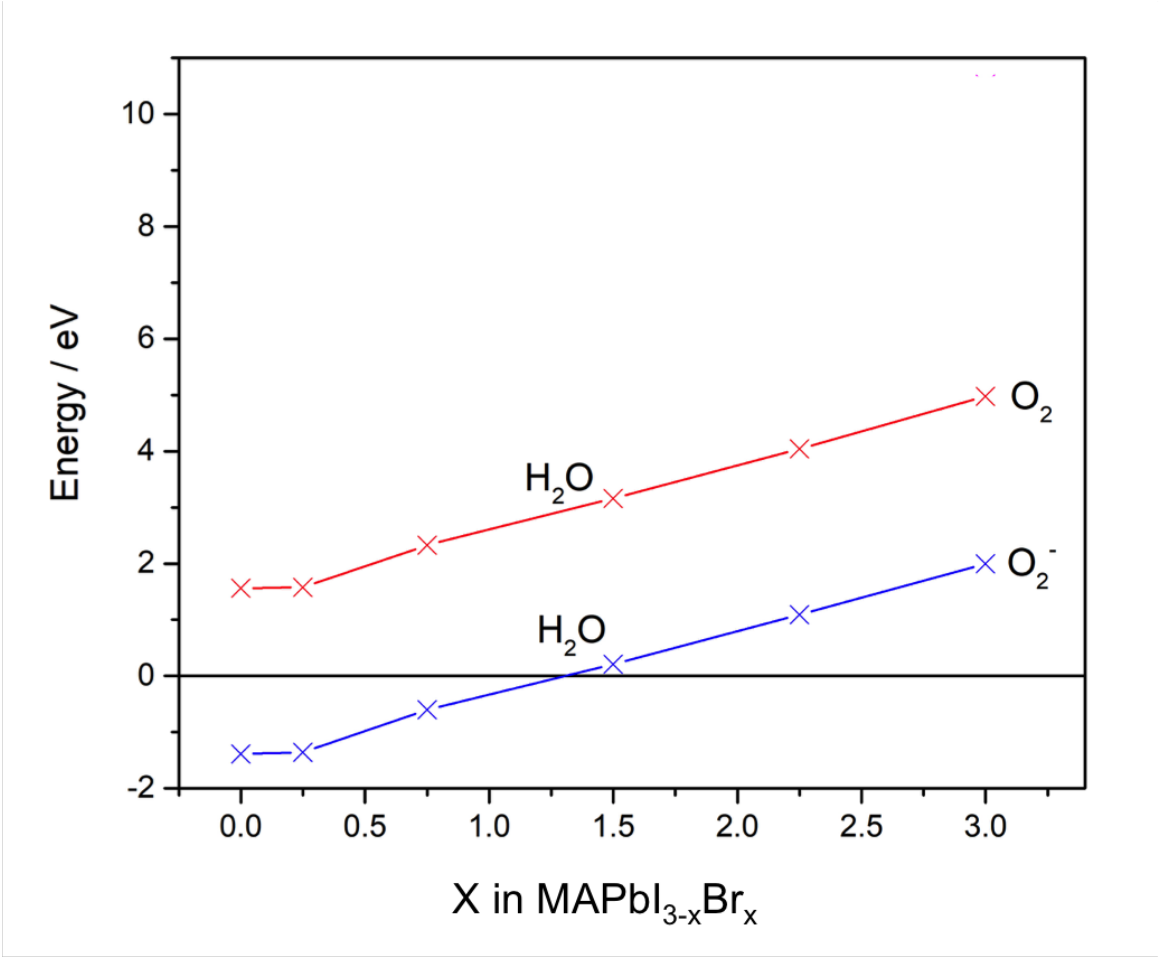


Figure 8.3: Calculated energies of reaction of $CH_3NH_3Pb(I_{(1-x)}Br_x)_3$ with oxygen and superoxide, with water production as the driving force. The energies were calculated for x= 0.0, 0.2, 0.5, 0.75 and 1.0. Results presented were obtained by Dr Alex Aziz of Bath university.

To identify the factors influencing the reactivity of the mixed halide perovskites with superoxide, additional computational experiments were employed to examine the change to bond strengths and lattice structure invoked by swapping iodide for bromide. A key factor identified is the bond dissociation energy. Where, Pb-I bonds are weaker than Pb-Br bonds. Consequently, when the perovskite crystal degrades the system loses lead-halide bonds and this accounts for a significant portion in the reaction energies. The following reaction and energies were calculated and obtained by Dr Alex Aziz:

$$CH_3NH_3PbX_3 + O_2 + hv \longrightarrow PbX_2 + CH_3NH_3X + H_2O + X_2 \tag{8.3}$$

$$PbI_2 \longrightarrow Pb + I_2 \quad \Delta E = 1.80eV \tag{8.4}$$

$$PbBr_2 \longrightarrow Pb + Br_2 \quad \Delta E = 3.07eV \tag{8.5}$$

From these calculations, it is noted that the stronger bonds of Pb-Br inherently make bromide perovskite systems more stable. This is because the energy required to lose these bonds is more significant compared to the weaker Pb-I system. Hence, more energy is required to breakdown perovskite crystal structures with increased bromide content, this is consistent with the previous findings that as bromide content increases the reaction with superoxide becomes less favourable (positive energy of reaction). A second factor that is induced by substituting bromide for iodide, is identified as a shrinking of the crystal lattice. As bromide is more electronegative than iodide, 2.96 vs 2.66 respectively,[25] increased H-bonding in the structure can occur. Consequently, increasing the strength of the H-bonding between protons on the cation with the halide anion causes the crystal structure to become more compact and causes a contraction in the lattice parameters. This contraction in the lattice, will inherently make the crystal structure more stable as the forces holding the crystal together are stronger and as such greater energies are required to overcome them if the crystal is to breakdown. The following Figure 8.4, shows that on swapping iodide for bromide leads to a contraction between the $NH_3^+$—X from 3.0$\mathring{A}$ to 2.8$\mathring{A}$ respectively at the longest distance found in the systems. A contraction in H-bonding length generates stronger forces of attraction.

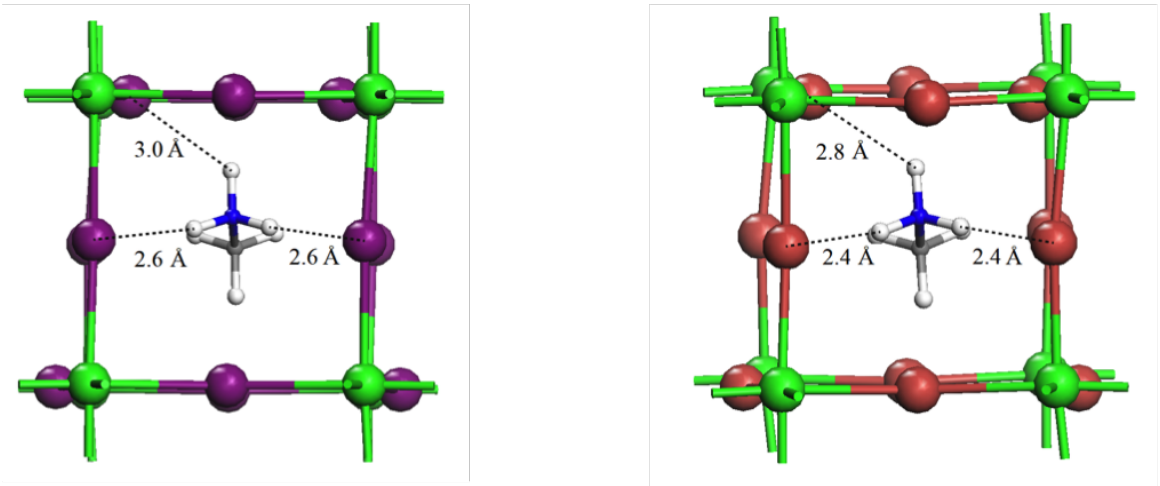


Figure 8.4: Diagrammatic illustration of the shorter H-bonding distances in $CH_3NH_3PbBRr_3$ compared to those in $CH_3NH_3PbI_3$. Computational results presented were obtained by Dr Alex Aziz of Bath university.

These results have shown that there is a fundamental weakness in the lead-iodide perovskite system, originating from its ability to efficiently produce superoxide and it's inherently weaker structure. As a result, systems with higher iodide proportions degrade rapidly when exposed to oxygen and light conditions. This has been shown by the increased degradation rate and the more favourable reaction energetics with superoxide. The systems is then vulnerable to superoxide, through iodide yielding weaker Pb-halide bonds and producing weaker H-bonding interactions. Furthermore, it is suspected that the quantity of defects also plays a vital role in the susceptibility of iodide rich perovskite systems towards oxygen and light. Since more superoxide is generated from these systems and it has previously been demonstrated that there is a strong correlation between iodide vacancy density and superoxide yield.

### 8.2.1 Superoxide formation from halide vacancies

Having previously established the favourable energetics of Iodide vacancies ($V_I$) to form superoxide, the energetics of bromide vacancies ($V_{Br}$) are now explored through computational simulations. It was shown that the size of iodide vacancies could also accommodate incoming oxygen and allow for superoxide to satisfy and restore the crystal octahedral structure. Since, Bromide is of a different ionic radii, this may cause the energetics of the superoxide formation reaction to change and to also impact the ability of the crystal structure to house superoxide. The exchange of iodide for bromide was simulated and the resulting energy of superoxide formation was calculated in both vacancy sites within the mixed halide systems. The resulting energies are displayed graphically in Figure 8.5 below. Additionally, the ionic radii of superoxide, bromide and iodide are displayed as an inset in the figure.

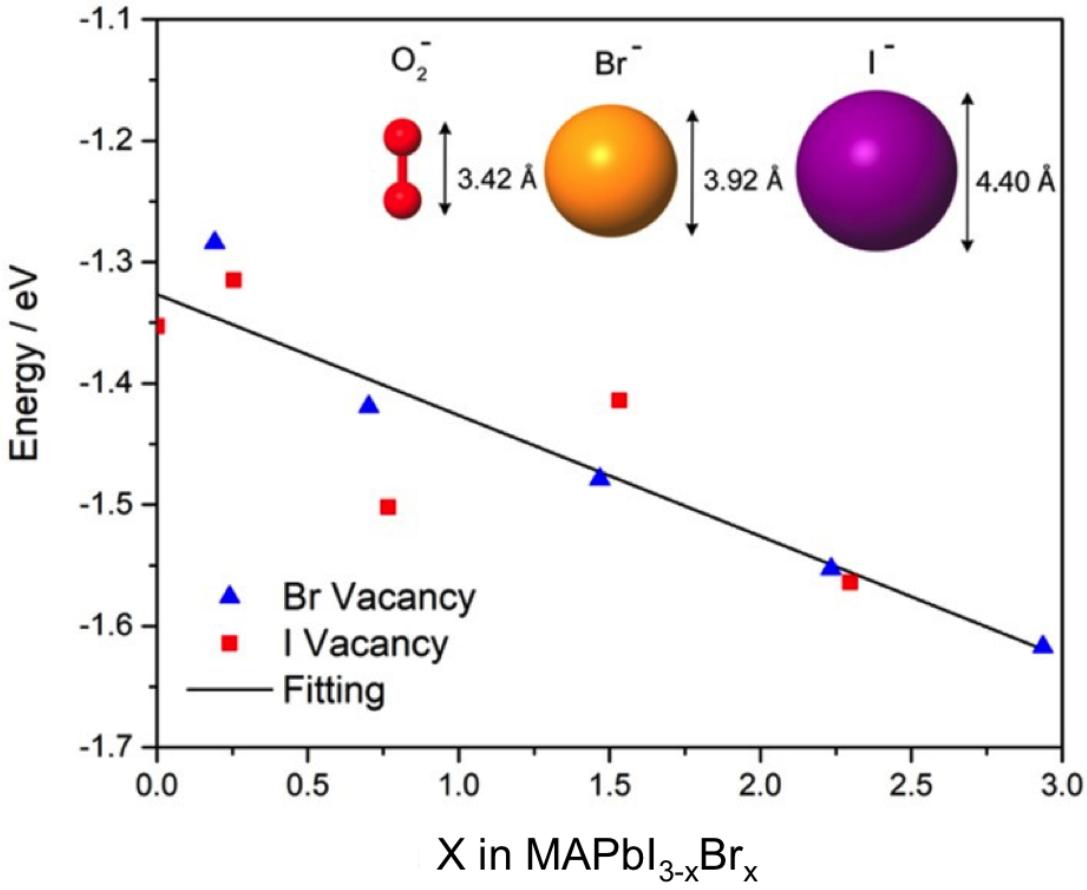


Figure 8.5: Superoxide formation energy as a function of changing halide composition. Red data points are the energy of superoxide formation in iodide vacancies, whilst blue points are the energy of formation of superoxide from bromide vacancies. Results presented were obtained by Dr Alex Aziz of Bath university.

Figure 8.5, shows that superoxide is formed in all vacancies and in all halide compositions. In all cases the energy is negative and favourable, consistent with the observed experimental data that all films produced superoxide. Interestingly, the contraction caused by substituting iodide for bromide leads to a decrease in superoxide formation energies, superoxide becomes more favourable to form with increasing bromide content. This may be rationalised by the fact that bromide vacancies are closer in size to the superoxide ion, where comparing the ionic radii it is noted that superoxide ($3.42\mathring{A}$) is closer to the size of bromide ($3.92\mathring{A}$) than iodide ($4.40\mathring{A}$). This better fit of superoxide will allow for better energetic match for the electron transfer process and lead to a greater stabilisation once superoxide forms, resulting in a more stable intermediate state. In turn this leads to more favourable energetics of superoxide formation. However, this result would suggest that more superoxide should have been recorded from the

perovskite films with higher bromide content. The $MAPbBr_3$ perovskite should have exhibited the greatest superoxide yield. Experimentally, this was not the case and the inverse trend was observed. Having established a clear relationship between defect density and superoxide yield in the previous works on $MAPbI_3$, this would indicate that bromide vacancies are less prevalent. If there are fewer defects then less superoxide can form, independently of how easily superoxide could form if they were present.

### 8.2.2 Oxygen diffusion and accommodation

Expanding on these findings, is to understand how the role of oxygen diffusion into films may be impacted by bromide substitution and if this can additionally account for enhanced stability. It is now suspected that fewer vacancies are present in bromide rich compositions as the energy of formation increases with increasing bromide content. If the lattice is shrinking as suggested by the computational experiments, then the ability of films to store oxygen may be impacted. From the previous findings on $MAPbI_3$, it was shown that oxygen uptake was rapid and films were saturated with oxygen. To investigate impact of bromide substitution and lattice shrinking, the previously reported technique of Isothermal gravimetric analysis (IGA) was used.[19] Samples are prepared and sealed in an inert atmosphere, and then the weight increase is measured as a function of time to oxygen flux into the chamber. From this, the time taken for films to saturate with oxygen can be extracted and secondly the experiment can demonstrate the normalised weight increase, which is proportional to the amount of oxygen that is then stored in the film. Here, these features are explored on five films with bromide substitution in the range, x=0-1 (Figure 8.6).

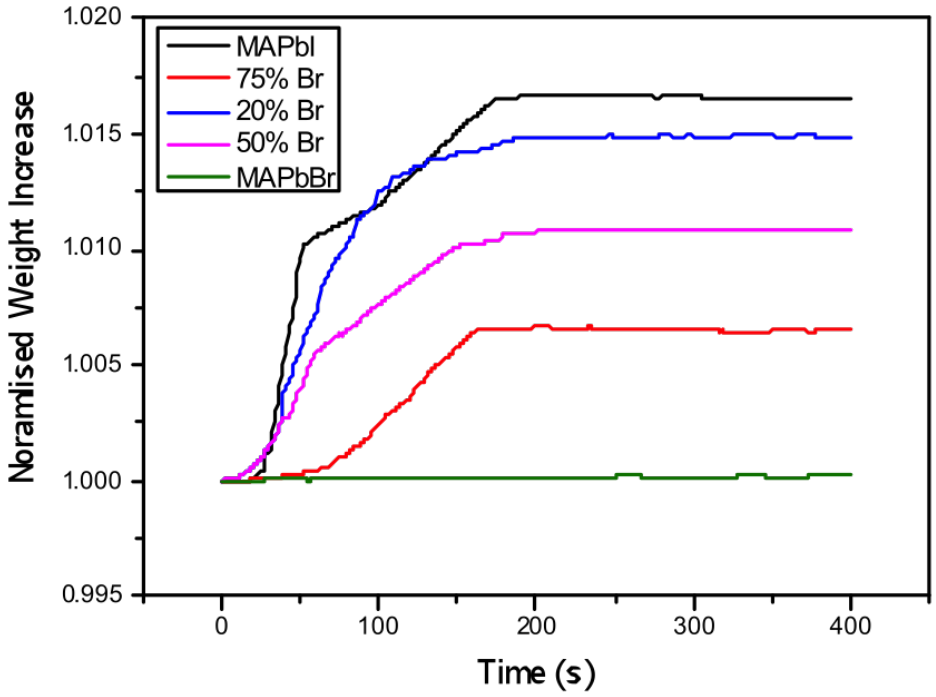


Figure 8.6: IGA data and the oxygen diffusion into films of $CH_3NH_3Pb(I_{(1-x)}Br_x)_3$ with x = 0.0, 0.2, 0.5, 0.75 and 1.0.

The data presented highlights two key pieces of information. First, the time taken to reach saturation appears to be independent of bromide substitution and secondly the weight increase decreases as a function of increasing bromide substitution. This implies exchanging iodide ions for bromide does not hinder the rate of oxygen diffusion. However, it does impact the availability for oxygen to be stored within films. This is consitent with the hypothesis that this is a direct consequence of removal of vacancies, as fewer halide vacancies form as bromide content is increased. Having shown through computational experiments that bromide ions are of similar size to oxygen. These vacancies should then be optimal to accommodate incoming oxygen and the resulting superoxide radical ion that forms during the photo-degradation process when films are exposed to dry air flux and light. It therefore follows that there are fewer bromide vacancies, which can store oxygen as the weight increase is reduced as bromide composition is raised. Further support is provided by the TRPL data that has indicated reduced defect concentration. Both iodide and bromide vacancies would provide non-radiative trap sites but increasing bromide content increases emission intensity and life-time. Consequently, the impact of exchanging iodide

for bromide leads to less oxygen stored within films, which can also account for the reduced superoxide yields observed for higher substitution levels. The effect of substitution therefore has a twofold impact on stability: i) less oxygen is available to undergo the parasitic electron transfer reaction and ii) there are fewer defects where the transfer can occur.

## 8.3 Salt passivation and iodide vacancy concentration

Having established that increased bromide content can induce enhanced stability, via reducing the superoxide yield, it could be desirable to move towards these mixed halide derivatives for solar cell devices. However, as the bromide content increases the optical properties become less favourable for highly efficient photovoltaic devices. Whereupon increasing bromide content the band edge shifts and there is less absorption at higher wavelengths. This translates to wasted energy and less efficient solar cell devices. Consequently, it is worth considering if stability can be further enhanced by employing the iodide salt treatments,[19] with the primary aim of seeing if enhanced stability can be achieved in the intrinsically more stable mixed halide films. As a secondary aim the experiments using salt passivation with altering concentrations could further prove that if there are fewer defects in the higher bromide content films. Here, the concentration of the salt treatment used to enhance stability should be lower as the bromide concentration increases. In these experiments methyl ammonium iodide (MAI) with concentrations of 0.01M, 0.005M and 0.001M were generted and applied to films with bromide content of x=0.2, x=0.5 and x=0.75. As above, UV/VIS was used to trace the degradation towards oxygen and light at a selected wavelength and the data normalised with respect to the fresh sample of each film and coating combination. The results of these salt treatment stability measurements are presented in Figure 8.7a-c.

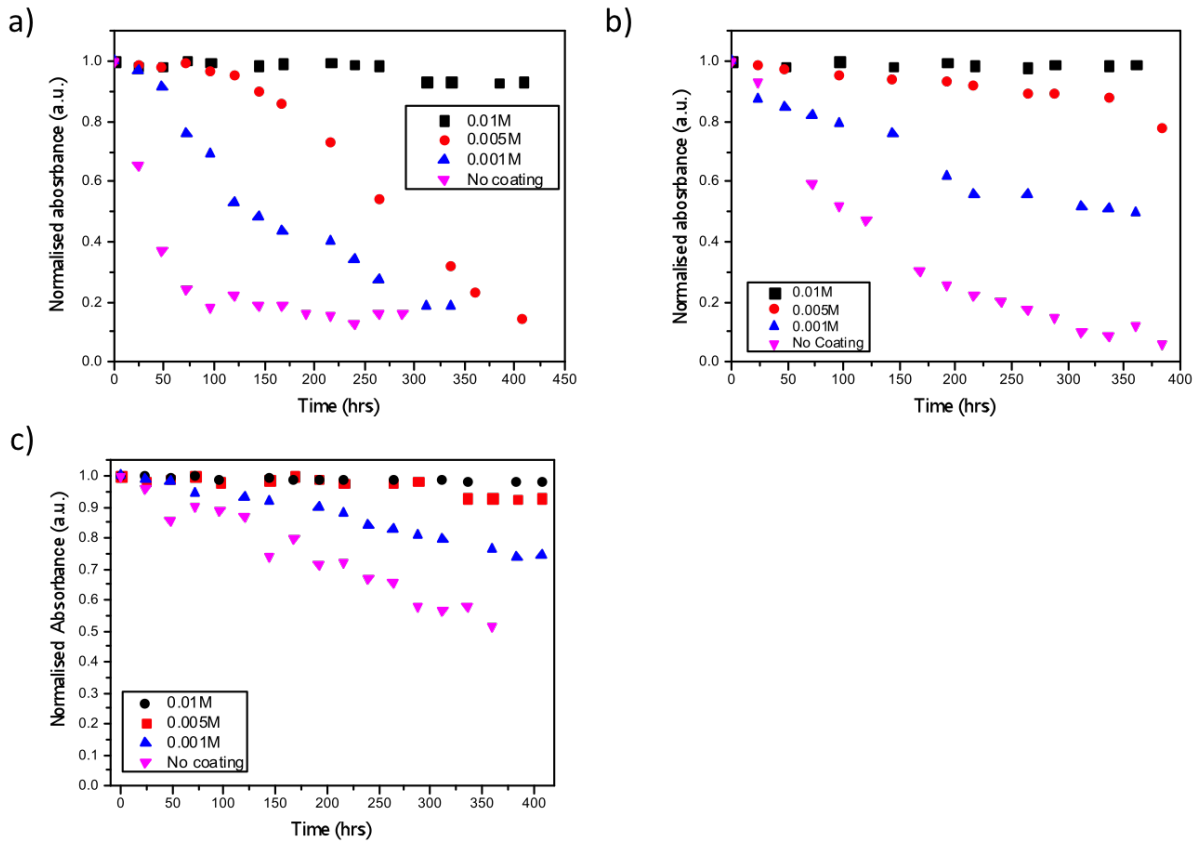


Figure 8.7: Application of MAI salt coatings (0.01M, 0.005M and 0.001M) to mixed halide systems with compositions of a) x=0.2, b) x=0.5 and c) x=0.75 and the impact on the normalised absorbance decay with exposure to the degradation conditions. As bromide content increase the salt concentration required to increase stability decreases.

It is clear from the data that the stability of all samples examined could be improved by the application of the MAI salt coating, and the stability enhancement is proportional to the amount of coating used. Where increasing coating concentration increases stability towards oxygen and light, this is in agreement with the previous studies on coating pristine $MAPbI_3$, (Chapter 5).[19] In the highest concentration applied (0.01M) all films gain enhanced lifetime, where little to no observable degradation occurs over the time frame examined. This implies that using this concentration passivates the majority of the defects within the films. A key observation from the experiment relates to the concentration of the salt coating correlating to the increase in stability. Where, as the bromine content increases the amount of salt coating required to increase stability decreases. Extrapolated from this is that the higher bromine content samples contain fewer iodide defects, hence less coating concentration is required to satisfy the defects present in the perovskite film. To confirm the increased stability from the

salt treatments is owed to the passivation of iodide defects, reducing superoxide generation, the superoxide yield test as described previously was employed to the same film compositions with the same concentration of MAI coatings. The results of which are presented in Figure 8.8a-c.

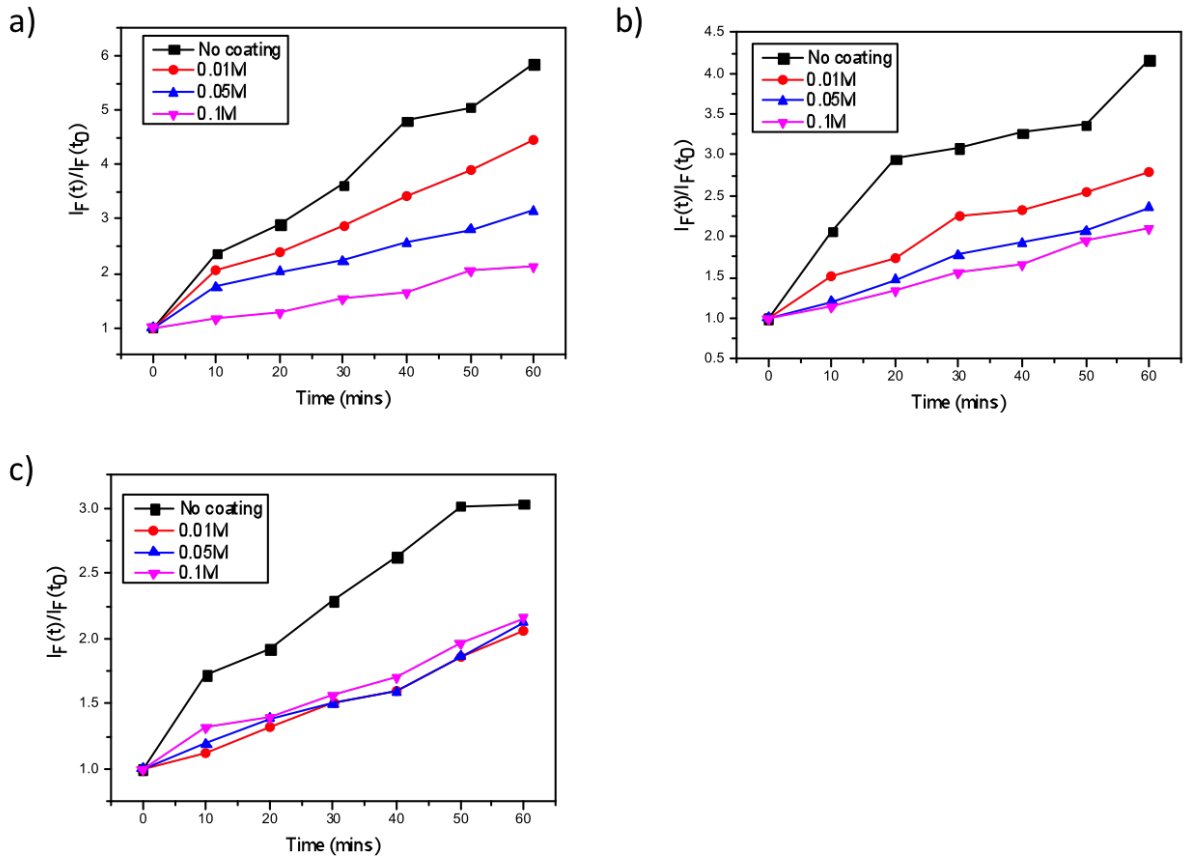


Figure 8.8: Superoxide generation yields for film compositions of a) x=0.2, b) x=0.5 and c) x=0.75 as a function of MAI salt coating (0.01M, 0.005M and 0.001M). Increasing bromide content reduces the salt concentration required to reduce the yields of superoxide .

The data reinforces our findings that for all bromide substitution compositions that increasing the salt treatment concentration leads to reduced superoxide yields. Likewise with the absorbance data in Figure 8.7a-c, the impact of the increasing concentration becomes less significant and lower concentrations of MAI can induce a greater impact on the yield. This further suggests that the quantities of iodide defects that are critical in the superoxide generation are reduced as the bromide content increases. Additionally, the impact of using Methyl ammonium bromide (MABr) as a stabilizing treatment was examined, which in agreement with the previous findings on alternative halide salts showed no improvement in increasing film lifetime or in reducing the

yield of superoxide.[19] The film coating was applied to both $MAPbI_3$ and $MAPbBr_3$ with a 0.01M concentration and the results of these experiments are shown in Figure 8.9a and b.

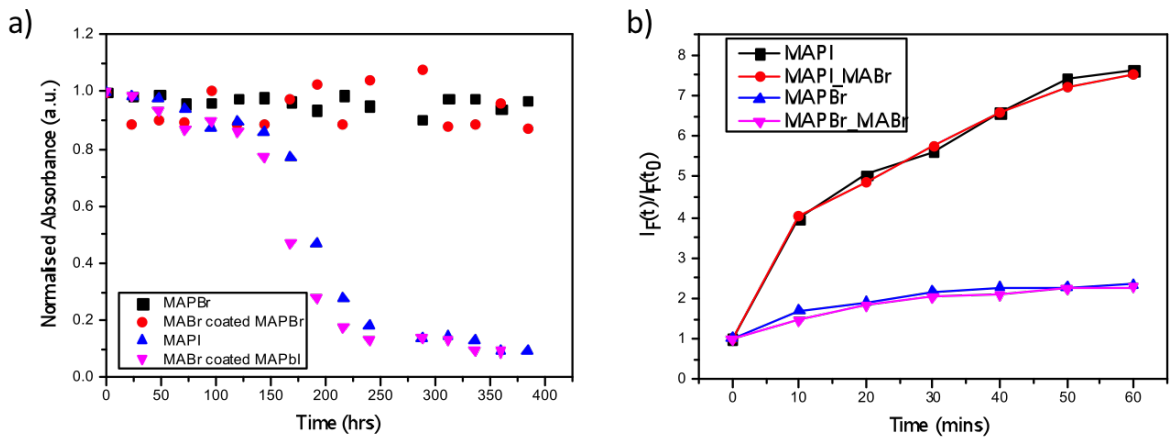


Figure 8.9: Application of MABr salt coating (0.01M) to both $MAPbI_3$ and $MAPbBr_3$ a) normalised absorbance degradation profile for both films with and without the coating. b) Superoxide generation yields for both films with and without the coating.

These findings further illustrate the key issues causing the fundamental instability of $MAPI_3$ towards oxygen and light as the Iodide defects. More importantly though, this illuminates the origin of enhanced stability owed to bromide substitution as a tool to decreasing the quantities of these vacancies.

### 8.3.1 Defect passivation for enhanced optoelectronic properties

To gain further insight into the role of bromide substitution and the impact of salt passivation, time-resolved Photoluminescence is again employed. Having already established that reduced iodide defect presence leads to longer emission lifetimes, the experiment sets out to monitor the impact of the salt coating on emission lifetime. It is hypothesised that applying the salt coating (0.01M MAI) to the mixed halide samples will increase emission life-time, as the coating will remove non-radiative recombination sites.[23, 26, 27, 28, 21, 29] Furthermore, as the bromide content of the perovskite phase increases the increase in emission intensity will be less pronounced as the number of non-radiative trap sites (Iodide vacancies, $V_I$) is proportional to the bromine content of the films. This relationship of bromine content correlating to emission lifetime was demonstrated in the previous time resolved photoluminescence experiments. Here, the TRPL

data is collected for samples with and without the salt coating to show its impact.

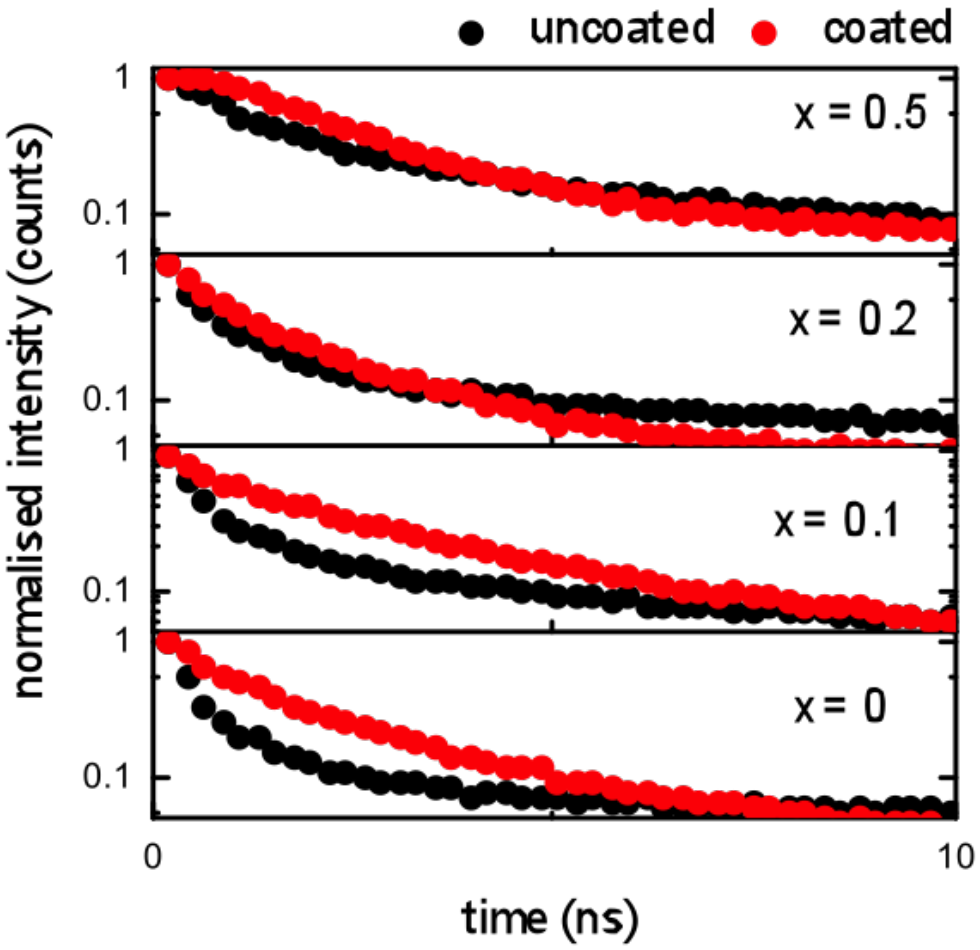


Figure 8.10: Time-resolved photoluminescence spectra for film compositions of x=0, x=0.1, x=0.2 and x=0.5 with and without a salt coating of 0.01M MAI. Salt coating concentration increases life-time emission intensity to a greater degree as the content of bromide decreases.

Figure 8.10, shows the TRPL data obtained for a range of four samples with a composition of x=0-0.5 with and without a MAI salt coating of 0.01M. Consistent with the previous findings, this result shows that increasing the bromide content from x=0 to x=0.5 generates longer emission lifetimes via a reduction in the number of iodide defects (reduced trap states). Now comparing the uncoated samples (black traces) with the MAI coated samples (red traces), it is also noted that there is an increase in PL lifetime. This demonstrates that the impact of passivating iodide vacancies leads to a reduced number of defect sites that increase quenching. It therefore follows that the impact bromide substitution has is to alleviate the number of

iodide vacancies and thus the number of trap states that reduce photoluminescence lifetime. Consequently, the role bromide substitution plays in enhancing stability towards oxygen and light is via defect reduction. Combining this with the findings described earlier supports that there is a strong correlation between bromide substitution and stability. Where increased bromide content reduces the presence of the problematic iodide defects that generate the key degradation component, superoxide. Furthermore, these findings reinforce the statement of the previous results that the fundamental flaw leading to the rapid degradation of $MAPbI_3$ is in most part associated with the presence of iodide defects.

## 8.4 Implications for device performance

Finally, the implications for charge separation losses upon exposure to oxygen and light for bromine substituted perovskite films are explored. The rate of these losses have been shown to be directly related to the decay of device performance in operating thin film perovskite solar cells.[18, 19] The yield of charge separation between the perovskite and hole-transporting phase, Spiro-OMeTAD, are measured using transient absorption spectroscopy. It has been shown that the yield between these phases decreases when films are exposed to dry air flux and light.[20] The rate of these loses is fast and of the order of the rate of oxygen diffusion into MAPI films, which suffer significant yield loses within 5-10 minutes. Films with substitution of x= 0, 0.2, 0.5, 0.75 and 1, are examined in an architecture of glass/mp-$Al_2O_3$/$CH_3NH_3Pb(I_{(1-x)}Br_x)_3$/Spiro-OMeTAD and probed at 1600 nm to obtain the charge separation yield. The $\Delta$OD value at 1 $\mu$s was obtained and then normalised against the starting value, where the sample has not been exposed to the degradation conditions. The films were then exposed to dry air flux and ambient illumination and measurements were recorded at regular time intervals over the course of an hour and under an inert nitrogen atmosphere. The normalised decay of charge separation loses for these samples are presented in Figure 8.11.

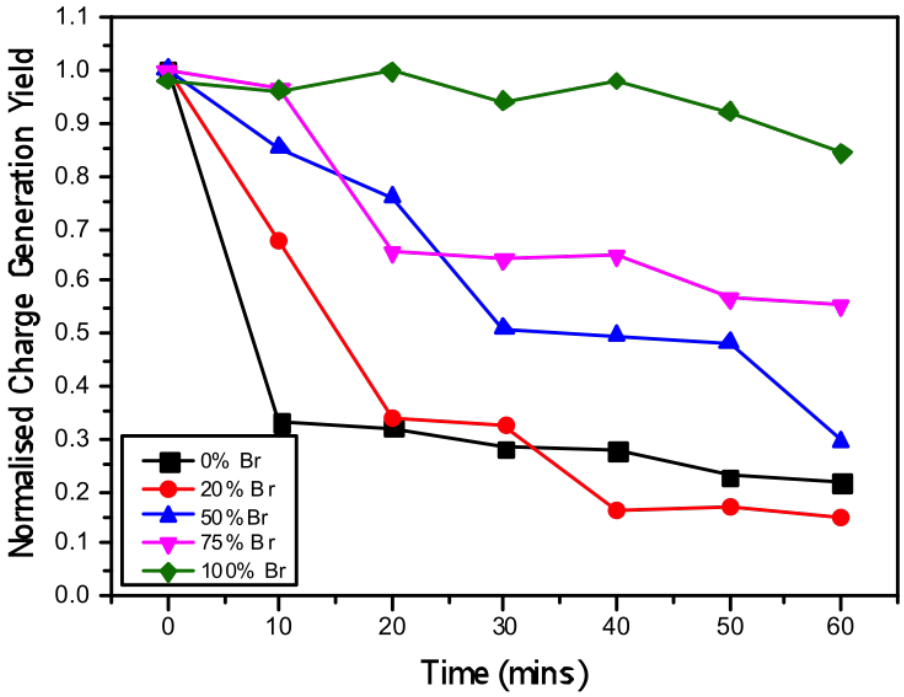


Figure 8.11: Normalised decay of charge separation loses, obtained from transient absorption spectroscopy for films with compositions x = 0, 0.1, 0.2, 0.5, 0.75 and 1. Charge losses are more rapid and significant for compositions with less bromide.

In accordance with the observations in the UV/VIS measurements, the rate of decay is reduced with increasing bromine content. Again for the fully substituted composition the impact on charge loss and therefore degradation is minimal, whilst in the lower substituted films charge loses are significant within the time frame explored. This is demonstrated in the figure by looking at the approximate time taken for the charge separation yield to drop by 50% (half-life). The time taken for this to occur increases approximately through 10, 15, 40 and 60+ minutes for the films x= 0, 0.2, 0.5 and 0.75, respectively. This further supports the findings that bromine substitution enhances stability towards oxygen and light, allowing films to retain optoelectronic properties for longer periods of time. This critically means that the number of holes being transferred from the perovskite phase to the hole-transporting layer is retained for a longer time upon exposure to the degradation conditions as bromine substitution increases. These findings overlap with the operational stability reported on these films,[16, 11, 10] where increasing bromine content creates more stable devices towards oxygen and light. Interestingly, combining this with the IGA

data in Figure 8.6, it is apparent that the exchange of iodide for bromide does not alter oxygen diffusion and therefore the rate of decay decrease is owed to reduced superoxide production. Further stipulating that the bromide substitution leads to reduced sites for superoxide formation.

Moreover, the application of the salt treatment to the mixed halide systems should result in charge separation losses being minimised, when the films are exposed to dry air flux and illumination. To test this, three mixed mixed halide films with 20%, 50% and 75% bromide content were probed using TAS and the effect of applying the salt coating was recorded. Individual films were recorded as uncoated and coated with a 0.01M MAI solution for all compositions. The 0.01M MAI concentration was employed, since this has been proven in the UV and superoxide experiments to cause the greatest level of stability enhancement in all halide compositions. The data was recorded using the same conditions as described previously and the results of the kinetic decay traces are shown in the following figure.

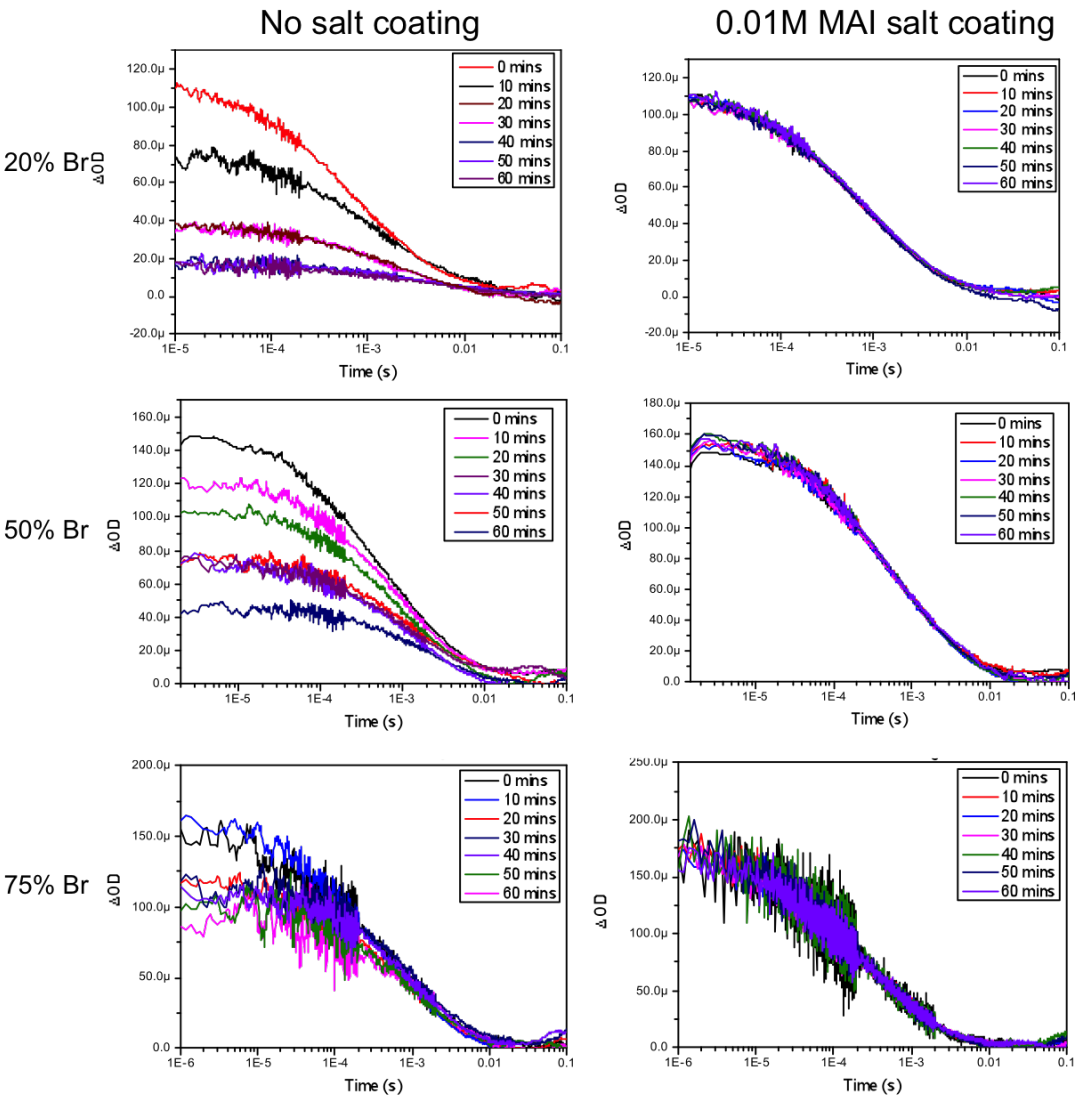


Figure 8.12: TAS kinetic decay traces for perovskite films without and with a 0.01M MAI coating. Left and right columns respectively. Descending down the rows increases the bromide content from 25% to 50% and to 75%.

Figure 8.12, highlights that the application of the MAI salt coating increases the stability of all halide compositions examined. Where, the magnitude of yield of charge separation is retained even after exposure to the degradation conditions. In all samples the coating leads to little to no degradation in the yield of charge separation over the time frame examined. This suggests, that the coating prevents the loss of charge carriers. The coating has been shown to alleviate defects and reduce superoxide production. Hence, the coating will remove sites where oxygen can satisfy the vacancies and reduces the number of parasitic electron transfer reactions that can occur from the perovskite phase to the incoming oxygen. Consequently more electrons, and therefore holes, can undergo transfer into their respective transport layers. TAS in these

experiments is measuring the number of holes in the Spiro-OMeTAD layer, so as the number of holes remains constant and their kinetic decay features remains the same the coating is serving to enhance stability by deactivating the transfer reaction to oxygen. Taking all previous findings into account, this confirms that the salt coating passivates Iodide vacancies, such that oxygen can't fill these sites where it would otherwise readily except a photo-excited electron from the perovskite phase. In contrast, when no coating is present, the magnitude of the charge separation yield decreases as a function of time under the oxygen and light atmosphere. Important to note when comparing the left hand panels in the figure, is that the rate and magnitude of the decrease is proportional to the bromide content. Increasing bromide content reduces the rate and retains the magnitude of the charge separation yield. It is hypothesized that this enhanced stability originates from the removal of iodide vacancies. Where as described and proved earlier this would lead to reduced sites for superoxide formation to occur from. To test this, employed in a systematic manner is the MAI salt treatment to MAPI (x=0, 0% Bromine). Where it is hypothesised that increasing the concentration of salt coating should decrease the number of iodide vacancies; in a similar way as increasing the bromine composition would reduce the number of these sites. Therefore both methods should increase stability and minimize charge loses. The same salt coating concentrations used previously (0.01M, 0.005M and 0.001M) are employed into the thin-film architecture glass/mp-$Al_2O_3$/$CH_3NH_3PbI_3$/Spiro-OMeTAD. The results of this investigation were obtained under the same conditions as described for the prior TAS measurements and equally the normalised charge yield decay for each sample is presented in Figure 8.13.

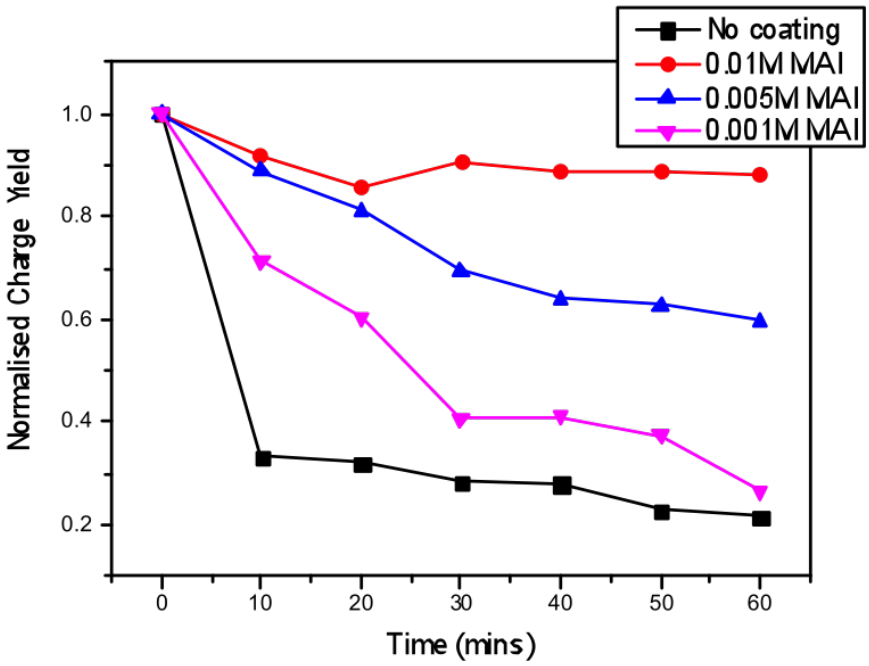


Figure 8.13: Normalised decay of charge separation loses for pure Methylammonium lead iodide as a function of MAI salt coating (0.01M, 0.005M and 0.001M). As the concentration increase the yield of charge separation is retained for a longer time period, demonstrating enhanced stability.

The data obtained confirms that increasing the concentration of the salt coating from 0.001M to 0.01M does reduce the rate of decay of charge separation. The magnitude of the charge separation yield at 1$\mu$s suffers less significant loss as the concentration of coating used increases. Consequently, this further confirms that the coating serves to alleviate the iodide defects and that by increasing the bromide content in films provides the same effect. Where by substituting in bromide for iodide the number of defect sites where oxygen can fill and then extract a photo-excited electron from decreases. This results in less superoxide being formed and so the number of catastrophic cation deprotonation events decreases, leading to a reduced rate in the breakdown of the crystal structure. The perovskite phase is then able to last longer periods of time under oxygen and light environments. This data also supports the previous observations that there is a concentration dependence with respect to stability and device performance. Overall, this implies the concentration of iodide vacancies dictates the rate of decay of charge separation, stability and device performance and justifies our hypothesis that the bromine substitution acts to increase stability by reducing the quantity of iodide vacancies.

### 8.4.1 Device stability and performance

To investigate how the impact of bromide substitution manifests itself in device stability and performance, solar cells of the architecture FTO/c-$TiO_2$/mp-$TiO_2$/$CH_3NH_3Pb(I_{(1-x)}Br_x)_3$/Spiro-OMeTAD/Au were fabricated. The current-voltage curves obtained for the fresh samples, where x = 0, 0.1, 0.2, 0.5, 0.75 and 1.0 are displayed in Figure 8.15a. Highlighted from this data, is that increasing bromide content leads to a reduced PCE of devices. Where the general trend of reduced open circuit voltage is observed as bromide increases, in line with the fact that the optical band gap shifts with increasing bromide content. The shift in the band-gap means higher bromide content samples have less efficient spectral overlap and absorb less energy, therefore less light energy can be converted to electricity and the power conversion efficiency is reduced. The shift in the band gap is highlighted in the optical absorbance data, Figure 8.15b, where the onset of absorption undergoes a red shift as the iodide content increases. These devices were then exposed to the degradation conditions of dry air flux and A.M. 1.5 light illumination, in accordance with previous device degradation studies. The stability of the solar cells is recorded as the magnitude of the normalised PCE as a function of time exposed to the degradation conditions implemented. The results of this are displayed in Figure 8.14c.

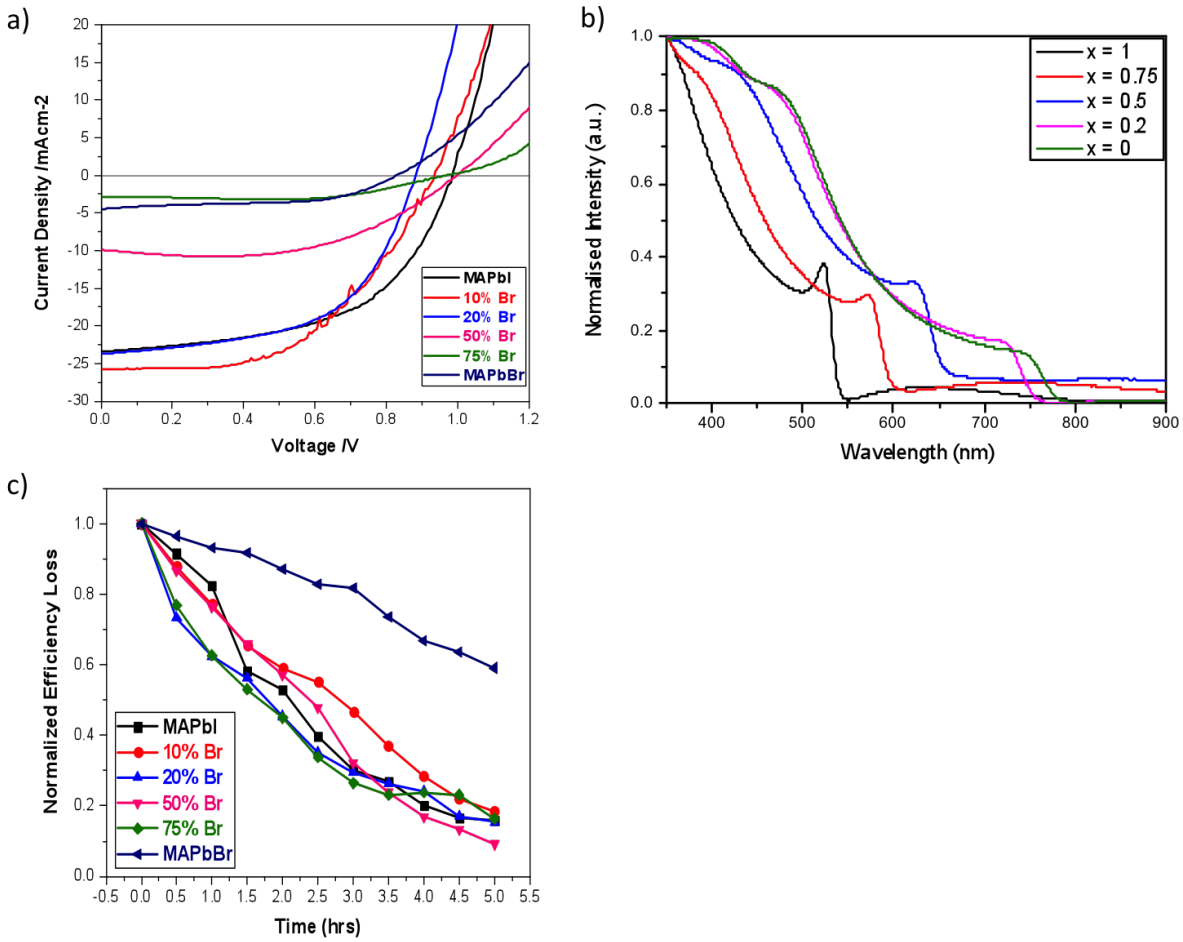


Figure 8.14: a) J-V curves obtained for pristine films of $CH_3NH_3Pb(I_{(1-x)}Br_x)_3$ for x = 0.0, 0.1, 0.2, 0.5, 0.75 and 1.0. b) Absorbance spectra for the mixed halide perovskite films and c) Normalised PCE loss as a function of aging for the same film compositions in the device architecture: FTO/c-$TiO_2$/mp-$TiO_2$/$CH_3NH_3Pb(I_{(1-x)}Br_x)_3$/Spiro-OMeTAD/Au. Raw device data was obtained in collaboration with Xiangnan Bu.

This data, raises a fascinating observation that for devices with x<1 the degradation of the PCE is approximately constant between all samples. The half-life of the PCE occurs at around 1.5 hours for all samples in this range. Meanwhile, in the 100% bromide substituted perovskite film ($MAPbBr_3$) the device demonstrates better stability, with the half-life increasing to in excess of 5 hours. It is noted that for all films that the optical degradation is slower relative to the loss in PCE, again indicating that even small amounts of degradation in the perovskite layer can drastically impact performance. It then follows that the reason the device stability for all iodide containing films, is due to the iodide component of the crystal breaking down first and causing performance losses. This hypothesis is supported by the literature findings that light

illumination can cause phase segregation. This would then manifest itself, in the perovskite films segregating and the iodide rich regions degrading first. It would then be expected that the rate of degradation of the iodide rich areas would be constant between samples and cause significant losses in performance. This would then account for the fact that all iodide containing samples degrade on a similar time-scale and independent of the bromide content. It is then the bromide rich regions, that take longer to degrade and account for the enhanced optical absorption stability noted in the UV/VIS degradation experiments with increasing bromide content. It is noteworthy though that the inclusion of bromide does not enhance stability as the performance is sensitive to even the smallest amount of degradation. The $MAPbBr_3$ based device exhibits significantly better stability relative to the $MAPbI_3$ system, however the difference in optical absorption stability is even greater. Where, almost no degradation was observed in the bromide system over 16 days. Meanwhile, the device performance does degrade even within a few hours. This degradation may be attributed to other layers in the device architecture being affected by the generation of superoxide, the reactive oxygen species may breakdown the perovskite/HTL interface. Organic layers are susceptible to attack from superoxide, as such the Spiro-OMeTAD layer may begin to degrade under superoxide stress. The degradation then associated with the bromide perovskite architecture is ascribed to the degradation of the organic hole transporting layer and subsequent losses in charge transport properties can be used to indicate that the perovskite layer is not the limiting stability factor in this device.

### 8.4.2 Application of salt coatings to $CH_3NH_3Pb(I_{(1-x)}Br_x)_3$ devices.

The application of an iodide salt coating has been shown previously to improve both optical and charge separation stability in all mixed halide systems. The extreme cases, where x = 0 ad x = 1 revealed that only the iodide component benefits from the salt coating. No stability enhancement is observed by applying a MABr salt to a $MAPbBr_3$ perovskite film. In contrast, a stability enhancement that is proportional to the concentration of the MAI salt can be obtained for $MAPbI_3$ perovskite films. Having attributed the degradation of mixed halide perovskite solar cells to the iodide component, where illumination causes phase segregation, the MAI salt

coating should inflict a stability enhancement to the iodide regions and ultimately to the device performance. As seen in the transient absorption spectroscopy measurements, the salt coating not only improved the retention of the yield of charge separation but also highlighted that less concentration of salt was need as the bromide content was increased to enhance stability. From this, it was ascribed that the vacancy defect density is lower in higher bromide content films. Accordingly, the devices of mixed halide perovskites should then exhibit a similar trend. Where, as bromide content increases the number of vacancies decreases (fewer iodide rich regions) and thus the concentration of iodide salt coating needed to stabilise the film will be reduced. To examine this hypothesis, mixed halide perovskite films with compositions of x = 0.20, 0.50 and 0.75 were fabricated into a FTO/c-$TiO_2$/mp-$TiO_2$/$CH_3NH_3Pb(I_{(1-x)}Br_x)_3$/Spiro-OMeTAD/Au architecture. Within these compositions, the MAI salt coating was applied to the perovskite layer, using concentrations of 0.001M, 0.005M and 0.01M. The coating was applied before subsequent layers were added to the device. These devices were then exposed to the degradation conditions of dry air flux and A.M. 1.5 solar illumination and their PCE were recorded as a function of time. The results of this investigation are displayed in the Figure 8.15 below.

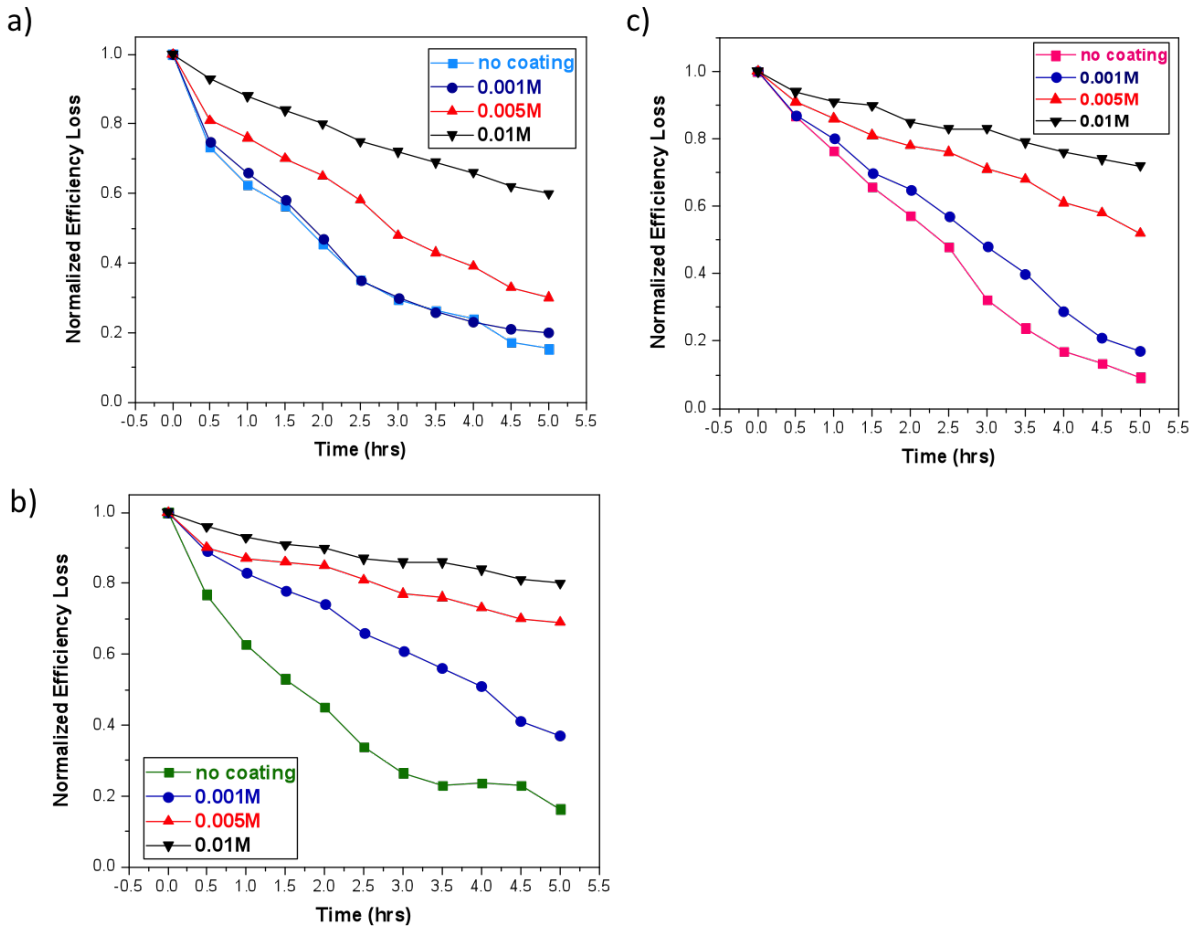


Figure 8.15: Normalised PCE device degradation with and without the application of the MAI salt coating to FTO/c-$TiO_2$/mp-$TiO_2$/$CH_3NH_3Pb(I_{(1-x)}Br_x)_3$/Spiro-OMeTAD/Au devices. a) x=0.20 b) x=0.5 c) x=0.75. Raw device data was obtained in collaboration with Xiangnan Bu.

In all mixed halide compositions probed, the application of the MAI slat coating invokes a stability enhancement. This magnitude of the stability is in all scenarios proportional to the concentration used. However, as expected the concentration needed to generate more stable devices decreases as bromide content increases. Illustrating this is the 0.001M MAI concentration, in the x=0.2 perovskite this generates little to no stability enhancement whilst for x=0.5 the stability is increased by half an hour when comparing the half-life of the device efficiency. In the x=0.75 perovskite an even greater stability enhancement of approximately 2 hours is observed in the device efficiency half-life. Then as the concentration of MAI is increased the difference in device stability becomes less significant between the samples, although there is still an observable difference. This observation overlaps with that of both the TAS and the UV/VIS degradation experiments. Again, this is attributed to the reduction in the presence of

the problematic iodide anion. Removal of this species means that there is a reduced iodide rich region which ultimately leads to fewer iodide vacancies in the perovskite. The computational results demonstrated that the halide vacancies become less favourable to form in higher bromide content samples and that in all compositions the bromide vacancy is less energetically favourable to form. Consequently, taking this all into consideration it can be proposed that substitution with bromide, leads to the removal of iodide defects in a two fold mechanism. First, by making them less favourable to form as the lattice contracts and the energy required to form them becomes greater, and secondly the area of iodide rich regions will be reduced as there is less crystal material that can form the more problematic halide vacancy.

## 8.5 Conclusions

The work has shown that bromide substitution can invoke a stability enhancement towards oxygen and light degradation, which is proportional to increasing bromide content. In the bromide-rich compositions, degradation is suppressed due to a combination of factors, namely enhanced hydrogen-bonding between the methylammonium cation and the lattice, and stronger lead-bromide bonds. It has also been shown that the increased stability of the bromide phase is partly due to higher formation energies of bromide vacancies compared to its iodide analogue. This leads to a lower number of vacancy sites for superoxide formation. These results provide insights into improving the stability of the mixed-halide systems through compositional engineering. Consistent with previous work for iodide vacancies, the work has highlighted through computational simulations that bromide vacancies also readily incorporate oxygen to form superoxide. This restores the full octahedral arrangement of the inorganic lattice. Oxygen acts as an electron scavenger attracting photo-excited electrons. However, the experimental data combined with an energetic analysis of the halide formation energies has revealed that bromide substitution reduces the vacancy defect density in films. Removing these defects, reduces the yield of superoxide. Any superoxide that does form in bromide rich films is less problematic due to the increased stability of the crystal structure towards superoxide degradation. These two features enable bromide substitution to bring about enhanced stability to oxygen and light for

perovskite films. This stability is mainly demonstrated in optical absorption properties, whilst devices still showed degradation. This device degradation is ascribed to the high sensitivity of device performance towards minor degradation. In mixed halide systems, illumination may cause phase segregation, leading to iodide rich regions which degrade and consequently cause device efficiency to degrade rapidly. These iodide rich regions in all mixed halide compositions could be expected to degrade with an approximately similar rate, since it would be expected to be the same crystal and have similar defects and therefore decay kinetics. Support for this is observed in the fact that all mixed halide devices, suffer performance losses on a similar time scale. Where this efficiency loss is attributed to the degradation of the iodide rich regions. Salt coatings have been applied in a systematic manor and demonstrate two key findings. Firstly, that stability of all mixed-halide films can be increased and this is observed in both optical and device properties. Secondly, the quantity of vacancy defects is reduced as bromide content is increased as the concentration of the salt coating required to enhance stability decreases as a function of increasing bromide.

# References

[1] N. J. Jeon, J. H. Noh, W. S. Yang, Y. C. Kim, S. Ryu, J. Seo, S. I. Seok, *Nature*, 2015, **517**, 476480.

[2] S. Aharon, B. E. Cohen, L. Etgar, *The Journal of Physical Chemistry C*, 2014, **118**, 17160–17165.

[3] P. Fedeli, F. Gazza, D. Calestani, P. Ferro, T. Besagni, A. Zappettini, G. Calestani, E. Marchi, P. Ceroni, R. Mosca, *The Journal of Physical Chemistry C*, 2015, **119**, 21304–21313.

[4] J. H. Noh, S. H. Im, J. H. Heo, T. N. Mandal, S. I. Seok, *Nano Letters*, 2013, **13**, 1764–1769.

[5] S. A. Kulkarni, T. Baikie, P. P. Boix, N. Yantara, N. Mathews, S. Mhaisalkar, *J. Mater. Chem. A*, 2014, **2**, 9221–9225.

[6] M. Ledinsk, P. Lper, B. Niesen, J. Holovsk, S.-J. Moon, J.-H. Yum, S. De Wolf, A. Fejfar, C. Ballif, *The Journal of Physical Chemistry Letters*, 2015, **6**, 401–406.

[7] L. Gil-Escrig, A. Miquel-Sempere, M. Sessolo, H. J. Bolink, *The Journal of Physical Chemistry Letters*, 2015, **6**, 3743–3748.

[8] F. Brivio, C. Caetano, A. Walsh, *The Journal of Physical Chemistry Letters*, 2016, **7**, 1083–1087.

[9] Z. Xiao, L. Zhao, N. L. Tran, Y. L. Lin, S. H. Silver, R. A. Kerner, N. Yao, A. Kahn, G. D. Scholes, B. P. Rand, *Nano Letters*, 2017, **17**, 6863–6869.

[10] D. P. McMeekin, G. Sadoughi, W. Rehman, G. E. Eperon, M. Saliba, M. T. Hörantner, A. Haghighirad, N. Sakai, L. Korte, B. Rech, M. B. Johnston, L. M. Herz, H. J. Snaith, *Science*, 2016, **351**, 151–155.

[11] S. Tombe, G. Adam, H. Heilbrunner, D. H. Apaydin, C. Ulbricht, N. S. Sariciftci, C. J. Arendse, E. Iwuoha, M. C. Scharber, *J. Mater. Chem. C*, 2017, **5**, 1714–1723.

[12] W. Wang, J. Su, L. Zhang, Y. Lei, D. Wang, D. Lu, Y. Bai, *CrystEngComm*, 2018, **20**, 1635–1643.

[13] S. Draguta, O. Sharia, S. J. Yoon, M. C. Brennan, Y. V. Morozov, J. S. Manser, P. V. Kamat, W. F. Schneider, M. Kuno, *Nat. Commun.*, 2017, **8**, 200–208.

[14] M. R. Ahmadian-Yazdi, F. Zabihi, M. Habibi, M. Eslamian, *Nanoscale Research Letters*, 2016, **11**, 408.

[15] F. Brivio, C. Caetano, A. Walsh, *The Journal of Physical Chemistry Letters*, 2016, **7**, 1083–1087.

[16] S. Pont, D. Bryant, C.-T. Lin, N. Aristidou, S. Wheeler, X. Ma, R. Godin, S. A. Haque, J. R. Durrant, *J. Mater. Chem. A*, 2017, **5**, 9553–9560.

[17] N. Aristidou, I. Sanchez-Molina, T. Chotchuangchutchaval, M. Brown, L. Martinez, T. Rath, S. A. Haque, *Angewandte Chemie International Edition*, 2015, **54**, 8208–8212.

[18] D. Bryant, N. Aristidou, S. Pont, I. Sanchez-Molina, T. Chotchunangatchaval, S. Wheeler, J. R. Durrant, S. A. Haque, *Energy Environ. Sci.*, 2016, **9**, 1655–1660.

[19] N. Aristidou, C. Eames, I. Sanchez-Molina, X. Bu, J. Kosco, M. S. Islam, S. A. Haque, *Nat. Comm.*, 2017, **8**, 15218.

[20] F. T. O'Mahony, Y. H. Lee, C. Jellett, S. Dmitrov, D. T. Bryant, J. R. Durrant, B. C. O'Regan, M. Graetzel, M. K. Nazeeruddin, S. A. Haque, *J. Mater. Chem. A*, 2015.

[21] J. M. Ball, M. M. Lee, A. Hey, H. J. Snaith, *Energy Environ. Sci.*, 2013, **6**, 1739–1743.

[22] J. M. Ball, A. Petrozza, *Nature Energy*, 2016, **1**, 16149.

[23] H. J. Queisser, E. E. Haller, *Science*, 1998, **281**, 945–950.

[24] N. K. Kumawat, N. Jain, A. Dey, K. L. Narasimhan, D. Kabra, *Adv. Func. Mater.*, 2016, **27**.

[25] L. Pauling, *Journal of the American Chemical Society*, 1932, **54**, 3570–3582.

[26] J. Kim, S.-H. Lee, J. H. Lee, K.-H. Hong, *The Journal of Physical Chemistry Letters*, 2014, **5**, 1312–1317.

[27] W.-J. Yin, T. Shi, Y. Yan, *Applied Physics Letters*, 2014, **104**, 063903.

[28] A. Buin, P. Pietsch, J. Xu, O. Voznyy, A. H. Ip, R. Comin, E. H. Sargent, *Nano Letters*, 2014, **14**, 6281–6286.

[29] S. D. Stranks, P. K. Nayak, W. Zhang, T. Stergiopoulos, H. J. Snaith, *Angewandte Chemie International Edition*, 2015, **54**, 3240–3248.

# Chapter 9

# Utilising superoxide from P3HT for contaminant cleaning

## 9.1 Introduction

Formation of the reactive oxygen species, superoxide, in methylammonium lead iodide leads to it's demise as a material for optoelectronic applications. The species causes the breakdown of the crystal structure and its rapid loss in device efficiencies and material life-time when exposed to oxygen and light stress. For this reason, methylammonium lead iodide may never become a realistic option for commercial employment despite it's promising properties making it an ideal candidate for optoelectronic applications. Furthermore, the lead content of the perovskite will also contribute to issues leading to its commercial manufacturing. However, the material has highlighted that photo-excited electrons can undergo electron transfer reactions with molecular oxygen in the atmosphere to generate superoxide. Superoxide is, as seen in MAPI, a highly reactive species and if it could be harnessed correctly could be used to degrade chemical contaminants or pollutants. The effects of the ROS have been widely documented in the literature within biological systems.[1, 2, 3, 4, 5, 6, 7, 8, 9, 10] Consequently, if the generation of superoxide from films could be manipulated in solutions to then react with contaminants in the solution it could effectively be used to clean the system. The principle for this, has first been demonstrated by the superoxide yield test measurement employed throughout the

previous works. Where, the superoxide generated from thin-films diffuses out and reacts with the DHE probe in the solution. The probe in this system could be hypothetically replaced with a contaminant and thus the superoxide could diffuse out and react with the contaminant leading to it's breakdown. However, the use of methylammonium lead iodide for this potential application has two drawbacks. First, is the fact that MAPI is a polar salt that will dissolve in aqueous solutions. This would restrict the application to only non-polar systems, where a vast majority of contaminants will exist in aqueous or polar media. Secondly, if the system is to be widely employed the issue of lead arises again and would cause manufacturing legislation and handling issues.

It is widely noted that some organic polymers also suffer oxygen and light induced degradation.[11, 12, 13, 14, 15, 16, 17, 18, 19] Consequently, this may be through the generation of either singlet oxygen or superoxide. Both reactive oxygen species can cause degradation issues leading to optoelectronic performance losses. However, with the potential application in mind organic polymers are advantageous as they can offer stability for use in aqueous media. Hence, the identification of an organic polymer system that could yield superoxide over singlet oxygen could help generate a working system that could be deployed to clear solutions of contaminants. Advancing the concept further, the polymer could be deployed in a solution and then sprayed onto surfaces that are contaminated and then under illumination, superoxide would be generated leading to the denaturing of the contaminants. It is known that some organic compounds can produce superoxide and work has shown that the superoxide formed can be used to react with other species.[20] Notably, investigations into the photo-oxidation of the polymer Poly(3-hexylthiophene-2,5-diyl), P3HT, have demonstrated that superoxide is a reactive species being generated. The structure of the monomer unit is displayed in Figure 9.1a. The detection of superoxide has been achieved through the employment of electron spin resonance measurements and have identified the species being formed within films.[21, 19] In a similar mechanism found in perovskite it is expected that the generation of the superoxide species occurs due to a photo-excited electron undergoing an electron transfer reaction with molecular oxygen. Here, incoming light is absorbed by the ground state of the polymer generating an exciton. The electron then transfers to oxygen and generates the reactive oxygen species superoxide. The

potential process is represented in Figure 9.1b.

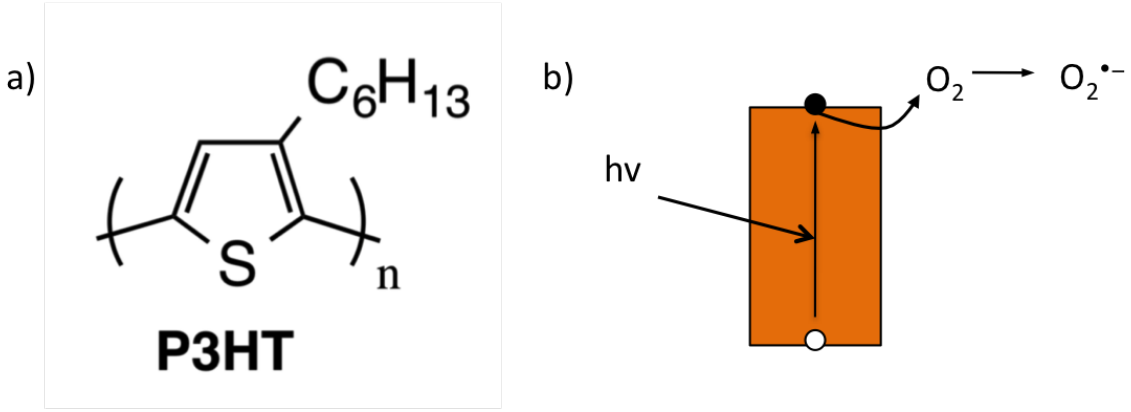


Figure 9.1: a) Chemical structure of the monomer unit of the Poly(3-hexylthiophene-2,5-diyl), P3HT polymer. b) Energy level diagram for the generation of superoxide from P3HT. Photoexcitation leads to an electron in the CB to undergo electron transfer to oxygen, forming superoxide.

The following works seek to explore the use of the superoxide probe technique deployed on perovskite films to monitor superoxide evolution from P3HT. Once the technique has been established to work for P3HT films this will pave the way for influencing parameters to be manipulated and to note the impact on superoxide yield. As a starting point, the role of electron extraction will be examined along with morphology alterations through annealing. These parameters were previously shown in perovskite thin-films to impact the superoxide yield generation. For this application, the yield of superoxide needs to be maximised such that the potency of the films could act in a meaningful way to clear contaminated systems. To this end, the ability of superoxide generated from P3HT films to react with a species that could mimic a contaminant will be explored. Where the rate of removal of the chemical species will be examined.

## 9.2 Superoxide generation from P3HT

To investigate the generation of superoxide from P3HT thin-films, samples were first fabricated onto cleaned plain glass using spin coating. The exact parameters employed are described in the methods section. In the perovskite superoxide tests, samples were then submerged in a toluene solution containing the Dihydroethidinium (DHE) probe that reacted with superoxide

causing an increase in emission intensity. However, this system required modification where a new solvent for P3HT thin-films needed to be discovered. Unfortunately, toluene dissolves P3HT destroying the ability to measure superoxide generation. The solvent must conform to two key principles. First it must be able to dissolve the probe and secondly it must not alter or degrade the composition of the film being submerged in the probe solution. A common orthogonal solvent for P3HT fabrication is methanol, since this does not dissolve the polymer.[22] Due to the polar nature of the solvent and the ability of DHE to dissolve in polar solvents, such as water, makes methanol a promising choice for a solvent system. The impact of methanol on the thin-film properties is examined using absorbance measurements as a function of submersion time in the solvent. In this experiment the absorbance of a P3HT film was measured before being submerged and then at 10 minute intervals over the course of an hour whilst being submerged in methanol. Since, the probe experiments for perovskite samples are conducted over the course of an hour the same time frame was used for these samples. The results of this are shown in Figure 9.2.

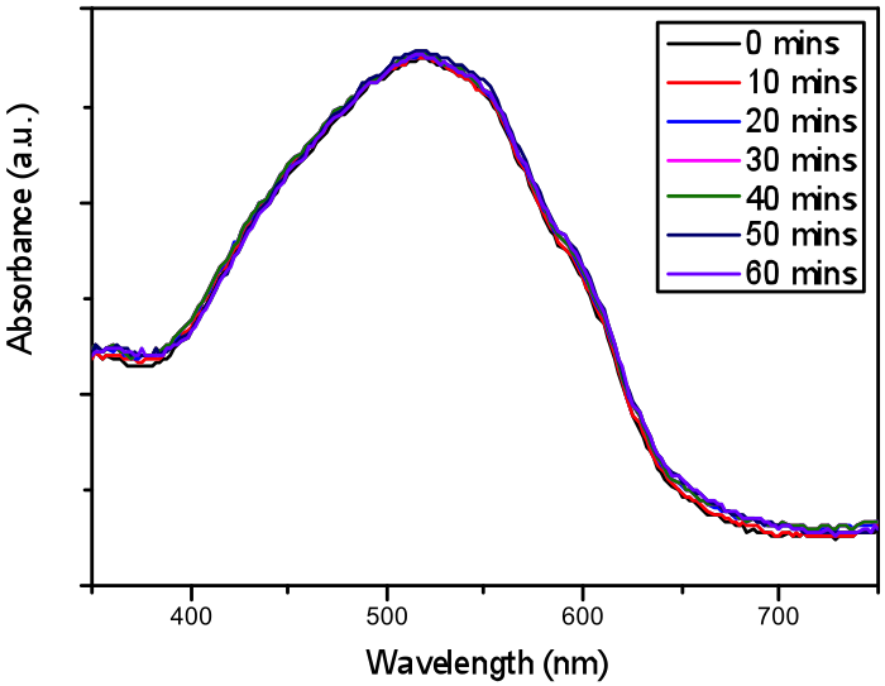


Figure 9.2: UV/VIS absorbance spectroscopy of a P3HT film submerged in methanol over the course of an hour. Spectra are taken at 10 minute time intervals, where the 0 minute spectra corresponds to the film before being submerged in the solvent.

The results of this test, Figure 9.2, demonstrate that no change in the optical absorbance properties of the film occurs as a result of being submerged in methanol for an hour. All absorbance spectra overlap, indicating no change in morphology and this implies no degradation or impact is being inflicted onto the film by the solvent. Consequently, this allows the solvent to be employed in the superoxide yield tests for P3HT films.

### 9.2.1 Superoxide degradation of P3HT films

Before assessing the generation of superoxide yields from P3HT films the optical absorbance degradation under dry air flux and illumination was characterised. Again, as was for the experiments involving perovskite films the change in absorbance indicates the degradation rate, which correlates to the yield of superoxide. It was noted in perovskite films, that longer retention of absorbance properties was a result of reduced superoxide yields. A feature that was clearly prominent in all perovskite materials, was the use of electron extraction layers increasing the

stability. In addition the impact of substrate surface area was also critical in determining the stability of films towards oxygen and light. Hence, here P3HT films are fabricated onto either plain glass, mp-$Al_2O_3$ or mp-$TiO_2$. It is hypothesised that in accordance with the previous understanding that the introduction of electron extraction, using the mp-$TiO_2$ layer, will increase stability by providing a competitive pathway to reduce the number of electrons undergoing transfer to molecular oxygen. Additionally, the increase in surface area glass to mp-$Al_2O_3$, should decrease stability, as the number of photo-excited electrons produced will increase and thus more electrons will be able to transfer to oxygen to form superoxide. To probe the stability of these films towards oxygen and light and to reveal if these conditions can inflict degradation of P3HT properties, UV/VIS absorbance measurements were recorded as a function of time exposed to the conditions. The spectra obtained are displayed in Figure 9.3a-c. Here, as in the previous experiments, films are sealed in an inert atmosphere and measured as fresh. Then dry air flux and illumination are introduced to the system and the absorbance recorded as a function of time.

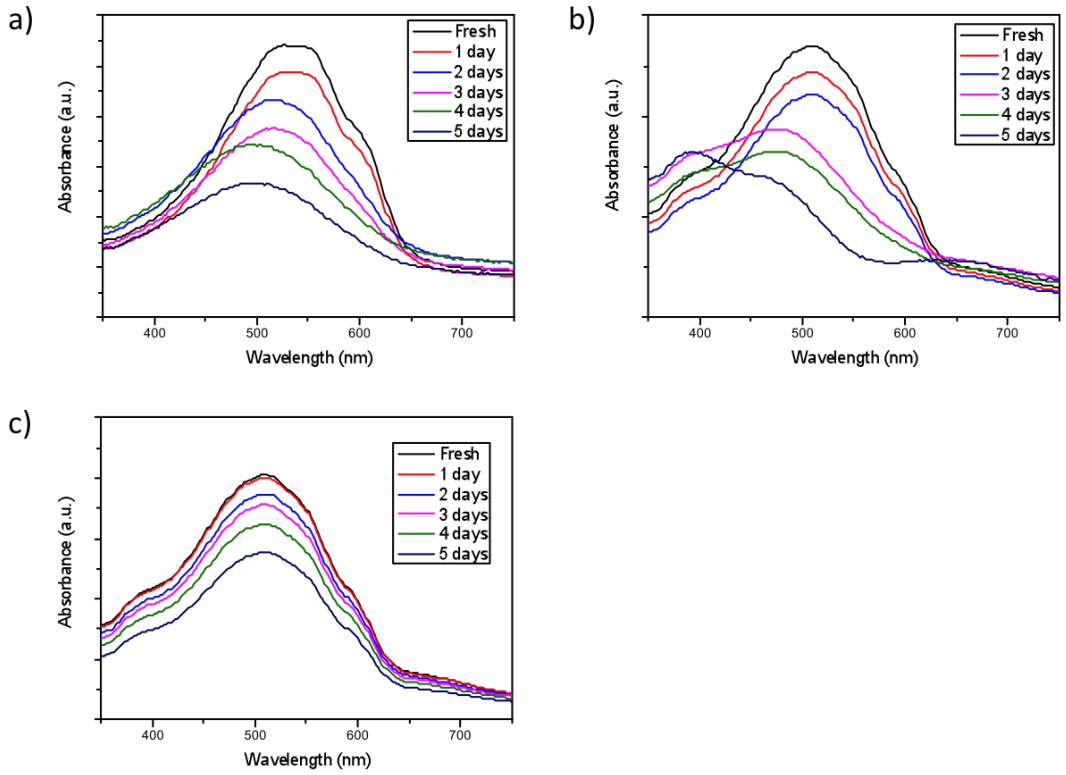


Figure 9.3: Absorbance spectra for P3HT films fabricated on a) plain glass b) mp-$Al_2O_3$ and c) mp-$TiO_2$. Films were exposed to dry air flux and one sun illumination and spectra were recorded at set time intervals.

Highlighted from the data is the fact that P3HT thin-films undergo degradation when exposed to oxygen and light. This is shown by the fact the absorbance spectra of all samples degrades as time under oxygen and light increases. Noted by the intensity of the absorbance decreasing. This confirms that the formation of a reactive oxygen species is highly likely to be the cause of the sensitivity of P3HT towards this degradation stress, resulting in photo-oxidation. Of particular interest is the fact that as expected the change in surface area from plain glass (Figure 9.3a) to mp-$Al_2O_3$ (Figure 9.3b) increases the degradation rate. As for perovskite samples, this is a consequence of an increased ability to absorb photons thus generating more photo-excited electrons, which in turn provides more electrons to react with molecular oxygen in the atmosphere to create reactive oxygen species. The data also confirms that introducing an electron extraction layer, mp-$TiO_2$ (Figure 9.3c), increases the stability of P3HT films. Here, the electron extractor can provide an alternative pathway for photo-excited electrons to compete with transfer to oxygen. As a result this leads to fewer electrons forming the reactive oxygen

species and an enhanced stability towards oxygen and light. This behaviour was characteristic of superoxide production in methylammonium lead iodide and it was demonstrated that increasing the electron extraction rate and energetics for the process drastically improved the tolerance of the material towards oxygen and light. Therefore, for P3HT a similar mechanism could be suggested that results in the generation of the reactive oxygen species, superoxide. The potential mechanism is depicted in Figure 9.4 a and b. The figure compares the use of mp-$Al_2O_3$ and mp-$TiO_2$, where the latter allows for the competitive deactivation of the photo-excited electron reducing the generation of superoxide.

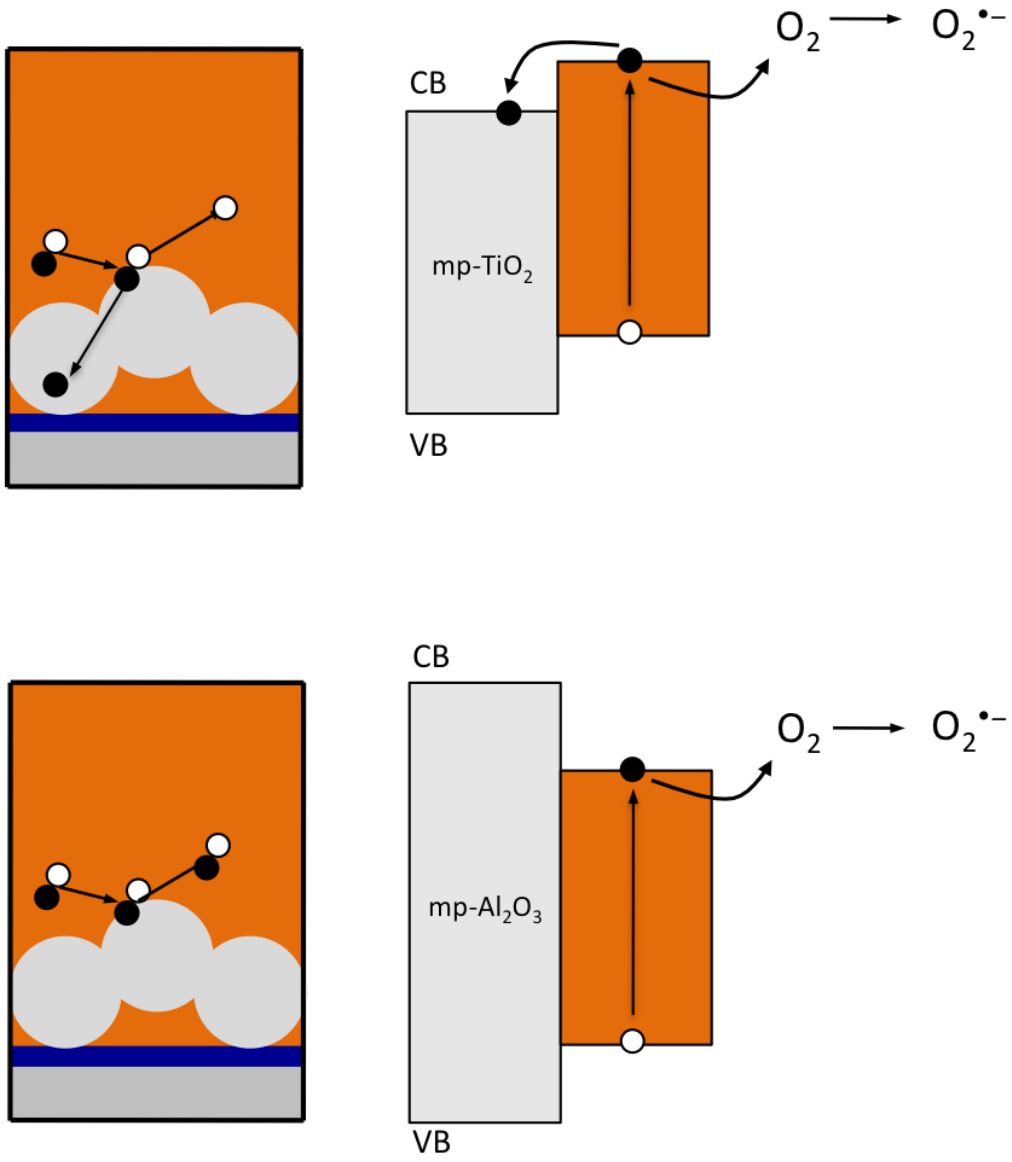


Figure 9.4: Energy level diagrams for P3HT fabricated onto either mp-$TiO_2$ or mp-$Al_2O_3$. The electron extraction ability of mp-$TiO_2$ provides a competitive pathway for photo-excited electrons that reduces the number of electrons generating superoxide.

As was the case for perovskite, the incoming photons are absorbed generating excitons. The photo-excited electron that resides in the valence band is then able to participate in an electron transfer reaction with oxygen, leading to the formation of superoxide. In electron extractor systems, an alternative competing pathway exists that reduces the number of electrons available to participate in this parasitic side reaction. Consequently, it is expected that this will manifest itself in the samples having different superoxide yields, which correlate to the observed stability of the absorbance of the films.

### 9.2.2 Superoxide yield measurements

The previous experiments have identified that a photo-oxidation degradation occurs in P3HT thin-films under dry air flux and illumination. This observation is in agreement with previous literature and demonstrates that on exposure to oxygen and light a reactive oxygen species forms. Now to identify if this species is superoxide and if the yield can be determined, the superoxide yield tests developed earlier is employed. Here the three P3HT films are fabricated onto either a plain glass, mp-$Al_2O_3$ or mp-$TiO_2$ platform. These films are then submerged in a methanol/DHE probe solution and then exposure to dry air flux and illumination is applied. Compressed dry air (CDA) was bubbled through the solvent and a 1.5 $mWcm^{-2}$ tungsten lamp acted as the light source. The emission intensity of the probe solution before the samples was recorded and used as the background reading to which all subsequent recordings were normalised against. The emission of the probe remains at 610 nm and the emission of the probe solution was recorded at 10 minute time intervals over the course of an hour. This protocol follows that of the superoxide yield tests developed and used in the previous works on perovskite films, except with the use of methanol as the solvent rather than toluene. The normalised intensity increase ($I_F(t)/I_F(t_0)$) for the three samples is shown in Figure 9.5.

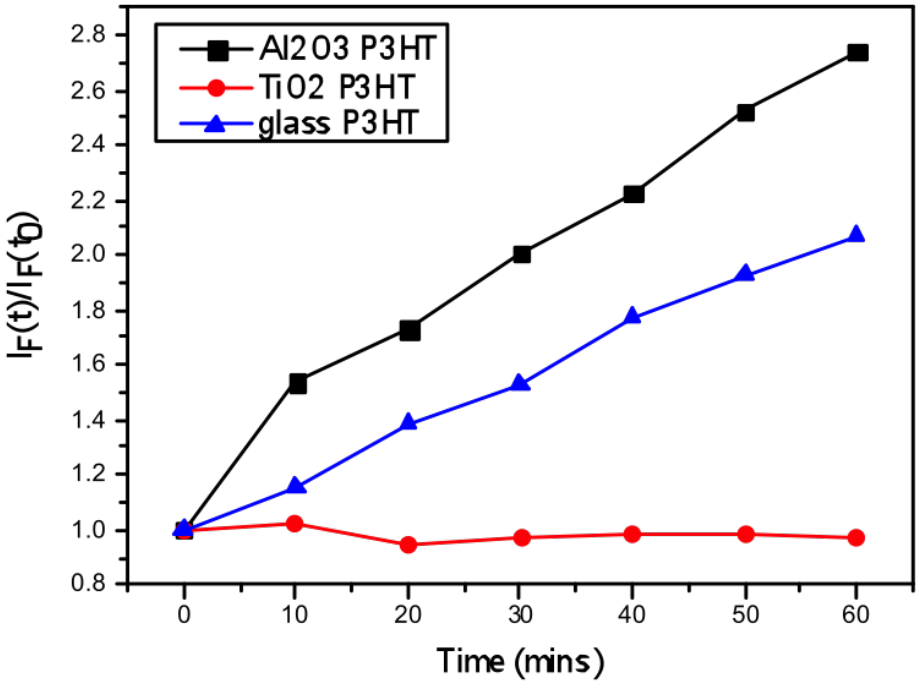


Figure 9.5: Superoxide yield plot for P3HT films fabricated onto plain glass, mp-$TiO_2$ and mp-$Al_2O_3$.

The results of this experiment demonstrate that this method can detect the evolution of superoxide from P3HT films. Where in both the P3HT films fabricated on plain glass and mp-$Al_2O_3$ the emission intensity of the probe solution increases. This confirms superoxide is formed from the film and able to react with the probe causing the deprotonation of the non-emissive state to form the emissive one. This provides an alternative method to measure superoxide generation in P3HT films over that of the previously employed ESR experiments.[21] Advantageously this technique also offers an easier method to compare yields from samples with different variables. The data can also rationalise the difference in stability between P3HT films fabricated on plain glass and mp-$Al_2O_3$, where the increased surface area of mp-$Al_2O_3$ leads to the generation of more superoxide. In the absorbance measurements the rate of degradation of P3HT on mp-$Al_2O_3$ was faster and this correlates to greater superoxide yields. Moreover, the ability of mp-$TiO_2$ to provide a competitive electron pathway causes the superoxide yields to drastically decreases. Again this sustains the observation of a greater tolerance towards oxygen and light stress via longer retention of absorbance properties. These observations are in line with

that of the trends observed in the perovskite samples and suggests that the mechanistic action proposed is the same. The time frame implemented may account for why the observed yields from mp-$TiO_2$/P3HT films are so low, where little to no increase is observed. Alternatively, the degradation mechanism that causes the absorbance properties to decrease in this system may stem from the ability of the films to also produce singlet oxygen, another reactive oxygen species that can contribute to photo-oxidation reactions. It is noted, however, that in general the yields observed from P3HT films are significantly lower than those observed in methylammonium lead iodide. This may be rationalised by the fact that only the pristine surface in P3HT can cause the formation of superoxide, whilst for MAPI the Iodide vacancies cause far larger yields to be observed due to the enhanced energetics of superoxide formation from these sites. Despite this, the method has been demonstrated to show that superoxide can be detected from P3HT films and that a comparison between systems can be observed. This allows for this test to be employed to explore the impact of changing fabrication variables, morphology and architectures on the yield of superoxide.

## 9.3 Optimising superoxide generation

In contrast to perovskite photovoltaics, where the generation of superoxide needed to be minimised for prolonged performance, the superoxide generation needs to be maximised for the desired application. If P3HT films or even potentially nano-particle suspensions are to be able to degrade contaminants/pollutants, the generation of superoxide needs to be maximal when illuminated as this is the active species that will react with contaminant species. It was shown earlier that the surface area and the selection of fabrication layers can alter the superoxide yield. Of particular interest is the potential impact that annealing may have on the yield of superoxide. It has been shown in the literature that annealing can impact the morphology of P3HT films and blends, leading to increased uniformity of the films with fewer grain boundaries and less trap sites. As a consequence annealing has the profound effect of increasing P3HT film photo-activity.[23, 24, 25] To examine this effect a set of glass/P3HT films were fabricated, then the films were annealed at either room temperature ( 25°C), 50°C, 100°C and 150°C. The

absorbance of these films was then recorded, where if the photo-activity increases the absorbance should increase. the results of absorbance data confirm this is the case as depicted in Figure 9.6a.

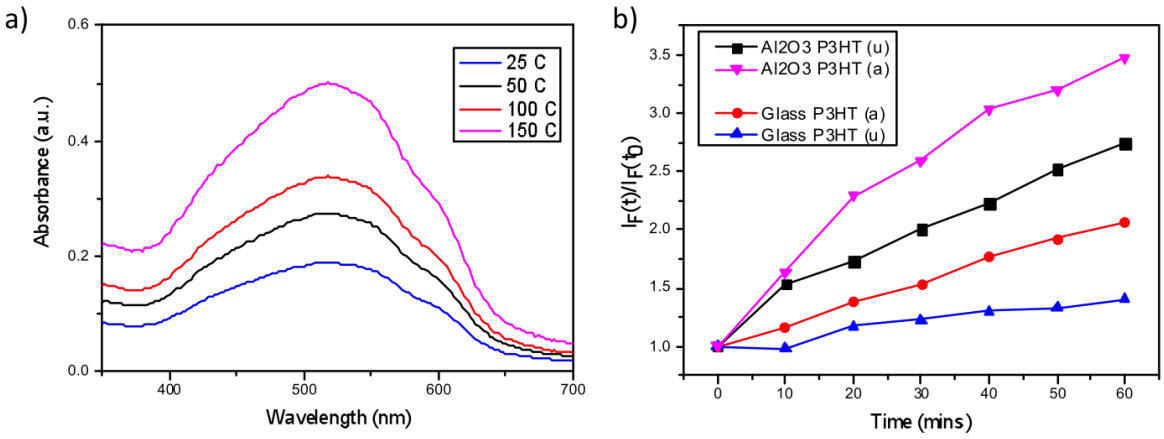


Figure 9.6: Impact of increasing photo-activity through annealing on a) absorbance of thin films and b) superoxide yield for P3HT films on both plain glass and mp-$Al_2O_3$.

The data, Figure 9.6a, confirms that increasing the annealing temperature increase the absorbance of the P3HT thin films. Consequently, since more photons are absorbed this should lead to higher yields of superoxide. There is a greater probability of an electron participating in the parasitic electron transfer reaction with molecular oxygen as more photons absorbed means there are more photo-excited electrons. To review the impact annealing may have on superoxide yields, an un-annealed and annealed P3HT film were fabricated on both plain glass and mp-alumina coated glass. These four samples were then subjected to the superoxide yield test and the results are shown in Figure 9.6b. From the data, it is clear that in both substrate systems the impact of annealing leads to an increase in superoxide yields over the time frame explored. This reinforces the hypothesis that increasing the photo-activity leads to more photo-electrons that can then participate in the electron transfer reaction and consequently increase the yields of superoxide. Furthermore, this sustains the potential mechanism of superoxide generation proposed. This result demonstrates that for the potential application described, that P3HT photo-activity needs to be maximised in order to generate the highest yields of superoxide. Moreover, the data collected again depicts the impact of surface area. Where, in all cases comparing either the annealed or un-annealed P3HT films swapping the plain glass substrate for the

glass/mp-$Al_2O_3$ system results in an increase in superoxide yields. As noted by the magnitude of the emission intensity increasing, blue vs black data and in the red vs pink traces in Figure 9.6b.

Surface area and superoxide generation are strongly correlated. This phenomenon was clearly demonstrated throughout the previous work on perovskite films and has emerged as a significant factor at play even in P3HT films. So far, the role of altering the deposition layer from plain glass to mesoporous scaffolds (mp-$Al_2O_3$) sustains this, as the surface area increases so does the yield of superoxide. Increasing surface area results in films absorbing more photons and consequently generates more excitons. Now there are more electrons that populate the CB and are able to undergo electron transfer to molecular oxygen. More superoxide can form. Taking this into account, the concept of using an intrinsically higher surface area morphology of P3HT is considered. Here, the fabrication of P3HT nanoparticle films are employed to explore the effect of morphological surface area on superoxide generation. It is hypothesised that the nanoparticles, once fabricated onto a substrate, will generate films with a higher surface area and thus will lead to higher superoxide yields. The synthesis of the P3HT nanoparticles is described in the methods section. However, in summary to generate P3HT nanoparticles, the polymer was dissolved in chloroform and then hot injection of a sodium dodecyl sulfate (SDS) solution was added to initiate the nanoparticle formation in conjugation with the use of ultrasonication and heating. After sufficient reaction time, the solution was cooled to room temperature and filtered through a PES membrane of 0.2$\mu$m pore size. The resulting P3HT nanoparticle solution was inkjet printed onto cleaned plain glass substrates. Film preparation was aided by Jan Kosco from KAUST. After fabrication, the superoxide yield of the sample was measured and the data obtained is presented in Figure 9.7 alongside the superoxide yield data for the previous samples for comparison.

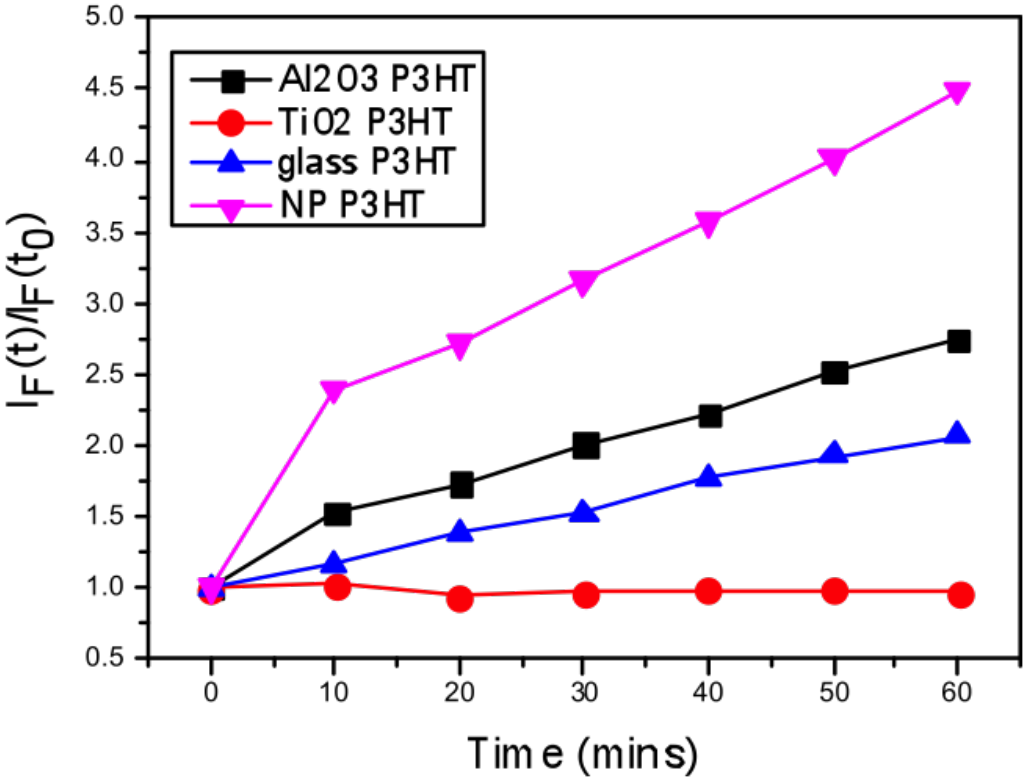


Figure 9.7: Superoxide yield plot for nanoparticle P3HT films. The previous superoxide data is added for comparative discussion.

The superoxide yield test, reveals that the nanoparticle film generates a higher magnitude of the reactive oxygen species compared to the other systems examined. As hypothesised earlier, this is likely the result of the increased surface area of the P3HT. Therefore, this data further sustains the correlation of surface area to superoxide generation. Where, surface area critically increases the absorption of incoming light and thus causes a greater yield of photo-excited electrons to form, that can then participate in the electron transfer reaction to oxygen. Hence, the observed superoxide yield rises as surface area is increased. Nanoparticle films thus demonstrate the most optimal surface for superoxide generation. In theory if the nanoparticle synthesis could be manipulated to generate smaller and more uniform particles with a narrow size distribution, the most optimal surface area of P3HT could be generated allowing for the highest yield of superoxide generation. Importantly, all the data so far highlights that superoxide can be detected from P3HT films and that the yield can be manipulated through substrate selection and material design. From this data it can also be suggested that the creation of a

P3HT nanoparticle suspension could be utilised for the desired application. The solution could be sprayed onto surfaces and then illuminated, the P3HT nanoparticles would then generate superoxide that could denature contaminants on the surface. The principle of this application is examined in the following section.

## 9.4 Simulating superoxide degradation action

The previous experiments have demonstrated the fact that superoxide is produced from P3HT thin-films and nanoparticle films. Now the ability of the superoxide generated from these systems to react with external species is examined. The fact that the emission intensity of the DHE probe increased with time as a function of exposure of P3HT films to oxygen and light suggests the superoxide is able to leave films and react with other species in solution. However, the probe is highly sensitive towards superoxide and so the concept needs to be expanded to another species as a proof of principle. From the previous work on perovskite films, the superoxide species has been clearly shown to react with the organic cation species methylammonium within the crystal structure. Additionally, work in the literature manipulated the reaction of potassium superoxide with methylammonium iodide to reinforce the degradation products of the reaction of methylammonium lead iodide with superoxide.[26] This work showed that the superoxide species was able to deprotonate the methylammonium component, resulting in the formation of methylammine and iodine. Consequently, the use of methylammonium iodide to imitate the presence of a contaminant on a surface or in a solution is used in conjugation with P3HT films. To simulate the application, a P3HT film is suspended in a sealed inert solution of methanol with MAI doped into the solution. The system is then exposed to dry air flux and illumination, to initiate the generation of superoxide from the films. As was used in the previous work on perovskites, NMR spectroscopy was implemented to monitor the change of methylammonium to methylamine. This conversion will only occur if the superoxide species is produced and sufficient amounts are able to leave the films and react with the MAI species in the solution. The NMR spectra of the solution before exposure to oxygen and light (Top spectrum) is shown whilst the NMR spectra of the solution after an hour of exposure with a glass/mp-$Al_2O_3$/P3HT system

(bottom spectrum) is also shown in Figure 9.8a.

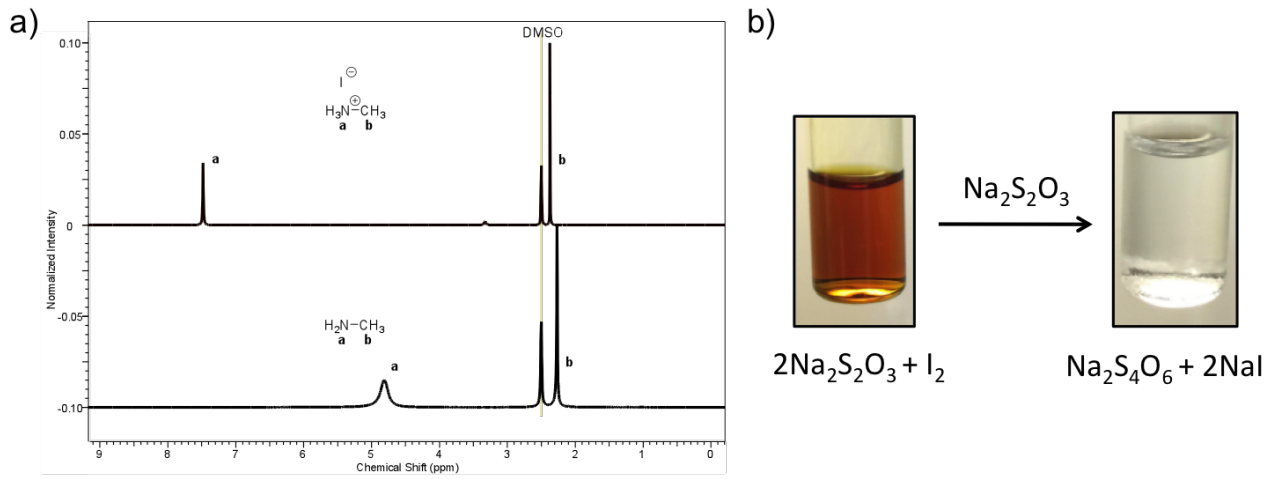


Figure 9.8: a) Proton NMR spectra for a P3HT film and MAI in methanol before exposure to oxygen and light (top spectrum) and after an hour of exposure (bottom spectrum). The shifts in the peaks corresponds to the deprotonation of methylammonium to methylamine. b) Orange solution obtained after exposure to oxygen and light. Attributed to the generation of iodine as the solution turns colourless after the addition of sodium thiosulfate.

The NMR data shows that before the simulation is exposed to oxygen and light that the MAI species is unreacted and is co-existing in the solution with the P3HT film with no consequence. The peak labeled a, is the proton environment associated with the nitrogen atom. Whilst the peak labeled b, are the methyl protons. Upon addition of light and oxygen (bottom spectrum), peak a, shifts upfield denoting the removal of a proton from the ammonium group. As expected the methyl group, peak b, remains unaffected with little to no shift in the environment observed. This is consistent with the reaction of superoxide with methyalammonium iodide. Consequently, this data confirms that the P3HT film can generate sufficient superoxide to deprotonate the MAI species. Furthermore, the solution when concentrated down using rotor evaporation, produced a dark orange solution. This is shown in Figure 9.8b. The origin of this colouration, was suspected to be due to the generation of iodine. Confirming this, was the implementation of the sodium thiosulfate test, which caused the solution to turn colourless (Figure 9.8b). This experiment further supports the fact that there is sufficient superoxide yield generated from P3HT films to react with another species in the system. This proof of principle experiment, supports the desired end application and allows for the next stages of using a range of other chemical species to see if the superoxide generated would be able to decompose these species and clean surfaces

or solutions.

### 9.4.1 Increasing the rate of superoxide action

The previous simulation demonstrated that the superoxide produced from a P3HT film could be harnessed to react with another species (MAI) in the solvent medium. The rate of reaction, will be a factor of the rate of superoxide production from the film. Therefore, it is hypothesised that the previous factors explored to manipulate superoxide production will impact the rate of removal of MAI from solution. To test this, the rate of production of iodine is monitored through UV/VIS spectroscopy. A unique peak at approximately 450 nm, corresponds to the presence of iodine in methanol. The amount of iodine in solution is correlated to the rate of reaction of superoxide with MAI as it is a product of this reaction. The faster the magnitude of this peak rises, the faster the rate of reaction of superoxide with MAI. Higher yields of superoxide from films, should increase the rate as the chance of a reaction collision between superoxide and MAI. In this experiment, a P3HT film is submerged in a methanol/MAI solution. To this, dry air flux and illumination is added and aliquots of the solution are taken at regular time intervals for UV/VIS spectroscopy to monitor iodine production as a function of time. It is important to note that, whilst the UV/VIS measurements occurred the dry air flux was ceased and the illumination was removed. Once the measurement was finished the aliquot was returned and the dry air flux and illumination resumed. The emission data for the glass/mp-$Al_2O_3$/P3HT system is shown Figure 9.9.

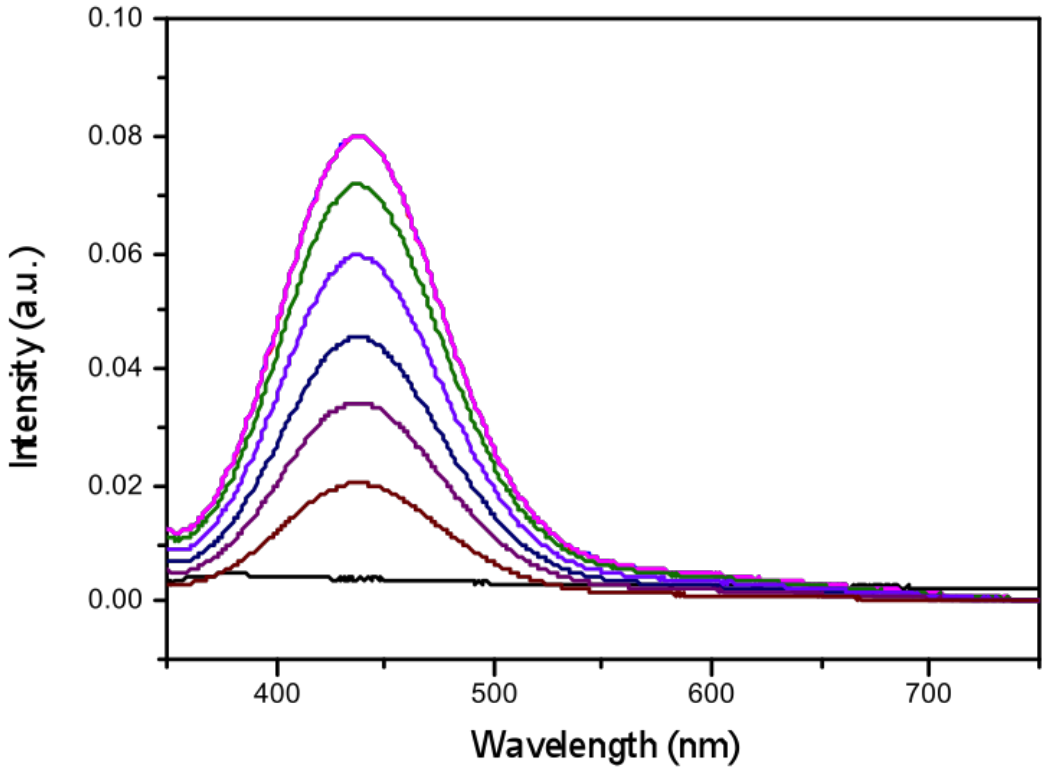


Figure 9.9: UV/VIS spectra for the generation of iodine from the reaction of P3HT films in an MAI/Methanol solution as a function of time exposure to oxygen and light illumination.

Figure 9.9, clearly shows that the intensity of the peak increases as a function of time under dry air flux and illumination. This translates to an an increase in the concentration of iodine and a reduction of MAI in solution. In combination with the superoxide yield tests, this sustains the fact that superoxide produced from the films reacts with the MAI dopant. Now, to monitor the rate of iodine evolution as a function of superoxide function the same protocol as previously described was employed, but the P3HT system was changed. Here, the systems previously explored, glass/P3HT, glass/mp-$Al_2O_3$/P3HT, glass/mp-$TiO_2$/P3HT and NP-P3HT films are employed. The rate of iodine evolution is plotted as a function of time by normalising the iodine concentration, likewise to the nomralisation used in the superoxide yield generation plots. The emission increase data from these samples is displayed in the figure below.

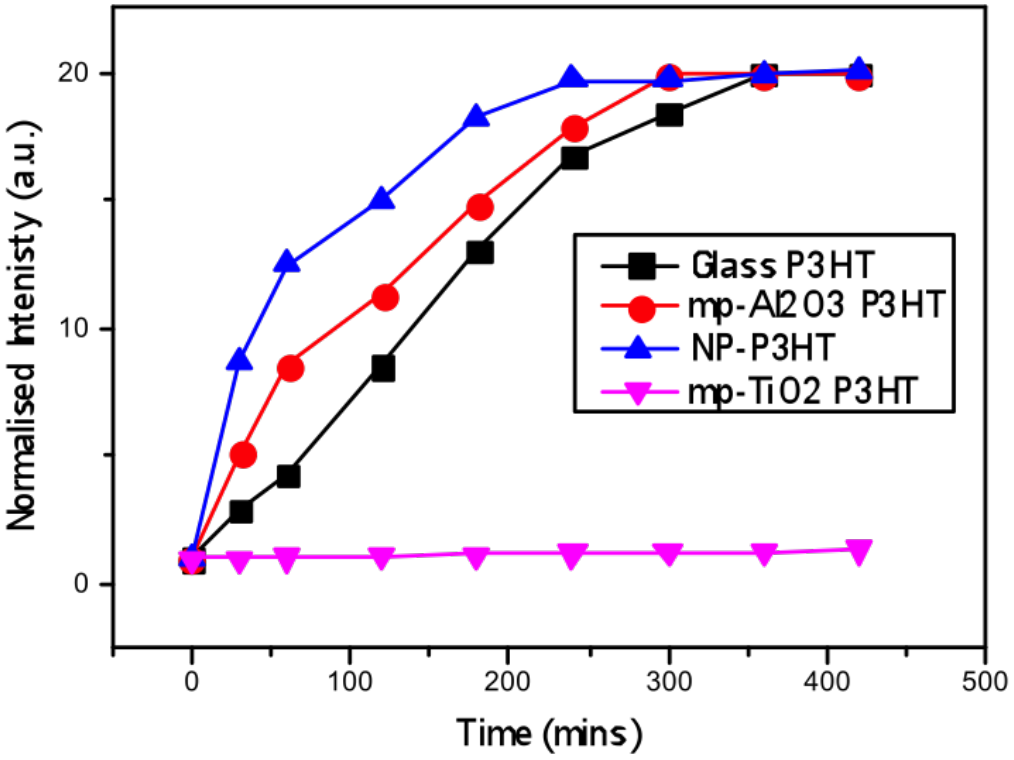


Figure 9.10: Normalised absorbance increase correlating to the increase in iodine in solution. Films of P3HT on plain glass, mp-$Al_2O_3$ and mp-$TiO_2$ are compared alongside the use of nanoparticle P3HT films.

Interestingly, the data confirms that there is a correlation between superoxide yield and the rate of iodine production (or MAI consumption). This is noted by the fact that as the sample is exchanged for a system that produces a higher yield of superoxide, the rate of iodine production increases. In the mp-$TiO_2$ based system, which produced the least amount of superoxide, demonstrates little to no superoxide reaction with MAI. As noted by the fact the normalised intensity doesn't increase as a function of reaction time. In contrast, all the other systems which displayed higher yields of superoxide generation show an increase in normalised emission intensity. As hypothesised the increase in emission intensity is proportional to the yield of superoxide generation. The nanoparticle P3HT film that had the highest yield of superoxide has the fastest increase. Whilst the glass/P3HT and glass/mp-$Al_2O_3$/P3HT systems produced less superoxide and demonstrated a slower increase in the normalised intensity. This data reinforces that for the desired application, maximisation of superoxide yields will be critical for the most

effective and efficient removal of contaminants. This applies to contaminants both on surfaces or within solutions.

## 9.5 Conclusions

In conclusion, the superoxide yield test has been used to probe the generation of the reactive oxygen species from the organic polymer, P3HT. It has confirmed that superoxide is produced when films are exposed to both dry air and illumination. The yield of superoxide can be manipulated through judicious choice of electron extraction layers and via maximising surface area. The experiments have shown that, introducing a favourable energy off-set to allow for electron injection from P3HT to mp-$TiO_2$ leads to a reduction in the yield of superoxide. The mechanistic action is ascribed to be similar to that of the formation of superoxide in perovskite materials. Where photo-excitation promotes a ground state electron into the CB, that can then undergo electron transfer to molecular oxygen forming superoxide. By adding an electron extraction layer a competitive pathway is introduced that reduces the number of electrons participating in the parasitic electron transfer reaction. Thus superoxide yields are lowered. Surface area has again been identified as a significant factor in the generation of superoxide. Increasing the surface area of films via introducing an electronically inert mesoporous scaffold (mp-$Al_2O_3$) or via changing the morphology through synthesis (NP-P3HT). In both cases the yield of superoxide generated increases relative to a P3HT thin film fabricated onto a plain glass substrate. This is a consequence of the fact that films with higher surface area have a greater ability to absorb photons that result in more electrons being excited and that are then able to undergo the electron transfer reaction to oxygen.

Additionally, the proof of principle that the superoxide generated from P3HT films could be utilised to react with bacteria was simulated using methylammonium iodide in methanol. The superoxide was shown to react with the salt, leading to it's decomposition into methylammine and iodine. The rate of this reaction can be enhanced through using P3HT films with greater yields of superoxide. For the desired application, where either a film could be added to a

contaminated solution or a nanoparticle suspension could be sprayed onto a contaminated surface and then illuminated the yield of superoxide will need to be maximised. This will ensure that the most effective and time efficient removal of the contaminant species can be achieved. The simulation employed has demonstrated that nanoparticle P3HT systems provide the best platform for this, with the highest surface area and consequently the highest yields of superoxide. These films caused the fastest breakdown of the MAI salt and have proven that the concept of using oxygen, light and a P3HT film for degradation action may be possible. Next, studies examining the potency of superoxide generated via this method on a range of potential contaminants need to be conducted. Key factors including the rate of degradation of the contaminant, the extent of degradation and the by products formed will be need to determine the success of this application. A potential future example, could arise from systems with biological contaminants, as these are widely known to denature in the presence of superoxide. Thus provided sufficient superoxide can form from P3HT suggests this could be a key area where this application could be successful.

# References

[1] S. Korshunov, J. A. Imlay, *J. Bacteriol.*, 2006, **118**, 6326 – 6334.

[2] L. C. Seaver, J. A. Imlay, *J. Biol. chem.*, 2004, **279**, 4874248750.

[3] J. A. Imlay, *Annu Rev Microbiol.*, 2003, **57**, 395418.

[4] K. B. Beckman, B. N. Ames., *J Biol Chem.*, 1997, **272**, 1963319636.

[5] M. T. Molsen, *Plenum Press; New York*, 1994.

[6] K. Passalacqua, N. Bergman, J. Lee, D. Sherman, P. Hanna, *J Bacteriol.*, 2007, **189**, 3996 – 4013.

[7] M. Gu, J. Imlay, *Mol Microbiol.*, 2011, **79**, 11361150.

[8] M. Fujikawa, K. Kobayashi, T. Kozawa, *J. Biol. Chem.*, 2012, **9**, 11361150.

[9] E. O'Regan, T. Quinn, J. Frye, J. Pags, S. Porwollik, P. Fedorka-Cray, M. McClelland, *Antimicrob Agents Chemother*, 2010, **54**, 367 – 374.

[10] T. van der Straaten, L. Zulianello, A. van Diepen, D. Granger, R. Janssen, J. van Dissel, *Infect Immun.*, 2004, **72**, 996 – 1003.

[11] E. Yousif, R. Haddad, *SpringerPlus*, 2013, **2**, 395.

[12] R. J. F., R. Bengt, *Journal of Polymer Science: Polymer Chemistry Edition*, 1974, **12**.

[13] Y. Aoyama, O. Douhret, P. Leclre, D. Moerman, J. Mizukado, H. Suda, R. Lazzaroni, Y. Yoshida, *Organic Electronics*, 2017, **43**, 142 – 147.

[14] A. Tournebize, P.-O. Bussire, A. Rivaton, J.-L. Gardette, H. Medlej, R. C. Hiorns, C. Dagron-Lartigau, F. C. Krebs, K. Norrman, *Chemistry of Materials*, 2013, **25**, 4522–4528.

[15] I. Fraga Domnguez, P. D. Topham, P.-O. Bussire, D. Bgu, A. Rivaton, *The Journal of Physical Chemistry C*, 2015, **119**, 2166–2176.

[16] A. Umut, E. Hans-Joachim, N. Peter, M. Michael, S. Stefan, E. Klaus, P. Heiko, C. Thomas, *ChemPhysChem*, 2014, **16**, 428–435.

[17] R. Pacios, A. Chatten, K. Kawano, J. Durrant, D. Bradley, J. Nelson, *Advanced Functional Materials*, 2006, **16**, 2117–2126.

[18] T. Wang, A. J. Pearson, D. G. Lidzey, *J. Mater. Chem. C*, 2013, **1**, 7266–7293.

[19] Y. Aoyama, T. Yamanari, T. N. Murakami, T. Nagamori, K. Marumoto, H. Tachikawa, J. Mizukado, H. Suda, Y. Yoshida, *Polymer Journal*, 2015, **47**, 26–30.

[20] M. Hayyan, M. A. Hashim, I. M. AlNashef, *Chemical Reviews*, 2016, **116**, 3029–3085.

[21] L. Chen, J. Mizukado, Y. Suzuki, S. Kutsuna, Y. Aoyama, Y. Yoshida, H. Suda, *Chemical Physics Letters*, 2014, **605**, 98 – 102.

[22] H. Shimizu, M. Yamada, R. Wada, M. Okabe, *Polymer Journal*, 2008, **40**, 33–36.

[23] Y.-C. Huang, Y.-C. Liao, S.-S. Li, M.-C. Wu, C.-W. Chen, W.-F. Su, *Solar Energy Materials and Solar Cells*, 2009, **93**, 888 – 892.

[24] S. Cataldo, B. Pignataro, *Materials*, 2013, **6**, 1159–1190.

[25] M. Islam, M. Islam, A. Ismail, H. Baerwolff, *Optics and Photonics Journal*, 2013, **3**, 28 – 32.

[26] N. Aristidou, I. Sanchez-Molina, T. Chotchuangchutchaval, M. Brown, L. Martinez, T. Rath, S. A. Haque, *Angewandte Chemie International Edition*, 2015, **54**, 8208–8212.

# Chapter 10

# Conclusions and Future Outlook

For a number of years, hybrid lead halide perovskites have relied on their impressive power conversion efficiencies, generating enormous interest in the field of photovoltaics. However, significant issues surrounding long term material stability have plagued their viability for optoelectronic applications. Initially, the mechanistic understanding of the degradation was poorly understood. Insights into the role of temperature, UV exposure and high humidity displayed revealed the materials sensitivity towards these environmental stresses and a common degradation component as lead halide derivatives. Critically, the archetypal methylammonium lead iodide species was shown to be highly sensitive towards oxygen and light stress. The material breaks down rapidly owed in part to the generation of the highly reactive oxygen species, superoxide. The main aims of this work was to improve the fundamental understanding of the factors influencing superoxide production and the sensitivity towards oxygen and light.

It has been determined that judicious choice of the electron extraction layer (ETL) can significantly impact the stability of MAPI towards oxygen and light. Improving the ability of a material to extract electrons from the perovskite layer, was proven to lower superoxide yields and thus enhance stability. ETL's provide a competitive pathway for photo-excited electrons and increasing the driving force for separation leads to more facile extraction and greater yields of electrons participating in this pathway. Moreover, the influence of surface area was demonstrated by changing the morphology of ETL from compact to mesoporous. Higher surface

areas lead to more surface contacts between the ETL and the perovskite phase. Consequently, more electrons per area can be extracted and again leads to fewer electrons forming superoxide.

Despite the promising results of improving electron extraction, the perovskite material still displays sensitivity towards the degradation conditions. More importantly, the work has shown that even swapping the organic cation to species that are less reactive towards superoxide, the reactive oxygen species is still generated. This suggested a fundamental feature of the material contributes towards the formation of the species. Isothermal gravimetric analysis, first pointed to the rapid diffusion of oxygen into the perovskite lattice. Then ToF-SIMS experiments illuminated the ubiquitous presence of oxygen throughout the system after only a short period of exposure to dry air flux. Both of these features alluded to the fact oxygen infiltrates the perovskite crystal and on a time scale consistent with the observed rates of degradation. Crystal size was manipulated to demonstrate that the size of the crystals had no impact on oxygen diffusion rates, but did influence degradation rates. Further identifying MAPI as having an intrinsic feature responsible to the generation of superoxide. Defects have previously been shown to influence performance and as such were examined through computational experiments to probe their impact on stability. From this, it was shown that iodide vacancies are the preferred sites for superoxide formation. Oxygen diffuses into the crystal, occupies an iodide vacancy where it then restores the octahedra structure by accepting an electron and forming superoxide. This rationalised the experimental results, smaller crystals have higher defect densities as surfaces are generally more defect rich, and also the oxygen diffusion pathway into the bulk is shorter. Both factors leading to greater yields in superoxide formation in smaller crystallites.

On the basis of the previous findings, a new method to prolong perovskite life-time was developed through defect passivation. A salt treatment was applied post fabrication, that facilitates the removal of the potent iodide vacancies that preferentially form the superoxide species. Noteworthy from the findings, is the fact that only iodide containing salts could stabilise the films, whilst changing the counter cation or the halide species resulted in no stabilisation. Sustaining the fact that iodide vacancies are key to the susceptibility of perovskite towards

oxygen and light. The experiments also depict a strong concentration dependence on the impact of the stability enhancement. Combined with the fact that the salt treatment was shown to not impact oxygen diffusion, the role of the treatment does alleviate the vacancies and not simply block oxygen entering the films. The works have also shown that any method to reduce the presence of iodide vacancies can reduce the superoxide yield and enhance stability. The defect density can be observed through the steady state photoluminescence, where defect removal generates films with fewer trap states and thus higher emission intensities and life-times.

Moving towards real world environmental conditions, the impact of the role of moisture upon the oxygen and light degradation was explored. Perovskite films were preloaded with variable quantities of water and the rates of degradation and superoxide yield generation monitored. These experiments have highlighted the fact that water acts to accelerate the degradation rate, increasing water content leads to faster rates of degradation. Moreover, the data has shown that this is not only due to increasing yields of superoxide but also to increasing the reactivity of the species. Combining the experimental results with computational simulations revealed that the presence of water serves to stabilise the superoxide species and aids in the reduction via protonation that in turn enhances the overall potency of the degradation. The impact of these findings were carried forward onto devices, where the PCE was found to rapidly decline in combined air, light and moisture environments. Again a strong correlation to the water content and the rate of PCE loss was observed.

In order to consider the findings that bromide containing perovskite photo-absorbers demonstrate enhanced stability, thin film perovskites with varying bromide content were fabricated and their degradation studied. Through systematic investigations, it was shown that increasing bromide content increased stability towards oxygen and light. Initially, it was suspected that this tolerance was derived from the fact that bromide substitution removes iodide defects that form superoxide. However, from computational experiments it was proven that bromide vacancies are also favourable sites for superoxide formation. The difference lies in the structural stability enhancement of increasing bromide content. Adding bromide causes a lattice contraction leading

to enhanced H-bonding and increase in structural strength towards oxygen and light degradation. Moreover, the computational findings combined with the experimental results suggests that it is harder to form bromide vacancies. Critically, the energetics of iodide vacancies also becomes less favourable in mixed halide samples. As such, films with higher bromide content have lower defect densities, and thus demonstrate enhanced tolerance to oxygen and light stress.

For perovskite photo-absorbers in the application of optoelectronics, the production of superoxide is deeply problematic. Short operational life-times and rapid material degradation occur as a consequence. Despite judicious design concepts and novel defect removal, the species is persistent and forms readily wherever systems are exposed to both oxygen and light. However, the concept of utilising superoxide for productive gain was explored. Even though perovskites have demonstrated an exceptional ability to produce superoxide, the polymer P3HT was examined due to its insolubility in polar media allowing for greater versatility in end applications. A potential application, relies on the use of films or nanoparticle suspensions in a contaminated media. For example a liquid may contain a contaminant species, which when the P3HT film is illuminated and exposed to oxygen produces superoxide that in turn can denature the contaminant. To review this novel idea, the ability of superoxide generation from P3HT was explored. The data showed that films can produce the reactive oxygen species and there was a strong correlation to surface area. Increasing the surface area of the film either through a mesoporous scaffold or through nanoparticle morphology increase superoxide yields. Furthermore, annealing was shown to enhance photo-activity and increase superoxide yields. Having established the fact the films can generate superoxide, a simulation of the desired application was generated. Here a film was suspended in a solution containing methylammonium iodide. The superoxide from the films could then deprotonate the species leading to the formation of methylamine and iodine. Where, the rate of iodine generation was first used to show the reaction was possible but later to show that films that generate more superoxide had faster rates of deprotonation. Overall, the experiments have confirmed that it is possible to generate superoxide from P3HT and harness it to remove another species in a solution. Developing films with greater yields of superoxide will lead to a greater ability to remove unwanted material

from systems and possibly allow for a real world application. It is possible that a system could be developed where a solution containing P3HT nanoparticles could be sprayed onto surfaces and then illumination and oxygen flow could allow for superoxide to be generated, that in turn would react and destroy any contaminants on the surface.